Synthesis, structural characterization and functional properties of Metal-Organic Frameworks based on poly(azolate) ligands

By

Alessandro Cimino

Università degli Studi dell'Insubria

Dipartimento di Scienza e Alta Tecnologia – Como

Supervisor: Dr. Angelo Maspero

Co-supervisor: Prof. Simona Galli

XXIX Ciclo di Dottorato in Scienze Chimiche e Ambientali

I've seen things you people wouldn't believe.

Roy Batty

List of abbreviations and acronyms

APT	attached proton test
aq	aqueous
ATR	attenuated total reflectance
CP	coordination polymer
CP MAS NMR	cross polarization magic angle spin nuclear magnetic resonance
DBU	1,8-diazabicyclo[5.4.0]undec-7-ene
DFF	2,5-diformylfuran
DEF	N,N-diethylformamide
DME	dimethoxyethane
DMF	N,N-dimethylformamide
DMSO	dimethyl sulfoxide
DMSO-d_6	deuterated dimethyl sulfoxide
DSC	differential scanning calorimetry
DRIFTS	diffuse reflectance infrared fourier transform spectroscopy
EDG	electron-donating group
EWG	electron withdrawing group
FG	functional group
FMOF	fluorous metal-organic frameworks
FN-PCP	fluorous non-porous coordination polymers
FW	formula weight
GC-MS	gas chromatography – mass spectrometry
H_2BPEB	1,4-bis(1*H*-pyrazolylethynyl)-benzene
H_2BPEB_{d4}	1,4-bis(1*H*-pyrazolylethynyl)-benzene-*d4*
H_2BPEBF	1,4-bis(1*H*-pyrazolylethynyl)-2-fluorobenzene
H_2BPEBF_2	1,4-bis(1*H*-pyrazolylethynyl)-2,3-difluorobenzene
H_2BPEBF_4	1,4-bis(1*H*-pyrazolylethynyl)-tetrafluorobenzene
H_3BTP	1,3,5-tris(1*H*-pyrazol-4-yl)benzene
H_2BTB	1,4-bis(1*H*-tetrazolyl)-benzene
H_2FBTB	1,4-bis(1*H*-tetrazolyl)-tetrafluorobenzene
HFMTB	1-(1*H*-tetrazolyl)-perfluorobenzene
HMF	5-hydroxymethyl-2-furfural
IC	integrated circuit
IR	infrared spectroscopy
LDA	lithium diisopropylamide
MOF	metal-organic framework
NMR	nuclear magnetic resonance
OAc	acetate
PECVD	plasma-enhanced chemical vapour deposition
Py	pyridine
Pz	pyrazole
PXRD	powder X-ray diffraction

RT	room temperature
SBU	secondary building unit
STA	simultaneous thermal analysis
TEA	triethylamine
Tf	triflate
TFA	trifluoroacetic acid
TGA	thermogravimetric analysis
THF	tetrahydrofuran
TLC	thin layer chromatography
TMS	tetramethylsilane
TMSA	(trimethylsilyl)acetylene
Tz	triazole
Ttz	tetrazole
VT-PXRD	variable temperature powder X-ray diffraction
XRD	X-ray diffraction

Contents

Preface

This Thesis work has been devoted to the isolation and characterization of non fluorinated and fluorinated Metal-Organic Frameworks (MOFs) and Non-Porous Coordination Polymers (N-PCP) to be tested for a number of practical applications.

In the firsts two **Chapters**, a brief introduction on the history of MOFs (**Chapter 1**), on the features of azolato- and poly(azolato)-based organic linkers (**Chapter 2**) and on the properties of fluorine and organofluorine compounds (**Chapter 2**) is exposed.

In **Chapter 3** the synthesis of six new non-fluorinated and fluorinated poly(pyrazolato)-, poly(tetrazolato)-, and tetrazolato-derivatives is described. Each linker has been designed for the specific application to be tested, namely: Low dielectric constant (low-κ) dielectrics, molecular and dipolar rotors or gas adsorption.

In **Chapter 4** the synthesis and characterization of a series of fluorinated and non fluorinated poly(pyrazolato)- poly(tetrazolato)-, and tetrazolato-based MOFs and N-PCPs are presented. The dielectric and CO_2 adsorption properties of these new compounds have been investigated. In this context, the well known **FMOF-1**, the first fluorous MOF ever appeared in literature, has been successfully added to these compounds as a potential low-κ dielectric material.

The synthesis and characterization of the first two Zn(II)-based MOFs ever used as molecular and dipolar rotors is presented in **Chapter 5**. The investigation on the rotational speed of their aromatic core has been performed with solid state NMR studies.

Finally, using four known poly(pyrazolato)-based MOFs, we have tested their catalytic activity in the selective oxidation of hydroxymethylfurfural to diformylfuran. More important, we have disclosed the catalytic mechanism by means of DRIFT and *in vacuo* FT-IR spectroscopy. All the FT-IR measurements and catalytic results are discussed in **Chapter 6**.

Chapter 1
Metal-organic frameworks: the molecular meccano

1.1 Introduction

Synthetic zeolites are microporous or mesoporous crystalline inorganic compounds, generally aluminosilicates, which have become extremely used in advanced industrial processes as detergents, adsorbents, desiccants and heterogeneous catalysts[1], due to the fact that they couple permanent porosity to extraordinary features[1] such as thermal and chemical robustness. The existence of permanent porosity leads to interesting peculiarities: *i*) high surface area and adsorption properties, *ii*) moderate control of the adsorption properties, and *iii*) moderate possibility to tune the acidity/basicity of the active sites. The electric fields that are generated in the pores[2], combined to the electronic confinement of the guest species[3], can be exploited, *e.g.*, for the activation of the substrate in a catalytic reaction. In spite of their ubiquity, due also to their all-inorganic nature, their performances are somehow limited by the stiffness of their framework, the features of which, above all pore size and functionalization, cannot be readily modified using self-assembly approaches.

Twenty years ago, Yaghi and coworkers first described[4] a new family of compounds, denominated "Metal-Organic Frameworks" (MOFs). Since then, starting from considering them as an "academic curiosity", MOFs have become one of the most rapidly developing areas in chemistry and materials science (**Figure 1.1**).

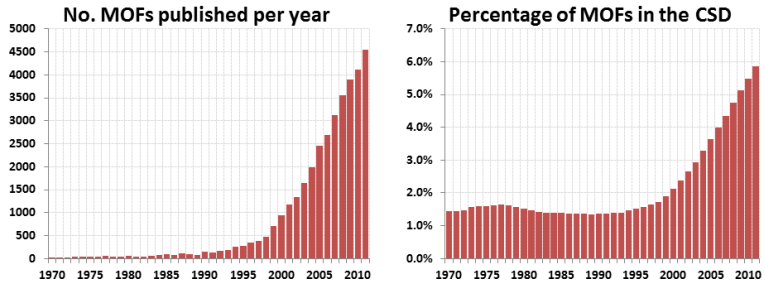

Figure 1.1: Histograms depicting the number of MOFs published *per* year since 1970 (left), and the percentage increase in the number of crystal structures of MOFs deposited in the Cambridge Structural Database since 1970 (right) [5].

MOFs, also addressed as porous coordination polymers (PCPs), are hybrid porous materials constructed with an organic linker and an inorganic moiety (usually called SBU, Secondary Building Unit), that can be a simple metal ion or an oxo-metallic cluster. The connection, by coordination bonds, between these two building units generates 1-D, 2-D or 3-D frameworks the topology and features of which depend upon the nature of the organic and inorganic moieties. The great interest generated by this class of compounds has lead to an immediate request for "readily available MOFs" for practical applications: for example, the so-called zeolitic imidazolate frameworks (ZIFs) are industrially prepared by a number of industrial suppliers as BASF under the name of BASOLITE™, and commercially available from Sigma Aldrich[6].

The structural and functional properties of MOFs can be potentially modulated depending upon the stereochemistry requirements of the metal ions and the size, shape, functionalization of the organic spacer (and combinations thereof), to provide researchers with a wide library of building units to reach their goals. Considering the organic moiety, its properties can be modified by substituting *e.g.* one CH group with one atom of nitrogen, or substituting one single bond with a double or triple bond. Modifications of this kind influence the shape (*e.g.* coordination angles) and size (*e.g.* expansion or shrinkage) as well as the electronic properties of the ligand. Another important feature of organic linkers is the possibility of functionalization: indeed, the perviousness and decoration of the pores, *i.e.* their electronic and steric properties, can be easily modulated by adding the desired functional group onto the skeleton of the ligand[7]. On the other side, the inorganic building unit

imparts to MOFs some of the peculiar properties of zeolites, such as catalytic activity and enhanced thermal and mechanical robustness[8] (with respect to that of the ligand alone).

The synthesis of MOFs is performed by directly reacting the inorganic moiety and organic linker, but the ways this characteristic self-assembly can be achieved are quite different (see **Section 1.2**). Typically, the reaction solvent does remain trapped in the pores during the self-assembly. With the exception of first generation MOFs[19], which do not possess permanent porosity, removal of the solvent by thermal activation does not affect the stability of MOFs, and yields high surface area materials that have deeply interested the academic and industrial realms. The challenge to obtain the "champion", the one possessing the highest surface area, begun in 1998 with the publication of the first MOF with permanent porosity, namely $Zn(BDC)\cdot(DMF)\cdot(H_2O)$ (BDC = 1,4-benzenedicarboxylate), showing a BET specific surface area of 310 m^2/g[20]. Since then, a number of candidates have appeared in the literature with values of specific surface area reaching 3800 m^2/g in 2005[21], and the remarkable 5200 m^2/g in 2009.[22] Among these materials, a representative set of which are listed in **Table 1.1**, the most renowned are MOF-5[23] (especially in its anhydrous form[24]), MOF-177[24,25], MIL-101,[21] HKUST-1[26], UMCM-1[27] and UMCM-2.[22]

MOF	BET specific surface area (m^2g^{-1})
PCN-61[9]	3000
$Cu_{24}(TPBTM)_8(H_2O)_{24}$[10]	3160
MOF-5[23]	3800
UMCM-1-NH_2[11]	3920
PCN-66[9]	4000
$Be_{12}(OH)_{12}(BTB)_{24}$[12]	4030
UMCM-1[27]	4160
MIL-101[21c]	4230
Bio-MOF-100[13]	4300
MOF-205[14]	4460
MOF-177[25]	4750
DUT-23-Co[15]	4850
PCN-68[16]	5110
UMCM-2[22]	5200
NU-100[17]	6140
MOF-210[14]	6240
NU-109E[18]	7010
NU-110E[18]	7140

Table 1.1: BET specific surface area for highly porous MOFs acquired 77 K.

One of the first challenges in the construction of ultra-high specific surface area MOFs was to avoid the collapse of the structure upon solvent removal[18]. Recently, new studies have been performed in this respect and new procedures, *e.g.* activation by supercritical CO_2, have been tested[28], allowing the isolation of MOFs with ultrahigh specific surface area. The next challenge is to reach the theoretical maximum specific surface area, calculated to be around 14600 m^2/g.[18]

Another key feature that MOFs should possess is an adequate degree of crystallinity: this characteristic is completely fulfilled by synthetic zeolites, but their all-inorganic nature implies lack of structural diversity and flexibility, while MOFs can overtake also this limit, by tuning the organic spacer and the inorganic SBU.

Why the high specific surface area of MOFs generates great excitement? In gas adsorption and separation applications, pore volume is important, but it loses efficacy if the interactions between the walls of the host and the guest molecules are negligible. Tuning the dimension and shape of the pores concurs to increase the interactions needed for a satisfactory uptake of weakly interacting gases[29].

The overall features described above can be exploited at the industrial level for a number applications. The first obvious applications are gas storage and separation: in this context, due to the continue increasing of anthropogenic CO_2 in the atmosphere, manifold studies have been devoted to CO_2 capture and storage[30,31]. Elimination of CO_2 from the atmosphere is not the only problem to which MOFs could be the solution: the increasing world-wide need for energy pushes scientists to develop new technologies based on low pollutant gases as CH_4 and H_2: more than CH_4, H_2 needs extreme conditions of pressure or temperature to be stored in reasonable quantities, *e.g.* as compressed gas in the range of 200-700 atm or liquefied and stored at a temperature of 20.5 K; these conditions are unworkable for practical applications but, thanks to recent progresses, the possibility to build up a molecular sponge for H_2 is becoming real[32]. The concept of molecular sponge can be exploited towards other important applications, like adsorption and trapping of organic pollutant molecules and desulphurization and denitrogenation of fossil fuels[33], as well as capture

and breaking down of nerve agents, mustard gas and, in general, chemical weapons[34]. The adsorption properties can be combined with direct interactions between the MOF structure and the substrate for chromathography[35]. The application of MOFs is not limited to the storage of gases for energetic purposes, but can be also extended to the direct storage of energy and its conversion at positive or negative electrodes in Li ion batteries or supercapacitors[36]. Another correlated implementation is the use of MOFs as electrocatalysts for fuel cell applications[36b]. MOFs have been also exploited as photo-catalysts in redox reactions, as water splitting and photoreduction of CO_2, and solar fuel production[37]. Moreover, the fact that the metal ions can possess exposed coordination sites allows the use of MOFs as heterogeneous catalysts[38], as biomimetic catalysts and for bio-related applications[39]. The possibility to combine the properties of the organic linker and the inorganic SBU provides a fascinating opportunity for designing novel luminescent materials exploiting the intrinsic luminescence of some metal ions, in particular lanthanides[40], and the luminescence features of some organic linkers[41]. The last, but not least, applications quoted in this overview are those regarding MOFs as electrically conductive[42], non-conductive[43] or semiconductive[44] materials.

As anticipated in the **Preface**, the primary aim of this Thesis is the use of fluorinated or non-fluorinated poly(azolate) bridging ligands, in particular with nitrogen-donor rings such as pyrazole, triazole and tetrazole, for applications as low-κ dielectrics, catalysts, adsorbents and molecular rotors. Pyrazolate-based linkers were chosen because they impart high stability to the resulting MOFs[45]. Regrettably, the synthesis of pyrazole and poly(pyrazole) derivatives is more difficult than that of the corresponding carboxylated counterparts:. Hence, to follow the aim instructed by the research topic, tetrazole derivatives were also studied, even if tetrazole shows lower thermal stability than pyrazole (**Chapter 2**). Triazole derivatives were studied as well to widen the screening of poly(azolate) ligands as spacers.

The next **Chapters** of this Thesis are focused on the synthesis and characterization of new poly(azole)-based ligands (**Chapter 3**) and on their coupling to a number of late-transition metal ions

leading to new CPs and MOFs (**Chapter 4-6**). All the compounds presented were fully characterized and studied for targeted applications, depending on their chemico-physical properties (hydrophobicity, structural motif, functionalization, *etc*.), namely as: low-dielectric constant materials, CO_2 adsorbents, molecular rotors, and catalysts.

1.2 Playing with the Molecular Meccano

Despite "Meccano" was invented in 1898 and patented in 1901[46], almost one century has passed before scientists could play in an analogous way with atoms and molecules. Meccano allows builders to fabricate whatever they want, *e.g.* a piece of a wall, a component of a crane, of a truck, *etc*., by selecting the correct piece for the particular purpose. In the same way, scientists can choose the organic and inorganic building units which will most likely lead to the target crystal structure. As in the case of Meccano metal pieces, the organic linker can be chosen because of its shape, geometry and intrinsic properties (*e.g.* for the Meccano pieces the number of holes, the length and bending ability; for the organic linker the steric, electronic and coordination properties); the screw and nut are simulated by the inorganic building units, since they direct the overall crystal structure as a function of their stereochemical preferences.

The first important aspect that must be considered for the synthesis of MOFs are the reaction conditions: in the case of Meccano, the type of screwdriver is important to fix the object; similarly, the reaction conditions must be wisely chosen in order to achieve the desired product. Unfortunately, this prediction is a very challenging issue that depends upon solvents, co-solvents, reagents, time, temperature, *etc*.

There are several reaction pathways for the construction of MOFs, ranging from conventional synthesis, solvothermal or hydrothermal reactions, microwave-assisted synthesis, electrochemical synthesis and post-synthesis modifications[47]. The synthetic pathway must be carefully selected, because different MOFs can be obtained from the same starting materials. Moreover, the reaction conditions have a strong impact on the degree of crystallinity and may have an important effect on

yield, crystallite size and morphology, pore occupation, *etc.* The incredible rush to the isolation of MOFs with new crystal structures and improved functional properties has led, as a side effect, to the rapid discovery of more precise and efficient synthetic strategies[47]. Prior to the 1980s, metal-organic chemistry was almost completely devoted to the isolation and characterization of coordination compounds (*e.g.*, Werner complexes[48]). The first idea for the construction of open frameworks based on the so-called node-space approach was proposed by Hoskins and Robson in 1989 (exactly 101 years after the invention of Meccano). The two scientists connected a tetrahedral metal ion (*e.g.* Zn^{2+}) to a spacer (*e.g.* the cyanide anion) to build up an open structure with the same structural topology of diamond (as in $Zn(CN)_2$, or [Cu(4,4',4'',4'''-tetracyanotetraphenylmethane)]$BF_4{\cdot}xC_6H_5NO_2$)[49]. After these pioneering examples, to better exploit the bridging ability of the ligand, polytopic organic linkers were used, *e.g.* 4,4'-bipyridines, the coordination mode of which is close to that of the cyanide anion, but extending the distance between the two inorganic nodes. This should grant larger pores, to the crystal structure, with respect to those of synthetic zeolites and metal cyanides[50].

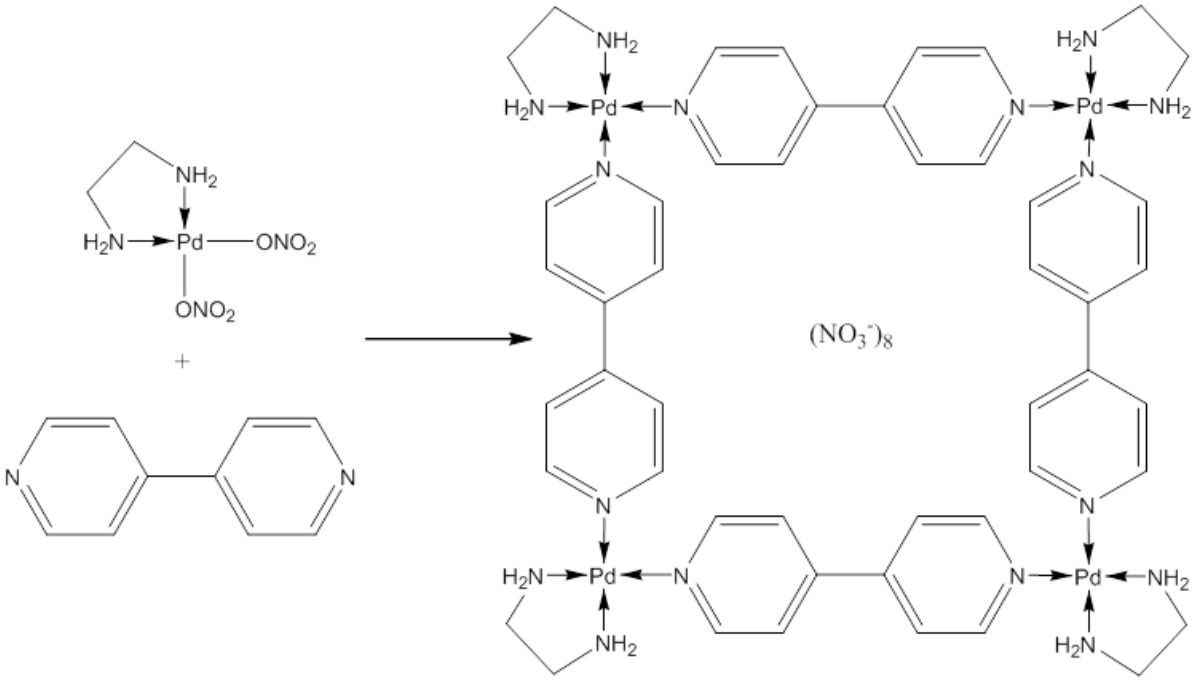

Scheme 1.1: The construction of "molecular squares" using ethylendiamine as capping agent and 4,4'-bypy as ligand in a Pd(II) complex[51].

The network topology of these compounds is strictly correlated to the stereochemical properties of the inorganic node, as well as to the nature (dimension, stereochemistry, hapticity, *etc*.) of the ligand. As a mean to control the framework topology, Fujita *et al.* used a "capping agent" (usually a chelating agent such as ethylendiamine) (**Scheme 1.1**) that blocked two specific coordination sites of the metal ion, "obliging" the ligand to coordinate the free positions[51].

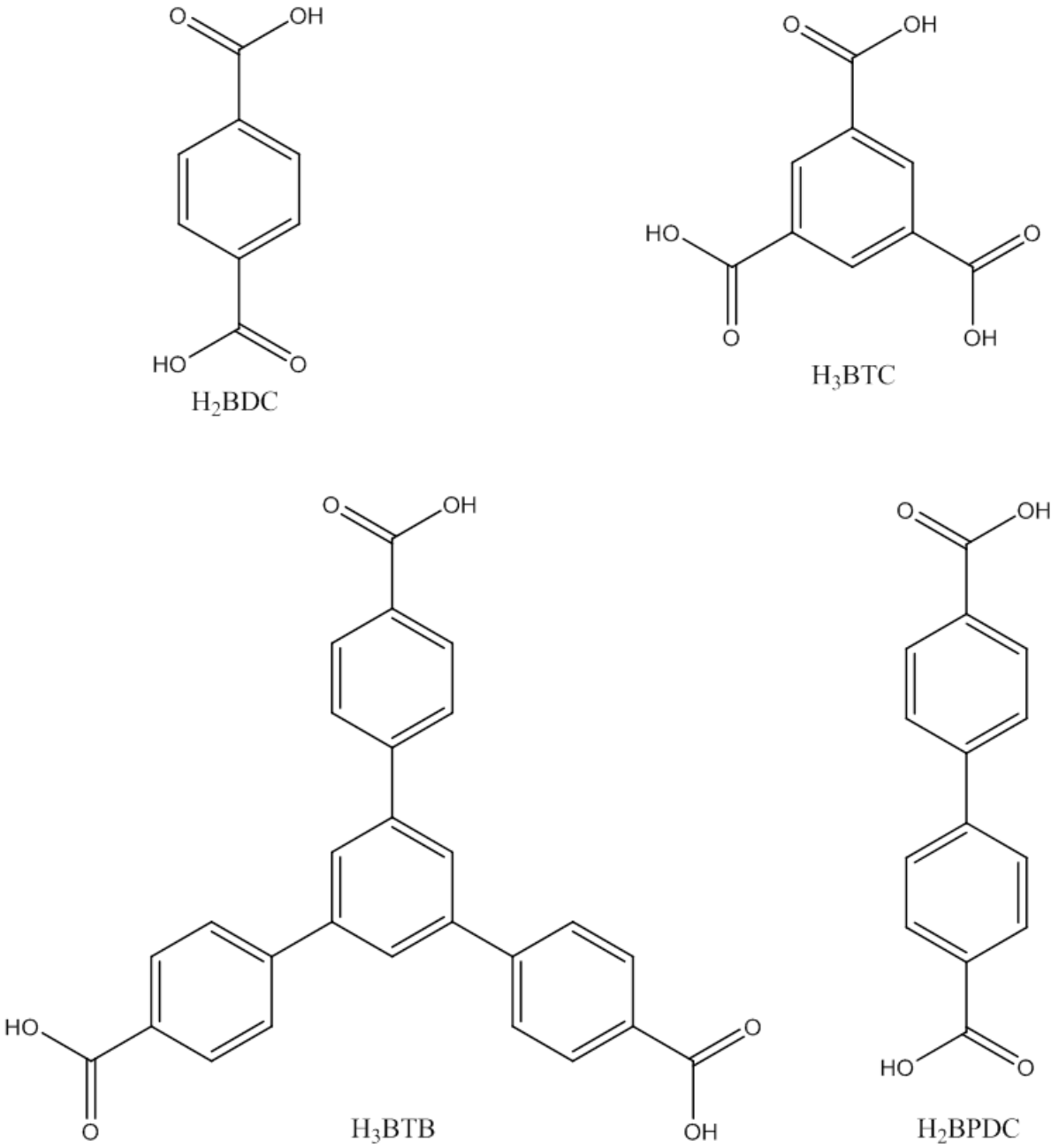

Scheme 1.2: Examples of carboxylate-based ligands. **H_2BDC**: benzene-1,4-dicarboxylic acid; **H_3BTC**: benzene-1,3,5-tricaboxylic acid; **H_3BTB**: 1,3,5-tris(4-carboxyphenyl)benzene; **H_2BPDC**: 4,4'-biphenyldicarboxylic acid.

As easily observable, 4,4'-bipyridines have been, for a long period, one of the most attractive types of linkers for the generation of 1-D chains[52] or ladders[53], 2-D grids[54] and 3-D frameworks[55]. Worthy of note, in these families of compounds with neutral bridging ligands the positive charge of the metal ion is balanced by the anions originating from the starting metal salt, *e.g.* NO_3^-, Cl^-, BF_4^-, SO_4^-, *etc*. Unfortunately, even if Kitagawa *et al.* were able to isolate the first porous 4,4'-bipyridine-based derivative in 1997[19], permanently porous frameworks of this type were scarce at the time, because they typically underwent a degradation with loss of crystallinity during exchange or removal of guest molecules[56].

Polytopic carboxylate-based ligands (**Scheme 1.2**) were the first solution to this problem: in the mid-1990s, they knew a quick rise in their use for the synthesis of MOFs, because: *i)* they can be easily deprotonated, so they can directly balance the charge of the metal ions; *ii)* they are affordable by either commercial suppliers, or synthetic pathways, and *iii)* they can bind the inorganic SBU in different ways, even mimicking the already mentioned *N*-donor ligands[57] (**Scheme 1.3**).

The hapticity of $\mathbf{BDC^{2-}}$, for example, can vary from two to four, depending upon the coordination mode of the two carboxylate moieties, typically allowing the formation of oxo-metallic clusters as nodes of stable 3-D frameworks with potentially open metal sites to be exploited in *e.g.* gas storage or catalysis[58]. The first important 3-D MOFs based on poly(carboxylates), HKUST-1[26] and MOF-5[23,24],

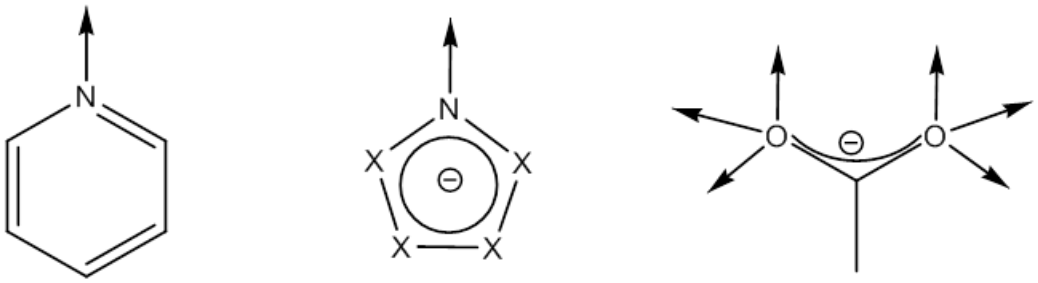

Scheme 1.3: Comparison of the coordination modes of pyridine, azolates, and carboxylate (X = C-H or N).

were synthesized in the late 1990s. HKUST-1 (namely $[Cu_3(BTC)_2(H_2O)_3]$ or CuBTC; $\mathbf{H_3BTC}$: 1,3,5-benzenetricarboxylic acid) shows a tetracoordinated copper unit, with the fifth coordination position

occupied by one water molecule. The latter can be removed by conventional heating providing one open metal site, or by replacement with a terminal ligand (*e.g.* pyridine), without hampering the framework stability (in air up to 240 °C)[59]. On the other hand, MOF-5, namely $Zn_4O(BDC)_3(DMF)_8$, is a 3-D network of **pcu** topology based upon octahedral $Zn_4O(O_2CR)_6$ nodes and linear BDC^{2-} spacers. Worthy of note, the calculated specific surface area of MOF-5, 3800[23] g/cm^2, is higher than that of the majority of synthetic zeolites, and is favourably coupled to the lowest density (0.59 g/cm^3) ever recorded for a crystalline material. One renown family of MOFs based on the $\{Zn_4O(O_2CR)_6\}$ node is the one labelled IR-MOF-*n* (*n* = 1-16)[60] which are isoreticular (hence the acronym IR) to MOF-5 but possess larger pore size, ranging from 3.8 to 29 Å, depending upon the length and shape of the ligand, and very high porosity (**Table 1.1**). This series of MOFs was constructed using the concept of *isoreticular synthesis* first reported by Yaghi[61]: this procedure is based upon keeping unaltered the inorganic SBU, in this particular case $\{Zn_4O(O_2CR)_6\}$, while changing the length of the spacer, **Scheme 1.4**. This approach allows the synthesis of MOFs sharing the same topology but with different features such as specific surface area, pore walls functionalization, *etc*. With the same SBU, Yaghi *et al.* synthesized, in 2004, another exceptional MOF, MOF-177[24], namely $Zn_4O(BTB)_3$. This MOF was built with an "evolution" of **H_3BTC**, namely 1,3,5-benzenetribenzoate (**BTB^{3-}**, **Scheme 1.2**), leading to the formation of a highly porous MOF, that with the highest surface area at the time, 4500 m^2/g, ~5 times higher than that of the most porous synthetic zeolite[62].

Other poly(carboxylate)-based MOFs are those of the series MIL (Materials Institute Lavoisier), based on metal ions with formal oxidation state +3, namely vanadium(III), chromium(III), iron(III), extended to *p-block* elements as aluminium(III), gallium(III) and indium(III). The more interesting family of MIL, MIL-53, shows the general formula $[M(\mu_4\text{-BDC})(\mu\text{-OH})]$[63]. Worthy of note, the framework of MIL-53 is highly flexible and its pores can assume different aperture depending on host-guest interactions and/or external stimuli[64]. As anticipated, MIL-101[21], namely $\{Cr_3F(H_2O)_2O[(BDC)_3]\cdot nH_2O$ (where *n* is *ca.* 25) is one of the frameworks with the highest specific surface area (**Table 1.1**).

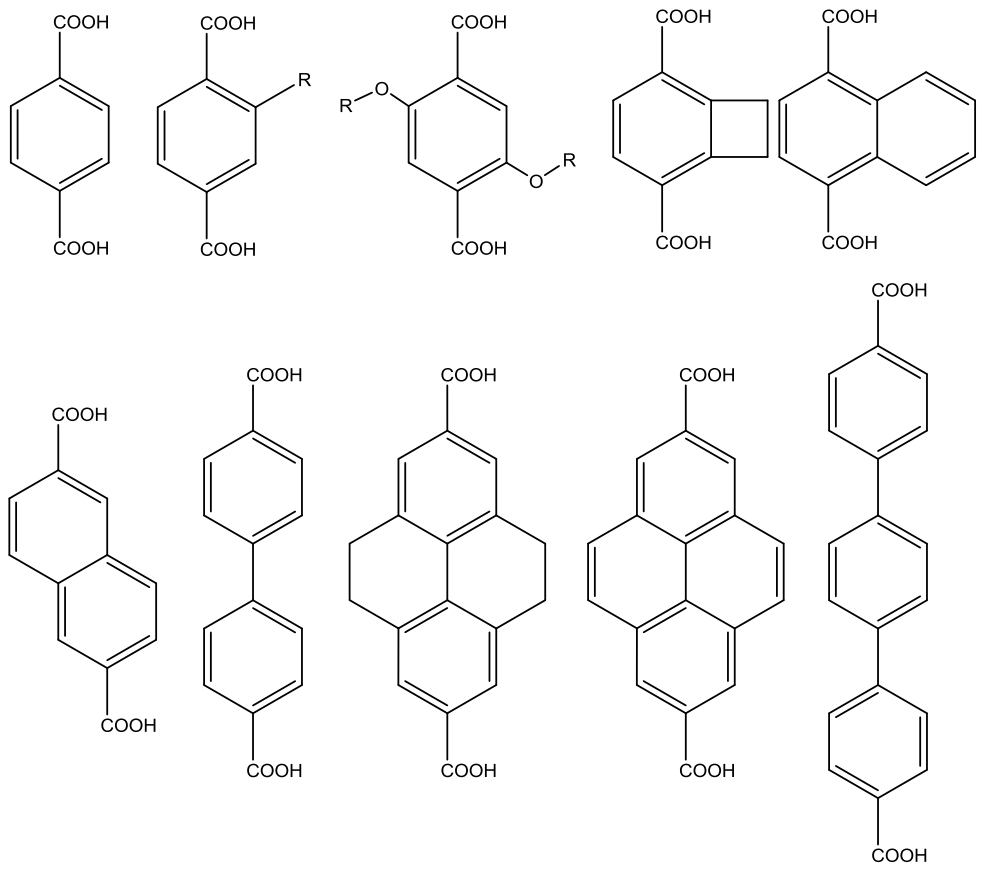

Scheme 1.4: Terephthalate-type linkers (L) used for the construction of the IR-MOF-n (n = 1–16) series, that is 3D-$[Zn_4O(L)_3]\cdot x$(DEF, DMF)$\cdot y H_2O$.

Not only late transition metal ions can be used to built up 3-D frameworks: in addition to the MIL MOFs, an interesting series of Zr(IV) derivatives, UiO-*n* (n = 66-68)[65], was constructed using terephtalate as the organic linker. The inorganic SBU, $\{Zr_6O_4(OH)_4(CO_2)_{12}\}$ (where CO_2 are the carboxylate functionalities of the organic linker), is reported to be among those with the highest coordination number in MOFs history. As already anticipated, this SBU consists of an inner $Zr_6O_4(OH)_4$ core in which the triangular faces of the Zr_6-octahedron are alternatively capped by μ_3-O and μ_3-OH groups (**Figure 1.2**[65,66]). All of the SBU edges are bridged by carboxylates from the organic spacers, this occurrence generating the $Zr_6O_4(OH)_4(CO_2)_{12}$ cluster. Each cluster is bridged to twelve nearby ones, which is the coordination typical of metal atoms in closed packed structures. The linkers used to build the UiO-*n* series are shown in **Figure 1.2** and have been chosen in order to generate progressively bigger cavities without conditioning the thermal stability (for UiO-66 and

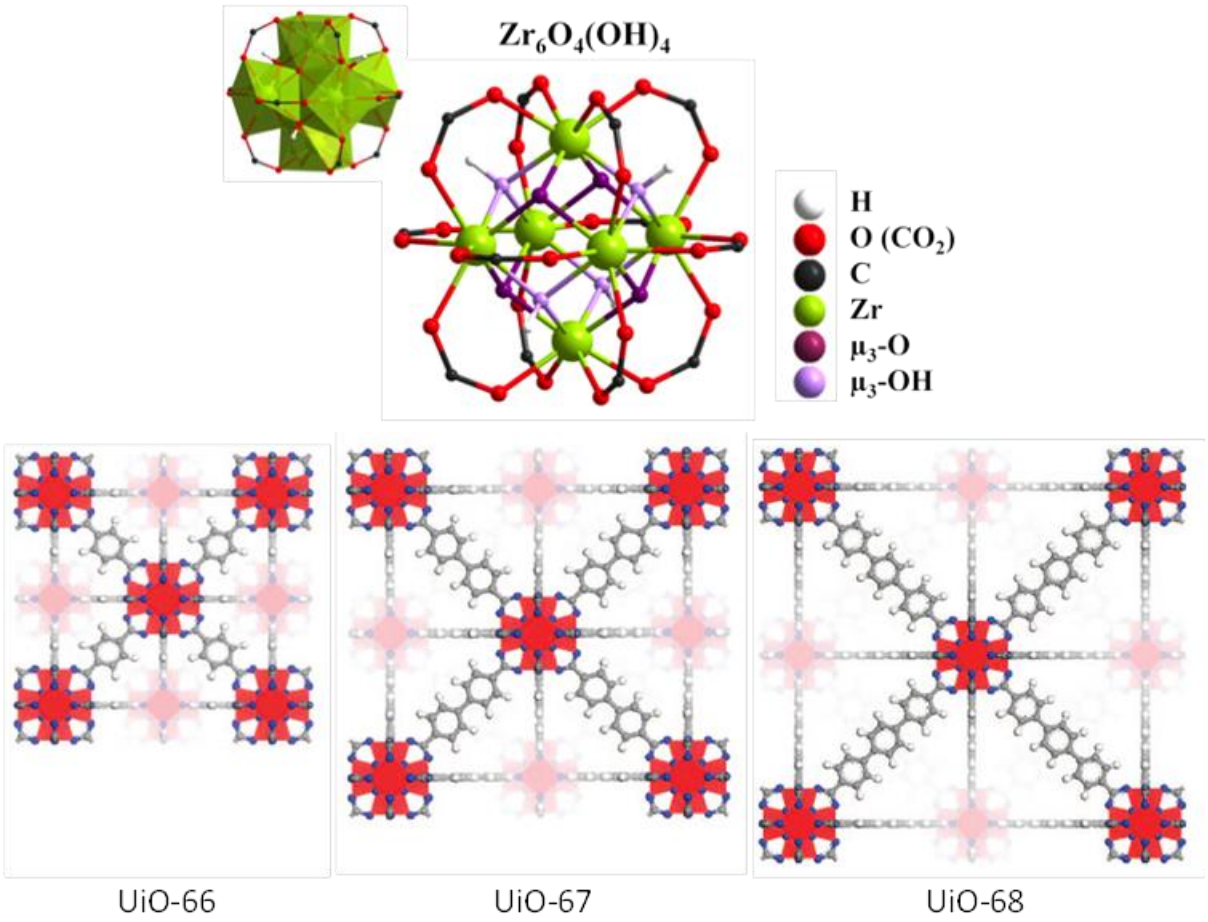

Figure 1.2: Top: the particular structure of the inorganic cluster for **UiO-66**. Bottom[65]: Zr-MOF **UiO-66**, with 1,4-benzene-dicarboxylate (BDC) as linker (left), Zr-MOF **UiO-67**, with 4,4'-biphenyl-dicarboxylate (BPDC) as linker (middle), and Zr-MOF **UiO-68**, with terphenyl dicarboxylate (TPDC) as linker (right). Zirconium, red; oxygen, blue; carbon, gray; hydrogen, white.

UiO-67: T_{dec} = 540 °C). The weak point of the framework is the C-C bond between the benzene ring and the carboxylic functionality: for this reason, modifications of the linker, *e.g.* increase of the length, do not affect the thermal stability of the material.

Recently, a new class of MOFs has emerged, the so-called metal-azolate frameworks (MAFs). Azolate ligands have the advantage to generate strong and directional coordination bonds with metal ions. Within metal-azolate frameworks, imidazolate- and tetrazolate-derivatives are the most used as organic spacers. The already mentioned ZIFs (ZIF-1 to ZIF-12), examples of which are shown in **Figure 1.3**, were firstly synthesized by Yaghi *et al.* in 2006[67]. The structural topology of ZIFs is quite similar to that of aluminosilicates: in ZIFs, the metal ion substitutes the Si(Al) tetrahedron, and imidazolates take the place of the bridging oxygens. Indeed, ZIFs have been synthesized as single crystals by

copolimerization of either Zn(II) or Co(II) with imidazolates as spacer. Worthy of note, ZIF-8, [Zn(2-methylimidazolate)], has been studied because of its high thermal stability (T_{dec} = 420 °C in air) and because of the porosity allowed by large 3-D intersecting cavities (d = 11.4 Å) and small apertures (d = 3.2 Å). This particular framework is one of the already mentioned few MOFs commercially available.

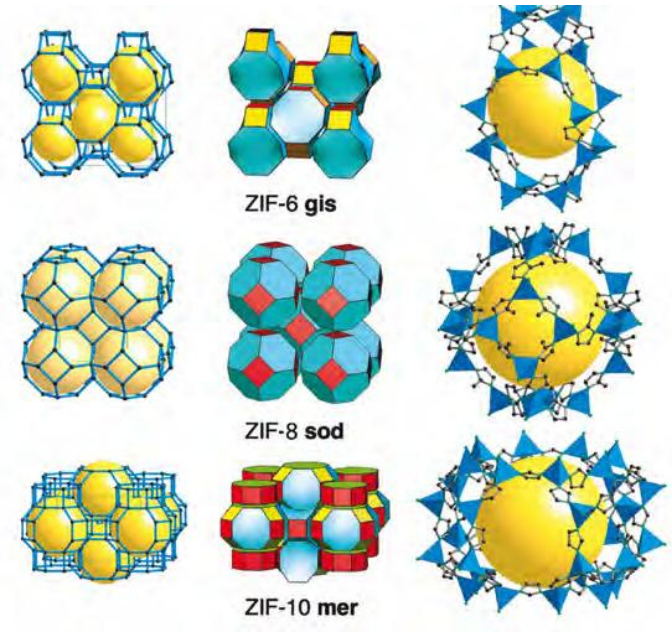

Figure 1.3: Three of the 12 ZIFs structures. Left, the net is shown as a stick diagram; center, the net is shown as a tiling and right, highlight of the larges cage of each MOF were the ZnN_4 tetrahedra in coloured in blue, from Ref. 69. Hydrogen atoms are omitted for clarity[69].

Tetrazolate derivatives were first proposed by Long *et al.* through the series of highly porous 3-D frameworks of general formula $[M_4Cl(ttz)_8(Solv)_4]$, (M = Mn^{2+}, Cu^{2+}, Fe^{2+}, Ni^{2+}). The metal ions are connected through poly(tetrazolate) linkers[68]. Among this series, $Mn_3[(Mn_4Cl)_3(BTT)_8]_2 \cdot 20MeOH$ (Mn-BTT; H_3BTT = 1,3,5-tris(2*H*-tetrazol-5-yl)benzene) possesses a rigid sodalite-like structure, as ZIF-8 **sod**[67c], with exposed Mn^{2+} sites which show high H_2 binding affinity and Lewis acid catalytic activity[68]. Unfortunately, the low thermal stability of the tetrazole ring influences that of the MOF, possesses a very low thermal stability (T_{dec}< 200 °C). More recently, new perfluorinated tetrazolate-base MOFs have been synthesized[69]. What is more, by the end of 2009, no less than 90 tetrazole-based ligands have been described in more than 160 publications[70].

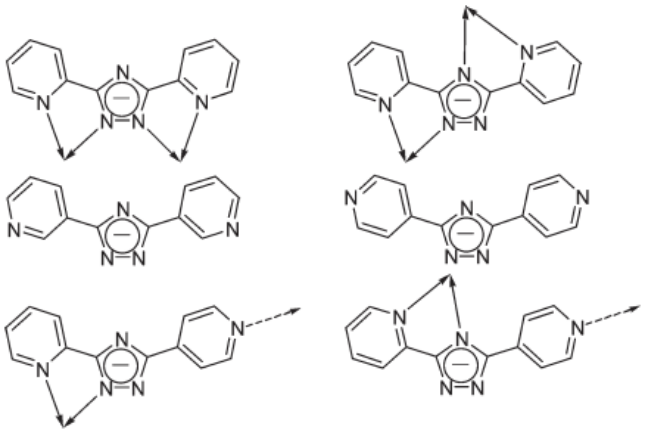

Figure 1.4: Different ways of coordination for dipyridyl-1,2,4-triazolate isomers. The chelating coordination sites are highlighted by solid arrows, while secondary coordination sites are highlighted by dashed arrows[73].

1,2,4-triazolates may behave as 3-connected nodes, with all three *N*-donors involved in coordination. Metal 1,2,4-triazolate coordination polymers remained almost unstudied before the development of a new solvothermal protocol along which the ligand is produced *in situ* by direct reaction of organonitriles and ammonia.[71] 1,2,4-triazole has been usually used as itself or with substituents in position 3 or 5 or even alkylated or arylated in position 1 (see **Chapter 2**), or has been functionalized with substituents bearing coordinative positions, *e.g.* one nitrogen atom, which give additional coordination ability: pyridyl-substituted 1,2,4-triazolate might be regarded as a size expanded azolate, see **Figure 1.4**. The position of the pyridyl nitrogen atom is crucial for the final structural motif of the coordination compounds: indeed, a 2-pyridyl group can cooperate with a triazolate nitrogen atom to function as a chelating group similar to 2,2'-bipyridines, which lead to the formation of neutral binary complexes with univalent tetrahedral metals such as Cu(I). More interestingly, symmetric substitution of 1,2,4-triazolate with two 3- or 4-pyridyl groups results in *exo*-pentadentate ligands with five potential coordination sites, **Figure 1.4**, which lead to a number of structural motifs as zig-zag chains[72], helical chains[73], zipper-like double chains and supramolecular isomers[73] (**Figure 1.5**). Asymmetric pyridyl substitution of triazole, as in 2,4-bis(2-pyridyl)-1,2,4-triazolate (L), generates a bidentate chelating site and three monodentate sites: when a divalent metal ion is used, *e.g.* Mn^{2+}, it should be chelated by two ligands to give a $Mn(L)_2$ neutral unit. If the metal is hexacoordinated, the two remaining sites can be occupied by other two ligands L

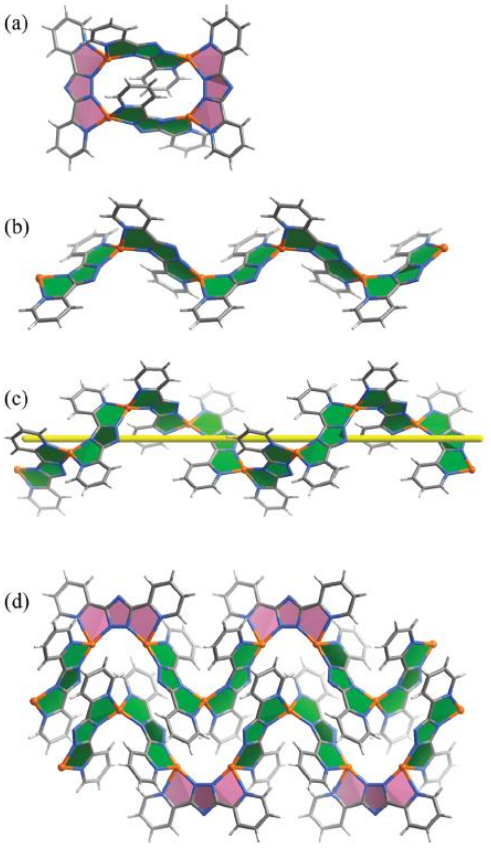

Figure 1.5: a) zigzag chain; b) helical chain; c) zipper-like double chain; d) supramolecular isomers, *e.g.*: $[Cu(dpt22)]$[73] (*cis*- and *trans*-bridging ligands are highlighted in different colours)[73].

using the free azoles *N*-donors to form other two $Mn(L)_2$ units to give a 4-connected coordination polymer[74]. Interestingly, this kind of complexes crystallizes in three different isomers.

Pyrazolate-based frameworks started to be developed in the past two decades, widening the research field for porous and highly porous MOFs. The shortest functionalized bis-pyrazole, 3,3',5,5'-tetramethyl-4,4'-bipyrazole, was studied because of its particular molecular structure: the two pyrazole rings are twisted by a dihedral angle of ~70° due to the steric hindrance of the four methyl groups, giving to the resulting MOFs some peculiarity[75]. Other interesting structures derive from 4,4'-bipyrazole itself that can be reacted with metal ions affording the series of compounds $[Cu(BPZ)(H_2O)_3(SO_4)]\cdot H_2O$, $[Cu(BPZ)_2(H_2O)_2](ClO_3)_2\cdot 4H_2O$, $Cu(BPZ)_2(H_2O)_2](CF_3CO_2)_2\cdot 2H_2O\cdot C_6H_5OH$ and $[Cu(H_2BPZ)_{1.5}(H_2O)_2(NO_3)](NO_3)$[76] where bis-pyrazole acts as a 4,4'-bypyridyl ligand: indeed, a counter ion is always present. Another key spacer for poly(pyrazolate) derivatives is 1,4-bis(pyrazolyl)benzene (**H_2BDP**)[77], which is commercially available[78]. MOFs built up with this ligand have been and are studied because of their porosity and ability to act as molecular sponges for gas storage and separation. The cobalt derivative, firstly obtained by Long *et al.* in 2008[79], was found to possess a very flexible network and high thermal stability. More recently, the vanadium derivative has been synthesized[80] which showed micro and mesoporosity useful for selective adsorption of gases[81].

Functionalization ("tagging") of the aromatic core of **H_2BDP** has been explored[82], giving birth to isoreticular structures (**Figure 1.6**) with specific gas adsorption and separation properties. Similarly to poly(carboxylato) linkers, modifications of poly(pyrazolato) linkers have been performed in order to follow the principles of the *isoreticular synthesis*, namely: elongation of the ligand by the use of alkyne groups[81], increasing the number of benzene rings in the skeleton[83], or expanding the core itself[83] (**Figure 1.7**). The MOF **$[Ni_3(BTP)_2]$**[84], built up with 1,3,5-tris(pyrazolyl)benzene (**H_3BTP**), has shown an amazing chemical and thermal stability. Moreover, it possesses an open coordination site which can be exploited for catalytic applications (see **Chapter 6**).

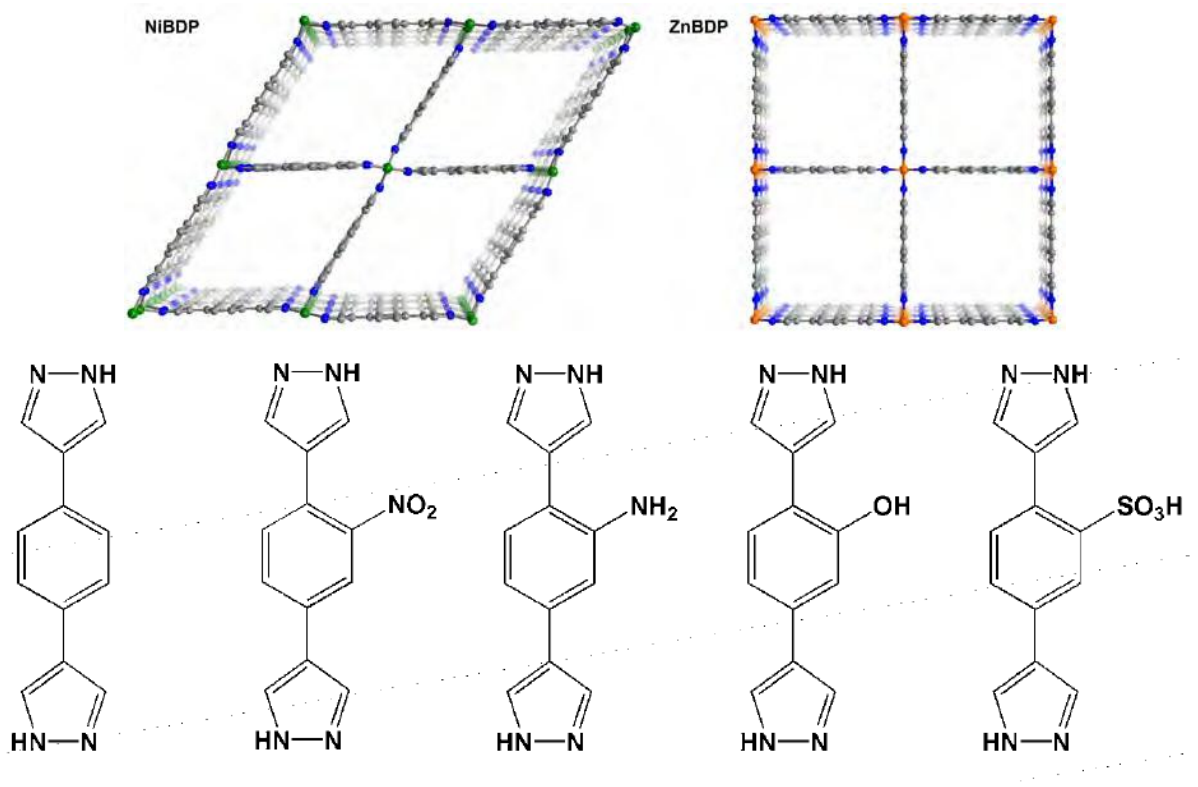

Figure 1.6: Top: structures of **[Ni(BDP)]**, left, and **[Zn(BDP)]**, right. Bottom: functionalised H_2BDP; the corresponding Ni(II) and Zn(II) derivatives possess the same structural motif of **[Ni(BDP)]** and **[Zn(BDP)]**, respectively.

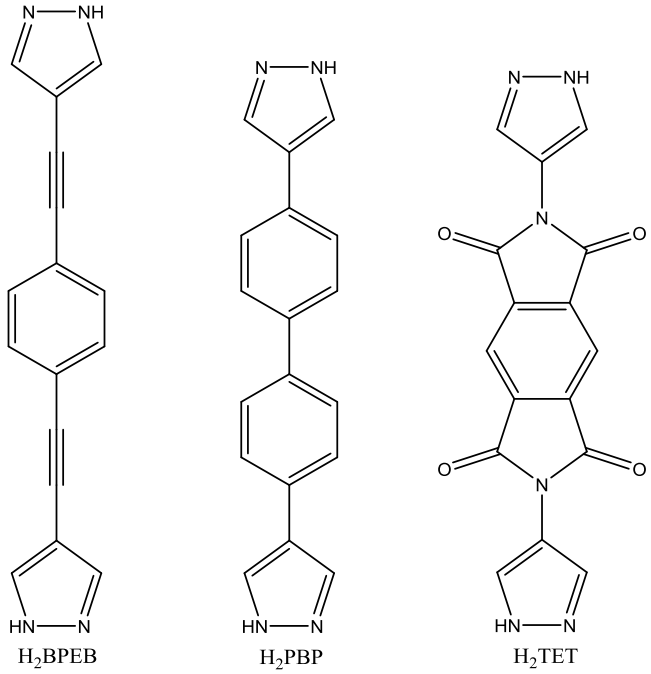

Figure 1.7: Examples of elongated poly(pyrazolato) based ligands. Left: 1,4-bis(1*H*-pyrazolylethynil)benzene (**H_2BPEB**); centre: 4,4'(1*H*-pyrazolyl)biphenyl (**H_2PBP**); right: 2,6-bis(1*H*-pyrazolyl)pyrrolo[3,4-*f*]isoindole-1,3,5,7(2*H*,6*H*)-tetrone (**H_2TET**).

1.3 Conclusions

This general overview has been written to demonstrate how MOFs chemistry is fascinating and multifaceted. Because of the generality of this introduction, none of the practical applications investigated during this Thesis work have been presented. However, in the next **Chapters**, specific compounds and their structural aspects and functional applications are presented and discussed in the frame of the recent literature.

So, let's move to the next **Chapter** and play with the Molecular Meccano, starting from the selection of the "metal pieces" to connect our nodes: the organic linkers.

References and Notes

[1] (a) Corma, A. *Chem. Rev.* **1997**, *97*, 2373-2420. (b) Maesen, T. and Marcus, B. in Introduction to Zeolite Science and Practice 2001, Van Bekkum, H.; Flanigen, E. M.; Jacobs, P. A. & Jansen, J. C. Eds. Elsiever, Amsterdam, pages 1-9. (c) Lauriente, D. H. and Inoguchi, Y. The Chemical Economics Handbook 2005, SRI Consulting, 599.1000 F, 14, 6. (d) Yilmaz, B. and Muller *U. Top. Catal.* **2009**, *52*, 888-895.

[2] Mirodatos, C. and Barthomeuf, D. *J. Catal.* **1985**, *93*, 246-255.

[3] Zicovich-Wilson, C. M.; Corma, A. and Viruela, P. *J. Phys. Chem.* **1994**, *98*, 10863-10870.

[4] Yaghi, O. M. and Li, H. L. *J. Am. Chem. Soc.* **1995**, *117*, 10401-10402.

[5] http://www.ccdc.cam.ac.uk; CSD = Cambridge Structural Database

[6] BASOLITE MOF at *www.sigma-aldrich.com* or at *www.mof.basf.com*

[7] a) Eddaoudi, M.; Kim, J.; Rosi, N.; Vodak, D.; Wachter, J.; O'Keeffe, M. and Yaghi, O. M. *Science* **2002**, *295*, 469-472; b) Kitagawa, S.; Kitaura, R. and Noro, S. *Angew. Chem. Int. Ed.* **2004**, *43*, 2334-2375; c) Jhon, Y. H.; Cho, M.; Jeon, H. R.; Park, I.; Chang, R.; Rowsell, J. L. C. and Kim, J. *J. Phys. Chem. C* **2007,** *111,* 16618-16625; d) Karra, J. R. and Walton, K. S. *J. Phys. Chem. C* **2010,** *114,* 15735–15740; e) Torrisi, A.; Bell, R. G. and Mellot-Draznieks, C. *Microporous and Mesoporous Materials* **2013**, *168*, 225–238.

[8] Férey, G. *Chem. Soc. Rev.* **2008**, *37*, 191-214.

[9] Zhao, D.; Yuan, D.; Sun, D. and Zhou, H.-C. *J. Am. Chem. Soc.* **2009**, *131*, 9186-9188.

[10] Zheng, B.; Bai, J.; Duan, J.; Wojtas, L. and Zaworotko, M. J. *J. Am. Chem. Soc.* **2011**, *133*, 748-751.

[11] Wang, Z.; Tanabe, K. K. and Cohen, S. M. *Chem. Eur. J.* **2010**, *16*, 212-217.

[12] Sumida, K.; Hill, M. R.; Horike, S.; Dailly, A. and Long, J. R. *J. Am. Chem. Soc.* **2009**, *131*, 15120-15121.

[13] An, J.; Farha, O. K.; Hupp, J. T.; Pohl, E.; Yeh, J. I. and Rosi, N. L. *Nat. Commun.* **2012**, *3*, 604-

[14] Furukawa, H.; Ko, N.; Go, Y. B.; Aratani, N.; Choi, S. B.; Choi, E.; Yazaydın, A. Ö.; Snurr, R. Q.; O'Keeffe, M.; Kim, J. and Yaghi, O. M. *Science,* **2010**, *329*, 424-428.

[15] Klein, N.; Senkovska, I.; Baburin, I. A.; Grü nker, R.; Stoeck, U.; Schlichtenmayer, M.; Streppel, B.; Mueller, U.; Leoni, S.; Hirscher, M. and Kaskel, S. *Chem. Eur. J.,* **2011**, *17*, 13007-13016.

[16] Yan, Y.; Telepeni, I.; Yang, S.; Lin, X.; Kockelmann, W.; Dailly, A.; Blake, A. J.; Lewis, W.; Walker, G. S.; Allan, D. R.; Barnett, S. A.; Champness, N. R. and Schröder, M. *J. Am. Chem. Soc.*, **2010**, *132*, 4092-4094.

[17] Farha, O. K.; Yazaydın, A. Ö.; Eryazici, I.; Malliakas, C. D.; Hauser, B. G.; Kanatzidis, M. G.; Nguyen, S. T.; Snurr, R. Q. and Hupp, J. T. *Nat. Chem.*, **2010**, *2*, 944-948.

[18] Farha, O. K.; Eryazici, I.; Jeong, N. C.; Hauser, B. G.: Wilmer, C. E.; Sarjeant, A. A.; Snurr, R. Q.; Nguyen, S. B. T.; Yazaydın, A. O. and Hupp, J. T. *J. Am. Chem. Soc.*, **2012**, *134*, 15016-15021.

[19] Kondo, M.; Yoshitomi, T.; Seki, K.; Matsuzaka, H. and Kitagawa, S. *Angew. Chem., Int. Ed. Engl.* **1997**, *36*, 1725.

[20] Li, H.; Eddaoudi, M.; Groy, T. L. and Yaghi, O. M. *J. Am. Chem. Soc.* **1998**, *120*, 8571-8572.

[21] Ferey, G.; Mellot-Draznieks, C.; Serre, C.; Millange, F.; Dutour, J.; Surble, S. and Margiolaki, I. *Science* **2005**, 309, 2040-2042.

[22] Koh, K.; Wong-Foy, A. G. and Matzger, A. J. *J. Am. Chem. Soc.* **2009**, *131*, 4184-4185.

[23] a) Li, H.; Eddaoudi, M.; O'Keeffe, M. and Yaghi, O. M. *Nature*, **1999**, *402*, 276-279; b) Kaye, S. S.; Dailly, A.; Yaghi, O. M. and Long, J. R. *J. Am. Chem. Soc.* **2007**, *129*, 14176-14177.

[24] Chae, H. K.; Siberio-Perez, D. Y.; Kim, J.; Go, Y.; Eddaoudi, M.; Matzger, A. J.; O'Keeffe, M. and Yaghi, O. M. *Nature*, **2004**, *427*, 523-527.

[25] Furukawa, H.; Miller, M. A. and Yaghi, O. M. *J. Mater. Chem.* **2007**, *17*, 3197-3204.

[26] Chui, S. S. -Y.; Lo, S. M. -F.; Charmant, J. P. H.; Orpen, A. G. and Williams, I. D. *Science* **1999**, *283*, 1148.

[27] Koh, K.; Wong-Foy, A. G. and Matzger, A. J. *Angew. Chem. Int. Ed.* **2008**, *47*, 677-680.

[28] a) Nelson, A. P.; Farha, O. K.; Mulfort, K. L. and Hupp, J. T. *J. Am. Chem. Soc.*, **2008**, *131*, 458-460; b) Farha, O. K. and Hupp, J. T. *Acc. Chem. Res.*, **2010**, *43*, 1166-1175; c) Wu, D. and Navrotsky, A. *J. Solid State Chem.*, **2015**, *223*, 53-58.

[29] Ma, S. and Zhou, H.-C. *Chem. Commun.* **2010**, *46*, 44-53.

[30] Andirova, D.; Cogswell, C. F.; Lei, Y. and Choi, S. *Microporous and Mesoporous Mat.*, **2016**, *219*, 276-305.

[31] a) D'Alessandro, D. M.; Smit, B. and Long, J. R. *Angew. Chem., Int. Ed.* **2010**, *49*, 6058-6082; b) Belmabkhout, Y.; Guillerm V. and Eddaudi, M. *Chem. Eng. J.*, **2016**, *296*, 386-397.

[32] Lai, Q.; Paskevicius, M.; Sheppard, D. A.; Buckley, C. E.; Thornton, A. W.; Hill, M. R.; Gu, Q.; Mao, J.; Huang, Z.; Liu, H. K.; Guo, Z.; Banerjee, A.; Chakraborty, S.; Ahuja, R. and Aguey-Zinsou, K.-F. *ChemSusChem*, **2015**, *8*, 2789-2825.

[33] a) Samokhvavlov, A. *Chem .Eur. J.*, **2015**, *21*, 16726-16742; b) Hasan, Z. And Jhung, S. H. *J. Hazard. Mater.*, **2015**, *283*, 329-339; c) Dias, E. M. and Petit, C. *J. Mater. Chem. A*, **2015**, *3*, 22484-22506. d) Ahmed, I. and Jhung, S. H. *J. Hazard. Mat.* **2016**, *301*, 259-276.

[34] a) Montoro, C.; Linares, F.; Procopio, E. Q.; Senkovska, I.; Kaskel, S.; Galli, S.; Masciocchi, N.; Barea, E. and Navarro J. A. R. *J. Am. Chem. Soc.*, **2011**, *133*, 11888-11891; b) Mondal, S. S. and Holdt, H.-J. *Angew. Chem Int. Ed.* **2016**, *55*, 42-44.

[35] Yusuf, K.; Aqel, A. and Alothman, Z. *J. Chromat.*, **2014**, *1348*, 1-16.

[36] a)Wang, L.; Han, Y.; Feng, X.; Zhou, J.; Qi, P. And Wang, B. *Coord. Chem. Rev.*, **2016**, *307*, 361-381; b) Zao, Y.; Song, Z.; Li, X.; Sun, Q.; Cheng, N.; Lawes, S. and Sun, X. *Energy Storage Mat.*, **2016**, *2, 35-62.*

[37] a) Meyer, K.; Ranocchiari, M. and van Bokhoven, J. A. *Energy Environ. Sci.*, **2015**, *8*, 1923-1937; b) Dhakshinamoorthy, A.; Asiri, A. M. and Garcia, H. *Angew. Chem. Int. Ed.*, **2016**, *55*, 5414-5445.

[38] a) Corma, A.; Garcia, H.; Llabré i Xamena, F. X. *Chem. Rev.*, **2010**, *110*, 4606−4655; b) Yoon, M.; Srirambalaji, R.; Kim, K. *Chem. Rev.*, **2012**, *112*, 1196−1231; c) Liu, J.; Chen, L.; Cui, H.; Zhang, L.; Zhang, J.; Su, C.-Y. *Chem. Soc. Rev.*, **2014**, *43*, 6011−6061; d) Chughtai, A. H.; Ahmad, N.; Younus, H. A.; Laypkov, A.; Verpoort, F. *Chem. Soc. Rev.*, **2015**, *44*, 6804-6849.

[39] a) Gu, Z.-Y.; Park, J.; Raiff, A.; Wey, Z. and Zhou, H.-C. *ChemCatChem*,**2014**, *6*, 67-75; b) Giménez-Marquez, M.; Hidalgo, T.; Serre, C. and Horcajada, P. *Coord. Chem. Rev.*, **2016,** *307,* 342-360.

[40] a) Cui, Y.; Chen, B. and Quian, G. *Coord. Chem. Rev.*,**2014**, *273-274*, 76-86; b) Xu, L.-J.; Xu, G.-T. and Chen, Z-N. *Coord. Chem. Rev.*, **2014**, *273-274*, 47-62.

[41] Galli, S.; Maspero, A.; Giacobbe, C.; Palmisano, G.; Nardo, L.; Comotti, A.; Bassanetti, I.; Sozzani, P. and Masciocchi, N. *J. Mater. Chem. A*, **2014**, *2*, 12208-12221.

[42] Sun, L.; Campbell, M. G. and Dinca, M. *Angew. Chem. Int. Ed.*, **2016**, *55*, 3566-3579.

[43] a) Allendorf, M. D.; Schwartzberg, A.; Stavila, V. and Talin, A. A. *J. Chem. Soc.*, **2010**, *17*, 11372-11388; b) Zagorodniy, K.; Seifert, G. and Hermann, H *Appl. Phys. Lett.*, **2010**, *97*, 251905-1-251905-2; c) Eslava, S.; Zhang, L.; Esconjauregui, S.; Yang, J.; Vanstreels, K.; Baklanov, M. R. and Saiz, E. *Chem. Mater.*, **2013**, *25*, 27−33; d) Warmbier, R.; Quandt, A. and Seifert, G. J. *Phys. Chem. C*, **2014**, *118*, 11799-11805; e) Usman, M.; Lee, C.-H.; Hung, D.-S.; Lee, S.-F.; Wang, C.-C.; Luo, T.-T.; Zhao, L.; Wu, M.-K. and Lu, K.-L. *J. Mater. Chem. C*, **2014**, *2*, 3762-3768; f) Yu, S.-S.; Yuan, G.-J. and Duan, H-.B. *RSC Adv.*, **2015**, *5*, 45213-45216; g) Guo, H.; Wang, M.; Liu, J.; Zhu, S. and Liu, C. *Microporous and Mesoporous Mat.*, **2016**, *221*, 40-47.

[44] Aguilera-Sigalat, J. and Bradshaw, D. *Coord. Chem. Rev.*, **2016**, *307*, 267-291.

[45] Colombo, V.; Galli, S.; Choi, H. J.; Han, G. D.; Maspero, A.; Palmisano, G.; Masciocchi, N and Long, J. R. *Chem. Sci.*, **2011**, *2*, 1311-1319.

[46] http://www.meccano.com/about

[47] Sun, Y. and Zhou, H.-C. *Sci. Technol. Adv. Mater.* **2015,** *16*, 054202 doi: 10.1088/1468-6996/16/5/054202.

[48] Lipowski, J. *Inclusion Compounds: Structural Aspects of Inclusion Compounds Formed by Inorganic and Organometallic Host Lattices*; In Atwood, J. L.; Davies, J. E. D.; MacNicol, D. D., Eds., Academic Press: London, **1984**, pp. 59–103 and references therein.

[49] (a) Hoskins, B. F. and Robson, R. *J. Am. Chem. Soc.* **1989**, *111*, 5962-5964. (b) Hoskins, B. F. and Robson, R. *J. Am. Chem. Soc.* **1990**, *112*, 1546-1554. (c) Gable, R. W.; Hoskins, B. F. and Robson, R. *J. Chem. Soc. Chem. Commun.* **1990**, 1677-1678.

[50] (a) Fujita, M.; Kwon, Y. J.; Washizu, S. and Ogura, K. *J. Am. Chem. Soc.* **1994**, *116*, 1151-1152; (b) Carlucci, L.; Ciani, G.; Prosperio, D. M. and Sironi, A. *J. Chem. Soc. Chem. Commun.* **1994**, 2755-2756; (c) Subramanian, S. and Zaworotko, M. J. *Angew. Chem. Int. Ed. Engl.* **1995**, *34*, 2127-2129; (d) Yaghi, O. M.; Richardson, D. A.; Li, G.; Davis, C. E. and Groy, T. L. *Mater. Res. Soc. Symp. Proc.* **1995**, *371*, 15; (e) Lu, J.; Paliwala, T.; Lim, S. C.; Yu, C.; Niu, T. and Jacobson, A. J. *Inorg. Chem.* **1997**, *36*, 923-929.

[51] See, e.g.: Fujita, M.; Tominaga, M.; Hori, A. and Therrien, B. *Acc. Chem. Res.* **2005**, *38*, 369-378.

[52] Kondo, M.; Shimamura, M.; Noro, S.-I.; Yoshitomi, T.; Minakoshi, S. and Kitagawa, S. *Chem. Lett.* **1999**, *4*, 285-286

[53] Cussen, E. J.; Claridge, J. B.; Rosseinsky, M. J. and Kepert, C. J. *J. Am. Chem. Soc.* **2002**, *124,* 9575.

[54] a) Li, J.-M.; Zhang, Y.-G.; Chen, J.-H.; Wang, Q.-M. and Wu, X.-T. *Chem. Commun.* **1997**, 1213; b) Tong, M.-L.; Chen, X.-M.; Yu, X.-L. and Mak, T. C. W. *J. Chem. Soc., Dalton Trans.* **1998**, 5; c) Lu, J. Y.; Cabrera, B. R.; Wang, R.-J.; Li, J. *Inorg. Chem.* **1999**, *38*, 4608; d) Li, J.-M.; Zhang, Y.-G.; Chen, J.-H.; Rui, L.; Wang, Q.-M. and Wu, X.-T. *Polyhedron* **2000**, *19*, 1117; e) Zheng, L.-M.; Yin, P. and Xin, X.-Q. *Inorg. Chem.* **2002**, *41*, 4084.

[55] (a) Subramanian, S. and Zawarotko, M. *Angew. Chem., Int. Ed. Engl.* **1995**, *34*, 2127; b) Lightfoot, P. and Snedden, A. *J. Chem. Soc., Dalton Trans.* **1999**, 3549; c) Inman, C.; Knaust, J. M.; Keller, S. W. *Chem. Commun.* **2002**, 156.

[56] Kitagawa, S. and Kondo, M. *Bull. Chem. Soc. Jpn* **1998**, *71*, 1739

[57] Eddaoudi, M.; Li, H.; Reineke, T. M.; Fehr, M.; Kelley, D. G.; Groy, T. L. and Yaghi, O. M. *Top Catal.* **1999**, *9*, 105.

[58] (a) Llabrés i Xamena, F. X.; Abad, A.; Corma, A. and Garcia, H. *J. of Catal.* **2007**, *250*, 294; (b) Vitillo, J. J.; Regli, L.; Chavan, S.; Ricchiardi, G.; Spoto, G.; Dietzel, P. D. C.; Bordiga, S. and Zecchina, A. *J. Am. Chem. Soc.* **2008**, *130*, 8386.

[59] Other syntheses of CuBTC: (a) Wang, Q. M.; Shen, D.; Bulow, M.; Lau, M. L.; Deng, S.; Fitch, F. R.; Lemcoff, N. O. and Semanscin, J. *Microporous Mesoporous Mater.* **2002**, *55*, 217. (b) Schlichte, K.; Kratzke, T. and Kaskel, S. *Microporous Mesoporous Mater.* **2004**, *73*, 81.

[60] (a) Eddaoudi, M.; Kim, J.; Rosi, N.; Vodak, D.; Wachter, J.; O'Keeffe, M. and Yaghi, O. M. *Science* **2002**, *295*, 469. (b) Tranchemontagne, D. J.; Mendoza-Cortés, J. L.; O'Keefe, M. and Yaghi, O. M. *Chem. Soc. Rev.* **2009**, *38*, 1257.

[61] Yaghi, O. M.; O'Keeffe, M.; Ockwig, N. W.; Chae, H. K.; Eddaoudi, M. and Kim, J. *Nature*, **2003**, *423*, 705–714.

[62] Chae, H. K.; Siberio-Perez, D. Y.; Kim, J.; Go, Y. B.; Eddaoudi, M.; Matzger, A. J.; O'Keeffe, M. and Yaghi, O. M. *Nature* **2004**, *427*, 523.

[63] (a) Barthelet, K.; Riou, D. and Férey, G. *Chem. Commun.* **2002**, 1492. (b) Serre, C.; Millange, F.; Surblé, S. and Férey, G. *Angew. Chem. Int. Ed.* **2004**, *43*, 6285. (c) Volkringer, C. and Loiseau, T. *Mater. Res. Bull.* **2006**, *41*, 948. (d) Serre, C.; Millange, F.; Thouvenot, C.; Nogues, M.; Marsolier, G.; Louer, D. and Férey, G. *J. Am. Chem. Soc.* **2002**, *124*, 13519. (e) Millange, F.; Guillou, N.; Walton, R. I.; Greneche, J.-M.; Margiolaki, I. and Férey, G. *Chem. Commun.* **2008**, 4732. (f) Millange, F.; Serre, C. and Férey, G. *Chem. Commun.* **2002**, 822.

[64] (a) Férey, G.; Serre, C.; Mellot-Draznieks, C.; Millange, F.; Surble, S.; Dutour, J. and Margiolaki, I. *Angew. Chem. Int. Ed.* **2004**, *43*, 6296. (b) Férey, G.; Mellot-Draznieks, C.; Serre, C.; Millange, F.; Dutour, J.; Surble, S. and Margiolaki, I. *Science* **2005**, *309*, 2040.

[65] Cavka, J. H.; Jakobsen, S.; Olsbye, U.; Guillou, N.; Lamberti,C.; Bordiga, S. and Lillerud, K. P. *J. Am. Chem. Soc.*, **2008**, *130*, 13850–13851.

[66] http://www.iycr2014.org/learn/crystallography365/articles/20141212.

[67] (a) Huang, X. C.; Zhang, J. P. and Chen, X. M. *Chin. Sci. Bull*., **2003**, *48*, 1531. (b) Park, K. S.; Ni, Z.; Côté, A. P.; Choi, J. Y.; Huang, R.; Uribe-Romo, F. J.; Chae, H. K.; O'Keeffe, M. and Yaghi, O. M. *Proc. Natl. Acad. Sci. USA* **2006**, *103*, 10186

[68] a) Dincă, M.; Dailly, A.; Liu, Y.; Brown, C. M.; Neumann, D. A. and Long, J. R. *J. Am. Chem. Soc.* **2006**, *128*, 16876. (b) Dincă, M.; Han, W. S.; Liu, Y.; Dailly, A.; Brown, C. M. and Long,J. R. *Angew. Chem. Int. Ed.* **2007**, *46*, 1419. (c) Dincă, M. and Long, J. R. *J. Am. Chem. Soc.* **2007**, *129*, 11172. (d) Dincă, M.; Dailly, A.; Tsay, C. and Long, J. R. *Inorg. Chem.* **2008**, *47*, 11. (e) Sumida, K.; Horike, S.; Kaye, S. S.; Herm, Z. R.; Queen, W. L.; Brown, C. M.; Grandjean, F.; Long, G. J.; Dailly, A. and Long, J. R. *Chem. Sci.* **2010**, *1*, 184.

[69] Chen, T.-H.; Popov, I.; Zenasni, o.; Daugulis, O. and Miljanic, O.S. *Chem. Commun.,* **2013**, *49*, 6846-6848.

[70] Aromi, G.; Barrios, L. A.; Roubeau, O. and Gamez, P. *Coord. Chem. Rev.,* **2011**, *255*, 485–546.

[71] Zhang, J.-P.; Zhang, S.-L.; Huang, X.-C. and Chen, X.-M. *Angew. Chem., Int. Ed.*, **2004**, *43*, 206.

[72] Zhang, J.-P.; Lin, Y.-Y.; Huang, X.-C. and Chen, X.-M. *Cryst. Growth Des.*, **2006**, *6*, 519-523.

[73] a) Zhang, J.-P.; Lin, Y.-Y.; Huang, X.-C. and Chen, X.-M. *Chem. Commun.*, **2005**, 1258–1260; b) Zhang, J.-P.; Zhang, Y.-B.; Lin, J.-B. and Chen, X.-M *Chem. Rev.* **2012**, *112*, 1001–1033; c) btp22$^-$ = 3,5-bis(2-pyridyl)-1,2,4-triazolate.

[74] Lin, J.-B.; Zhang, J.-P.; Zhang, W.-X.; Xue, W.; Xue, D.-X. and Chen, X.-M. *Inorg. Chem.*, **2009**, *48*, 6652-6660.

[75] a) Rusanov, E. B.; Ponomarova, V. V.; Komarchuk, V. V.; Stoeckli-Evans, H.; Fernandez-Iba˜nez, E.; Stoeckli, F.; Sieler, J. and Domasevitch, K. V. *Angew. Chem.*, **2003**, *115*, 2603-2605; b) Domasevitch, K. V.; Boldog, I.; Rusanov, E. B.; Hunger, J.; Blaurock, S.; Schröder,M. and Sieler, J. *Z. Anorg. Allg. Chem.*, **2005**, *631*, 1095-1100.

[76] Pettinari, C.; Tăbăcaru, A. and Galli, S. *Coord. Chem. Rev.*, **2016**, *307*, 1–31.

[77] (a) Lozan, V.; Solntsev, P. Y.; Leibeling, G.; Domasevitch, K. V. and Kersting, B. *Eur. J. Inorg. Chem.*, **2007**, *20*, 3217; (b) Maspero, A.; Galli, S.; Masciocchi, N. and Palmisano, G. *Chem. Lett.*, **2008**, *37*, 956.

[78] *e.g.* www.strem.com

[79] Choi,H. J.; Dincă, M. and Long, J. R. *J. Am. Chem. Soc.*, **2008**, *130*, 7848–7850.

[80] Augustyniak, A. W.; Fandzloch, M.; Domingo, M.; Łakomskab, I. and Navarro, J. A. R. : *Chem. Commun.*, **2015**, *51*, 14724-14727.

[81] a) Padial, N. M.; Quartapelle Procopio, e.; Montoro, C.; Lopez, E.; Oltra, J. E.; Colombo, V.; Maspero, A.; Masciocchi, N.; Galli, S.; Senkovska, I.; Kaskel, S.; Barea, E. and Navarro, J. A. R. *Angew. Chem. Int. Ed.*, **2013**, *52*, 8290 –8294; b) Galli, S.; Maspero, A.; Giacobbe, C.; Palmisano, G.; Nardo, L.; Comotti, A.; Bassanetti, I.; Sozzani, P. and Masciocchi, N. *J. Mater. Chem. A*, **2014**, *2*, 12208-12221.

[82] Colombo, V.; Montoro, C.; Maspero, A.; Palmisano, G.; Masciocchi, N.; Galli, S.; Barea, E. and Navarro, J. A. R. *J. Am. Chem. Soc.*, **2012**, *134*, 12830−12843.
[83] Masciocchi, N.; Galli, S.; Colombo, V.; Maspero, A.; Palmisano, G.; Seyyedi, B.; Lamberti, C. and Bordiga, S. *J. Am. Chem. Soc.***, 2010**, *132*, 7902–7904.
[84] Colombo, V.; Galli, S.; Choi, H. J.; Han, G. D.; Maspero, A.; Palmisano, G.; Masciocchi, N. and Long, J. R. *Chem. Sci.*, **2011**, *2*, 1311-1319.

Chapter 2
Playing with the molecular meccano: the nature of the organic linker

2.1 Introduction

Heterocycles are a special class of organic, aromatic or aliphatic compounds in which one or more CH_x groups are substituted by atoms of other elements, such as oxygen or sulphur, or by NH groups, *etc*. The substitution imparts specific properties to the heterocyclic compound, different from those of the parent species. For example, starting from cyclopentadiene, the substitution of the CH_2 group by one oxygen atom generates furan: the properties of the latter are completely different from those of cyclopentadiene: significantly, furan is an aromatic molecule, while cyclopentadiene is not. The substitution of the CH_2 group of cyclopentadiene with one NH group generates pyrrole. Not only the chemical and physical behaviour of pyrrole is different from that of cyclopentadiene; also, furan and pyrrole possess different properties, *e.g.* boiling/melting point (−85.6/31.3 °C for furan *vs*. 23/130 °C for pyrrole); acidity: furan is not acid, while pyrrole is a weak acid (pKa = 17.5[1]); basicity: furan is not basic, while pyrrole can be protonated in position C2 (pKa = -4)[1].

From these simple examples it should appear clear that the choice of the heteroatom is fundamental to tune the properties of the heterocyclic molecule. Nonetheless, one important aspect is common to all heterocycles and legitimizes their wide preparation and characterization, namely their

biological and chemical importance: as representative examples, let us recall here porphyrin[2] in the photosynthetic process, nucleobases[2], aminoacids[2] and drugs[2,3].

One of the most used classes of heterocyclic compounds is that of azoles, not only because of their occurrence in natural and synthetic molecules with biological activity[2], as anti-inflammatory agents[3], antidiabetic agents[3], cardiovascular agents[3] *etc*., but also due to their particular coordination chemistry, which is exploited in a wide range of applications[4], *e.g.* in the synthesis of (porous) coordination polymers for gas storage, gas separation, heterogeneous catalysis, luminescence, *etc*., as pointed out in the previous **Chapter**.

Azoles are characterized by the presence of at least one nitrogen atom and, in some occasions, another heteroatom between oxygen or sulphur. Azoles are aromatic systems: one of the heteroatoms participates to the aromaticity of the system by sharing two of its valence electrons. Even if the majority of azoles is known to be basic (the protonated form is the azolinium cation), five-membered rings with nitrogen as the only heteroatom – imidazole, pyrazole, triazole, and tetrazole (**Figure 2.1**) - possess also an acidic behaviour, because the pyrrolic nitrogen atom can be deprotonated with a base such as TEA, LDA or NaH, to yield the corresponding azolate anion.

As for their possible use in coordination chemistry, non-deprotonated azoles are neutral ligands possessing *n-1* coordination sites (*n* = number of nitrogen atoms in the ring) because the pyrrolic nitrogen atom employs all of its valence electrons: two valence electrons participate into the aromaticity of the system, while the remaining three are employed in two N-E (E = C, N, *etc*.) and one N-H bonds. When deprotonated, the pyrrolic nitrogen atom is negatively charged and prone to coordinate a metal cation. Moreover, this boost of negative charge on the aromatic ring imparts a higher basicity to all the other coordination sites of the ligand: this occurrence allows azolates to form stronger coordinative bonds with the metal ion, potentially generating coordination compounds with a particularly high thermal and chemical stability, which are frequently among the most important features requested to a CP in view of practical applications.

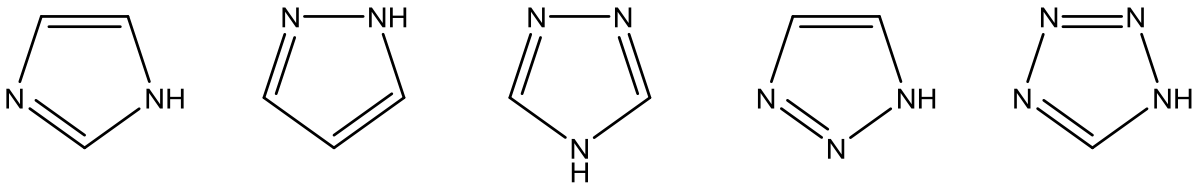

Figure 2.1: Azole heterocyclic rings: 1*H*-imidazole (1*H*-im); 1*H*-pyrazole (1*H*-pz); 1*H*-1,2,4-triazole (1*H*-1,2,4-tz); 1*H*-1,2,3-triazole (1*H*-1,2,3-tz) and 1*H*-tetrazole. Note the two different isomers for triazole.

Due to these appealing characteristics, scientists started to develop the coordination chemistry of poly(azolate) derivatives more than forty years ago[5]. This interest can be traced back, *inter alia*, to the fact that azolates form short, hence strong, coordination bonds. The formation of strong coordination bonds imparts a high insolubility to coordination polymers; typically, poly(azolate)-containing CPs rapidly precipitate from the reaction medium in the form of an insoluble (microcrystalline) powder, hampering the formation of single crystals of adequate quality for X-ray diffraction structural investigations. Fortunately, powder X-ray diffraction (PXRD) may allow to unveil otherwise non-accessible key structural aspects[6].

After this brief introduction on azoles, in the following **Sections** we will focus the attention exclusively on the three azoles used to build up the poly(azole) linkers adopted during this Thesis work, namely: pyrazole, 1,2,4-triazole and tetrazole and on the effect of fluorination on the features of organic molecules.

2.2 Pyrazole, 1,2,4-triazole and tetrazole

Pyrazoles, triazoles and tetrazoles are families of azoles in which the number of nitrogen atoms increases from two to four, respectively. In pyrazoles the two nitrogen atoms are adjacent (**Figure 2.1**). In triazoles the position of the three nitrogen atoms is ambiguous (hence the need of numbering); indeed, two different isomers exist: 1,2,3-triazoles, in which the three nitrogen atoms are consecutive, and 1,2,4-triazoles, in which only two nitrogen atoms are adjacent, while the third one is between the two carbon atoms (**Figure 2.1**). Tetrazoles are the least stable azoles of this

series - pentazoles are not considered in this discussion - because the four nitrogen atoms are consecutive (**Figure 2.1**).

Tautomerism is quite common in azoles. It can be inhibited by alkylation or aryilation at one of the nitrogen atoms.

Azoles are considered electronrich molecules, because of the presence of 6 π electrons that generate the aromaticity of the system. Indeed, the inductive effect of the nitrogen atom(s) is compensated by π-donation[7]. The inductive effect of nitrogen is well pointed out by analyzing the acidic/basic properties of the title azoles: they possess the acidic pyrrolic N-H group, and at least one pyridinic nitrogen atom with a lone pair imparting basicity. Hence, two different pKa can be estimated: the pKa of the N-H group and the pKaH of the protonated form. Basicity and acidity change as a function of the number of nitrogen atoms in the ring: for pyrazole, pKaH = 2.5, while pKa = 14.2[7]. In the case of triazoles, also the position of nitrogen atoms affects basicity: for 1,2,3-triazole, pKaH = 1.2 and pKa = 9.3, while 1,2,4-triazole has a pKaH of 2.2 and a pKa of 10.3[1a,4]. 1,2,3-triazole may undergo tautomerism, but the two tautomers are identical. On the contrary, for 1,2,4-triazole tautomerism brings about the formation of different tautomers. In 1,2,4-triazole the ”isolated” nitrogen atom is more pyridine-like, so more weakly basic than in the case of 1,2,3-triazole, but it increases the acidity of the entire molecule, so that the corresponding triazolate anion is easier to obtain[1,4]. 1,2,4-triazoles have found a wide use as antifungal agents for agricultural purposes and drugs for fungal diseases in humans[2,3]. Tetrazoles possess two identical tautomers and only one isomer, since only one carbon atom is present in the aromatic ring. The presence of four nitrogen atoms imparts a high acidity to the molecule, while basicity is negligible: pKa is ~5, comparable to that of a carboxylic acid[4,7], while it is almost impossible to protonate the tetrazole ring. Indeed, we can expect tetrazole derivatives to have intermediate properties between those of pyrrole and pyridine[1a]. Due to the similarity in acidity between tetrazoles and carboxylic acids, the former have been employed in drugs when the use of CO_2H groups has led to unsatisfactory properties in drugs[1a,4].

The presence of one N-H group that can be deprotonated yielding the N^- functionality and at least one neutral nitrogen atom with an available lone pair makes azoles remarkably versatile ligands in coordination chemistry.

In the next **Section**, the most important synthetic routes toward the title azoles are presented; subsequently, their coordination chemistry is briefly discussed.

2.3 General synthesis of pyrazole, 1,2,4-triazole and tetrazole

Azoles, which can be used as precursors to prepare more complex ligands, are accessible through general, well-established synthetic procedures, which can be employed for the synthesis of a huge library of azole derivatives with different substituents, even if the presence of EW groups can raise problems along the general synthetic pathways (see the last paragraph of this **Section**).

After H. Pechmann discovered diazomethane in 1898, pyrazole was prepared by direct reaction between diazomethane and acetylene with a classic [3+2] cycloaddiction to give 3*H*-pyrazole, which immediately isomerizes to 1*H*-pyrazole[8] (**Scheme 2.1**). With this synthetic pathway, the substitution of C3 and C5 is not easy to achieve, since the activated position for an electrophilic attack on the pyrazole ring is C4. Hydrazinolysis is a possible alternative for the synthesis of substituted pyrazoles: direct reaction between 1,3-dicarbonyls and hydrazines is a feasible way to synthesize pyrazoles substituted in any possible position by tuning the substituents on 1,3-dicarbonyl and hydrazine[1b] (**Scheme 2.2**). Another protocol suitable for the synthesis of substituted pyrazoles is the Vilsmeyer-Haack reaction[9] (**Scheme 2.3**). This protocol allows scientists to build the pyrazole ring directly on a substrate possessing a C=O (aldehydic or carboxylic) functionality. The substitution on C4 can be obtained through a cycloaddition mechanism involving hydrazine and a 2-substitued-1,3-diketone, previously prepared with the already mentioned Vilsmeyer-Haack protocol[9]. Substitution in position C4 is easily afforded by a simple alogenation, but other electrophilc reactions can be performed in position C4 as well as in position N1[1b].

1,2,4-triazoles can be synthesized starting from hydrazines or substituted hydrazines: direct condensation between diacylamines and hydrazines gives 1,2,4-triazoles[4] (**Scheme 2.4**). Recently, a direct one-pot reaction in MW-assisted conditions has allowed the synthesis of substituted 1,2,4-triazoles in less than 1 h[10]. Unfortunately, the synthesis of 3,5-EWG-substituted triazoles does not work with this general pathway. To isolate EWG-substituted triazoles, principally with fluorinated substituents, the reaction pathway involves the four-step synthesis previously described by Tipping *et al.*[11].

Tetrazoles can be obtained through a quite easy way of synthesis because the four nitrogen atoms are consecutive and there is only one carbon atom on the ring: the easiest way to isolate tetrazoles is the Demko-Sharpless protocol[12] (**Scheme 2.5**), along which sodium azide directly reacts with a nitrile in water, in the presence of a strong Lewis acid such as $ZnBr_2$. Other synthetic pathways involve imidoyl halides reacting with sodium azide[4] or an activated amide; the reaction between trimethylsilyl azide and a nitrile group catalysed by copper(I) oxide is very efficient for the production of *N*-unsubstituted tetrazoles.[1b] Generally, also tetrazoles can undergo electrophilic attacks: alkylation can be performed on N1 and/or N2, the regioselectivity depending, in part, on the substituent at C5[1b]. Remarkably, some *C*-electrophilic substitutions such as bromination, iodination and even Mannich reactions, but not nitration, can be achieved[1b].

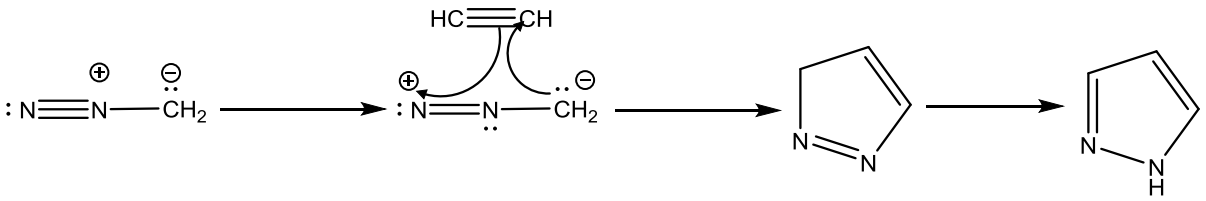

Scheme 2.1: Pechmann's reaction: concerted [3+2] cycloaddition between diazomethane and acetylene

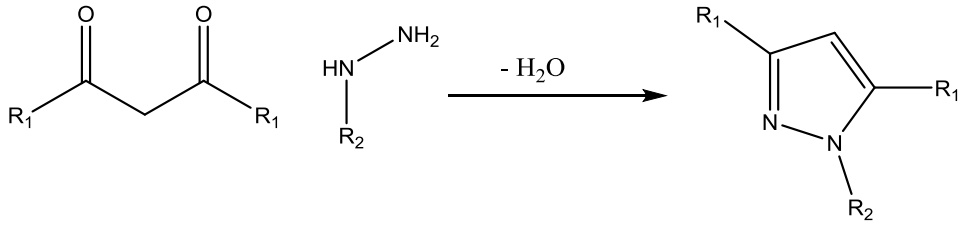

Scheme 2.2: Cyclocondensation reaction of akyl- or arylhydrazines with 1,3-dicarbonyl compounds

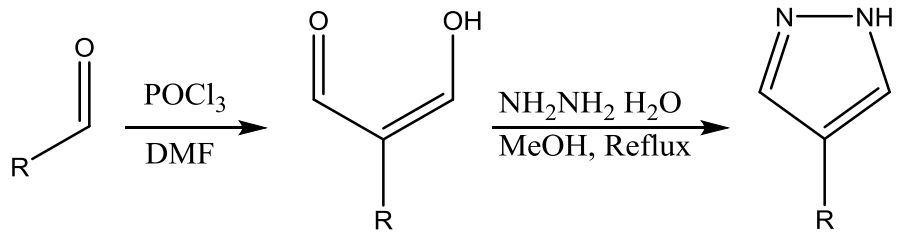

Scheme 2.3: The Vielsmeier-Haak reaction followed by hydrazinolysis for the synthesis of C4 substituted pyrazoles

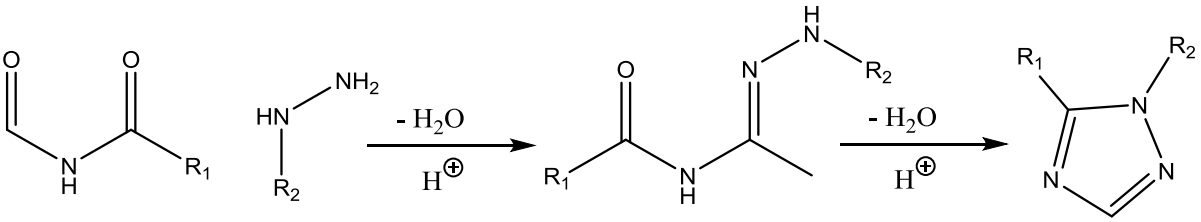

Scheme 2.4: Direct condensation between diacylamine and hydrazine for the synthesis of substituted triazoles

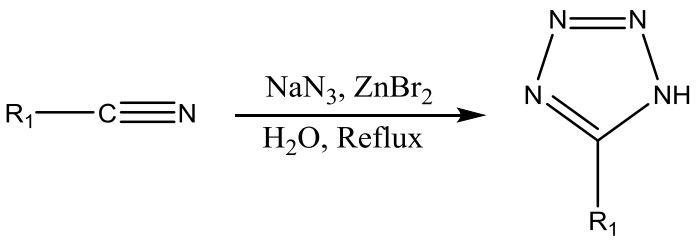

Scheme 2.5: The Demko-Sharpless protocol for the synthesis of tetrazoles. R_1 = alkyl and aryl

2.4 Pyrazole, 1,2,4-triazole and tetrazole as ligands in coordination chemistry

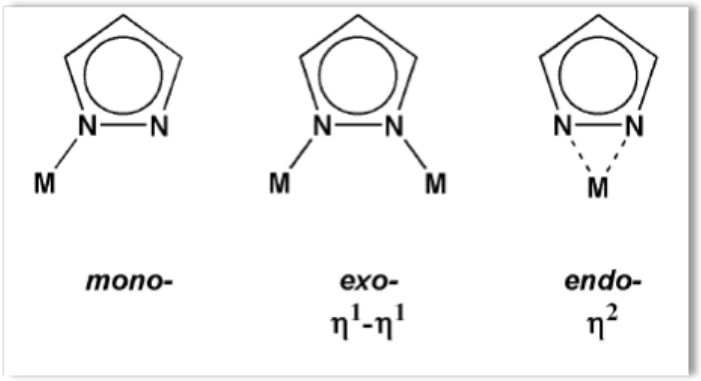

Figure 2.2: common coordination ways for the pyrazolate anion

As already underlined, the azoles adopted during this Thesis work have attracted considerable interest in coordination chemistry, mainly because of the versatility of their conjugated bases. After deprotonation, pyrazolates, triazolates and tetrazolates show different coordination modes, due also to the number of nitrogen atoms they possess.

On the whole, pyrazolates possess three different coordination modes: i) *mono*-dentate; ii) *exo*-bidentate (μ_2); and iii) *endo*-bidentate (η^2) (**Figure 2.2**). The most common coordination mode of pyrazolates is the *exo*-bidentate one, which allows the formation of olygomeric or polymeric structures. A representative example in this respect are pyrazolate-based CPs containing coinage metal ions, which feature triangular oligomers of general formula $M_3(Pz)_3$ (M = Cu^I, Ag^I, Au^I)[13]. $M_3(Pz)_3$ compounds have been constructed also with functionalized pyrazolates and have been extensively studied for their strong luminescence and host-guest properties[13]. These properties are essentially due to the close arrangement of three coordinatively unsaturated coinage-metal ions, which may interact with each other within the trimers, *via* metallophilicity, or with other trimers via π-coordination or Lewis acid-base pairing[13].

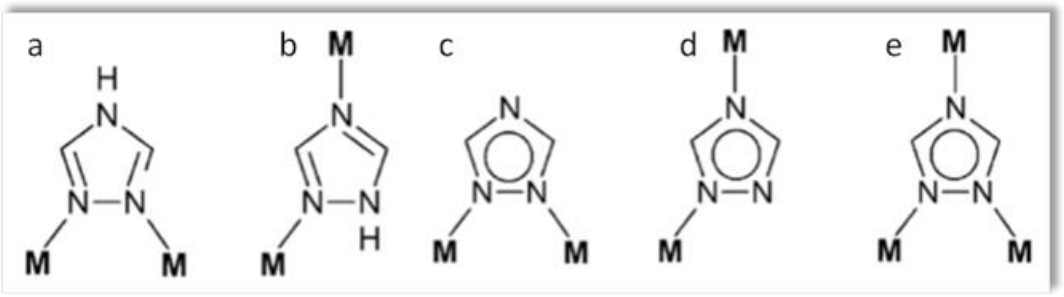

Figure 2.3: Coordination modes for 1,2,4-triazolate and 1,2,4-triazolate: a) $\mu_{3,4}$; b) $\mu_{2,4}$; c) $\mu_{1,2}$; d) $\mu_{1,4}$ and e) $\mu_{1,2,4}$.[14]

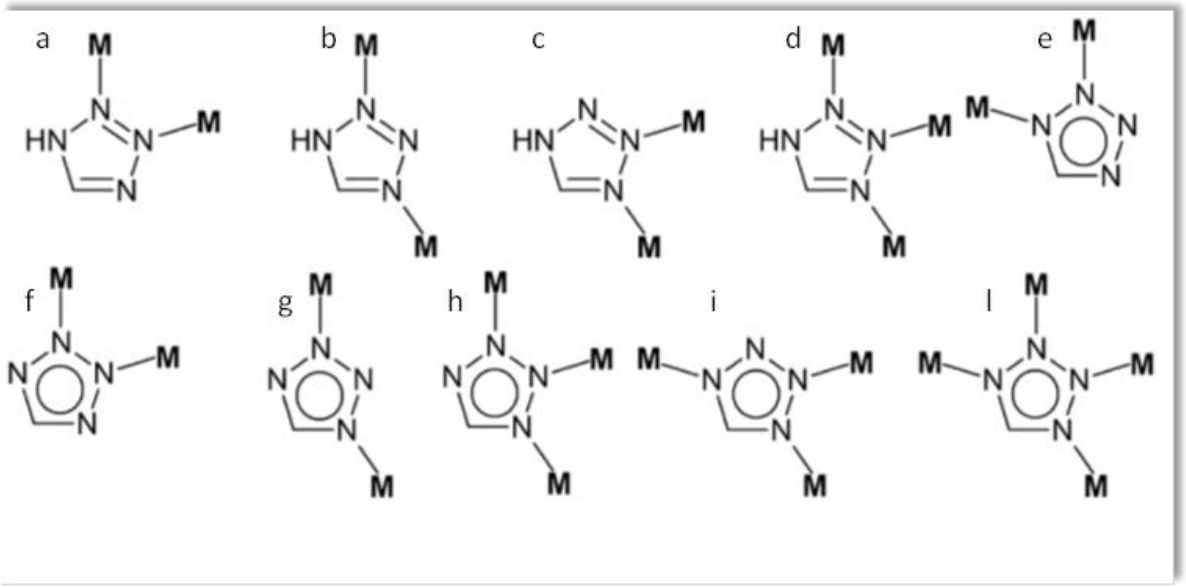

Figure 2.4: Coordination modes for tetrazole and tetrazolate: a) $\mu_{2,3}$; b) $\mu_{2,4}$; c) $\mu_{3,4}$; d) $\mu_{2,3,4}$; e) $\mu_{1,2}$; f) $\mu_{2,3}$; g) $\mu_{1,3}$; h) $\mu_{1,2,3}$; i) $\mu_{1,3,4}$; l) $\mu_{1,2,3,4}$.[14]

Worthy of note, when pyrazole is substituted in C3 and C5 positions with bulky groups, the final structural motif, when univalent coinage metal ions are used, can be a distorted tetranuclear ring[13]. On the opposite way, when no steric hindrance is at work, 1-D zig-zag chains can be obtained[13]. Interestingly, in the presence of simple anions such as OH^- or O^{2-}, high symmetry complexes can be produced[14], *e.g.* $[Co_4(\mu_4\text{-}O)(\mu\text{-}pz)_6]$[15], $[Ni_8(\mu_4\text{-}OH)_6(\mu\text{-}pz)_{12}]$[16], $[Cu_3(\mu_3\text{-}O)(\mu\text{-}pz)_3(H_2O)_3]^+$ [13], $[Cu(\mu\text{-}OH)(\mu\text{-}pz)]_8$[13], *etc*.

Neutral 1,2,4-triazoles may show the three coordination modes quoted for pyrazole, since the pyrrolic nitrogen atom is obviously unavailable for coordination. Upon deprotonation, the third nitrogen atom can be involved in the formation of coordination bonds. (**Figure 2.3**). When tri-coordinated, due to its Y-shaped coordination geometry 1,2,4-triazolate can lead to low-density derivatives showing 3-D relatively porous crystal structures.[13,14] On the whole, 1,2,4-triazolates preferably form $M_2(tz)_2$ planar dinuclear structures, the packing of which strongly depends upon the dimension of the substituents in position C2 and C5[13,14].

Tetrazolates obviously show more coordination modes (**Figure 2.4**). Zhao and co-workers identified at least nine coordination modes[17]. A search[18] in the Cambridge Structural Database (v.1.18) for transition metal complexes with ligands containing one or more *exo*- poly(dentate) tetrazolate

moieties, unveiled a diversified landscape, in which the hapticity of the ring may vary from two to four, the *exo*-bidentate coordination being the most recurring one (**Figure 2.5**).

For example, the *exo*-bidentate coordination mode can be realized through the N1,N2 couple; the N1,N3 couple [as in Zn(N,N'''-μ-ttz)$_2$, where the Zn(II) ions possess a tetrahedral coordination geometry and the crystal structure is interpenetrated[13]]; the N1,N4 couple; the N2,N3 couple. Moreover, tetrazolates can behave as *exo*-tridentate linkers with the N1,N2,N3 atoms, as in [Zn(N,N',N''-μ$_3$-mttz)$_2$] where Zn(II) adopt an octahedral coordination geometry[13], or with the N1,N2,N4 atoms, as in [Cu$_{10}$(N,N',N'''-μ$_3$-mttz)$_3$(μ$_4$-mttz)$_7$]·2H$_2$O[13] or [Ag$_3$(N,N',N'''-μ$_3$-pttz)$_2$(μ$_4$-pttz)] (Hmttz = 5-methyltetrazole), Hpttz = 5-propyltetrazole)[13].

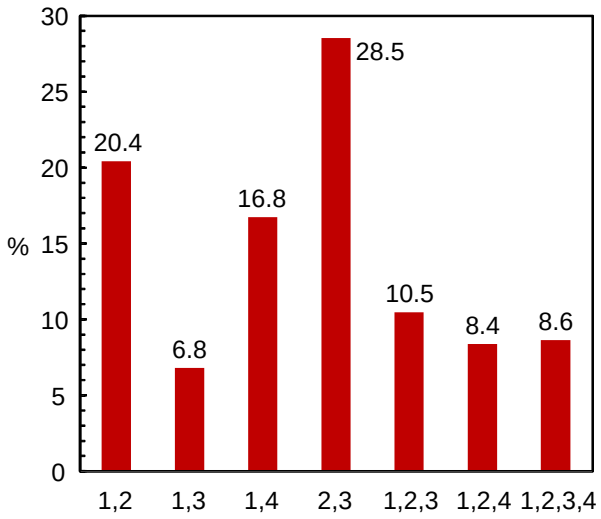

Figure 2.5: Type and frequency (expressed as percentage) of hapticity shown by poly(coordinated) tetrazolate anions in transition metal-based coordination compounds.

Finally, tetrazolates can behave as *exo*-tetradentate ligands. One of the first examples of *exo*-tetradentate tetrazolate was reported by Ciani *et al.* in [Ag$_2$(N,N',N'''-μ$_3$-ttz)(μ$_4$-ttz)] and [Ag$_{1.5}$(μ$_4$-ttz)](NO$_3$)$_{0.5}$[19]. In a similar way, in some Cu(I) derivatives tetrazolates show the μ$_4$-η^1:η^1:η^1:η^1 coordination mode[13,14].

2.5 Fluorine and its behaviour in organic chemistry

Fluorine derives its name from the use of its salt CaF_2 as a flow (from the Latin "*fluĕre*" that means "*to flow*"). It was isolated for the first time by Moissan in 1886[20] and the name was suggested to Sir H. Davy by A.-M. Ampère in 1812[21]. Due to its position in the periodic table, fluorine is the most electronegative atom along the Pauling scale (F, 4.0; O, 3.4; CI, 3.2; C, 2.6; H, 2.2). In its elemental form, fluorine is very reactive, a fact superbly underscored in the early 1960s by the direct synthesis of the noble-gas fluorides XeF_x (x = 2, 4, 6) (for example, XeF_2 is prepared by simply reacting Xe with F_2 in the sunlight[21]). The corrosive properties of HF are known since Schwanhard of Nürberg used it for decorative etching of glass[21]. Remarkably, HF is the only acid that can dissolve glass since Si-O bonds are less stable than Si-F bonds, which are among the strongest single bonds known in chemistry[22], as highlighted in **Table 2.1**.

Bond	ΔH^0 kcal/mol
O-O	35
F-F	36.6
Si-Si	52
C-N	73
Si-H	75
Si-C	76
C-O	85.5
Si-Cl	90
Si-O	110
C-F	116
O=O	119
H-F	135
Si-F	135
C=N	147
B-F	150
C=O (CO_2)	192
C≡N	213

Table 2.1: Average bond dissociation entalpies[22]

Organofluorine chemistry was readily developed after Dumas and Peligot prepared the first organic fluoride, CH_3F, from dimethyl sulphate and potassium fluoride[23]. The synthesis of fluorinated compounds can procede through two different approaches: i) purchase of the starting material already containing the C-F bond(s) needed (the so-called "building-block" approach); or ii) insertion of the required C-F bond(s) at a convenient stage using a fluorinating agent. Since the use of fluorinating agents is rather dangerous if HF or F_2

are involved, and particular techniques are needed to use fluorinating agents, the former approach has been the preferred one for the goals of this Thesis work.

ACID	pK_a
CH_3CO_2H	4.76
CF_3CO_2H	0.52
$C_6H_5CO_2H$	4.21
$C_6F_5CO_2H$	1.75
CH_3CH_2OH	15.9
CF_3CH_2OH	12.4
$(CH_3)_2CHOH$	16.1
$(CF_3)_2CHOH$	9.3
$(CH_3)_3COH$	19.0
$(CF_3)_3COH$	5.4
C_6H_5OH	10.0
C_6F_5OH	5.5
$HClO_4$	-9
HCl	-3
H_2SO_4	-3
HNO_3	-1.3

Table 2.2: Acidity of fluorinated and non-fluorinated organic acids, and strong inorganic acids

Due to the high electronegativity of fluorine, C-F bonds are highly polarized towards the fluorine atom: this occurrence imparts a high dipole moment to the bond (and, possibly, to the whole molecule). Unexpectedly, polarization does not impart a good donor ability to the fluorine atom in spite of its three lone pairs: these valence electrons are held tightly due to the high electronegativity of the atom and, unlike in the case of oxygen or nitrogen, they do not get involved in resonance; indeed, when the fluorine atom of a C–F bond does interact with its environment, it is usually through ion/dipole or dipole/dipole interactions[24]. Another important feature of fluorinated organic compounds is their lipophilicity (or hydrophobicity). It is common thought that fluorine atoms increase the lipophilicity of organic compounds: this is true only for aromatic fluorination or fluorination adjacent to conjugated π-systems: as a matter of fact, monofluorination or trifluoromethylation of aliphatic molecules decrease lipophilicity[23].

Since fluorine is the most electronegative element of the periodic table, its presence close to an acidic functional group strongly increases the acidity of the compound: for example, TFA has a pKa of 0.52, comparable to those of the strongest inorganic acids[23] (**Table 2.2**) (acetic acid possesses a pKa

equal to 4.74). A consequence of this feature is the ability of fluorinated molecules to give strong hydrogen bonds not only through heteroaromatic hydrogen atoms, but also through acidic C-H bonds. Intramolecular hydrogen bonds can be also formed if the F---H distance is shorter than the sum of the van der Waals radii of fluorine and hydrogen.

Due to the strong inductive effect of fluorine, the basicity of fluorinated organics decreases if fluorine is close to the basic site: for example, pyridine is a weak base but can easily coordinate soft metal ions, while perfluoropyridine does not react with metal ions, is not protonated by HCl, and does not react with BF_3. Moreover, hexafluoroacetone cannot be protonated in solution by superacids[23].

The common belief that the radii of F and H^- are similar, so that the substitution of H with F does not affect the steric properties but strongly modifies the electronic properties, is not completely correct: as emerged from recent calculations, fluorine has dimension similar to that of the O-H group, and the CF_3 functionality is as large as $CH(CH_3)_2$[23]. This feature is important because the steric hindrance of the fluorinated functionality can affect the overall reactivity of fluorinated compounds. Anyway, as already underlined, also the electronic properties are strongly modified by fluorination.

C-F bonds are the strongest single bonds that carbon can make with any element. Carbon fluorides are less reactive than all the other carbon halides, principally because of the strength of the bond, but also because of the shielding and the inductive effect of fluorine over carbon, and the poor leaving group ability of fluorine. Moreover, functional aliphatic hydrocarbons show stronger bonds if fluorination is present: for example, RCF_2Br compounds are inert to halide exchange under classical reaction conditions[23]. More interesting for some of the goals of this Thesis work, fluorination of unsaturated systems imparts strength to C-F bonds[23]; yet, thermodynamic calculations[23] indicate that monofluorination stabilizes double bonds, while higher degree of fluorination destabilizes the system. Strong differences are found if the molecule is simply fluorinated or alkylfluorinated: for example, fluorination increases the strength of C=O bonds, while trifluoromethylation strongly

decreases it[23]. However, perfluoroalkylation can kinetically stabilize organic compounds containing highly strained rings through the so-called "perfluoroalkyl effect"[23].

Despite the poor ability of fluorine as leaving group and the strength of C-F and C=C bonds derived by fluorination, perfluoro- and fluoro-aromatic molecules present a specific reactivity depending on the degree of fluorination. The higher the degree of fluorination, the higher the probability that the C-F bond can undergo a classical nucleophilic attack: for example, N_3^- can substitute up to two fluorine atoms on perfluorobenzene, showing an EWG-substituent, *via* classical nucleophilic attack under microwave conditions[25]. Moreover, also Zn(II) insertion on aromatic C-F bonds has been observed,[26] which has led to the use of perfluorinated aryl-compounds as reagents for reactions which up to then were considered impossible to perform with fluorinated aryl-compounds.

2.6 Conclusions

As highlighted in this **Chapter**, azoles are very versatile ligands in coordination chemistry: once deprotonated and coupled to transition metal ions, they may generate a huge library of crystal structures, ranging from polynuclear complexes to metallacycles or 1-D to 3-D polymers. Fluorination of poly(azole)-containing ligands, as performed in this Thesis project, imparts particular properties to the ligand itself and the corresponding CPs: the higher acidity and lower basicity of fluorinated azoles influence the coordination to the metal ion. Fluorinated CPs possess specific electronic and steric properties to be exploited in a number of applications, from adsorption and separation of gases to the preparation of molecular rotors, or low-dielectric constant materials. All these properties will be discussed in the next **Chapters**.

References and Notes

[1] a) Clayden, J.; Greeves, N.; Warren, S. and Whoters, P *Organic Chemistry*, Oxford University Press, **2001**; b) Joule, J. A. and Mills, K *Heterocyclic Chemistry* Fifth Ed., John Wiley & Sons, Ltd. **2010**.

[2] Pozharskii, A. F.; Soldatenkov, A. and Katritzky, A. R. *Heterocycle In Life And Society* 2nd. Ed., **2011**, A John Wiley & Sons, Ltd., Publication.

[3] a) Corey, E. J.; Czakó, B. and Kürti, L. *Molecules and Medicine*, 1st Ed, **2007**, A John Wiley & Sons, Ltd., Publication; b) Sica, D. and Zollo, F. *Chimica dei Composti Eterocicli farmacologicamente attivi*, 1st Ed., **2008**, Piccin Nuova Libraria S.p.A., Padova.

[4] Eicher, T. and Hauptmann, S. *The Chemistry of Heterocycles: Structure, Reactions, Syntheses, and Applications* 2nd Ed., **2003**, Wiley-VCH. ISBN 3527307206.

[5] Garnovskii, A. D.; Osipov, O. A.; Kuznetsova, L.,I.; Bogdashev, N. N. *Russ. Chem.Rev.*, **1973**, *42*, 89.

[6] (a) Masciocchi, N.; Galli, S. and Sironi, A. *Comments Inorg. Chem.* **2005**, *26*,1. (b) Fackler, J. P. and Falvello, L. *Techniques in Inorganic Chemistry*, CRC Press Taylor and Francis: Boca Raton, **2010**, Florida.

[7] Broggini, G and Zecchi, G *Chimica degli etero cicli*. LaScientifica.it, **2003**, Italia

[8] Pechmann, H. v. *Berichte der deutschen chemischen Gesellschaft* **1898**, *31*, 3, 2950.

[9] (a) Marson, C. M. *Tetrahedron* **1992**, *48*, 3659. (b) Jutz, C. *Advances in Organic Chemistry* (Eds. Taylor, E. C.). John Wiley & Sons, New York, **1976**, Vol. 9, 252. (c) Reichardt, C. *J. Prakt. Chem.* **1999**, *341*, 609.

[10] Lee, J.; Hong, M.; Jung, Y.; Cho, E. J. and Rhee, H. *Tetrahedron,* **2012,** *68,* 2045-2051

[11] a) Bell, D. (in part); Eltoum, A. O. A. (in part); O'Reilly, N. J. and Tipping, A. E. *J. Fluor. Chem*, **1993**, *64*, 151-166; b) Abdul-Ghani, M. M. and Tipping, A. E. *J. Fluor. Chem.*, **1995**, *72,* 95-106.

[12] a) Demko, Z. P. and Sharpless, K. B. *J. Org. Chem.* **2001,** *66,* 7945-7950.

[13] Zhang, J.-P.; Zhang, Y.-B.; Lin, J.-B. and Chen, X.-M. *Chem. Rev.*, **2012**, *112*, 1001–1033.

[14] Aromì, G.; Barriosa, L. A.; Roubeaub, O. and Gameza, P. *Coord. Chem. Rev.*, 2011, *255*, 485−546.

[15] Ehlert, M. K.; Rettig, S. J.; Storr, A.; Thompson, R. C. and Trotter, J. *Acta Crystallogr. ,Sect. C*, **1994**, *50*, 1023.

[16] Xu, J. Y.; Qiao, X.; Song, H. B.; Yan, S. P.; Liao, D. Z.; Gao, S.; Journaux, Y. and Cano, J. *Chem. Commun.*, **2008**, 6414.

[17] Zhao, H.; Qu, Z.-R.; Ye, H.-Y.; Xiong, R.-G. *Chem. Soc. Rev.* **2008**, *37*, 84-100.

[18] The search was performed excluding, from the potential hits, those having errors and containing ions, and those referring to the same phase but derived from data acquired in different experimental conditions, yielded a total of 387 hits.

[19] Carlucci, L.; Ciani, G.; Proserpio, D. M. *Angew. Chem. Int. Ed.*, **1999**, *38*, 3488-3492.

[20] R. B. Banks, D.W.A. Sharp, and 1. C. Tatlow (eds.), *Fluorine: The First Hundred Years (1886-1986),* Blsevier Sequoia, Lausanne and New Yode **1986** [reproduced in *J. Fluor. Cherm.*, 1986, *33*]

[21] Greenwood, N. N. and Earnshaw, A. *Chemistry of the Elements,* Second Ed., Chapter 17 (''The Halogens''), Pergamon Press, Oxford, **1984.**

[22] a) Sanderson, R. T., *Chemical Bonds and Bond Energy*, Elsevier Science, Oxford, **1976**; b) Sanderson, R. T., *Polar Covalence*, New York : Academic Press, **1983**.

[23] Banks, R. E.; Smart, B. E. and Tatlow, J. C. *Organofluorine Chemistry Principles and Commercial Applications*, Springer Science+Business Media New York, **1994**.

[24] O'Hagan, D. *Chem. Soc. Rev.*, **2008**, *37*, 308–319.

[25] Leyva, E.; Leyva,S.; Moctezuma, E.; Gonzalez-Balderas, R. M. and de Loera, D. *J. Fluor. Chem.* **2013**, *156*, 164–169.

[26] Miller, A. O.; Krasnov, V. I.; Peters, D.; Platonov, V. E. and Miethchen, R. *Tetrahedron Let.*, **2000**, *41*, 3817–3819.

Chapter 3
Design and synthesis of poly(pyrazolate)- and poly(tetrazolate)-based ligands

3.1 Introduction

Together with the judicious choice of the metal ions, the design of the organic linkers is a key point for the construction of useful MOFs for practical applications. Conversely to the inorganic SBUs, which are generated *in situ*, organic linkers are designed and synthesized before the complexation. This occurrence enables scientists to strictly control the chemical and physical properties of the spacers, which concur to modulate the structure and properties of MOFs or CPs. Expansion of the library of the organic linkers is thus motivated not only to enrich the diversity of MOF structures but, mainly to tune MOFs features for the desired applications. As already extensively discussed, the main donor group used for the synthesis of MOFs is carboxylate, but also pyridyl, amine, sulphonate, phosphonate donor groups and, of course, azoles have been used[1]. As already mentioned, the majority of donor groups are based on oxygen because of its versatility in coordination: each O-donor atom can bind one, two or even three metal ions affording a wide range of possible structures for the inorganic SBUs. Moreover, poly(carboxylate) ligands are simple to synthesize and easily affordable from commercial suppliers. Azole-based MOFs were firstly achieved by using imidazole as organic spacer[2], and were further prepared by the use of tetrazole-based linkers[3].

By exploiting the coordination chemistry of azoles, the concept of basicity must be recalled to better understand the chemical stability of poly(azolate) MOFs. The strength of the M-N bond (M = metal ion) is strictly related to the pKa values for the deprotonation of the N-H group. The presence of a boost of electron density on the aromatic ring and, consequently, on the donor atom, leads to the formation of a strong donor-M bond.

Due to their high electronegativity and strong inductive effect, the presence of fluorine atoms reduces the coordination ability of the ligand: this issue addresses the choice of strong donor moieties in order to balance the fluorine effect. Poly(azolate)-based ligands satisfy this condition because of their ability to form strong M-N bonds. Moreover, as highlighted in the next Chapters, the fluorine atoms will play a major role in the stability of the final MOF or CP.

Among the presented azolates, see **Chapter 2**, pyrazolate- and imidazolate-based CPs show a higher stability than triazolate- and tetrazolate-based ones due to their pKa values[4] (see also **Chapter 2**).

The design of the ligands presented in this Thesis was driven by the specific application targeted: the construction of low dielectric constant (low-κ) materials or of molecular rotors, and the exploitation of exposed metal ions for catalysis.

Herein, the syntheses of a series of new bis(pyrazolates), bearing different functionalization on the aromatic core, and of two new perfluorinated mono- and bis-tetrazolate-based ligands are presented. The syntheses, structural characterization and functional properties of the corresponding MOFs or CPs will be extensively discussed in the next **Chapters**.

3.2 The Sonogashira cross-coupling

The formation of new C-C bonds has always been in the core of organic chemistry. In the last 100 years multiple ways to reach this goal have been explored with[5] or without[6] the help of metal ions. The major catalytic reactions available for the formation of C-C bonds are: i) Kumada coupling[7]; ii) Mizoroki-Heck reaction[8]; iii) Migita-Kosugi-Stille reaction[9]; iv) Negishi coupling[10]; v) Suzuki-Miyaura coupling[11], iv) Hiyama coupling[12] and v) Sonogashira-Hagihara coupling[13]. All of these reactions,

except some modifications for Kumada and Negishi coupling where the main catalytic cycle is catalyzed by Ni(II)[7,10] are catalyzed by Pd, but they differ in the nature of the co-catalyst and of the organic substrates, and in the FG tolerance[7-13]. For our purposes, the Sonogashira coupling is the preferred catalytic reaction, since it allows the coupling of aryl-X (X = Br, I, OTf) and terminal alkynes.

The first studies on sp-sp^2 coupling reactions were performed independently by Cassar[14] and Heck[15] in 1975. The first investigation was based on the use of a Pd-based catalyst in the presence of sodium methoxide as base and DMF as solvent. The second study was based on the already mentioned Mizoroki-Heck reaction and made use of Pd(0)- or Pd(II)-based catalysts and TEA or piperidine as base and solvent. The main flaw of these procedures was the reaction temperature, usually over 100 °C. In the same year, Sonogashira and Hagihara reported[13] that the addition of a catalytic amount of a Cu(I) salt, usually CuI, speeded up the reaction, allowing the use of milder reaction conditions, even at RT. This solution was achieved by the exploitation of the well-known Stephens-Castro[16] coupling between Cu(I)-acetylides and phenyl- or vinyl-halides. Interestingly, not only aryl-halides, but also alkyl- and alkenyl-halides could be coupled with acetylides using the Sonogashira protocol; however, this kind of sp-sp^3 coupling is recent and requires particular reaction conditions and catalysts.[17]

The presence of Cu(I) salts implies one main drawback: the formation *in situ* of copper acetylides can lead to the homo-coupling reaction between two terminal alkynes, following the Glaser coupling[18], when exposed to air or oxidizing agents. This side reaction is problematic especially if the terminal alkynes are expensive or difficult to obtain. Some solutions envisage the use of a reducing atmosphere/system, and the slow addition of the alkyne[19] to reduce the homo-coupling; moreover, a number of copper-free methodologies have been developed.[20] Curiously, some Pd(II) salts commercially available, *e.g.* $PdCl_2$ or $Pd(OAc)_2$, which are the most common precursors for Pd-based catalysts, contain low quantities of copper impurities, which instils the doubt that those protocols are not really copper-free.[21]

The copper co-catalyzed reaction mechanism is still unclear[22]. Some catalytic systems have been developed[22,23] to unveil the mechanism, but some hurdles may happen: the already mentioned Cu(I) impurities in the Pd(II) precursor and the invalidation of some kinetic measurements due to the fact that catalytic activity is observed after the quenching of the reaction (using the classical method of adsorption on silica gel), symptom that traces of Pd pass through the silica gel[22,24].

The generally accepted catalytic mechanism is based on two catalytic cycles, namely the Pd-cycle and the Cu-cycle.

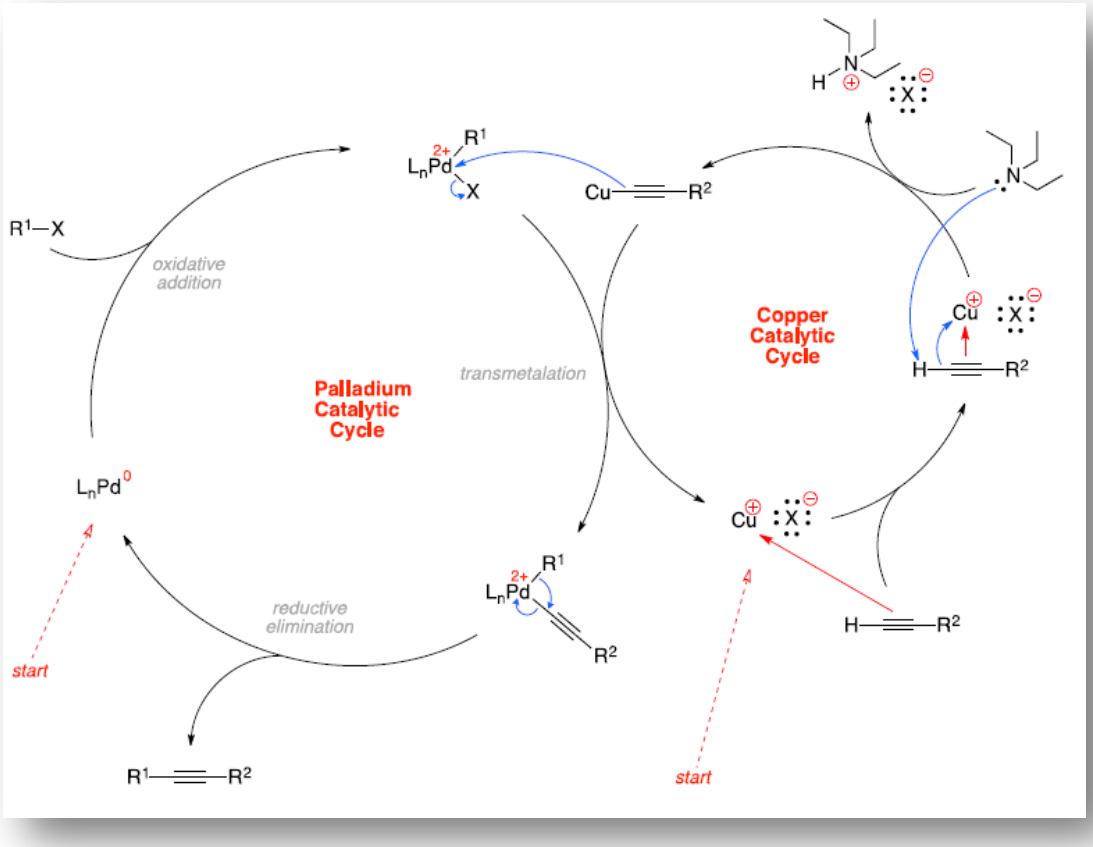

Figure 3.1: Catalytic cycle for the Sonogashira cross-coupling[25]

The active catalyst is generated *in situ*, starting from a mixture of a commercially available Pd(II) salt (*e.g.* $Pd(OAc)_2$) and the ligand: it is known that *n*-electron donors, such as phosphanes, amines, and ethers, used as ligands and solvents, can reduce Pd(II) species typically via *σ*-complexation-dehydropalladation-reductive elimination[26].

The first step of the Pd-cycle is the, usually fast, oxidative addition to the catalyst by the aryl-, vinyl- or hetaryl-halide (R^1-X) affording a [Pd(R^1)(X)(L_2)] species. The second step is strictly correlated to the Cu-cycle: a transmetallation from the Cu(acetylide) formed in the Cu-cycle would generate a [Pd(R^1)(acetylide)(L_2)] species, which gives the final coupled alkyne after *trans*/*cis* isomerisation and reductive elimination with regeneration of the catalyst[22].

The nature of the Cu-cycle is unclear: in the accepted mechanism the base is supposed to extract the proton from the terminal alkyne forming a Cu(acetylide) in the presence of a Cu(I) salt, usually CuI. The most used bases for this process, TEA or K_2CO_3, are not basic enough to abstract the acetylenic proton, thus a π-alkyne-Cu complex could be involved in the cycle, turning the alkyne acid enough to be deprotonated[27]. Recently, NMR studies have demonstrated that π-alkyne-Ag complexes are formed after the generation of Ag(acetylides) in silver co-catalyzed Sonogashira couplings[28]: the results of these studies could be expanded to the copper co-catalyzed reactions. Oddly, the presence of Cu(acetylides) in the reaction mixture has not been proved yet, even if some evidences have been found[27]. Moreover, some questions have been raised on the nature of the real catalysts of the reaction[29]: it has been observed that *mono*-ligated Pd complexes could be formed in the presence of bulky ligands and have been suggested as possible active species in catalytic reactions[29]. Furthermore, the presence of halides and anions raises doubts about the existence of the Pd(0)L_2 species in solution because halides would coordinate Pd generating anionic species such as [Pd(0)L_2X]$^{-}$[30] which can participate in cross-coupling reactions[31].

The general reactivity of the sp^2 substrates is: vinyl iodide ≥ vinyl triflate > vinyl bromide > vinyl chloride > aryl iodide > aryl triflate ≥ aryl bromide >> aryl chloride. Moreover, if the sp^2 species is activated, namely if it is electron poor, the reaction becomes more favourable compared to the non-activated one. Generally, the use of the more expensive and unstable aryl- or vinyl-iodide induces an easier and quicker reaction, while aryl- or vinyl bromides are “unfriendly” substrates, and aryl- or vinyl-chlorides, if not activated, are a real challenge for any reaction method[32].

3.3 Experimental Details

3.3.1 Synthesis of 1,4-bis(trimethylsilylethynyl)-fluorobenzene

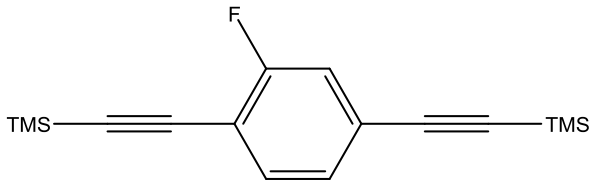

An oven-dried Schlenk flask was purged with Ar and charged with 1,4-dibromo-fluorobenzene (2.200 g, 8.66 mmol), $PdCl_2(PPh_3)_2$ (0.330 mg, 0.47 mmol) and CuI (0.090 g, 0.47 mmol). The flask was cooled with an acetone/dry ice bath and sealed with a rubber septum. Ar-purged TEA (25 mL) and THF (25 mL), previously filtered over Al_2O_3, were added by means of a syringe. The obtained mixture, purged by Ar at RT, was stirred for 20 min; afterwards, TMSA (3.780 mL, 26.75 mmol) was added. The resulting yellow mixture was sealed under N_2 atmosphere and kept at 45 °C under stirring for 4 h. The colour of the mixture changed from yellow to brown and then to black as the temperature was raised. The extent of the reaction was controlled by GC-MS. Additional portions of TMSA (0.100 mL, 0.71 mmol) were periodically added. After 4 h, GC-MS analysis showed the complete consumption of 1,4-dibromo-fluorobenzene. The reaction mixture was cooled down to RT and filtered. The solid was washed with AcOEt (50 mL) and the combined organic layers were evaporated under reduced pressure to obtain a black solid. The latter was dissolved in AcOEt (100 mL) and washed with 30 % aq NH_4OH (2×50 mL) and water (50 mL). The organic layer was dried over Na_2SO_4 and evaporated under reduced pressure. The black residue was purified by silica-gel flash chromatography (eluent: hexane) to afford the title compound as a white solid (1.720 g, 69 %). IR (ATR, cm^{-1}): 3270 (vs), 2116 (w), 1912 (w), 1748 (w), 1612 (m), 1551 (s), 1478 (s), 1410 (s), 1411 (s), 1266 (m), 1251 (s), 1140 (m), 1106 (s), 951 (s), 868 (vs), 824 (vs), 712 (m). ^{1}H NMR ($CDCl_3$) δ (ppm) 7.41 (1H, dd, *J* = 8.8, 7.8 Hz), 7.22 (1H, dd, *J* = 7.8, 2.0 Hz), 7.19 (1H, dd, *J* = 10.23, 2.0 Hz), 0.20 (9H, s), 0.19 (9H, s). ^{13}C NMR ($CDCl_3$) δ 164.8, 161.9, 134.3, 127.7, 127.6, 125.6, 125.0, 119.9, 118.00, 112.9, 112.7, 103.7, 102.5, 102.9, 3.4. ^{19}F NMR ($CDCl_3$) δ (ppm) −110.91. Elem. Anal. Calcd. for $C_{16}H_{21}FSi_2$ (FW = 288.51 g/mol): C, 66.61%, H, 7.34%; found C, 67.31%, H, 7.89.%.

3.3.2 Synthesis of 1,4-bis(ethynyl)-fluorobenzene

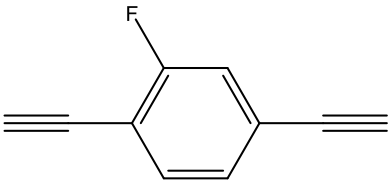

1,4-bis(trimethylsilylethynyl)-fluorobenzene (1.400 g, 4.87 mmol) was dissolved in a 1:1 mixture of CH_2Cl_2 and MeOH (24 mL). The solution was heated up to 40 °C and, under stirring, K_2CO_3 (7.000 g, 50,65 mmol) was added. After 3 h, a GC-MS analysis showed the complete consumption. The mixture was then cooled down to RT and filtered, the excess of K_2CO_3 was washed Et_2O (50 mL). The organic layer was evaporated under reduced pressure, the obtained solid was re-dissolved in Et_2O (20 mL), and washed with water (15 mL). The organic layer was dried over Na_2SO_4 and evaporated under reduced pressure to afford the title compound as a brownish solid. (0.600 g, 86 %). IR (ATR, cm^{-1}): 3265 (vs), 2115 (w), 1908 (w), 1750 (w), 1615 (m), 1546 (s), 1489 (s), 1418 (s), 1405 (s), 1279 (m), 1246 (s), 1143 (m), 1104 (s), 949 (s), 871 (vs), 826 (vs), 707 (m). ^{1}H NMR ($CDCl_3$) δ 7.49 (1H, t, *J* = 8.3 Hz), 7.31 (1H, dd, *J* = 8.3, 1.4 Hz), 7.23 (1H, dd, *J* = 10, 1.4 Hz), 3.31 (1H, s), 3.22 (1H, s). ^{13}C NMR ($CDCl_3$) δ (ppm) 164.9, 161.3, 134.2, 133.9, 128.1, 127.9, 124.7, 124.8, 119.0, 119.2, 111.7, 111.7, 84.3, 84.2, 82.2, 82.0, 80.2, 77.1. ^{19}F NMR ($CDCl_3$) δ −110.91. Elem. Anal. Calcd. for $C_{10}H_5F$ (FW = 144.15 g/mol): C, 83.32%, H, 3.50%; found C, 82.95%, H, 3.97%.

3.3.3 Synthesis of 1,4-bis(1-ethoxyethylpyrazolyl)ethynyl)-fluorobenzene

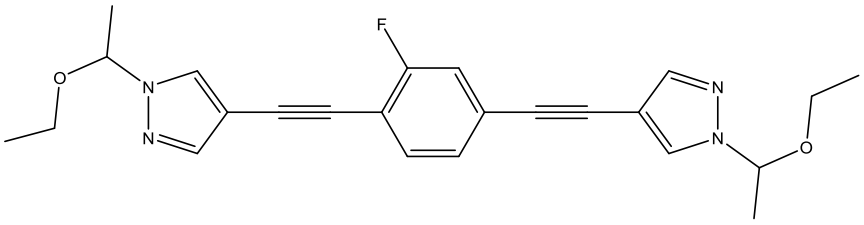

An oven-dried Schlenk flask was purged with Ar and charged with 4-iodo-(1-ethoxyethyl)-pyrazole (1.980 g, 7.45 mmol), $Pd(PPh_3)_2Cl_2$ (0.200 g, 0.28 mmol) and CuI (0.065 g, 0.34 mmol). The flask was sealed with a rubber septum and Ar-purged TEA (25 mL) and THF (25 mL), previously filtered over Al_2O_3, were added by means of a syringe. The obtained yellowish solution, cooled with an acetone/dry ice bath and purged by bubbling Ar, was stirred for 20 min; afterwards, 1,4-bis(ethynyl)-fluorobenzene (0.500 g, 3.47 mmol) was added and the resulting mixture was heated up to 60 °C and

kept at this temperature under stirring. The colour of the mixture changed from pale yellow to red-brown as the temperature was raised. After 4 h, TLC analysis (silica gel; hexane:AcOEt = 4:1) showed the complete consumption of 1,4-bis(ethynyl)-fluorobenzene. Then, the mixture was filtered and the solution was evaporated under reduced pressure affording an orange paste. The latter was dissolved in AcOEt (50 mL) and washed with 30 % aq NH_4OH (2×50 mL) and water (50 mL). The organic layer was dried over Na_2SO_4 and evaporated under reduced pressure to afford an orange paste. This solid was stirred with pentane (5 mL) for 15 min to remove the excess of 4-iodo-(1-ethoxyethyl)-pyrazole and then filtered. The obtained yellow-orange powder was transferred to a Soxhlet and washed with refluxing pentane (100 mL) for 25 min. The solvent was removed under reduced pressure to afford the title compound as a bright yellow powder. (0.410 g, 27%). IR (ATR, cm^{-1}): 3108 (w), 3083 (w), 2977 (w), 2906 (w) 2222 (s), 1613 (w), 1563 (w), 1538 (w), 1488 (s), 1436 (m), 1417 (m), 1361 (m), 1237 (w), 1118 (vs), 1064 (vs), 1009 (s), 980 (s), 943 (s), 864 (vs), 826 (vs), 787 (m), 751 (s), 704 (s), 663 (m), 640 (vs). ^{1}H-NMR (DMSO-*d6*): δ (ppm) 8.37 (1H, s), 8.34 (1H, s), 7.80 (1H, s), 7.78 (1H, s), 7.56 (1H, t, J = 7.92; 7.84), 7.44 (1H, dd, J = 1.4; 10.2), 7.33 (1H, dd, J = 1.4; 8), 5.56 (1H, q), 3.43 (1H, m), 3.20 (1H, m), 1.59 (3H, d, J = 6), 1.03 (3H, t, J = 7). ^{13}C-NMR (DMSO-*d6*): δ (ppm) 164-162, 139.5, 131.4, 130.9, 122.3, 120.8, 110.9, 105.3, 84.3, 83.8, 80.2, 78.2, 66.3, 65.7, 23.1, 21.2, 12.6, 11.3. ^{19}F NMR ($CDCl_3$) δ −111.01. Elem. Anal. Calcd. for $C_{24}H_{25}FN_4O_2$ (FW = 420.49 g/mol): C, 68.55%, H, 5.99%, N, 13.32; found C, 69.32%, H, 5.27%, N, 14.01.

3.3.4 Synthesis of 1,4-bis(1*H*-pyrazolylethynyl)-fluorobenzene (H_2BPEBF)

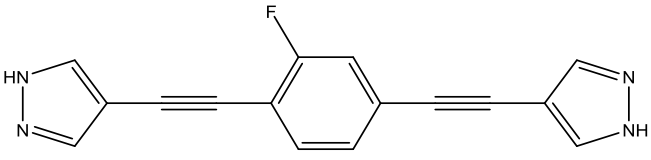

1,4-bis(1-ethoxyethylpyrazolyl)ethynyl)-difluorobenzene (0.644 g, 1.48 mmol) was dissolved in 1,4-dioxane (10 mL). 6 N HCl (4 mL) was added. The precipitation of a yellow solid occurred very quickly. The reaction mixture was heated up to 40 °C and kept at this temperature under stirring for 2 h. Then the precipitate was

filtrated, washed with 1,4-dioxane (5 mL) and MeOH (20 mL) and dried *in vacuo* overnight to afford the title compound as a bright yellow solid. (0.370 g, 90 %).

IR (ATR, cm^{-1}): 3095 (w), 2934 (w), 2430 (m), 2225 (m), 1615 (w), 1539 (m), 1482 (m), 1470 (m), 1372 (m), 1272 (w), 1180 (w), 1111 (m), 1071 (w), 994 (m), 943 (m), 810 (s), 742 (m). ^{1}H-NMR (DMSO-*d6*): δ (ppm) 7.96 (2H, s), 7.94 (2H, s), 7.56 (1H, t, J = 7.84), 7.43 (1H, dd, J = 1.4; 11), 7.31 (1H, dd, J = 1.4; 7.86). ^{13}C-NMR (DMSO-*d6*): δ (ppm) 162-160, 137.4, 133.9, 127.1, 124.3, 118.7, 111.1, 100.3, 89.0, 88.1, 85.7, 83.1. ^{19}F NMR ($CDCl_3$) δ (ppm) −111.01. Elem. Anal. Calcd. for $C_{16}H_9FN_4$ (FW = 276.27 g/mol): C, 69.56%, H, 3.28%, N, 20.28; found C, 69.02%, H, 3.89%, N, 20.01.

3.3.5 Synthesis of 1,4-bis(trimethylsilylethynyl)-2,3-difluorobenzene

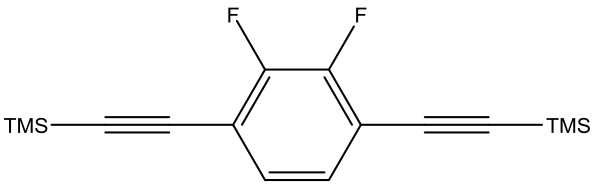

In a Schlenk flask, TEA (20 mL) was degassed with Ar for 20 min. Under vigorous stirring, 1,4-dibromo-2,3-difluoro benzene (0.760 g, 2.79 mmol), $PdCl_2(PPh_3)_2$ (0.098 g, 0.14 mmol), TMSA (0.500 mL, 3.54 mmol) and CuI (0.027 g, 0.14 mmol) were added. The reaction mixture was heated up to 70 °C for 4 h. After that, TMSA (0.500 mL, 3.54 mmol) was added and the mixture was let at 70 °C for further 4 h. The reaction progress was monitored with TLC (hexanes). TMSA (0.200 mL, 1.42 mmol) was further added until the TLC plates showed the complete consumption of 1,4-dibromo-2,3-difluoro benzene. Once the reaction was completed, usually after 12 h, the mixture was filtered over a Celite plug. The Celite plug was washed with hexanes (40 mL) and then evaporated under reduced pressure. The solid obtained was solubilised in AcOEt (20 mL) and washed with 30 % aq NH_4OH (2×50 mL) and water (50 mL). The organic layer was dried over Na_2SO_4 and evaporated under reduced pressure affording a dark brown solid. The obtained solid was purified by column chromatography (hexanes) to afford the title compound as a white solid. (0.539 g, 63 %). IR (ATR, cm^{-1}): 3271 (vs), 2209 (m), 1978 (m), 1798 (w), 1768 (m), 1550 (s), 1471 (s), 1409 (m), 1391 (s), 1245 (w), 1211 (s), 1130 (w), 1116 (s), 950 (s), 880 (vs), 831 (vs), 709 (m). ^{1}H NMR ($CDCl_3$) δ (ppm) 7.23 (2H, m), 0.18 (9H, s). ^{13}C NMR ($CDCl_3$) δ (ppm)

149.3, 130.4, 111.3, 107.7, 100.6, 3.4. ^{19}F NMR ($CDCl_3$) δ (ppm) −110.91 (2F). Elem. Anal. Calcd. for $C_{16}H_{20}F_2Si_2$ (FW = 306.50 g/mol): C, 62.70%, H, 6.58%; found C, 62.31%, H, 7.01.%.

3.3.6 Synthesis of 1,4-bis(ethynyl)-2,3-difluorobenzene

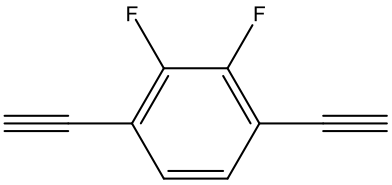

1,4-bis(trimethylsilylethynyl)-2,3-difluorobenzene (0.700 g, 2.28 mmol) was dissolved at RT in a round bottomed flask charged with MeOH (10 mL) and CH_2Cl_2 (10 mL). Then, the solution was heated at 40 °C and K_2CO_3 (5.000 g, 36.18 mmol) was added. A white suspension was formed. The reaction progress was monitored by TLC (9:1 = hexanes:AcOEt). Once the reaction was completed, usually after 6 h, the suspension was filtered and the excess of K_2CO_3 was washed directly in the funnel with Et_2O (30 mL). Et_2O was evaporated under reduced pressure and the obtained solid was solubilised again in Et_2O (20 mL) and washed with brine (2×20 mL). The organic layer was dried over Na_2SO_4 and evaporated under reduced pressure affording the title compound as a brown solid. (0.255 g, 69 %). IR (ATR, cm^{-1}): 2219 (m), 1998 (m), 1895 (w), 1768 (m), 1598 (s), 1459 (m), 1356 (s), 1221 (s), 1120 (s), 960 (s), 890 (vs), 830 (vs), 719 (m). ^{1}H NMR ($CDCl_3$) δ (ppm) 7.23 (2H, m), 0.18 (9H, s). ^{13}C NMR ($CDCl_3$) δ (ppm) 149.2, 130.2, 111.6, 82.1, 81.6. ^{19}F NMR ($CDCl_3$) δ (ppm) −110.71 (2F). Elem. Anal. Calcd. for $C_{10}H_4F_2$ (FW = 162.14 g/mol): C, 74.08%, H, 2.49%; found C, 73.78%, H, 2.21.%.

3.3.7 Synthesis of 1,4-bis(1-ethoxyethylpyrazolylethynyl)-2,3-difluorobenzene

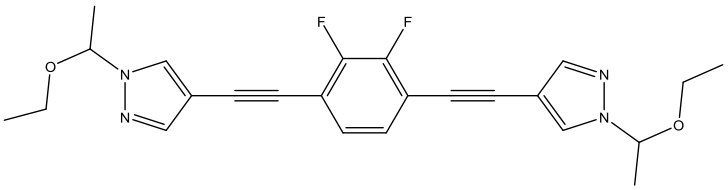

In a Schlenk flask, TEA (30 mL) was degassed with Ar for 20 min. Under vigorous stirring, 1,4-bis(ethynyl)-2,3-difluorobenzene (0.250 g, 1.54 mmol), $PdCl_2(PPh_3)_2$ (0.215 g, 3.39 mmol), 4-iodo-(1-ethoxyethyl)pyrazole (1.660 g, 6.24 mmol) and CuI (0.062 g, 0.33 mmol) were added. The flask was heated up to 70 °C for 4 h; then 1,4-bis(ethynyl)-2,3-difluorobenzene (0.250 g, 1.54 mmol) was added and the mixture was let react for further 4 h. The reaction progress was monitored with TLC

(hexanes:AcOEt = 4:1). Once the reaction was completed, usually after 16 h, the mixture was filtered over a Celite plug. The Celite plug was washed with AcOEt (40 mL) and then evaporated under reduced pressure affording a dark brown solid. The latter was solubilised in AcOEt (30 mL) and washed with 30 % aq NH_4OH (2×50 mL) and water (50 mL). The organic layer was dried over Na_2SO_4 and evaporated under reduced pressure affording a dark brown solid. The latter was purified by column chromatography (hexanes:AcOEt = 4:1) to afford the title compound as a yellow solid. (0.554 g, 41 %). IR (ATR, cm^{-1}): 3118 (w), 3103 (m), 2970 (m), 2916 (w) 2226 (s), 1610 (m), 1569 (w), 1531 (m), 1484 (s), 1429 (w), 1410 (w), 1360 (m), 1233 (m), 1110 (vs), 1060 (vs), 1000 (s), 986 (m), 940 (m), 870 (vs), 820 (vs), 784 (w), 750 (s), 710 (s), 660 (w), 649 (vs). ^{1}H-NMR (DMSO-*d6*): δ (ppm) 8.10 (1H, s), 7.98 (1H, s), 7.81 (1H, s), 7.79 (1H, s), 7.23 (2H, m), 5.60 (1H, m), 3.88, 1.51 (3H, m), 1.18 (3H, m). ^{13}C-NMR (DMSO-*d6*): δ (ppm) 151.3, 149.2, 136.5, 129.2, 110.9, 107.3, 96.2, 91.7, 86.7, 64.5, 18.4, 15.3. ^{19}F NMR ($CDCl_3$) δ −111.01 (2F). Elem. Anal. Calcd. for $C_{24}H_{24}F_2N_4O_2$ (FW = 438.48 g/mol): C, 65,74%, H, 5.52%, N, 12.78; found C, 65.32%, H, 5.27%, N, 12.31.

3.3.8 Synthesis of 1,4-bis(1*H*-pyrazolylethynyl)-2,3-difluorobenzene (H_2BPEBF_2)

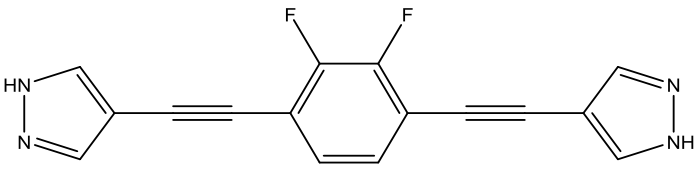

1,4-bis(1-ethoxyethylpyrazolylethynyl)-2,3-difluorobenzene (0.600 g, 1.82 mmol) was solubilised in a round bottomed flask charged with 1,4-dioxane (10 mL). Under vigorous stirring, 6 M HCl (1.5 mL) was added and the reaction mixture was stirred for 3 h. Immediately after the addition of HCl, a yellow solid started to precipitate. The reaction progress was monitored by TLC (hexanes:AcOEt = 4:1). Once the reaction was complete, usually after 4 hours, the yellow solid was filtered, washed with MeOH (10 mL) and dried *in vacuo* at RT overnight affording the title compound as a yellow solid. (0.428 g, 80 %). IR (ATR, cm^{-1}): 3100 (w), 2924 (m), 2426 (w), 2220 (m), 1610 (m), 1534 (w), 1492 (m), 1475 (w), 1378 (m), 1278 (m), 1185 (m), 1121 (m), 1075 (w), 990 (s), 948 (s), 815 (vs), 748 (w). ^{1}H-NMR (DMSO-*d6*): δ (ppm) 13.78 (1H, s), 8.03 (4H, s), 7.37 (2H, m).

^{13}C-NMR (DMSO-*d6*): δ (ppm) 149.3, 138.4, 129.2, 110.8, 101.3, 91.6, 86.7. ^{19}F NMR ($CDCl_3$) δ (ppm) −111.41. Elem. Anal. Calcd. for $C_{16}H_8F_2N_4$ (FW = 294.26 g/mol): C, 65.31%, H, 2.74%, N, 19.04; found C, 65.07%, H, 2.97%, N, 18.89.

3.3.9 Synthesis of 1,4-diiodo-tetrafluorobenzene

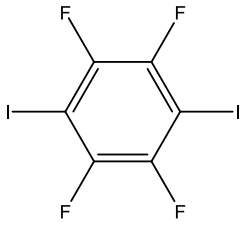

In a round bottomed flask, H_2SO_4 conc. (5 mL) was cooled down in an ice bath. Then HIO_3 (0.246 g, 1.40 mmol) was added. The mixture was stirred for 10 min, then I_2 (0.200 g, 0.79 mmol) and 1,2,4,5-tetrafluorobenzene (0.335 mL, 3.00 mmol) were added. The mixture was allowed to warm up to RT without heating under vigorous stirring, then KI (0.500 g, 3.01 mmol) was added. The temperature was raised up to 70 °C. The reaction mixture started to change colour from dark violet to orange. KI (0.250 g, 1.51 mmol) was added every time the reaction mixture turned from dark violet to orange. Further HIO_3 (0.246 g, 1.40 mmol) was added. When the reaction mixture maintained its violet colour for 2 h, no more KI was needed and the reaction mixture was kept at 70 °C for one additional h. The reaction mixture was cooled down to RT and then further cooled in an ice bath. Ice was added to the reaction mixture under vigorous stirring; then $NaHSO_3$ was added to eliminate the excess of I_2. The mixture was extracted with Et_2O (20 mL). The organic layer was washed with a saturated solution of $NaHSO_3$ (2×20 mL) and water (20 mL), dried over Na_2SO_4 and evaporated under reduced pressure to afford the title compound as a white solid. (0.759 g, 63 %) IR (ATR, cm^{-1}): 1470 (s), 940 (m), 758 (m). ^{13}C-NMR (DMSO-*d6*): δ (ppm)146.5 (dm, ^{1}J = 220 Hz), 72.9.

^{19}F NMR ($CDCl_3$) δ (ppm) −116.31. Elem. Anal. Calcd. for $C_{16}H_9FN_4$ (FW = 276.27 g/mol): C, 69.56%, H, 3.28%, N, 20.28; found C, 69.02%, H, 3.89%, N, 20.01.

3.3.10 Synthesis of 1,4-bis(trimethylsilylethynyl)-tetrafluorobenzene

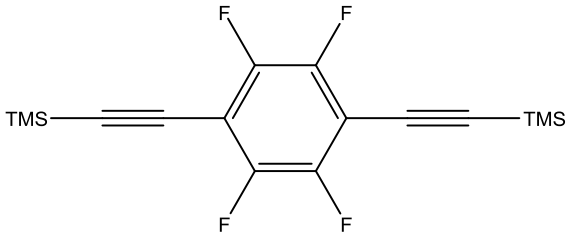

In a Schlenk flask, TEA (30 mL) was degassed with Ar for 20 minutes. Under vigorous stirring 1,4-diiodo-tetrafluorobenzene (2.000 g, 4.98 mmol), $PdCl_2(PPh_3)_2$ (0.380 g, 0.54 mmol), and CuI (0.140 g, 0.73 mmol) were added. Then TMSA (0.500 mL, 3.54 mmol) was added and the mixture was let to react for 4 h. The reaction progress was followed by TLC (hexanes). Further TMSA (0.200 mL, 1.42 mmol) was added until TLC showed the complete conversion of the starting material. Once the reaction was complete, the mixture was filtered through a Celite plug to eliminate the metal salts. This was washed with hexanes (50 mL). Then, the solvent was evaporated under reduced pressure affording a dark brown solid. The solid was solubilised in AcOEt (30 mL) and washed with 30 % aq. NH_4OH (2×50 mL) and water (50 mL). The organic layer was dried over Na_2SO_4 and evaporated under reduced pressure affording a dark brown solid. The latter was purified by column chromatography (hexanes) affording the title compound as a white solid. (1.290 g, 76 %).IR (ATR, cm^{-1}): 2985 (m),2920 (w), 2085 (s),1500 (s), 1250 (m), 990 (m); ^{1}H NMR ($CDCl_3$) δ (ppm) 1.51 (18H, s). ^{13}C-NMR ($CDCl_3$): δ (ppm) 147.6 (dm, ^1J = 225 Hz), 110.5, 107.2, 72.9, 3.8. ^{19}F NMR ($CDCl_3$) δ (ppm) −116.26. Elem. Anal. Calcd for $C_{16}H_{18}F_4Si_2$: C, 56.11; H, 5.30. Found: C, 56.32; H, 5.36.

3.3.11 Synthesis of 1,4-bis(ethynyl)-tetrafluorobenzene

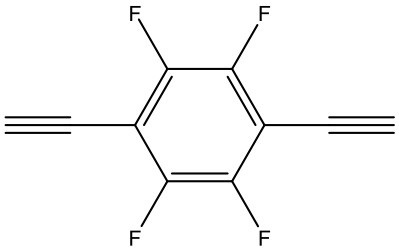

1,4-bis(trimethylsilylethynyl)-tetrafluorobenzene (0.700 g, 2.05 mmol) was solubilised at RT in a round bottomed flask charged with MeOH (10 mL) and CH_2Cl_2 (10 mL). Then the solution was heated up to 40 °C and K_2CO_3 (5.000 g, 36.18 mmol) was added. A white mixture was formed. The reaction progress was monitored by TLC (9:1 = hexanes:AcOEt). Once the reaction was completed, the mixture was filtered and the excess of K_2CO_3 was washed with Et_2O (30 mL). Et_2O was evaporated under reduced pressure and the solid was solubilised again in

Et_2O (20 mL) and washed with brine (2×20 mL). The organic layer was dried over Na_2SO_4 and evaporated under reduced pressure affording the title compound as a brown solid. (0.280 g, 69 %).

IR (ATR, cm^{-1}): 3296 (m), 2127 (s), 1485 (s) cm^{-1}. ^1H NMR ($CDCl_3$,) 1.51 (2H, s)**.** ^{13}C-NMR ($CDCl_3$): δ (ppm) 146.4 (dm, ^1J = 220 Hz) 107.7, 74.2, 73.1. ^{19}F NMR ($CDCl_3$) δ (ppm) −116.30. Elem. Anal. Calcd for $C_{10}H_2F_4$: C, 60.62; H, 1.02. Found: C, 60.31; H, 1.31

3.3.12 Synthesis of 1,4-bis(1-ethoxyethylpyrazolylethynyl)-tetrafluorobenzene

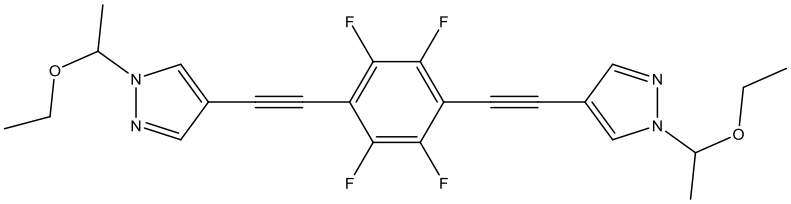

In a Schlenk flask, TEA (30 ml) was degassed with Ar for 20 min. Under vigorous stirring, 1,4-bis(ethynyl)-tetrafluorobenzene (0.250 g, 1.26 mmol), $PdCl_2(PPh_3)_2$ (0.215 g, 3.39 mmol), 4-iodo-(1-ethoxyethyl)pyrazole (1.660 g, 6.24 mmol) and CuI (0.062 g, 0.33 mmol) were added. The reaction mixture was heated at 70 °C for 4 h; 1,4-bis(ethynyl)-tetrafluorobenzene (0.250 g, 1.54 mmol) was added and the reaction mixture was let at 70 °C for 4 h. The reaction progress was monitored with TLC (hexanes:AcOEt = 4:1). Once the reaction was complete, the reaction mixture was filtered over a Celite plug. This was washed with AcOEt (50 mL) and then the solvent was evaporated under reduced pressure. The solid obtained was solubilised in AcOEt (30 mL) and washed with 30 % aq. NH_4OH (2×50 mL) and water (50 mL). The organic layer was dried over Na_2SO_4 and evaporated under reduced pressure affording a dark brown solid. The latter was purified by column chromatography (hexanes: AcOEt = 4:1) to afford the title compound as a yellow solid. (0.490 g, 41 %).

IR (ATR, cm^{-1}): 3112 (w), 3089 (w), 2967 (w), 2897 (w) 2212 (s), 1603 (w), 1543 (w), 1518 (w), 1458 (s), 1431 (m), 1410 (m), 1331 (m), 1231 (w), 1123 (vs), 1074 (vs), 1001 (s), 986 (s), 941 (s), 869 (vs), 827 (vs), 787 (m), 750 (s), 710 (s), 661 (m), 647 (vs). ^1H NMR ($CDCl_3$): δ 7.81 (1H, s), 7.76 (1H, s), 5.45 (1H, q, J = 6), 3.40 (1H, m), 3.27 (1H, m), 1.58 (3H, d, J = 6), 1,30 (3H, t, J = 7). ^{13}C-NMR ($CDCl_3$): δ (ppm) 133.2 (dm, ^1J = 220 Hz), 131.6, 123.0, 106.4, 101.3, 89.7, 84.5, 65.7, 12.6, 11.3. ^{19}F

NMR ($CDCl_3$) δ −138.1. Elem. Anal. Calcd. for $C_{24}H_{22}F_4N_4O_2$ (FW = 474.46 g/mol): C, 60.76%, H, 4.67%, N, 11.81; found C, 61.02%, H, 5.07%, N, 11.21.

3.3.13 Synthesis of 1,4-bis(1*H*-pyrazolylethynyl)-tetrafluorobenzene (H_2BPEBF_4)

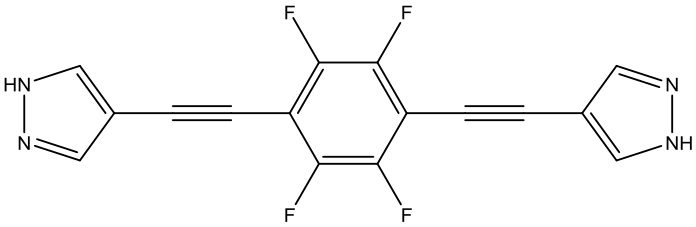

1,4-bis(1-ethoxyethylpyrazolylethynyl)-tetrafluorobenzene (0.600 mg, 1.27 mmol) was dissolved at RT in 1,4-dioxane (10 mL). Under vigorous stirring, 6 M HCl (1.5 mL) was added. Precipitation of a yellow solid occurred very quickly. The reaction mixture was stirred for 3 h at RT. The reaction progress was monitored by TLC (hexanes:AcOEt = 4:1). Once the reaction was completed, the yellow solid was filtered, washed with MeOH (10 mL) and dried *in vacuo* at RT overnight to afford the title compound as a yellow solid. (0.377 g, 90%). IR (ATR, cm^{-1}): 2235 (m); 1475 (s); 1379 (m); 1318 (m); 1136 (w); 1012 (m); 976 (s); 939 (m). ^1H NMR (DMSO-*d6*, ppm): δ 7.88 (1H, s), 7.86 (1H, s). ^{13}C NMR (DMSO-*d6*): δ 133.2 (dm, ^1J = 225 Hz), 131.6, 123.0, 101.3, 89.7, 84.5. ^{19}F NMR (DMSO-*d6*) δ (ppm): -138.70 (s). Elem. Anal. Calcd. for $C_{16}H_6F_4N_4$ (FW = 330.25 g/mol): C, 58.19%, H, 1.83%, N, 16.97; found C, 57.79%, H, 1.56%, N, 16.45.

3.3.14 Synthesis of [$^2H_4$]-1,4-bis(trimethylsilylethynyl)-benzene

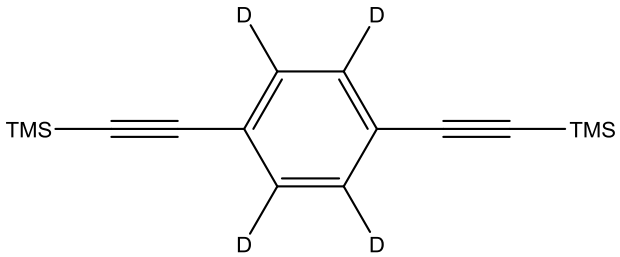

An oven-dried Schlenk flask was purged with Ar and charged with [$^2H_4$]-1,4-dibromobenzene (0.400 g, 1.67 mmol), $PdCl_2(PPh_3)_2$ (0.075 g, 0.11 mmol) and CuI (0.030 mg, 0.16 mmol). The flask was cooled with an acetone/dry ice bath and sealed with a rubber septum. Ar-purged TEA (5 mL) and THF (5 mL), filtered over Al_2O_3, were added by means of a syringe. The obtained mixture, purged by bubbling Ar at RT, was stirred for 20 min. Afterwards, TMSA (0.950

mL, 6.68 mmol) was added. The resulting yellow mixture was sealed under Ar atmosphere, heated up to 45 °C and kept at this temperature under stirring for 4 h. The colour of the mixture changed from yellow to black as the temperature was raised. The extent of the reaction was controlled by GC-MS. Additional portions of TMSA (0.100 mL, 0.71 mol) were periodically added. After 16 h, GC-MS analysis showed complete consumption of [$^2H_4$]-1,4-dibromobenzene and a 4:1 mixture of the title compound and its monosubstituted intermediate. The reaction was cooled down to RT and filtered. The gray residue was washed with AcOEt (30 mL) and the organic layer was evaporated under reduced pressure to obtain a black solid. This was dissolved in AcOEt (100 mL) and washed with 30 % aq NH_4OH (2×50 mL) and water (50 mL). The organic layer was dried over Na_2SO_4 and the solvent was removed under reduced pressure. The black residue was purified by silica-gel column chromatography (*n*-hexane) to afford [$^2H_4$]-1,4-bis(trimethylsilylethynyl)-benzene as a white solid (0.300 g, 65%). IR (ATR, cm^{-1}): 2956 (m), 2899 (w), 2153 (s), 1407 (s), 1322 (w), 1243 (s), 1129 (s), 1108 (w), 875 (s), 831 (vs), 754 (s), 744 (s), 726 (s), 697 (m), 626 (m); ^{1}H-NMR ($CDCl_3$): δ (ppm) 0.25 (18H, s); ^{13}C NMR δ(ppm) ($CDCl_3$) 131.6, 123.1, 104.7, 96.8, 0.12. Elem. Anal. Calc. for $C_{16}H_{18}D_4Si_2$ (FW = 274.55 g/mol): C, 70.00%, H, 9.54%; found C, 70.65%, H, 8.97%.

3.3.15 Synthesis of [$^2H_4$]-1,4-bis(ethynyl)-benzene

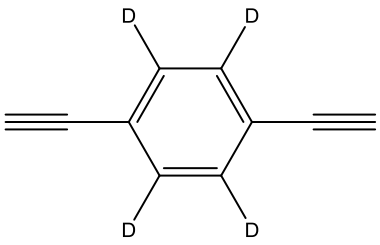

[$^2H_4$]-1,4-bis(trimethylsilylethynyl)-benzene (0.165 g, 0.61 mmol) was dissolved in a 1:1 mixture of THF and MeOH (12 mL) and heated up to 50 °C under stirring. KF (0.086 g, 1.48 mmol) was added to the solution. After 4 h, a GC-MS analysis showed the complete consumption of the starting material. The mixture was then cooled down to RT and concentrated under reduced pressure without drying completely. The residual solvent was diluted with CH_2Cl_2 (10 mL) and washed with water (10 mL). The organic layer was dried over Na_2SO_4 and evaporated under reduced pressure affording [$^2H_4$]-1,4-bis(ethynyl)-benzene as a white solid. (0.075 g, 94%). IR (ATR, cm^{-1}): 2969 (m), 2856 (w), 2189 (s), 1399 (s), 1267 (s), 1178 (s), 886 (s), 836 (vs), 775

(s), 739 (s), 720 (s), 631 (m). ^{1}H-NMR ($CDCl_3$): δ (ppm) 3.18 (2H, s); ^{13}C-NMR ($CDCl_3$) δ (ppm) 132.2, 123.5, 82.7, 80.5. Elem. Anal. Calc. for $C_{10}H_2D_4$ (FW = 130.18 g/mol): C, 92.26%, H, 7.74%; found C, 91.93%, H, 7.32%.

3.3.16 Synthesis of [$^{2}H_4$]-1,4-bis(1-ethoxyethylpyrazolyl)ethynyl)-benzene

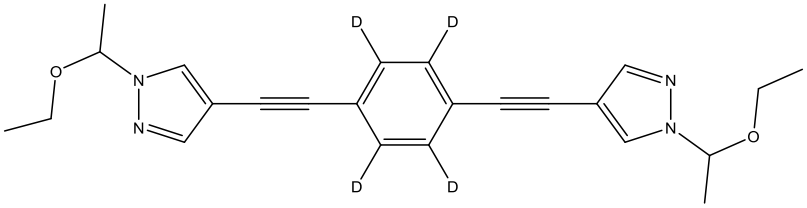

An oven-dried Schlenk flask was purged with Ar and charged with 4-iodo-(1-ethoxyethyl)-pyrazole (0.850 g, 1.39 mmol), $Pd(PPh_3)_2Cl_2$ (0.060 g, 0.084 mmol) and CuI (0.020 g, 0.11 mmol). The flask was sealed with a rubber septum and Ar-purged TEA (25 mL) and THF (25 mL), filtered over Al_2O_3, were added by means of a syringe. The obtained yellowish solution was cooled down with an acetone/dry ice bath, purged by bubbling Ar and then stirred for 20 min; afterwards, [$^{2}H_4$]-1,4-bis(ethynyl)-benzene (0.180 g, 1.39 mmol) was added and the resulting mixture was heated up to 60 °C and kept at this temperature under stirring. The colour of the mixture changed from pale yellow to dark brown as the temperature was raised. After 4 h TLC analysis (hexane:AcOEt = 4:1) showed complete consumption of [$^{2}H_4$]-1,4-bis(ethynyl)-benzene and the presence of two new compounds. Further 4-iodo-(1-ethoxyethyl)-pyrazole (0.300 g, 0.49 mmol) was added to the reaction mixture. After 2 h at 60 °C the mixture was cooled down to RT and the solid was filtered; the solution was evaporated under reduced pressure affording an brown/orange paste. This solid was dissolved in AcOEt (40 mL) and washed with 30% aq NH_4OH (2×50 mL) and water (50 mL). The organic layer was dried over Na_2SO_4 and evaporated under reduced pressure to afford an orange paste. This solid was washed with pentane (5 mL) to remove the excess of 4-iodo-(1-ethoxyethyl)-pyrazole and filtered. The obtained yellow-orange powder was transferred to a Soxhlet and washed with refluxing pentane (100 mL) for 25 min. The solvent was removed under reduced pressure affording the title compound as a bright yellow powder (0.300 g, 53%). IR (ATR, cm^{-1}): 3106 (w), 3076 (w), 2978 (w), 2907 (w), 2212 (m), 1669 (w), 1553 (w), 1438 (s), 1388 (s), 1344 (m), 1328 (s), 1295 (w), 1252 (m),

1174 (m), 1120 (vs), 1101 (vs), 1064 (s), 1002 (m), 980 (s), 943 (m), 927 (w), 865 (vs), 745 (s), 725 (vs), 663 (vs). ^{1}H-NMR ($CDCl_3$): δ (ppm) 7.80 (1H, s), 7.67 (1H, s), 5.52 (1H, q, J = 6), 3.48 (1H, m), 3.37(1H, m), 1.68 (3H, d, J = 6), 1.17 (3H, t, J = 8,2). ^{13}C-NMR ($CDCl_3$): δ (ppm) 141.5, 130.8, 128.1, 122.3, 103.9, 89.3, 87.6, 82.2, 64.1, 22.0, 14.5. Elem. Anal. Calcd. for $C_{24}H_{22}D_4N_4O_2$ (FW = 406.22 g/mol): C, 70.09%, H, 5.42%, N, 13.79 %; found C, 70.05%, H, 6.25%, N, 13.29%.

3.3.17 Synthesis of [$^{2}H_4$]-1,4-bis(1*H*-pyrazolylethynyl)-benzene (H_2BPEB-*d4*)

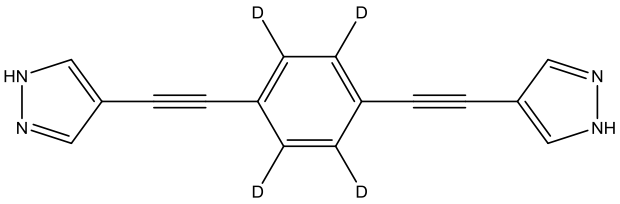

[$^{2}H_4$]-1,4-bis(1-ethoxyethylpyrazolyl)ethynyl)-benzene (0.170 g, 0.42 mmol) was dissolved in 1,4-dioxane (3 mL). 6 N HCl (2 mL) was added. Precipitation of a yellow solid occurred very quickly. The reaction mixture was heated up to 40 °C and kept at this temperature under stirring for 1 h. Then, the pale yellow precipitate was filtered, washed with 1,4-dioxane (5 mL) and MeOH (15 mL) and dried *in vacuo* overnight at RT affording the title compound as a pale yellow solid (0.070 g, 72%). IR (ATR, cm^{-1}): 3119 (s, br), 3048 (w), 2960 (s, br), 2213 (m), 1659 (w, br), 1557 (w), 1506 (w), 1425 (s), 1369 (s), 1335 (m), 1142 (m), 1034 (m), 993 (s), 949 (s), 860 (vs), 788 (s, br), 722 (vs), 660 (vs), 617 (vs). ^{1}H-NMR (DMSO-*d6*): δ (ppm) 7.49 (2H, s); ^{13}C-NMR (DMSO-*d6*): δ (ppm) 141.3, 132.8, 131.7, 122.5, 101.1, 89.0, 84.4. Elem. Anal. Calcd. for $C_{16}H_6D_4N_4$ (FW = 262.31 g/mol): C, 73.26%, H, 5.38%, N, 21.36 %; found C, 73.69%, H, 5.90%, N, 20.98%.

3.3.18 Synthesis of 1,4-bis(1*H*-tetrazol-5-yl)-tetrafluorobenzene (H_2FBTB)

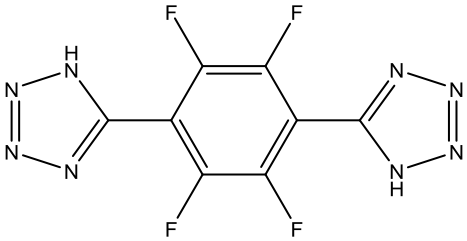

In a round bottomed flask, $ZnBr_2$ (2.250 g, 9.99 mmol) and NaN_3 (0.715 g, 11.00 mmol) were solubilised in distilled water (10 mL). Under vigorous stirring, tetrafluoroterephthalonitrile (1.000 g, 4.99 mmol) was added and the white suspension was heated at 120 °C for 30 h. The reaction mixture was cooled

down to RT. Then, 1 M NaOH was added to the mixture until the white solid was completely solubilised. The resulting solution was stirred for 30 min; then, it was acidified with 1 M HCl until pH 1 and stirred for further 30 min. A white solid started to precipitate. The mixture was filtered, the solid was washed with water (30 mL) and dried *in vacuo* at 130 °C for 4 h affording the title compound as a brownish solid. (0.985 g, 69 %). IR (ATR, cm^{-1}): 3059 (w, br), 2977 (w, br), 2866 (w, br), 2781 (w, br), 1679 (vw), 1596 (m), 1503 (s), 1478 (s), 1377 (s), 1272 (w), 1249 (m), 1235 (m), 1101 (m), 1085 (w), 1055 (s), 1001 (s), 981 (vs), 861 (m, br), 792 (vs), 749 (s), 712 (m). ^{1}H-NMR (DMSO-*d6*): δ (ppm) 4.81 (s, broad, NH). ^{13}C-NMR (DMSO-*d6*): δ (ppm) 148.2 (s), 144.6 (dm), 109.0 (m). ^{19}F-NMR (DMSO-*d6*): δ (ppm) -137.9. Elem. Anal. Calcd. for $C_8H_2F_4N_8$ (FW: 286.14 g/mol): C, 33.58; H, 0.70; N, 39.16 %; found: C, 33.70; H, 0.71; N, 38.56 %.

3.3.19 Synthesis of 1-(1*H*-tetrazol-5-yl)-pentafluorobenzene (HFMTB)

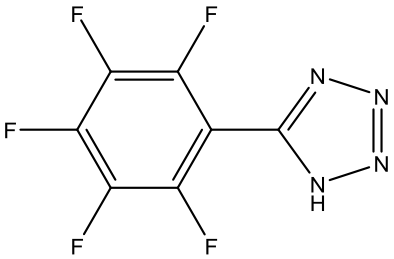

In a round bottomed flask, NaN_3 (1.000 g, 15.38 mmol) was solubilised with distilled water (30 mL). Then, under stirring, $ZnBr_2$ (3.440 g, 15.27 mmol) and AcOH (8 mL) were added. The solution was stirred at RT for 10 min and then pentafluorocyanobenzene (3.000 g, 15.54 mmol) was added. The reaction mixture was heated up to 110 °C for 6 h and then cooled down to RT, treated with 1 M HCl to adjust the pH to 1 and stirred for 30 min. The mixture was then filtered and washed with water (30 mL). The obtained orange solid was stirred in CH_2Cl_2 (30 mL) at RT for 30 min and then filtered and dried *in vacuo* affording the title compound as a white powder. (2.100 g, 58 %). IR (ATR, cm^{-1}): 3259 (m, br), 1665 (w), 1541 (m), 1495 (s), 1386 (m), 1222 (w), 1108 (w), 1062 (w), 989 (vs), 843 (s), 837 (s). NMR: ^{1}H-NMR (DMSO-*d6*): δ (ppm) 9.75. ^{13}C-NMR (DMSO-*d6*): δ (ppm) 162.9, 143.5, 137.9, 137.1, 110.1. ^{19}F-NMR (DMSO-*d6*): δ (ppm) = -139.62 (m, 2F); -154.54 (m, 1F); -162.88 (m, 2F). Elem. Anal. Calcd. for $C_7HF_5N_4$ (FW: 236.11 g/mol): C, 35.61; H, 0.43; N, 23.73 %; found: C, 35.70; H, 0.71; N, 24.29 %.

3.4 Results and Discussions

3.4.1 Pyrazole-based ligands

When the main skeleton of the ligand remains the same and only the functionalization of the inner aromatic core changes, a common synthetic procedure can be envisaged. Indeed, the synthesis of this first class of ligands exploits the Sonogashira protocol that easily allows to couple aryl-halides with terminal alkynes. In this Thesis, aryl-iodides have been successfully utilised as the preferred substrate for the coupling reactions; all of the aryl-iodides were synthesized following standard procedures (see **Material and Methods** and **Section 3.3**). When the aryl-iodide was arduous to prepare or not commercially available, aryl-bromides were purchased and used.

This family of ligands was devised starting from 1,4-bis(1*H*-pyrazol-4-ylethynyl)benzene (**H_2BPEB**)[33] by the modification of the inner aromatic core. This modification consists of the substitution of the hydrogen atoms of the benzene ring with: i) one fluorine atom (**H_2BPEBF**); ii) two fluorine atoms (**H_2BPEBF_2**); iii) four fluorine atoms (**H_2BPEBF_4**) and iv) four deuterium atoms (**H_2BPEB-*d4***).

Before its use in the catalytic reaction, pyrazole must undergo a small modification in order to be activated for the coupling and to protect the catalytic system from its free NH group. Ethyl vinyl ether was used as protecting group for the NH functionality and the C4 position was activated by classic iodination, performed as a classical electrophilic substitution[34].

The synthetic pathway to obtain the four derivatives is the same, as highlighted in **Scheme 3.1**, with some modifications due to the different reactivity connected to the substituent(s) on the aromatic core.

Curiously, only the synthesis of **H_2BPEBF** presented some issues, mainly during the last Sonogashira coupling. Essentially, the first coupling between 1,4-bis(ethynyl)-fluorobenzene and 4-iodo-(1-ethoxyethyl)-pyrazole proceeded without problems but, at this point, the homo-coupling started to be competitive with the second insertion of 4-iodo-(1-ethoxyethyl)-pyrazole, leading to very low yields of the final product. As already underlined, the homo-coupling between two terminal alkynes is promoted by a Cu(II) salt in air or in the presence of oxidizing agents[18]: copper-free Sonogashira

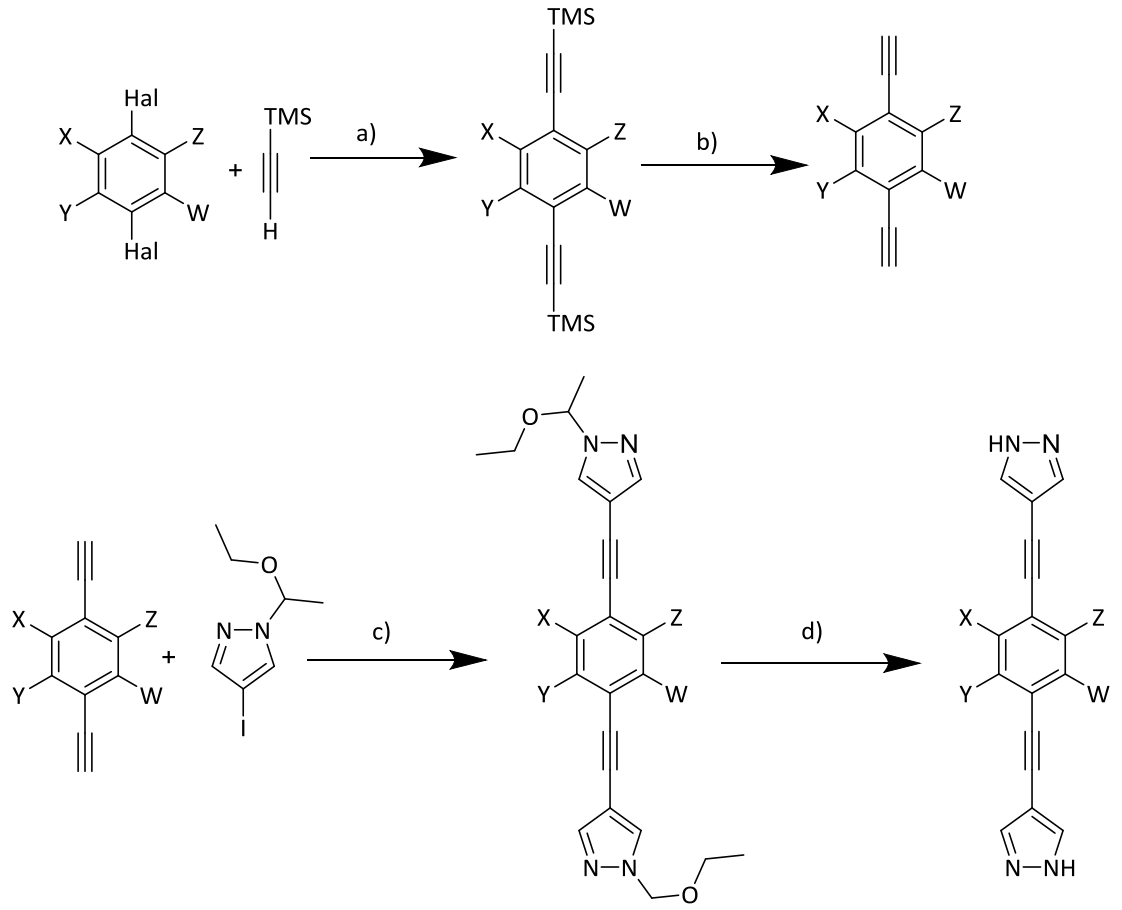

Scheme 3.1: Synthesis of 1,4-bis(1*H*-pyrazolylethynyl)-benzene derivatives. **H_2BPEBF**: Hal = Br; X = F;Y,Z,W = H; **H_2BPEBF_2**: Hal = Br; X,Y = F; Z,W = H; **H_2BPEBF_4**: Hal = I; X,Y,Z,W = F; **H_2BPEB-*d4***: Hal = Br; X,Y,Z,W = ^{2}H. Reaction conditions a), b), c) and d) depend upon the ligand (see Section 3.3).

protocols[20] were tested in order to avoid the problem. In this case, the absence of the co-catalyst inhibited the catalytic reaction: actually, no conversion was observed. This fact demonstrates that our system needs a Cu(I) salt to run. Modification/change of the solvent is another possibility to achieve better results; beyond TEA and piperidine, THF, DMF, DME, Et_2O, MeOH etc. can be used as solvent for the Sonogashira coupling[20]. After some attempts, the best combination of solvents resulted to be TEA/THF = 1:1 (v/v). Unfortunately, despite these adjustments, the yields remained poor even if the homo-coupling side reaction was reduced. The purification method was also changed, passing from classic flash chromatography to Soxhlet extraction, because it is less "aggressive" towards the substrate and it was difficult to find an efficient eluent for the flash column chromatography.

As described in the **Section 3.3**, the final molecules were fully characterized with different techniques including elemental analysis, IR and NMR. Worthy of note, in the IR spectra, the C≡C stretching band, usually poorly visible due to its lack of polarity, is present as a strong band at ~2200 cm^{-1} because of the polarization generated by the different substituents bore, namely pyrazole and the fluorinated/deuterated aromatic core, by the alkynes. Clearly, the intensity of this IR band changes depending upon the number of fluorine atoms on the benzene ring: the higher the number of fluorine atoms present on the aromatic core, the more intense are the resulting IR bands. To better understand which kind of side-product was obtained after the already mentioned competitive homo-coupling along the **H_2BPEBF** synthesis, HPLC-(ESI+)MS analyses were performed: according to already published data[35], the quasi-molecular peak $[M+H]^+$ can be ascribed to two possible isomers (**Scheme 3.2**). Confirmation of the presence of isomer **a** was obtained by ^{1}H-NMR analysis: the absence of the alkenyl CH_2 peaks expected at 5.60 ppm and 5.80 ppm[35] excludes the formation of isomer **b**.

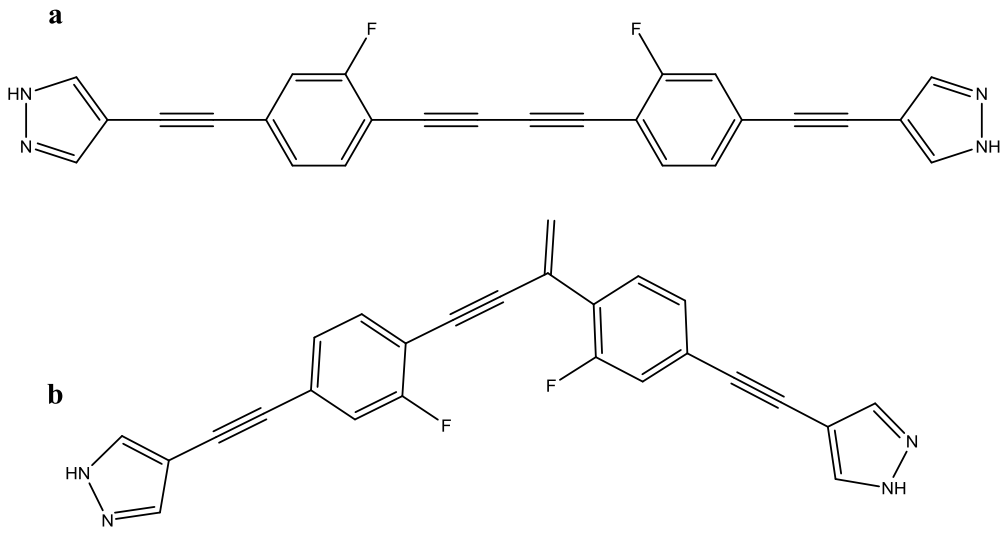

Scheme 3.2: Two of the possible isomers of the homo-coupling for the synthesis of **H_2BPEBF**. The absence of the alkenyl CH_2 peaks confirm the formation of compound **a** instead of compound **b**.

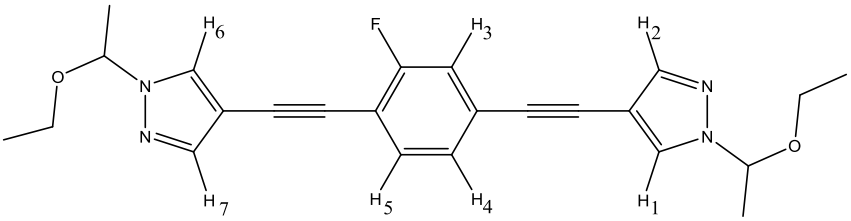

	ppm
H1	7.78
H2	7.80
H3	7.44
H4	7.33
H5	7.56
H6	8.34
H7	8.37

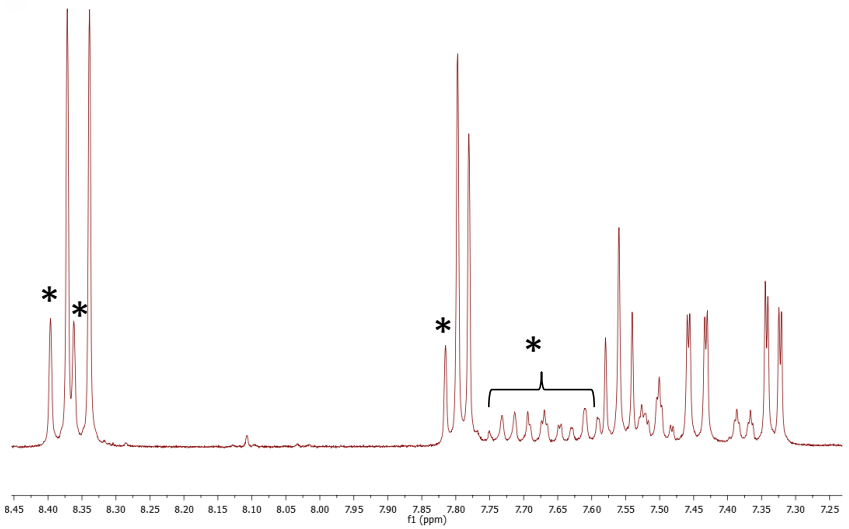

Figure 3.2a: ^{1}H-NMR spectrum of 1,4-bis(1-ethoxyethylpyrazolyl)ethynyl)-fluorobenzene after column chromatography. The peaks that can be ascribed to the impurities mentioned in the text and are easily noticeable (marked with *). Moreover, there are a lot of small peaks in the region 7.75-7.55 ppm, also ascribable to the side-product.

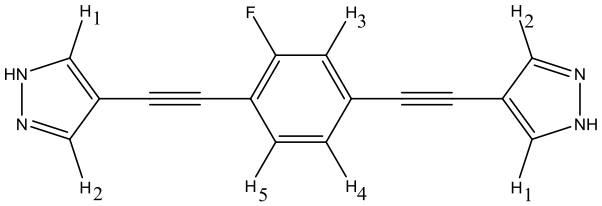

	ppm
H1	7.96
H2	7.94
H3	7.43
H4	7.31
H5	7.56

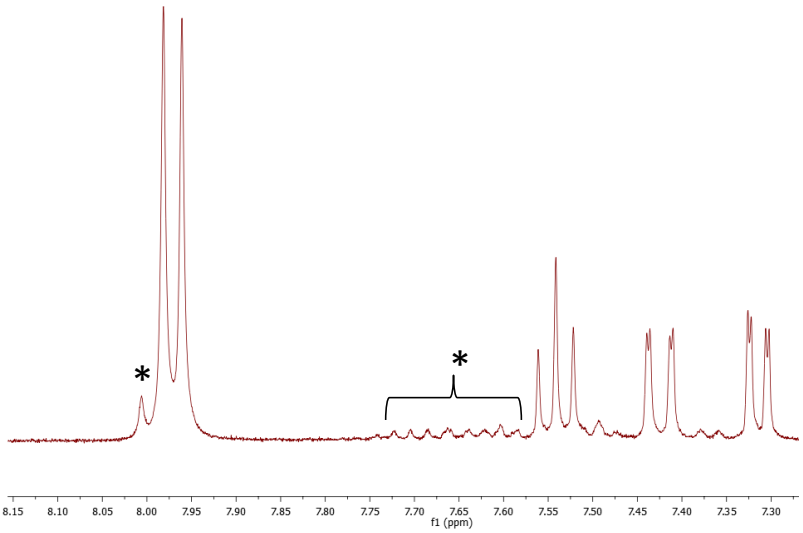

Figure 3.2b: ^{1}H-NMR spectrum after deprotection of the compound shown in **Figure 3.2a**. We expected that the free ligand would precipitate pure but, as easily noticeable, the impurities (marked with *) were not eliminated.

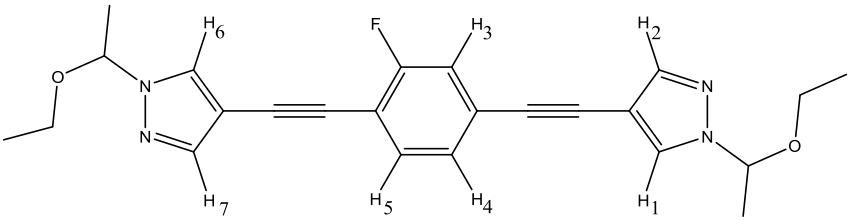

	ppm
H1	7.78
H2	7.80
H3	7.44
H4	7.33
H5	7.56
H6	8.34
H7	8.37

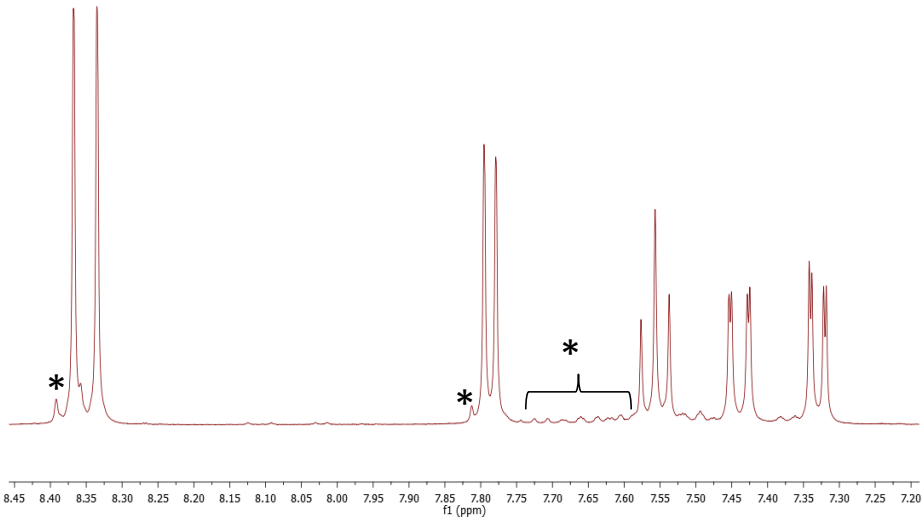

Figure 3.2c: ^{1}H-NMR spectrum after purification with a soxhlet extractor of the compound shown in **Figure 3.2a**. As easily noticeable, almost all the impurities (marked with *) were eliminated. It was impossible to have a completely pure compound because we used the extractor in the opposite way: the solubilised compound was the desired material.

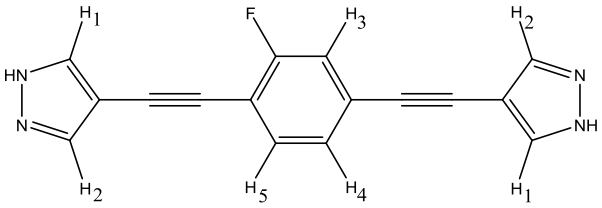

	ppm
H1	7.96
H2	7.94
H3	7.43
H4	7.31
H5	7.56

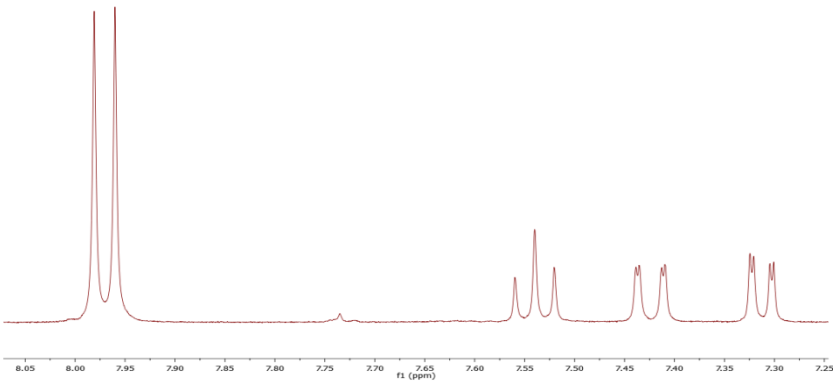

Figure 3.2d: ^{1}H-NMR spectrum after deprotection of the compound shown in **Figure 3.2c**. As expected, the impurities did not survived the deprotection process, affording the pure free ligand.

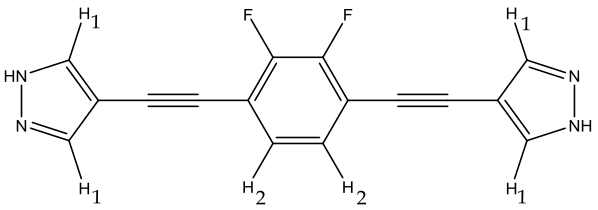

	ppm
H1	8.03
H2	7.37

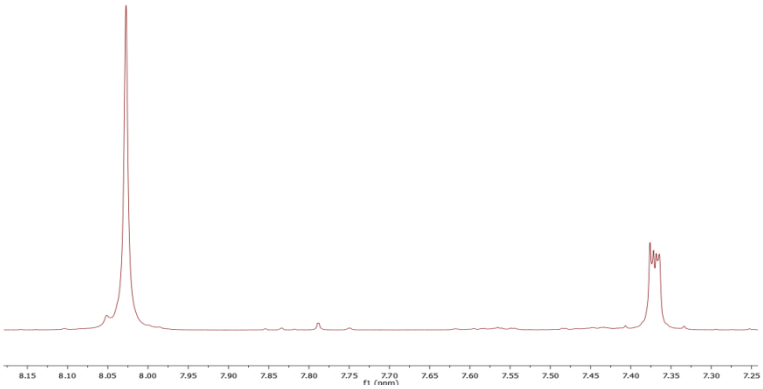

Figure 3.3: ^{1}H-NMR spectrum of **H_2BPEBF$_2$**. As easily noticeable, no impurities were present in the final product.

3.4.2 Tetrazole-based ligands

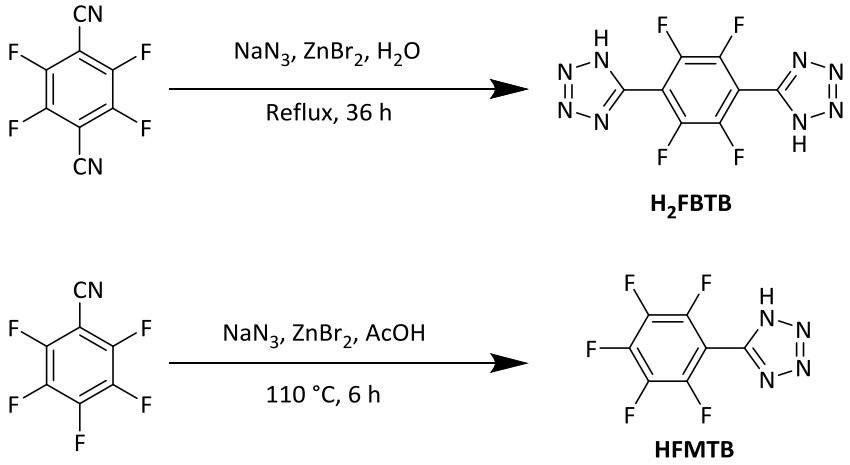

Scheme 3.3: Synthesis of 1,4-bis(1*H*-tetrazol-5-yl)-tetrafluorobenzene (**H_2FBTB**), top, and 1-(1*H*-tetrazol-5-yl)-perfluorobenzene (**HFMTB**), bottom

The chance to built up the tetrazole ring directly on a substrate bearing a CN group using NaN_3 and $ZnBr_2$ in water, the Demko-Sharpless protocol[36], allows the straightforward construction of the ligand, compared to the four-step approach needed for pyrazole derivatives. Starting from the already known tetrazole-based ligand **H_2BTB**[37], we have synthesized the perfluorinated counterpart,

H_2FBTB, following the reaction pathway highlighted in **Scheme 3.3**. An acid treatment of the reaction mixture, to eliminate the excess of Zn, is crucial before the final purification, because Zn can stay coordinated to the bis(tetrazolate). Remarkably, due to the moderate stability of aromatic C-F bonds in perfluorinated systems, the temperature must be strictly controlled in order to avoid the insertion of Zn in the C-F bond[38] and the nucleophilic attack of N_3^- on the C-F[39] bond generating the C-N_3 functionality.

H_2FBTB crystallizes in the monoclinic space group $P2_1/c$, as **H_2BTB**. Nevertheless, the two species are not isomorphous: in **H_2BTB**, the molecules, lying about crystallographic inversion centres, generates 2-D sheets through strong hydrogen bond interactions (N---N 2.77 Å). Also **H_2FBTB** lies on an inversion centre but the molecules are in columns along the crystallographic axis **c**, with a pace of 5.03 Å (the length of the crystallographic axis *c*). Overall, the reciprocal disposition of the columns create a herringbone motif. The formation of a 2-D supramolecular architecture is promoted by the presence of N-H···N hydrogen bonds between the molecules belonging to nearby columns.

HMTB is more sensitive than **H_2FBTB** due to the presence of five fluorine atoms on the same benzene ring. In this case, the fluorine atoms in para- and ortho-positions could undergo nucleophilic attack[39] and insertion (oxidative addition)[38] quite easily. In order to reduce this undesired side reactions, the temperature must be strictly controlled and the presence of a weak acid, namely acetic acid, is required.

3.5 Conclusions

In this **Chapter**, the synthesis of four new pyrazolate- and two new tetrazolate-based organic spacers has been discussed. The Sonogashira coupling, with small modifications, resulted to be the best approach for the insertion of alkyne moieties in the final pyrazolato-based ligand.

Generally, the implementation of a *scale-up* for the synthesis of this family of ligands was a big issue because, as underlined in the previous **Section**, the purification by column chromatography

significantly lowers the yield of the reaction. For this reason, further studies will be performed in order to find other purification methods which do not affect significantly the yield of the reaction.

On the other side, the Demko-Sharpless protocol was successfully used for the direct synthesis of the tetrazole ring on the desired substrate. As foreseen, the presence of fluorine atoms created some issues, which have been successfully solved with slight modifications of the original procedures. In these cases, the *scale-up* of the reaction was easily obtained as the synthetic pathways involve only one step and only quick purifications are needed.

References and Notes

[1] a) Natarajan, S. and Mahata, P. *Curr. Opin. Solid State Mater. Sci.* **2009**, *13*, 46. b) Almeida Paz, F. A.; Klinowski, J.; Vilela, S. M. F.; Tomé , J. P. C.; Cavaleiroc, J. A. S. and Rocha, J. *Chem. Soc. Rev.* **2011**, DOI: 10.1039/c1cs15055c. (c) Zhao, D.; Timmons, D. J.; Yuan, D. and Zhou, H.-C. *Acc. Chem. Res.* **2011**, *44*, 123.

[2] a) Huang, X. C.; Zhang, J. P. and Chen, X. M. *Chin. Sci. Bull*., **2003**, *48*, 1531. (b) Park, K. S.; Ni, Z.; Côté, A. P.; Choi, J. Y.; Huang, R.; Uribe-Romo, F. J.; Chae, H. K.; O'Keeffe, M. and Yaghi, O. M. *Proc. Natl. Acad. Sci. USA* **2006**, *103*, 10186.

[3] a) Dincă, M.; Dailly, A.; Liu, Y.; Brown, C. M.; Neumann, D. A. and Long, J. R. *J. Am. Chem. Soc.* **2006**, *128*, 16876. (b) Dincă, M.; Han, W. S.; Liu, Y.; Dailly, A.; Brown, C. M. and Long,J. R. *Angew. Chem. Int. Ed.* **2007**, *46*, 1419. (c) Dincă, M. and Long, J. R. *J. Am. Chem. Soc.* **2007**, *129*, 11172. (d) Dincă, M.; Dailly, A.; Tsay, C. and Long, J. R. *Inorg. Chem.* **2008**, *47*, 11. (e) Sumida, K.; Horike, S.; Kaye, S. S.; Herm, Z. R.; Queen, W. L.; Brown, C. M.; Grandjean, F.; Long, G. J.; Dailly, A. and Long, J. R. *Chem. Sci.* **2010**, *1*, 184.

[4] a) Bordwell, F. G. *Acc. Chem. Res.* **1988**, *21*, 456; b) Masciocchi, N.; Ardizzoia, G. A.; LaMonica, G.; Maspero, A. and Sironi, A. *Eur. J. Inorg. Chem.* **2000**, 2507; c) Barea, E.; Navarro, J. A. R.; Salas, J. M.; Masciocchi, N.; Galli, S. and Sironi, A. *Inorg. Chem.* **2004**, *43*, 473; d) Dincă, M.; Yu, A. F. and Long, J. R. *J. Am. Chem. Soc.* **2006**, *128*, 8904; e) Dincă, M.; Dailly, A.; Liu, Y.; Brown, C. M.; Neumann, D. A. and Long, J. R. *J. Am. Chem. Soc.* **2006**, *128*, 16876; f) Park, K. S.; Ni, Z.; Côté, A. P.; Choi, J. Y.; Huang, R.; Uribe-Romo, F. J.; Chae, H. K.; O'Keeffe, M. and Yaghi, O. M. *Proc. Natl. Acad. Sci. USA* **2006**, *103*, 10186; g) Dincă, M.; Han, W. S.; Liu, Y.; Dailly, A.; Brown, C. M. and Long, J. R. *Angew. Chem. Int. Ed.* **2007**, *46*, 1419; h) Dincă, M. and Long, J. R. *J. Am. Chem. Soc.* **2007**, *129*, 11172; i) Dincă, M.; Dailly, A.; Tsay, C. and Long, J. R. *Inorg. Chem.* **2008**, *47*, 11; l) Sumida, K.; Horike, S.; Kaye, S. S.; Herm, Z. R.; Queen, W. L.; Brown, C. M.; Grandjean, F.; Long, G. J.; Dailly, A. and Long, J. R. *Chem. Sci.* **2010**, *1*, 184; m) Horike, S.; Dincă, M.; Tamaki, K.and Long, J. R. *J. Am. Chem. Soc.* **2008**, *130*, 5854. n) Demessence, A.; D'Alessandro, D. M.; Foo, M. L. and Long, J. R. *J. Am. Chem. Soc.* **2009**, *131*, 8784.

[5] Clayden, J.; Greeves, N.; Warren, S. and Whoters, P *Organic Chemistry*, Oxford University Press, **2001**.

[6] a) Denmark, S. E. and Beutner, G. L. *Angew. Chem. Int. Ed.*, **2008**, *47*, 1560–1638; b) Melchiorre, P.; Marigo, M.; Carlone, A. and Bartoli, G. *Angew. Chem. Int. Ed.*, **2008**, *47*, 6138–6171; c) Nielsen, M.; Worgull, D.; Zweifel, T.; Gschwend, B.; Bertelsen, S. and Jørgensen, K. A. *Chem. Commun.,* **2011**, *47*, 632–649.

[7] a) Tamao, K.; Sumitani, K. and Kumada, M *J. Am. Chem. Soc.*, **1972**, *94*, 4374–4376; b) Corriu, R. J. P. and Masse, J. P. *J. Chem. Soc., Chem. Commun.*, **1972**, 144a.

[8] a) Heck, R. F. and Nolley, J. P. *J. Org. Chem.*,**1972**, *37* (14), 2320–2322; b) Mizoroky, T.; Mori, K. and Ozaki, A. *BCSJ*, **1971**, *44*, 581.

[9] Sheffy, F. K.; Godschalx, J. P. and Stille, J. K. *J. Am. Chem. Soc.*, **1984**, *106*, 4833-4840.

[10] a) Baba, S and Negishi, E. *J. Am. Chem. Soc.*, **1976**, *98*, 6729–6731; b) King, A. O.; Okukado, N and Negishi, E. *J. Chem. Soc., Chem. Commun.*, **1977**, 683-684.

[11] a) Miyaura, N.; Yamada, K. and Suzuki, A. *Tetrahedron Lett.*, **1979**, *20*, 3437-3440; b) Miyaura, N. and Suzuki, A. *J. Chem. Soc., Chem. Commun.*, **1979**, 866-867; c) Miyaura, N. and Suzuki, A. *Chem. Rev.*, **1995**, *95*, 2457–2483.

[12] Hatanaka, Y.; Hiyama, T *J. Org. Chem.*, **1988**, *53*, 918–920.

[13] Sonogashira, K., Tohda, Y., Hagihara, N., *Tetrahedron Lett.*, **1975**, *6*, 4467.

[14] Cassar, L., *J. Organomet. Chem.*, **1975**, *93*, 253.

[15] Diek, H. A. and Heck, F. R., *J. Organomet. Chem.*, **1975**, *93*, 259.

[16] a) Stephens, R. D. and Castro, C. E., *J. Org. Chem.*, **1963**, *28*, 2163; b) Stephens, R. D. and Castro, C. E., *J. Org. Chem.*, **1963**, *28*, 3313.

[17] a) Eckhardt, M. and Fu, G. C., *J. Am. Chem. Soc.*, **2003**, *125*, 13642; b) Altenhoff, G.; Würtz, S. and Glorius, F., *Tetrahderon Lett.*, **2006**, *47*, 2925; c) Cahiez, G.; Gager, O. and Buendia, J. *Angew. Chem.*, **2010**, *122*, 1300–1303; d) Thaler, T.; Guo, L.-N.; Mayer, P and Knochel, P. *Angew. Chem. Int. Ed.*, **2011**, *50*, 2174–2177; d) Vechorkin, O.; Godinat, A.; Scopelliti, R. and Hu, X. *Angew. Chem.* **2011**, *123*, 11981–11985; e) Yi, J.; Sun, Y.-Y.; Xiao, B. and Liu, L. *Angew. Chem. Int. Ed.*, **2013**, *52*, 12409–12413; f) Tang, S.; Wang, P.; Li, H and Lei, A. *Nat. Comm.*, **2016**, DOI: 10.1038/ncomms11676.

[18] a) Kotora, M. and Takahashi, T. *Handbook of Organopalladium Chemistry for Organic Synthesis*, Negishi, E., de Meijera, A., Eds., Wiley-Interscience, New York; b) Siemens, P., Livingston, R. C. and Diederich, F., *Angew. Chem. Int. Ed.*, **2000**, *39*, 2632.

[19] a) Elangovan, A.; Wang, Y.-H. and Ho, T.-I., *Org. Lett.*, **2003**, *5*, 1841; b) Thorand, S. and Krause, N., *J. Org. Chem.*, **1998**, *63*, 8551.

[20] a) Li, J.-H.; Zhang, X.-D. and Xie, Y.-X. *Eur. J. Org. Chem.*, **2005**, 4256–4259; b) Feng, Z.; Yu, S. and Shang, Y. *Appl. Organometal. Chem.*, **2008**, *22*, 577–582; c) Samantaray, M. K.; Shaikh, M. M. and Ghosh, P. *J. Organometal. Chem.*, **2009**, *694*, 3477–3486; d) Hajipoura, A. R.; Shirdashtzadeaand, Z. and Azizi, G. *Appl. Organometal. Chem.*, **2014**, *28*, 696–698; e) Valishinaa, E. A.; Guedes da Silva, M. F. C.; Kinzhalov, M. A.; Timofeeva, S. A.; Buslaevaa, T. M.; Haukka, M.; Pombeiro, A. J. L.; Boyarskiy, V. P.; Kukushkind, V. Y. and Luzyanin, K. V. *Journal of Molecular Catalysis A: Chemical*, **2014**, *395*, 162–171; f) Moghaddam, F. M.; Tavakoli, G.; Rezvani, H. R. *Cat. Comm.*, **2015**, *60*, 82–87.

[21] Gil-Moltó, J. and Nájera, C*., Adv. Synth. Catal.*, **2006**, *348*, 1874.

[22] Chinchilla, R. and Nàjera, C. *Chem. Rev.*, **2007**, *107*, 874−922.

[23] an der Heiden, M. R.; Plenio, H.; Immel, S.; Burello, E.; Rothenberg, G. and Hoefsloo, H. C. J. *Chem. Eur. J.*, **2008**, *14*, 2857–2866.

[24] Niemelä, E. H.; Lee, A. F. and Fairlamb, I. J. S. *Tetrahedron Lett.*, **2004**, *45*, 3593–3595.

[25] www. Name-Reaction.com

[26] *Handbook of Organopalladium Chemistry for Organic Synthesis*; **2002**, Negishi, E., de Meijere, A., Eds.; Wiley: New York.

[27] Bertus, P.; Fécourt, F.; Bauder, C. and Pale, P. *New J. Chem.* **2004**, *28*, 12.

[28] Létinois-Halbes, U.; Pale, P. and Berger, S. *J. Org. Chem.* **2005**, *70*, 9185.

[29] Stambuli, J. P.; Bühl, M. and Hartwig, J. F. *J. Am. Chem. Soc.* **2002**, *124*, 9346-9347.

[30] Amatore, C. and Jutand, A. *Acc. Chem. Res.* **2000**, *33*, 314.

[31] Grosshenny, V.; Romero, F. M. and Ziessel, R. *J. Org. Chem.* **1997**, *62*, 1491.

[32] Littke, A. and Fu, G. C. *Angew. Chem. Int. Ed.*, **2002**, *41*, 4176-4211.

[33] Galli, S.; Maspero, A.; Giacobbe, C.; Palmisano, G.; Nardo, L.; Comotti, A.; Bassanetti, I.; Sozzani, P. and Masciocchi, N. *J. Mater. Chem. A*, **2014**, *2*, 12208-12221.

[34] Lin, Q.; Meloni, D.; Pan, Y.; Xia, R.; Rodgers, J.; Shepard, S.; Li, M.; Galya, L.; Metcalf, B.; Yue, T.-N.; Liu, P. and Zhou, J. *Org. Lett.*, **2009**, *11*, 1999–2002.

[35] a) Elangovan, A.; Wang, Y.-H. and Ho, T.-I *Org. Lett.,* **2003**, 5, 1841-1844; b) Wu, Y.-T-; Lin, W.-C.; Liu, C.-J. and Wua, C.-Y. *Adv. Synth. Catal.*, **2008**, *350*, 1841-1849

[36] Demko Z. P. and Sharpless K. B*. J. Org. Chem.*, **2001**, *66*, 7945-7950.

[37] Maspero, A.; Galli, S.; Masciocchi, N. and Palmisano, G. *Chem. Lett.*, **2008**, *37*, 956-967.

[38] Miller, A. O.; Krasnov, V. I.; Peters, D.; Platonov, V. E. and Miethchen, R. *Tetrahedron Let.*, **2000**, *41*, 3817–3819.

[39] Leyva, E.; Leyva,S.; Moctezuma, E.; Gonzalez-Balderas, R. M. and de Loera, D. *J. Fluor. Chem.* **2013**, *156*, 164–169.

Chapter 4
Exploitation of fluorinated coordination polymers and metal-organic frameworks for electronic device, insulation and adsorption applications

4.1 Introduction on low-κ materials

The quest for low-dielectric-constant (low-κ) materials to be employed in integrated circuit (IC) components has become a priority for the microelectronics industry due to increased industrial demands for transistors of decreased size and increased speed[1]. Presently, IC mean size is on the order of tens of nm, which has increased microprocessor working frequency to THz levels. This rising speed of operation is accompanied by the so called resistance-capacitance delay, namely the signal propagation delay at the conductor-insulator interconnection, which limits the operational speed of the device; dynamic power consumption and electronic "cross talk" are other side effects that account for loss of performances. To avoid these inconveniences, the Cu/low-κ material technology was developed to substitute the Al/SiO_2 technology.

The replacement of amorphous silica films (κ *ca.* 4), as insulators, with low-κ (κ < 2.5) materials has become an important challenge for the microelectronic industries. Studies that tackle this challenge focused on either bonds of lower polarizability than that for Si-O, or materials with lower density than that for silica. These aims were chased with the synthesis of silicon oxycarbides (SiOCs) or fluorosilicate glasses (FSGs), in which the Si-O bonds were substituted with Si-C or Si-F bonds, leading to some lowering of κ down to 3.2-4.0 or 2.7-3.3, respectively; for example,

PECVD-deposited amorphous κ-SiOC-0 featured a κ of 2.78 at 1 MHz[2]. Fluorinated organic materials showed excellent behaviour due to the already mentioned advantages of C-F bonds over C-H bonds (see **Chapter 2**). For example, polytetrafluoroethylenes (PTFEs) showed κ values down to *ca.* 2.1[3]; however, such Teflon materials usually suffer thermal stability issues, which are expected to be overcome in fluorinated coordination polymers or metal–organic frameworks.

One of the advantages of porous materials is the fact that the main components of air, N_2 and O_2, are non-polar, hence the dielectric constant of air is, at a first approximation, equal to that of vacuum (κ = 1). Remarkable results were obtained with porous xerogels and aerogels, attaining κ values lower than 2[4]. However, these classes of materials present some disadvantages: at the end of IC processing, devices undergo annealing at temperatures within the range 425-450 °C under forming gas (N_2:H_2 = 1:9 v/v); PTFEs do not meet these stability requirements (the melting point of Teflon is only 260 °C), while SiOCs do (PECVD-deposited α-SiOC-0 is stable up to ca. 550 °C[5]). On the other hand, the integration of aerogels or xerogels is difficult because the mechanical properties of these amorphous porous dielectrics are severely compromised by the increase in porosity[4]. Generally, new low-κ materials should ameliorate key properties such as mechanical and thermal stability and integration issues.

Within this landscape, and according to the most recent guidelines of the International Technology Roadmap for Semiconductors (ITRS)[6], fluorous metal-organic frameworks (FMOFs) and fluorous non-porous coordination polymers (FN-PCPs) containing azolato-based spacers appear to be promising alternatives as low-κ materials. This family of materials comprises low-polarity bonds (mainly C-C, C-N, N-N) with controlled stoichiometry, hence controlled functionality, which is not always the case with amorphous materials, and high thermal stability, which are among the principal traits for useful dielectrics. Indeed, as demonstrated also by our work, azolato-[7] and poly(azolato)-based[8] spacers impart remarkable thermal stability to the resulting MOFs.

Adsorption of high-κ species, namely polar molecules, dramatically increases the overall value of κ for the material, as already experienced with κ-SiOC-0/1/22. Fluorination and the absence of

porosity, as in FN-PCPs, inhibit the adsorption of high-κ species such as water (κ *ca.* 80) and other polar species produced during IC processing or post-fabrication. Due to fluorination, FMOFs potentially show a remarkable hydrophobicity, despite their porosity. Indeed, the porosity of FMOFs offers a platform to potentially attain further decrease in κ versus Teflons and FN-PCPs without compromising its value due to water adsorption, by taking advantage of the hydrophobic (or superhydrophobic) behaviour of FMOFs. This investigation, therefore, allows us to assess the advantages and limitations of FMOFs and FN-PCPs as potential low-κ materials for IC insulation (interconnect insulation and packaging) under practical conditions vs. other conventional low-κ materials and recently-investigated MOFs, ZIFs, etc5[,9].

In this context, the already known compound **FMOF-1** ({$[Ag_2[Ag_4Tz_6]]_n$; Tz = 3,5-bis(trifluoromethyl)-1,2,4-triazolate), the first fluorous MOF to ever appear in the literature7[a], possesses a rather high density (1.8 kg/L), it is air-stable up to 400 °C and superhydrophobic (contact angle *ca.* 160°). A periodic distribution of homogeneous pores and controlled functionality complete a remarkable set of features which make **FMOF-1** a good candidate for low-κ applications. On the other hand, high material density, especially in FN-PCPs, grant a high concentration of low-κ centres, increasing transistor density (hence, satisfying the continuing industry need for smaller and smaller next-generation transistors), and the absence of pores, which helps decrease high-κ centres and adsorption of high-κ compounds of relevance to IC processing (water and others) on the premise that even miniscule quantities of such high-κ materials will compromise the insulation action. Indeed, studies by Nijem et al. have shown that water interacts with MOFs even in situations where such interaction is undetectable by adsorption isotherms of hydrophobic/superhydrophobic MOFs such as **FMOF-1**[7]. Despite these premises, only a few papers, regarding exclusively MOFs, not N-PCPs, as low-κ materials, have appeared to date[5,9]. The work herein, therefore, allows us to conduct "apples-to-apples" comparisons for fluorinated vs non-fluorinated organic molecules, MOFs and N-PCPs, and assess the interplay between lowering the κ due to higher porosity vs sustaining the

low-κ values under humid conditions in these classes of unconventional low-κ materials with varying degrees of hydrophobicity.

Using the already known MOF **[Cu(BTB)]**[10], and N-PCP **[Ag_2(BTB)]**[11] as starting skeletons, we have synthesized the fluorinated counterparts, which show the same structural motif, *i.e.* **[Cu(FBTB)]** (**FMOF-3**), and **[Ag_2(FBTB)]** (**FN-PCP-1**). These new **FMOF-3** and **FN-PCP-1** materials are evaluated mainly for dielectric applications, together with **FMOF-1**. Moreover, we have expanded the FN-PCPs family by synthesizing **[Ag(FMTB)] (FN-PCP-2)**, **[Ag_2(FMTB)$_2$$Py_2$]Py (FN-PCP-3)** and **[Zn(FMTB)(CH_3COO)] (FN-PCP-4)**. The latter compounds are newly born, and only structural investigations have been performed to date with their future studies for low-κ and other applications to be pursued later.

4.2 Introduction on adsorption measurements on fluorinated compounds

The increase of the concentration of CO_2 in the atmosphere is becoming one of the most pressing environmental concerns of our age. Between 1970 and 2004 the annual global emission of CO_2 has increased by 80%[12]. This incredible rise is attributed to the increased use of fossil fuels, such as coal, natural gas and petroleum which account for 86% of the anthropogenic greenhouse effect; the remaining 14% is attributed to land use change, such as deforestation, and chemical processing[13]. Capture and storage of carbon dioxide, the major greenhouse gas, is a central strategy to lower the level of anthropogenic CO_2 in the atmosphere. By considering the remarkable magnitude of global CO_2 emissions[14], two major issues must first be faced with regards to capture materials and capture technologies. Firstly, if CO_2 capture is performed by disposable chemicals, they will rapidly exhaust their global supplies; secondly, any chemical produced from CO_2 as a reactant will rapidly saturate global markets for that chemical. Consequently, the capture materials used must be regenerable even if, in this case, the key factors which determine the efficiency and cost of the process is the energy input for regeneration. According to these considerations, three CO_2 separation methods are considered to hold the greatest promise for reducing CO_2 emissions, namely *i*) separation from

power plant flue streams, *ii*) separation from sour natural gas wells, and *iii*) separation from fuel gas (*i.e.*, syngas). Clearly, each application involves the separation of different gasses each of which imposes the use of specific materials which must follow distinct requirements and constraints[15]. Examples of materials in this context are *i*) physical absorbents (as Selexol[16], a mix of dimethylethers of polyethylene glycol, or Rectisol[16], methanol chilled to -40 °C, or ionic liquids[17]), *ii*) adsorption materials[18] *iii*) microporous and mesoporous materials (as zeolites or surface modified zeolites)[18g,19]; *iv*) carbonaceous adsorbents[15]; *v*) organic solids[15] and *vi*) metal-organic frameworks (containing either open metal sites or interpenetrated, flexible, and functionalized networks)[15](see **Table 4.1**[15]). Functionalization of the ligand with fluorine atoms is one of the strategies to prepare materials with high affinity to carbon dioxide[20]. So far, few examples of fluorinated MOFs are known in the literature and extremely rare are also publications which compare an isostructural fluorinated MOF to the non-fluorinated analogue[7a,c,20,21].

Starting from the already known MOFs **[Ni(BPEB)]**[22] and **[Zn(BPEB)]**[22], we have synthesized the fluorinated counterparts **[Ni(BPEBF$_4$)]** and **[Zn(BPEBF$_4$)]** and, together with **[Cu(BTB)]** and **FMOF-3**, we have tested their ability as CO_2 adsorbents.

Material[a]	Category	Separation, application, selectivity[b]	Reference
$[Zn_4O(fma)_3]$	4	CO_2/CH_4	23
$[Sc_2(bdc)_3]$	4	CO_2/CH_4; CO_2/H_2	24
$[Zn_2(bpdc)_2(dpni)]$	4	CO_2/CH_4	25
$[Cu_3(btc)_2]$	1	CO_2/CH_4; CO_2/N_2	26
$[Cr_3F(H_2O)_2O(btc)]_3$ (MIL-100)	1	CO_2/CH_4	27
$[Ni_2(pbmp)]$	1	CO_2/CH_4; CO_2/N_2	28
$[Mg_2(dobdc)]$	1	CO_2/CH_4	29
$Zn(adc)(Bpe)_{0.5}]$	2	CO_2/CH_4; CO_2/N_2	30
$[Ni(cyclam)_2(mtb)]$	2	CO_2/CH_4; CO_2/N_2	31
[Mg(tcpbda)]	1,2	CO_2/CH_4; CO_2/N_2	32
[Cr(OH)(bdc)] (MIL-53(Cr))	3	CO_2/CH_4	33
$[Co(F\text{-}pymo)_2]$	3	CO_2/CH_4	34
$[Zn(F\text{-}pymo)_2]$	3	CO_2/CH_4	34
$[(Ni_2L_1)(bptc)]$ (ethyl-bridged)	3	CO_2/CH_4; CO_2/H_2 ; CO_2/N_2	35
$Zn_2(bttb)(py\text{-}CF_3)_2]$	4	CO_2/N_2; CO_2/CH_4	36
$[Zn_2(bttb)]$	1	CO_2/N_2; CO_2/CH_4	36
$[H_3O][Zn_7(\mu_3\text{-}OH)_3(bbs)_6]$ (UoC-1)	4	CO_2/CH_4; CO_2/N_2; CO_2/H_2	37
$[Al(OH)(NH_2bdc)]$	3,4	CO_2/CH_4	38
[Al(OH)(bdc)] (MIL-53(Al))	3	CO_2/CH_4	39

Table 4.1: CO_2 capture and separation properties of selected metal–organic frameworks categorized as 1) containing open metal sites, 2) interpenetrated, 3) flexible, and 4) functionalized. [a] Abbreviations: bdc=1,4-benzenedicarboxylate, fma=fumarate, bpdc=biphenyl-4,4'-dicarboxylate, dpni=N,N'-di(4-pyridyl)-1,4,5,8-napthalenetetracarboxydiimide, btc=1,3,5-benezenetricarboxylate, pbmp=N,N'-piperazinebismethylenephosphonate, H_4dobdc=2,5-dihydroxyterephthalic acid, mtb=methanetetrabenzoate, H_2tcpbda=N,N,N',N'-tetrakis(4-carboxyphenyl)-biphenyl-4,4'-diamine, adc=4,4'-azobenzenedicarboxylate, Bpe=trans-bis(4-pyridyl)ethylene), cyclam=1,4,8,11-tetraazacyclotetradecane, F-pymo=5-fluoropyrimidin-2-olate, L1=ethyl-bridged Ni_2 macrocyclic complexes, bptc=1,1'-biphenyl-3,3',5,5'-tetracarboxylate, bttb=4,4',4'',4'''-benzene-1,2,4,5-tetrayltetrabenzoate, bbs=dianion of 4,4'-bibenzoic acid-2,2'-sulfone. [b] Reported selectivities from single adsorption isotherms.

4.3 Experimental Details

4.3.1 Synthesis of [Cu(FBTB)] (FMOF-3)

In a Schlenk flask, **H_2FBTB** (0.100 g, 0.35 mmol) was solubilised in DMF (5 mL) at RT. The temperature was slowly raised up to 60 °C, then $[Cu(OAc)_2]\cdot H_2O$ (0.069 g, 0.35 mmol) was added. The solution was heated up to 135 °C and kept at this temperature for 4 h. A dark cyan solid started to precipitate. The reaction mixture was gently cooled down to RT, then it was filtered. The dark cyan solid was washed with DMF (3 mL) and MeOH (5 mL) and dried *in vacuo* at 100 °C overnight affording the title compound as a pale cyan solid. (0.110 g, 90 %). IR: 1498 (s), 1485 (s), 1416 (w), 1403 (w), 1383 (w), 1355 (vw), 1273 (vw), 1219 (vw), 1104 (w), 1070 (vw), 984 (s), 801 (s), 736 (m), 669 (m). Elem. Anal. Calcd. for $C_8CuF_4N_8$ (FW = 347.7 g/mol): C, 27.64; H, 0.00; N, 32.23 %; found: C, 27.11; H, 0.20; N, 31.89 %.

4.3.2 Synthesis of [Ag_2(FBTB)] (FN-PCP-1)

In a Schlenk flask, **H_2FBTB** (0.100 g, 0.35 mmol) was suspended in water (5 mL) at RT. The temperature was slowly raised up to 60 °C, then $AgNO_3$ (0.118 g, 0.69 mmol) was slowly added to the mixture, which was refluxed for 4 h. A brownish solid started to precipitate. The reaction mixture was cooled down to RT, then, it was filtered. The brownish solid was washed with H_2O (3 mL) and MeOH (5 mL) and dried *in vacuo* at 100 °C overnight affording the title compound as a pale brownish solid. (0.161 g, 92 %). IR: 1492 (s), 1481 (s), 1398 (m), 1355 (w), 1258 (w), 1151 (w), 980 (s), 792 (s). Elem. Anal. Calcd. for $C_8Ag_2F_4N_8$ (FW = 499.9 g/mol): C, 19.22; H, 0.00; N, 22.42 %; found: C, 19.63; H, 0.15; N, 22.45 %.

4.3.3 Synthesis of [Ag(FMTB)] (FN-PCP-2)

In a Schlenk flask, **HFMTB** (0.100 g, 0.42 mmol) was suspended in distilled water (4 mL) at RT. The temperature was slowly raised up to 60 °C and a solution of $AgNO_3$ (0.072 g, 0.42 mmol) in water (2 mL) was slowly added to the reaction mixture. The mixture was then heated up to 100 °C and

maintained at this temperature for 5 h. The reaction mixture was cooled down to RT, then it was filtered. The white solid obtained was washed with H_2O (3 mL) and MeOH (5 mL) and dried *in vacuo* at RT for 4 h affording the title compound as a white solid. (0.128 g, 89 %). IR: 1662 (w), 1543 (s), 1506 (vs), 1491 (vs), 1388 (m), 1153 (m), 1110 (s), 1060 (s), 1035 (m), 987 (vs), 836 (vs). Elem. Anal. Calcd. for $C_7AgF_5N_4$ (FW: 342.97 g/mol): C, 24.51; H, 0.00; N, 16.34 %; found: C, 24.23; H, 0.02; N, 16.94 %.

4.3.4 Synthesis of $[Ag_2(FMTB)_2Py_2]Py$ (FN-PCP-3)

In a vial, **[Ag(FMTB)]** (0.050 g, 0.21 mmol) was dissolved in the minimum amount of Py. Then, Py was evaporated slowly at RT affording the title compound as white crystals.

Elem. Anal. Calcd. for $C_{29}H_{15}Ag_2F_{10}N_{11}$ (FW: 923.24 g/mol): C, 37.73; H, 1.64; N, 16.69 %; found: C, 36.98; H, 1.57; N, 16.94 %.

4.3.5 Synthesis of $[Zn(FMTB)(CH_3COO)]$ (FN-PCP-4)

In a Schlenk flask, HFMTB (0.100 g, 0.42 mmol) was suspended in CH_3CN (6 mL) at RT. The temperature was slowly raised up to 70 °C, then $Zn(OAc)_2{\cdot}2H_2O$ (0.046 g, 0.21 mmol) was added. The reaction mixture was then heated up to 100 °C for 5 h, cooled down to RT, and filtered. The white solid obtained was washed with MeOH (10 mL) and dried *in vacuo* at RT for 4 h affording the title compound as a white solid. (0.104 g, 69 %). IR: 1543 (s), 1515 (vs), 1497 (vs), 1462 (s), 1408 (s), 1397 (s), 1162 (m), 1082 (m), 1054 (m), 1032 (m), 993 (vs), 838 (vs), 749 (w), 693 (m). Elem. Anal. Calcd. for $C_9H_3F_5N_4O_2Zn$ (FW: 359.52 g/mol): C, 29.90; H, 1.39; N, 15.50 %; found: C, 30.08; H, 1.12; N, 15.71 %.

4.3.6 Synthesis of $[Ni(BPEBF_4)]$

In a Schlenk flask, H_2BPEBF_4 (0.080 g, 0.24 mmol) was dissolved in Py (5 mL) at RT. The temperature was slowly raised up to 60 °C, then $[Ni(BF_4)_2]{\cdot}6H_2O$ (0.081 g, 0.24 mmol) was slowly added to the

solution. As TEA (1 mL) was added dropwise, a yellow solid started to precipitate. Then the reaction mixture was refluxed for 4 h. The mixture was filtered, the recovered yellow solid was washed with Py (3 mL) and MeOH (5 mL) and dried *in vacuo* at 120 °C for 4 h affording the title compound as a brownish solid. (0.076 g, 82 %). IR: 2213 (m), 1542 (w), 1471 (s), 1297 (w), 1210 (w), 1024 (m), 978 (s), 851 (w), 663 (w), 635 (w). Elem. Anal. Calcd. for $C_{16}H_4F_4N_4Ni$ (FW = 386.92 g/mol): C, 49.67; H, 1.04; N, 14.48 %; found: C, 49.03; H, 1.50; N, 14.97 %.

4.3.7 Synthesis of [Zn(BPEBF$_4$)]

In a Schlenk flask, H_2BPEBF$_4$ (0.070 g, 0.21 mmol) was dissolved in Py (5 mL) at RT. The temperature was slowly raised up to 60 °C, then $[Zn(ClO_4)_2]\cdot 6H_2O$ (0.078 g, 0.21 mmol) was slowly added to the solution. The solution was stirred at 60 °C for 2 min, then TEA (1 mL) was slowly added dropwise. An ochre solid started to precipitate while the solution turned to red. The reaction mixture was refluxed for 2 h. While refluxing, the reaction mixture changed colour from dark red to orange. The mixture was filtered, the ochre solid was washed with Py (3 mL) and MeOH (5 mL) and dried *in vacuo* at 100 °C for 2 h affording the title compound as a pale ochre solid. (0.064 g, 78 %). IR: 2241 (m), 1568 (w), 1482 (vs), 1385 (m), 1366 (m), 1299 (s), 1165 (w), 1070 (m), 1028 (s), 1008 (w), 979 (s), 862 (m), 854 (m), 659 (vs), 636 (vs). Elem. Anal. Calcd. for $C_{16}H_4F_4N_4Zn$ (FW = 393.61 g/mol): C, 48.70; H, 1.28; N, 14.20 %; found: C, 48.16; H, 1.37; N, 13.52 %

4.3.8 Powder X-ray diffraction structural analysis

Polycrystalline samples of **FMOF-3**, **FN-PCP-1, [Ni(BPEBF$_4$)]**, **[Zn(BPEBF$_4$)]**, **FN-PCP-2**, and **FN-PCP-4** were ground in an agate mortar. Then, they were deposited in the hollow of a silicon zero-background plate. After fast preliminary acquisitions in the 2θ range 3-35° for qualitative analysis, diffraction data for structure refinements or solutions were collected overnight, at room temperature, in the 2θ range 3-105° or 5-105°, with steps of 0.02°, on a Bruker AXS D8 Advance diffractometer. Tentative unit cell parameters and space groups were adopted based on the

isostructurality between **FMOF-3** and **[Cu(BTB)]**, **FN-PCP-1** and **[Ag(BTB)]**, as suggested by a visual comparison of their PXRD patterns. The independent portion of the **FBTB^{2-}** ligand was described through a rigid, idealized model. [To describe the ligand, the z-matrix formalism was used, imposing idealized bond distances (Å) and angles (°) as follows: C-N, N-N of the penta-atomic ring, 1.36; C-C of the hexaatomic ring, 1.39; C-F, 1.31; exocyclic C-C, refined in the range 1.45-1.50; penta-atomic ring internal bond angles, 108; penta-atomic ring external bond angles, 126; hexaatomic ring bond angles, 120°]. The position of the metal ions and the centre of mass of the ligand were adopted starting from the available structural information for **[Cu(BTB)]** and **[Ag(BTB)].** The structure refinements were carried out by the Rietveld method. In all of the cases, the peak shapes were described with the fundamental parameters approach[40]. The background was modeled by a polynomial function. A refinable, isotropic thermal parameter (B_M) was assigned to the metal atoms; lighter atoms were given an isotropic thermal parameter 2.0 Å^2 higher.

4.3.9 Variable-Temperature Powder X-ray Diffraction

Variable-temperature powder X-ray diffraction (VT-PXRD) experiments were performed on as-synthesized **FMOF-1**, **FMOF-3** and **FN-PCP-1**. As a first experiment, 30-mg samples of the three compounds were ground in an agate mortar and deposited in the hollow of an aluminium sample holder. By means of a custom-made sample heater (Officina Elettrotecnica di Tenno, Ponte Arche, Italy), mounted on a Bruker AXS D8 Advance diffractometer, the samples were heated in air from 30 °C up to decomposition, with steps of 20 °C; a PXRD pattern was acquired at each step, covering a sensible low-to-medium-angle 2θ range. Treating the data acquired before loss of crystallinity by means of a Le Bail parametric refinement allowed us to disclose the behaviour of the unit cell parameters as a function of the temperature. As a second experiment, 30-mg samples of **FMOF-1**, **FMOF-3** and **FN-PCP-1** were monitored by PXRD during five heating-cooling cycles, in air, in the range 30-200 °C.

Note: When comparing the results of STA and VT-PXRD, the reader must be aware that the thermocouple of the VT-PXRD set-up is not in direct contact with the sample, this determining a slight difference in the temperature at which the same event is detected by the two techniques. The temperatures derived from STA must be considered more reliable.

4.3.10 Chemical stability tests

To perform a typical test, 15-mg samples of **FMOF-1**, **FMOF-3** and **FN-PCP-1** were deposited in the hollow of an aluminium sample-holder. Preliminary PXRD data were acquired in a suitable low-to-medium angle 2θ range. Then, the sample-holder was introduced in a water vapour-saturated environment or the sample was suspended in 10 mL of liquid water. At different time intervals of water vapour exposure, each sample was analysed by PXRD, adopting the same acquisition conditions employed for the preliminary acquisitions.

4.3.11 Estimation of the contact angle

Contact angle measurements were carried out by laying down a drop of distilled water on a pellet of the desired material, produced by compression of the powder with a press at 1000 or 2000 psi for 5 minutes. A series of pictures was taken with a common digital camera; the images were processed by the software ImageJ[41].

4.3.12 Measurements of the dielectric constant

Dielectric constant values were obtained with an Agilent E4980A Precision LCR Meter with a connection Agilent 16048A Test Leads, a custom-made sample holder and measuring head (Officina Elettrotecnica di Tenno, Ponte Arche, Italy). The measurements were performed on a pellet of the desired material, produced by compression of the powder with a press at 1000 or 2000 psi for 5 minutes.

4.4 Results and Discussion

4.4.1 Synthesis of fluorinated CPs and MOFs

The synthesis of **FMOF-3** was carried out in DMF using $Cu(OAc)_2 \cdot H_2O$ as the starting material. The nature of the anion of the metal salt plays a key role in the synthesis of this MOF. Due to the combination of the acidity of tetrazole[42] and the effect of the fluorine atoms on the phenyl ring, the overall acidity of **H_2FBTB** is quite strong: the acetate counterion in the metal precursor is basic enough (see **Chapter 2**) to deprotonate the two tetrazole rings, generating the **$FBTB^{2-}$** anion *in situ*.

The non-fluorinated counterpart **[Cu(BTB)]** was not possible for us to obtain in the desired crystalline phase originally published by Long and coworkers[10]. As already noticed also by those authors, the material is tricky to obtain and requires a strict control of pH and temperature. Furthermore, it undergoes a phase transition already at 100 °C[10]. Despite a number of attempts, varying the temperature, solvent and/or reaction time, the desired phase was not obtained.

On the other hand, the synthesis of **FN-PCP-1** was carried out in refluxing water in the presence of $AgNO_3$. **H_2FBTB** is slightly soluble in water, but the reaction with $AgNO_3$ proceeds rather easily in a few hours with high yield.

Similarly to the synthesis of **FN-PCP-1**, **[Ag(FMTB)]** was synthesized in refluxing water without the presence of any base. The reaction proceeds without any hitch, affording the pure desired product in six hours.

During the characterization of **[Ag(FMTB)]**, we found that it is soluble in coordinative solvents as Py, DMSO, DMF, etc. Therefore, we were able to obtain single crystals from Py. The solubilisation is due to the fact that Py can coordinate the silver(I) ions in place of one nitrogen atom belonging to one tetrazolate ring, disrupting the structure of the parent species. This substitution probably takes place because the coordination ability of tetrazole is lowered by the effect of the five fluorine atoms.

The same considerations can be carried out for **[Zn(FMTB)(CH_3COO)]**: even if the coordinative ability of the acetate anion is lower than that of tetrazolate, the deactivation effect generated by the five fluorine atoms on the benzene ring makes tetrazolate more acidic, henceforth less able to

coordinate. The synthesis is slow and the yields are not excellent, but the product is recovered rather pure with no further purification steps needed.

Conversely to tetrazole derivatives, the synthesis of **[Ni(BPEBF$_4$)]** needs the presence of a base to deprotonate pyrazole. The synthesis is quite tricky; indeed, the degree of crystallinity of the final product is poor and any small glitch leads to amorphous compounds (PXRD evidence).

The same considerations hold true for the synthesis of **[Zn(BPEBF$_4$)]**. More interestingly, after the filtration of the desired material, if the solution is treated with MeOH, another dark-ochre solid starts to precipitate, which resulted in a yet unknown, still uncharacterized phase.

4.4.2 Powder X-ray diffraction structural analysis

[Cu(FBTB)] or **FMOF-3** is isomorphous to its non-fluorinated analogue **[Cu(BTB)]**. It crystallizes in the orthorhombic space group *Imma*. Each metal centre is coordinated, in a square-planar stereochemistry, by four nitrogen atoms of four **FBTB^{2-}** anions (**Figure 4.2**). Interestingly, in **FMOF-3**, the tetrazolate moieties have pyrazolate-like coordination mode; indeed, they coordinate to the Cu(II) centres with the N2 and N3 atoms (**Figure 4.2a**). With one of their tetrazolate rings, the ligands bridge collinear Cu(II) ions, thus creating 1-D chains parallel to the crystallographic axis **a**. The 3-D network is formed by the connection of each 1-D chain to four nearby ones through the spacers, with the consequent formation of large rhombic channels running along the crystallographic axis **a** (see **Figure 4.2**).

As expected, **FN-PCP-1** is isomorphous to **[Ag$_2$(BTB)]**. It crystallizes in the orthorhombic space group *Fddd*. Overall, the crystal structure of **FN-PCP-1** is a non-porous 3-D network, in which the **FBTB^{2-}** anions act as spacers and the Ag(I) ions act as nodes possessing tetrahedral stereochemistry. Interestingly, the **FBTB^{2-}** anion shows the already mentioned μ_4-η^1:η^1:η^1:η^1 coordination mode (**Chapter 2**) to connect eight, tetra-coordinated nodes. Viewing the structure along the crystallographic axis **c** (**Figure 4.3**), the complexity of the crystal packing can be appreciated. As evident in **Figure 4.3**, 1-D strands are constructed by a sequence of hexanuclear –Ag–N–N–Ag–N–N–

rings, which run parallel to the crystallographic axis **b**. The 3-D network is obtained through the connection of the 1-D strands by bridging **FBTB**$^{2-}$ anions along the crystallographic axes **a** and **c**.

[Ag(FMTB)] shows a complex PXRD pattern. At the time of writing this dissertation, no hypothesis on the crystal structure could be advanced.

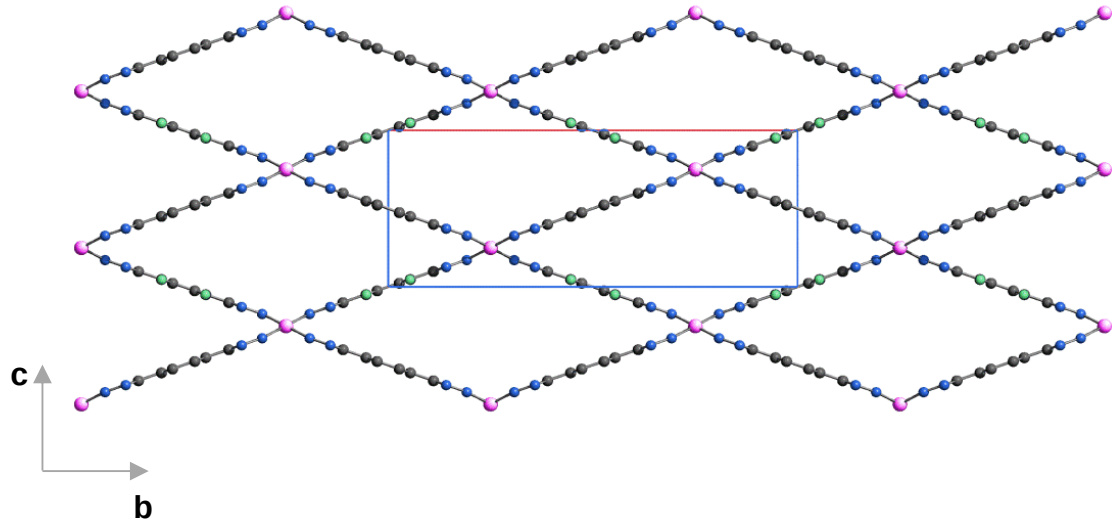

Figure 4.2: schematic drawing of the crystal structure of **FMOF-3** viewed down the crystallographic axis **a**. Carbon, grey; nitrogen, blue; fluorine, green; copper, pink.

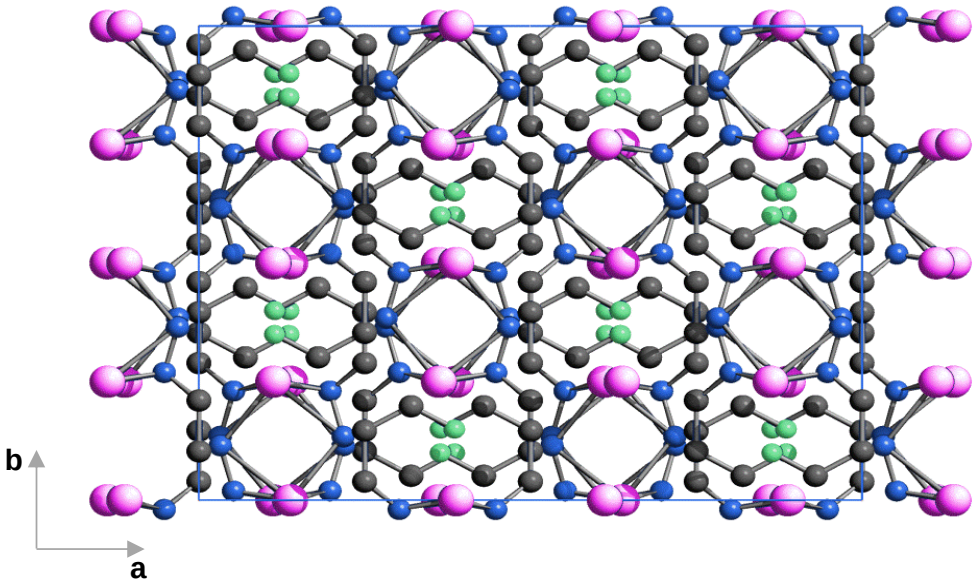

Figure 4.3: Schematic drawing of the crystal structure of **FN-PCP-1** viewed down the crystallographic axis **a**. Carbon, grey; nitrogen, blue; fluorine, green; silver, fuchsia.

[Ag_2(FMTB)$_2Py_2$]Py is the only compound presented in this dissertation which structure was obtained from single crystal XRD. It crystallizes in the triclinic space group *P*-1 (**Figure 4.4**). The asymmetric unit is constituted by a dimer in which two tetrazolate moieties coordinate to two tetrahedral Ag(I) centres. The other two coordination positions of the Ag(I) centres are occupied by one Py molecule in one case, and by another tetrazolate moiety in the other case. The latter bridges another dimeric unit, affording 1-D sheets running along the crystallographic axis **b**. Clathrated molecules of Py are located between two adjacent 1-D sheets. The latter interact through π-interaction between two perfluorinated rings facing each other.

[Zn(FMTB)(CH_3COO)] crystallizes in the monoclinic space group *P*21/*c* (**Figure 4.4**). The basic unit is a tetrahedral Zn(II) centre coordinated to two tetrazolate moieties and two acetate ions. Each tetrazolate ligand bridges two Zn(II) centres affording 1-D chains. The acetate bridges two Zn(II) ions of two different 1-D chains affording a 2-D non-porous structure.

Despite showing the same structural motif of **[Zn(BPEB)]**, the compound **[Zn(BPEBF_4)]** crystallizes in the monoclinic space group *C*2/*c*. The asymmetric unit is constituted by one Zn(II) centre and one organic linker, both lying on special positions. Each metal centre is coordinated by four nitrogen atoms of four ligands and possesses a distorted tetrahedral stereochemistry (**Figure 4.5**), building up 1-D chains of collinear metal centres running along the crystallographic axis **c**.

Adjacent chains are connected by the spacers in such a way as to generate two mutually interpenetrated 3-D networks, reciprocally displaced by about 7.75 Å along **b.**

Even if **[Ni(BPEBF_4)]** shows a low degree of crystallinity, it could be inferred that it is isomorphous to the non-fluorinated counterpart, **[Ni(BPEB)]**. It crystallizes in the orthorhombic space group *Imma*. The asymmetric unit is constituted by one Ni(II) ion possessing a square-planar stereochemistry, and one ligand, both lying on special positions. Each pyrazolate ring bridges two Ni(II) ions generating 1-D chains; each 1-D chain is further linked, along the [0,1,1] direction, to four nearby chains by the spacers affording a 3-D network possessing big rhombic channels running along the crystallographic axis **a** (**Figure 4.6**). It is known in literature that MOFs crystal structuresmight show defects, such as

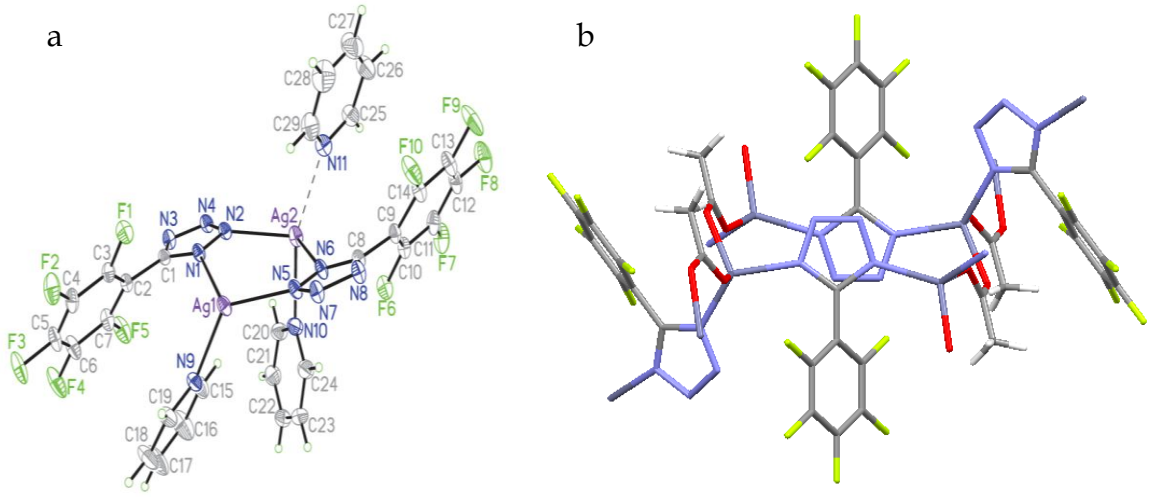

Figure 4.4: Schematic drawing of the crystal structure of a) **[Ag_2(FMTB)$_2Py_2$]Py.** Carbon, grey; nitrogen, blue; fluorine, green; silver, violet and b) **[Zn(FMTB)(CH_3COO)]**. Carbon, grey; nitrogen, violet; fluorine, green; silver, deep violet.

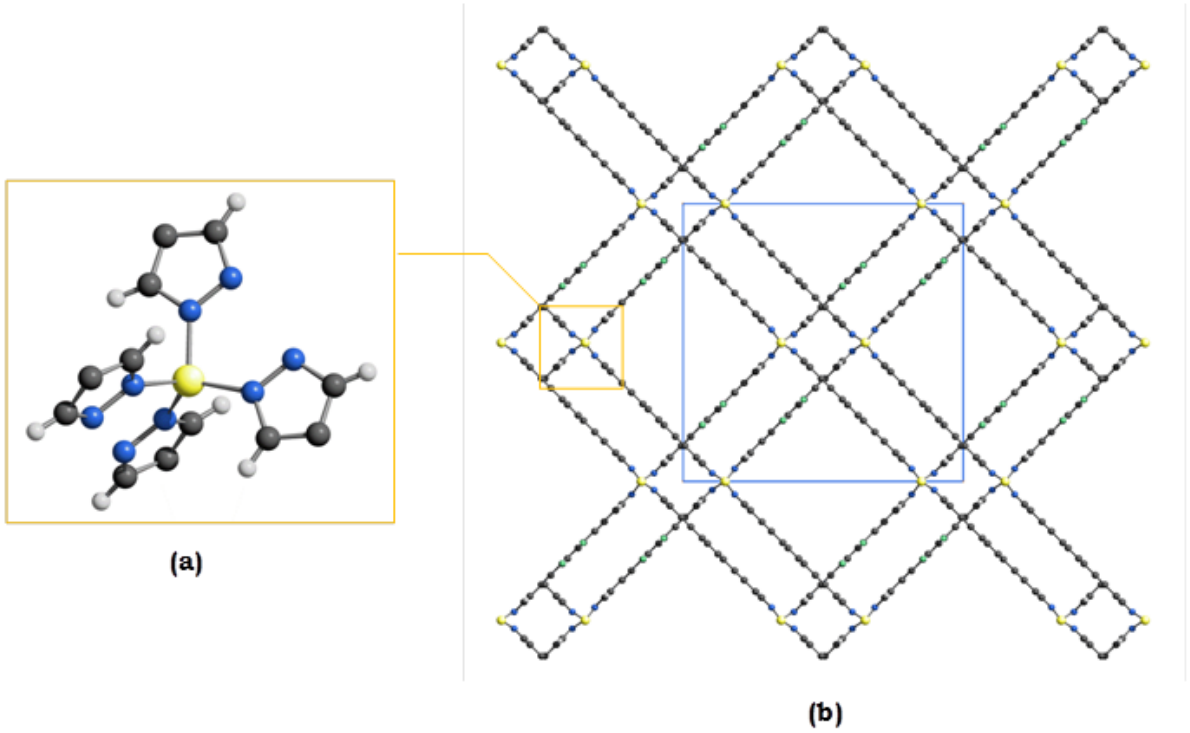

Figure 4.5: Representation of the crystal structure of **[Zn(BPEDF$_4$)]**: a) the tetrahedral coordination sphere of the metal centre; b) the crystal packaging viewed along the crystallographic axis **c** (horizontal axis **a**; vertical axis **b**). The interpenetrated networks and the two different types of channels can be clearly distinguished. Carbon, grey; hydrogen, light grey; fluorine, green; nitrogen, blue; zinc, yellow.

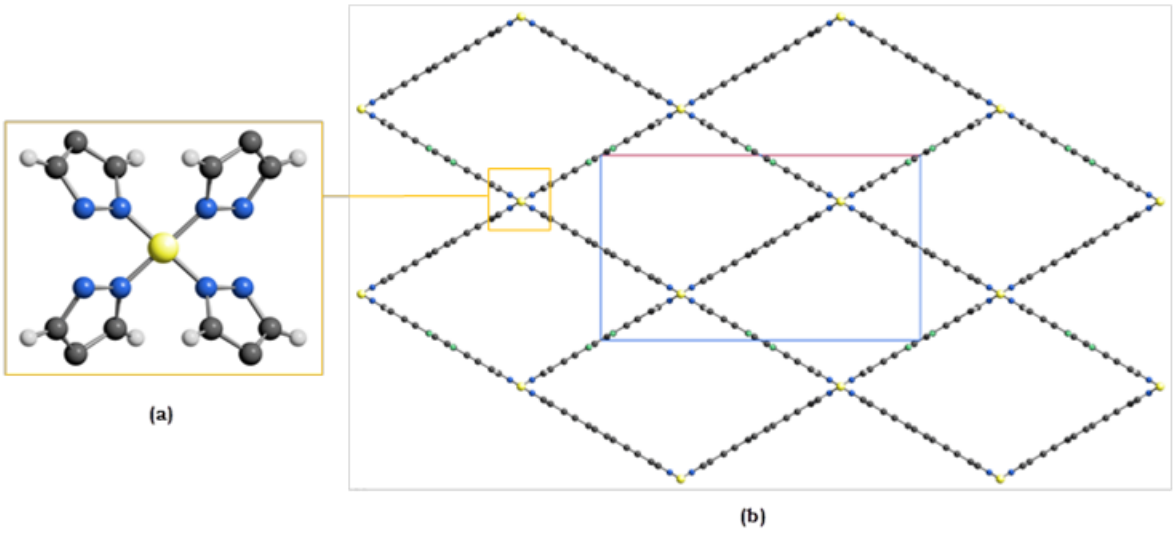

Figure 4.6: Schematic representation of the crystal structure of **[Ni(BPEBF$_4$)]**: a) the square planar coordination sphere of the metal center; b) the crystal packing, visualized along the crystallographic axis **a** (horizontal axis **b**; vertical axis **c**). The 1-D rhombic channels can be clearly seen running along **a**. Carbon, grey; hydrogen, light grey; nitrogen, blue; fluorine, green; nickel, yellow.

missing linker of missing metal defects. The nature and amount of these defects may influence the functional properties of the material[43] to a great extent.

Unfortunately, our FMOFs shows a very modest degree of crystallinity and the studies devoted to the identification of *missing linker or missing metal defects* are consequently hampered.

4.4.3 Thermal behaviour

STA measurements coupled to VT-PXRD were performed on all the compounds investigated herein.

H$_2$FBTB is stable, both under nitrogen and in air, up to 320 °C, the temperature at which its decomposition starts. A parametric Le Bail treatment of the VT-PXRD data acquired in the 30-310 °C range highlights that all of the three crystallographic axes increase monotonically upon increasing the temperature (by 1.1, 2.4 and 0.7% for **a**, **b** and **c**, respectively), thus implying an overall volumetric thermal expansion of 4.2% over this entire temperature range.

H$_2$BPEBF$_4$ is stable, under nitrogen, up to 350 °C.

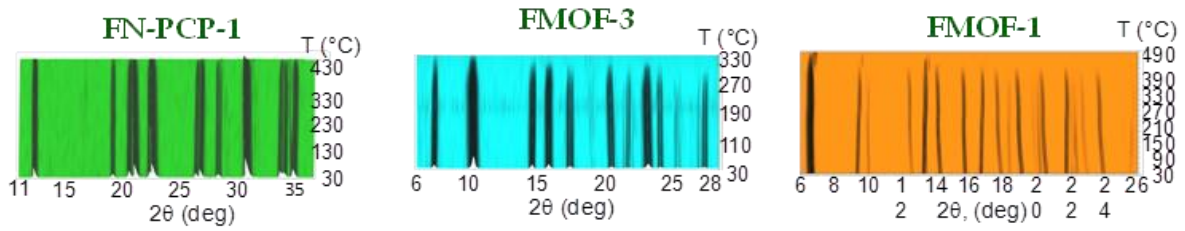

Figure 4.1: VT-PXRD acquired for **FN-PCP-1**, left, **FMOF-3**, middle and **FMOF-1**, right.

FMOF-3 is stable, both under nitrogen and in air (**Figure 4.1**), up to 260 °C, temperature at which its decomposition starts. Notably, the homologous compound **[Cu(BTB)]** undergoes a transformation to a low-crystallinity phase already at 100 °C[10], thus demonstrating to be less thermally robust than **FMOF-3**. A parametric Le Bail treatment of the VT-PXRD data of **FMOF-3** acquired in the range 30-250 °C highlights that, while **a** remains almost unchanged, **b** and **c** vary by 0.3 and 1.2%, respectively, thus implying an overall volumetric thermal expansion of 0.8%, speaking for an almost negligible flexibility of this porous MOF in the essayed conditions.

FN-PCP-1 is stable, both under nitrogen and in air (**Figure 4.1**), up to 400 °C. Also in this case, the introduction of fluorine atoms brings about an increase of the decomposition temperature, that of **[Ag_2(BTB)]** being 380 °C8[a]. A parametric Le Bail treatment of the VT-PXRD data acquired in the range 30-390 °C highlights that, while **a** and **b** vary negligibly (less than 0.2% each), **c** increases by about 1.7%, thus implying an overall volumetric thermal expansion of 1.7%.

[Ni(BPEBF_4)] is stable, under nitrogen, up to 430 °C. The presence of fluorine atoms enhances the thermal stability of the compound by only 8 °C, given that the decomposition temperature of **[Ni(BPEB)]** is 422 °C[22].

[Zn(BPEBF_4)] is remarkably stable under nitrogen, as it survives up to 475 °C, a temperature at which its decomposition starts. In this case, however, the presence of fluorine atoms enhances the stability of the resulting MOF more significantly – by *ca.* 65 °C – compared to the non-fluorinated counterpart, **[Zn(BPEB)]**, that is stable up to 410 °C[22].

4.4.4 Chemical stability

The stability of **FN-PCP-1**, **FMOF-3** and **FMOF-1** was tested under water vapour and in liquid water.

FMOF-3 undergoes loss of crystallinity when exposed to water vapours for 3 days, PXRD evidences.

FN-PCP-1 is stable when exposed to water vapours for 48 days and for at least 3 days when suspended in liquid water, PXRD evidences (**Figure 4.7**).

FMOF-1 has been found to be stable when exposed to water vapour for at least 32 days, also based upon PXRD evidence (**Figure 4.7**).

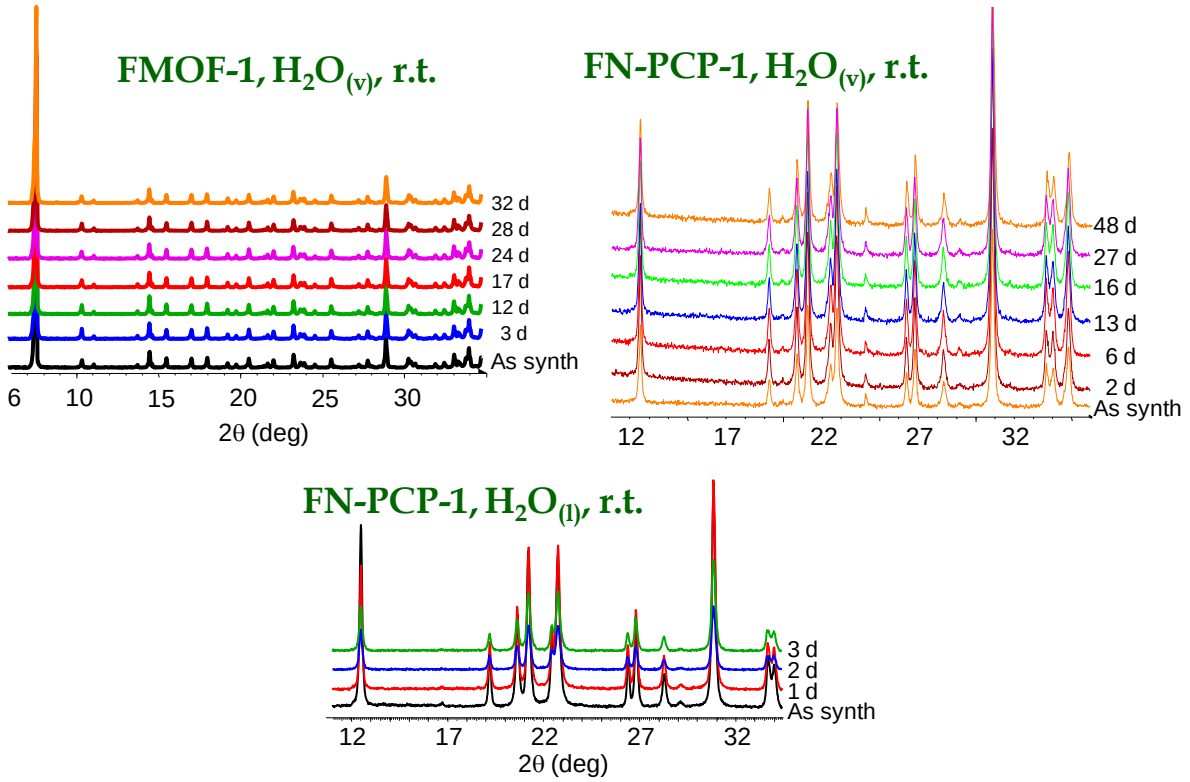

Figure 4.7: Comparison of the PXRD patterns monitoring the stability of **FMOF-1** (upper left), **FN-PCP-1** (upper right) and of **FN-PCP-1** in liquid water (bottom centre) vs. time (days).

4.4.5 Estimation of the contact angle

The contact angle was estimated only for **FMOF-1**, **FN-PCP-1** and **[Ag_2(BTB)]**. Due to the mentioned experimental difficulties and stability issues, the contact angle for **FMOF-3** and **[Cu(BTB)]** could not be measured. As already predicted[7c], **FMOF-1** was found to be superhydrophobic, attaining a contact angle of *ca.* 160° (**Figure 4.8**). This behaviour is reasonably due to the CF_3 functionalities of the triazolate moieties that protect the surface of the material and, consequently, the channels from water.

Despite the high density, namely 2.9 kg/L, and the absence of porosity, **FN-PCP-1** is not superhydrophobic, attaining a value for the contact angle of *ca.* 75°. This result suggests that **FN-PCP-1** is only slightly more hydrophobic than its non-fluorinated counterpart **[Ag_2(BTB)]**, for which the the contact angle value obtained is *ca.* 55°. In this case, the presence of fluorine atoms enhances hydrophobicity only qualitatively, but not as well as expected quantitatively.

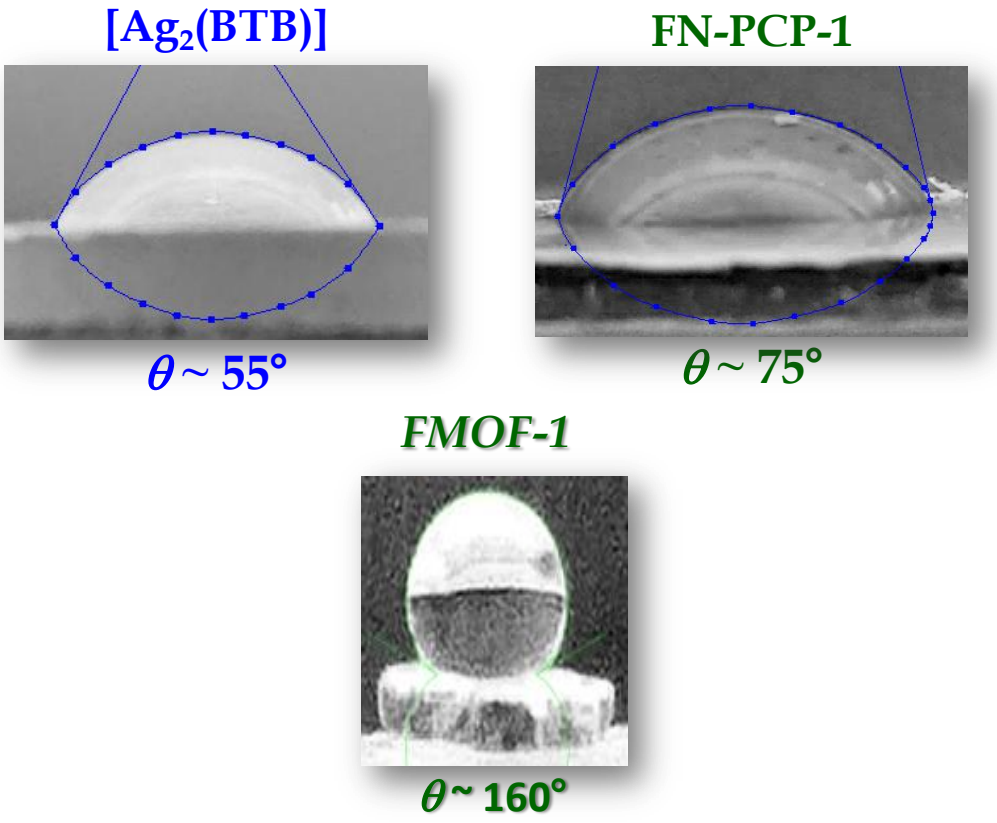

Figure 4.8: Estimation of the contact angle for **[Ag_2(BTB)]** (upper left), **FN-PCP-1** (upper right) and **FMOF-1** (bottom).

4.4.6 Dielectric constant measurements

The aim of these measurements was the evaluation of the effects of fluorine atoms and of porosity on the value of κ in order to identify potentially novel low-κ materials. As expected, the substitution of hydrogen atoms with fluorine atoms decreases the value of κ. Indeed, the effect of fluorination can be easily appreciated already by κ values of 4.8 and 2.8 for pellets of the free organic ligands, **H_2BTB** and **H_2FBTB**, respectively, at room temperature and 2 MHz frequency. The same trend is observed for **[Ag(BTB)]** and **FN-PCP-1**: As a matter of fact, the κ values estimated at room temperature and at a frequency of 2 MHz are 3.8 and 2.6, respectively; these results suggest that replacing protons by the a transition metal cation impart further lowering of κ for both the fluorinated and non-fluorinated species. Due to the difficulties faced during the synthesis of **[Cu(BTB)]** (see **Section 4.3.1**), the comparison with **FMOF-3** could not be carried out. Despite its porosity and lower density than that for **FN-PCP-1** (1.5 kg/L for **FMOF-3** vs 2.9 kg/L for **FN-PCP-1**), **FMOF-3** possesses a remarkably-low value of κ, estimated to be 2.4 at room temperature and at a frequency of 2 MHz. Beside the structural diversity, another important difference exists between **FN-PCP-1** or **FMOF-3** and **FMOF-1**: While the first two compounds have fluorine atoms directly bonded to the aromatic core, the latter possesses trifluoromethyl groups; this feature is deemed more significant for a better protection of the pores towards polar and high-κ molecules (see **Sections 4.3.4** and **4.3.5**).

Worthy of note is the finding that **FMOF-1** undergoes amorphization while exposed to high pressure. Indeed, as easily appreciable, it loses crystallinity depending upon the value of the pressure applied to prepare the pellet. Therefore, different values of κ could be obtained for this material as a function of pressure: for the pellet fabricated at 1000 psi, we obtained κ = 2.0 at room temperature and at a frequency of 2 MHz, while for the pellet fabricated at 2000 psi we obtained κ = 2.1 at room temperature and at a frequency of 2 MHz. The "best" values of κ obtained for all the **FMOF-1** pellets produced at room temperature and at a frequency of 2 MHz even trumped 2.0 when we attempted to fabricate pellets at even higher pressures than 2000 psi; however, such pellets were not easy-to-

fabricate consistently due to some mechanical difficulties so we have not been able to reproduce such $\kappa \leq 2.0$ values with high precision. Due to the loss of crystallinity, a direct evaluation of the effects of trifluoromethylation and/or porosity on the value of κ for this material has not been possible to be carried out; further investigations on thin films instead of pellets fabricated on IC-relevant substrates are in order to be carried out in a future expansion of this work.

4.4.7 Gas adsorption properties

Adsorption measurements of N_2 at 77 K were performed on **FN-PCP-1** to demonstrate the lack of porosity: Indeed, it possesses a negligible BET specific surface area, amounting to *ca.* 4 m^2/g.

Following the adsorption measurements already carried out for **FMOF-1**[7a,c], we started to perform some experiments on the pyrazolate- and tetrazolate-based MOFs.

FMOF-3 presents an interesting behaviour: the specific surface area retrieved from the N_2 adsorption isotherm acquired at 77 K amounts to only 61.6 m^2/g. Moreover, immediately after recovering it at 77 K, it exhibits a light-violet colour, whereas its usual colour at room temperature is cyan. The light-violet colour change suggests a change in the coordination sphere of the metal centres, but it lasts for less than one minute while the sample is being warmed up to room temperature. Low-temperature PXRD studies are in progress to unveil the structure of this fleeting phase. The recovered cyan powder was found to have a triclinic unit cell, the unit cell parameters of which can be traced back to those of the parent orthorhombic phase; the triclinic phase survives for a few days: PXRD demonstrated that the orthorhombic *Imma* phase is fully recovered (**Figure 4.9**). This behaviour suggests a certain flexibility of the framework.

In order to calculate the specific surface area of the MOF, adsorption of CO_2 at 273 K was performed: The framework possesses a quite small specific surface area, around 180 m^2/g. Experiments are in progress to optimize the activation of the material, given that modelling of the porous crystal structure above obtained at room temperature using the Materials Studio program attains a surface area of 941 m^2/g using CO_2 and 779 m^2/g using N_2 as the guest molecules (based on a kinetic radius

of 1.60 Å for CO_2 and 1.84 Å for N_2). Further spectral and structural investigations of the origin of the thermochromism and associated channel closure-opening phenomena are in progress.

Adsorption studies were performed also on **[Ni(BPEBF$_4$)]** and **[Zn(BPEBF$_4$)]**. For these materials, a comparison with the non-fluorinated counterpart, **[Ni(BPEB)]** and **[Zn(BPEB)]**, is important, because it enables us to estimate the different steric and electronic effects of the fluorine atoms on adsorption. As expected, the specific surface area of **[Zn(BPEBF$_4$)]** and **[Ni(BPEBF$_4$)]** is lower than that of **[Zn(BPEB)]** and **[Ni(BPEB)]**; see **Table 4.2**. The lower surface area is ascribable to the larger van der Waals radium of fluorine, 1.4 Å, compared to that of hydrogen, 1.2 Å. Moreover, this effect is magnified if the values are reported in m^2/g because of the difference in the molar weight of the two ligands. In **Table 4.2**, BET-specific surface areas are reported also as m^2/mol. As easily observable, the specific surface areas referred to the moles of Zn(II) derivatives are comparable;

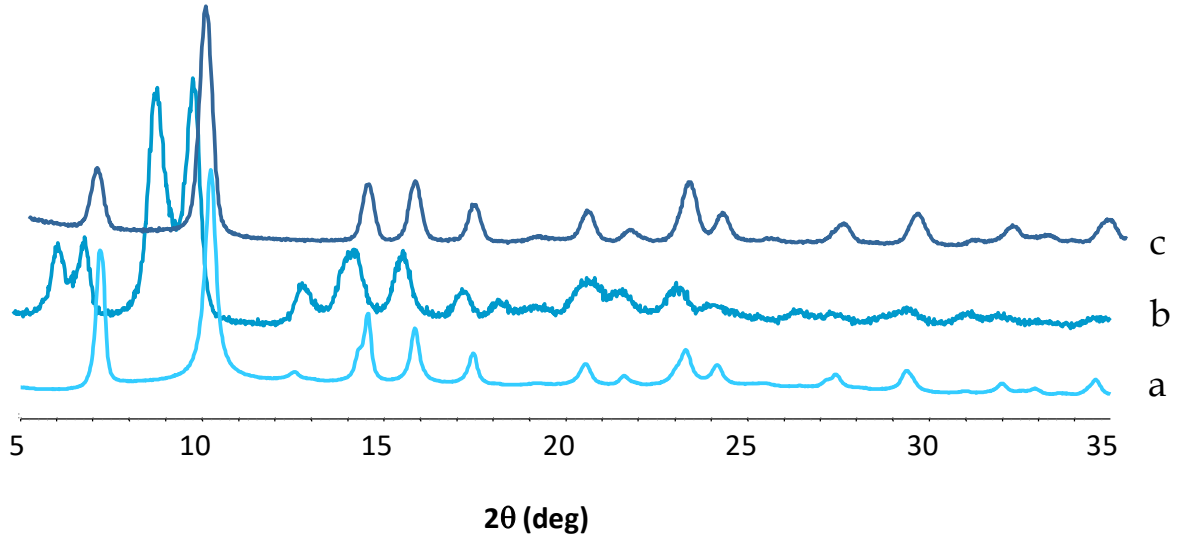

Figure 4.9: PXRD plots for a) starting **FMOF-3** orthorombic *Imma* phase; b) recovered *P*-1 triclinic phase after N_2 adsorption; c) fully recovered orthorhombic *Imma* phase after a few days at room temperature.

	[Zn(BPEB)]	**[Zn(BPEBF$_4$)]**	**[Ni(BPEB)]**	**[Ni(BPEBF$_4$)]**
BET surface area [m^2/g]	985	756	1900	824
BET surface area [m^2/mol]	316678	297486	597550	318476

Table 4.2: Specific surface area for bis-pyrazolate derivatives corresponding to N_2 adsorption at 77 K.

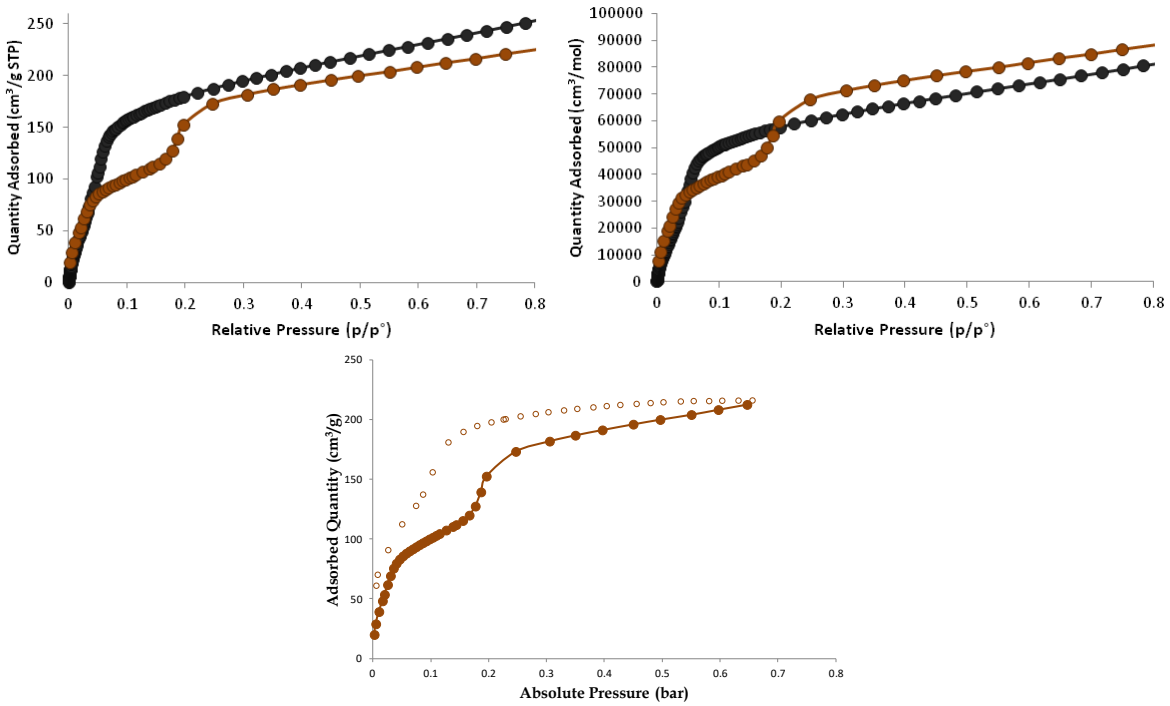

Figure 4.10: Adsorption isotherm of CO_2 at 195 K. Top: comparison between **[Zn(BPEB)]** (black curve) and **[Zn(BPEBF$_4$)]** (brown curve) expressed in cm^3/g, left graph, and cm^3/mol, right graph. Bottom: desorption isotherm is marked with empty symbols.

the slight difference could be bestowed to the smaller degree of crystallinity of **[Zn(BPEBF$_4$)]** in comparison to that of **[Zn(BPEB)]**. Different considerations must be carried out for the Ni(II) derivatives: as shown in **Table 4.2**, the specific surface area for **[Ni(BPEB)]** is almost doubled vs. that of **[Ni(BPEBF$_4$)]**. This huge difference cannot be due exclusively to the steric hindrance of fluorine atoms. Apparently, the presence of fluorine atoms prevents the formation of a highly crystalline compound, see **Section 4.3.1**; the degree of crystallinity for the fluorinated derivatives is, indeed, poor.

For the reasons highlighted above, **[Zn(BPEB)]** shows higher adsorption of CO_2 per gram of MOF than **[Zn(BPEBF$_4$)]** (**Figure 4.10**). To better compare the behavior of two materials with different molar weight, it is very important to analyze also the gas uptake per mol of material; indeed, as shown in **Figure 4.10**, **[Zn(BPEBF$_4$)]** shows a higher CO_2 adsorption per mol of MOF when the relative pressure is higher than 0.2. Moreover, in the case of **[Zn(BPEBF$_4$)]**, a step in the isotherm at the relative pressure p/p° of 0.2 was observed.

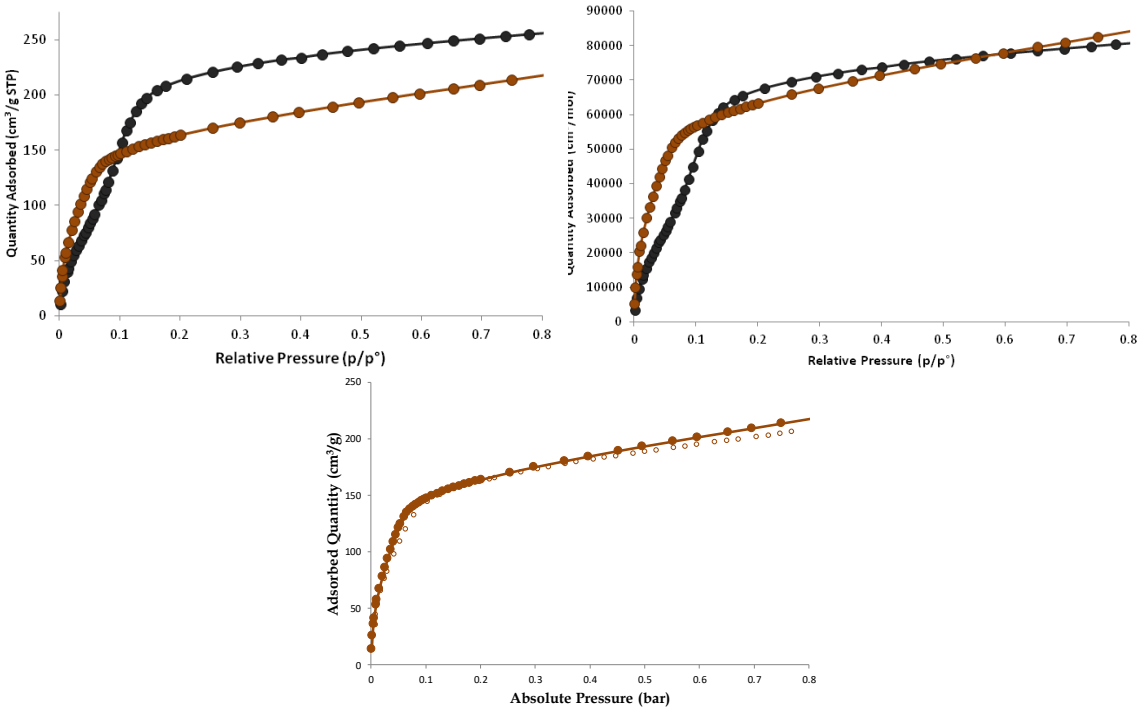

Figure 4.11: Adsorption isotherm of CO_2 at 195 K. Top: comparison between **[Ni(BPEB)]** (black curve) and **[Ni(BPEBF$_4$)]** (brown curve) expressed in cm^3/g, left graph, and cm^3/mol, right graph. Bottom: desorption isotherm is marked with empty symbols.

This interesting behaviour was already observed in some highly crystalline materials such as zeolites or carbons, obtained *via* template methods[44], and MOFs[10,45]. The reasons of this behaviour in our MOFs have not been completely clarified yet, but some hypotheses have been proposed which consist in: *i*) blocking effects[46]; *ii*) phase transition in the essayed experimental conditions[45]; *iii*) de-interpenetration of the framework[47]; *iv*) presence of a higher micropore volume in **[Zn(BPEBF$_4$)]** vs. **[Zn(BPEB)]**, and *v*) the polar nature of the C-F bonds. Actually, the presence of fluorine atoms causes the formation of smaller pores that can increase the total micropore surface area, which is responsible for the adsorption of CO_2. Moreover, C-F bonds could have strong electrostatic interactions with a quadrupolar molecule like CO_2, which could lead to the observed behaviour.

As shown in **Figure 4.11**, **[Ni(BPEBF$_4$)]** shows a smaller CO_2 uptake than **[Ni(BPEB)]** when the relative pressure is higher than 0.1, expressed per gram of MOF: this behaviour can be due to the different degree of crystallinity of the samples: indeed, **[Ni(BPEB)]** shows a specific surface area twice that of **[Ni(BPEBF$_4$)]**. Indeed, the adsorption isotherms (**Figure 4.11**), expressed as cm^3/mol, are

comparable. This clearly demonstrates the importance of the fluorine atoms for CO_2 adsorption and storage: despite the lower degree of crystallinity and specific surface area, **[Ni(BPEBF$_4$)]** is able to adsorb the same quantity of CO_2 as **[Ni(BPEB)]**.

4.4.8 Pore size distribution

By exploiting the N_2 adsorption isotherm at 77 K, it was possible to estimate the pore size distribution of **[Zn(BPEBF$_4$)]** and **[Ni(BPEBF$_4$)]** using the Tarazona method.

The pore distribution found for **[Zn(BPEBF$_4$)]** is centered in the micropore region (2-20 Å) (**Figure 4.12**), as anticipated by crystallographic data. The most intense peak is observed at 6 Å. The smaller pores of the interpenetrated structure are not visible using this analysis: indeed, the width calculated for the small cavities from the crystal structure is 2.1 Å, while the van der Waals radius of N_2 is approximately 3.1 Å. Furthermore, another peak is visible at 10 Å.

The pore distribution found for **[Ni(BPEBF$_4$)]** is centered in the micropore region (2-20 Å) (**Figure 4.12**), as assessed by crystallographic data. The most intense peak is observed at 6 Å.

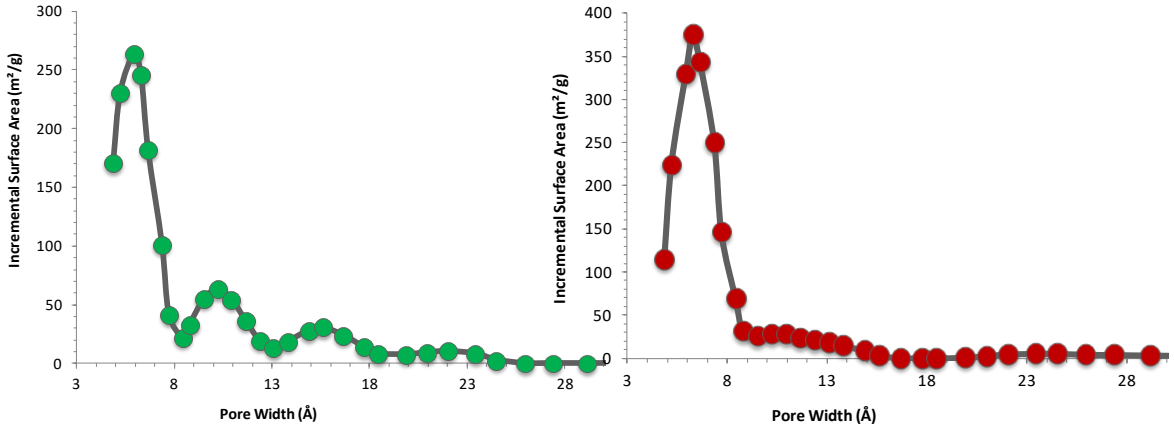

Figure 4.12: Pore size distribution for **[Zn(BPEBF$_4$)]**, left graph, and **[Ni(BPEBF$_4$)]**, right graph.

	[Zn(BPEB)]	**[Zn(BPEBF$_4$)]**	**[Ni(BPEB)]**	**[Ni(BPEBF$_4$)]**
Total pore volume (cm^3/g)	0.60	0.41	1.05	0.67

Table 4.3: Total pore volume for bis-pyrazolate derivatives.

The values obtained for both MOFs enable us to estimate the total pore volume of the two MOFs, the values of which are listed in **Table 4.3**. For the sake of completeness, the values of **[Zn(BPEB)]** and **[Ni(BPEB)]** are reported.

The total pore volume of **[Zn(BPEBF$_4$)]** (0.41 cm^3/g) is lower than that of **[Zn(BPEB)]** (0.60 cm^3/g). This slight difference could be ascribed to the steric hindrance of the four fluorine atoms and to the different degree of crystallinity of the two materials.

The total pore volume of **[Ni(BPEBF$_4$)]** is considerably lower than that of **[Ni(BPEB)]**, 0.67 and 1.05 cm^3/g, respectively. In this case, as already supposed, the difference may be bestowed to the different degree of crystallinity of the two materials.

4.5 Conclusions

Though these results demonstrate that FMOFs and FN-PCPs are definitely promising as low-κ materials, improvements are needed to meet thermal stability requirements, and further investigation is necessary to unravel the mechanical properties in functional forms (i.e. thin films on Ta or W, their nitrides, or Cu).

Moreover, FMOFs show interesting behaviour as adsobents of CO_2 and other gases and guest molecules, as shown by the comparison with isostructural non-fluorinated counterparts. These features enable us to assert that the substitution of hydrogen atoms with fluorine atoms has a positive impact upon CO_2 uptake in the resulting FMOFs. The presented results were thought as a preliminary investigation of the behaviour of FMOFs as adsorbent of gasses. As an obvious consequence, more studies will be performed in order to better describe the functional properties of these materials, starting from the evaluation of the host-guest interaction energies for CO_2, and CO_2 adsorption in wet conditions, in order to better evaluate the hydrophobic effect of fluorine. In connection with these latter experiments, the measurements of the contact angle and of the dielectric constant for the pyrazole-based MOFs will be performed.

References and Notes

[1] a) Martin, S. J.; Godschalx, J. P.; Mills, M. E.; Schaffer, E. O. and Townsend, P. H. *Adv. Mater.*, **2000**, *12*, 1769; b) Wang, W. C.; Vora, R. H.; Kang, E.: Neoh, K. G.; Ong, C. K. and Chen, L. F. *Adv. Mater.*, **2004**, *16*, 54; c) Volksen, W.; Miller, R. D. and Dubois, G. *Chem. Rev.,* **2010,** *110,* 56–110.

[2] Chiang, C.-C.; Chen, M.-C.; Li, L.-J.; Wu, Z.-C.; Jang, S.-M. and Liang, M.-S. *J. Electrochem. Soc.*, **2004**, *151*, G612-G617.

[3] a) Teflon PTFE Handbook, DuPont, 220313D Printed in U.S.A.;
b) http://www.clippercontrols.com/pages/Dielectric-Constant-Values.html

[4] a) Smith, D. M.; Johnston, G.P.; Ackerman, W. C.; Jeng, S.-P. and Gnade, B. E. U.S. Pat. 6,437,007 B1 **2002**; b) Smith, D. M.; Johnston, G.P.; Ackerman, W. C.; Stoltz, R. A.; Maskara, A.; Ramos, T.; Jeng, S.-P. and Gnade, B. E. U.S. Pat. 6,645,878 B2, **2003**.

[5] Eslava, S.; Zhang, L.; Esconjauregui, S.; Yang, J.; Vanstreels, K.; Baklanov, M. R. and Saiz, E. *Chem. Mater.*, **2013**, *25*, 27−33.

[6] http://www.itrs.net. International Technology Roadmap of Semiconductors (ITRS), 2013/2011/2009 Editions.

[7] a) Yang, C.; Wang, X. and Omary, M. A. *J. Am. Chem. Soc.*, **2007**, *129*, 15454-15455; b) Yang, C.; Wang, X. and Omary, M. A. *Angew. Chem. Int. Ed.*, **2009**, *48*, 2500-2505; c) Yang, C.; Kaipa, U.; Mather, Q. Z.; Wang, X.; Nesterov, V.; Venero, A. F. and Omary, M. A. *J. Am. Chem. Soc.*, **2011**, *133*, 18094; d) Nijem , N.; Canepa, P.; Kaipa, U.; Tan, K.; Roodenko, K.; Tekarli, S. M.; Halbert, J.; Oswald, I. W. H.; Arvapally, R. K.; Yang, C.; Thonhauser, T.; Omary, M. A. and Chabal, Y. J. *J. Am. Chem. Soc.*, **2013**, *135*, 12615; e) Yang, C. and Omary, M. A. U.S. Pat. 8,343,260 **2013**; f) Yang, C. and Omary, M. A. U.S. Pat. 8,715,395, **2014**; g) Yang, C.; Arvapally, R. K.; Tekarly, S. M.; Salazar, G. A.; Elbjeirami, O.; Wang, X. and Omary, M. A. *Angew. Chem. Int. Ed.*, **2015**, *54*, 4842.

[8] a) Colombo, V.; Galli, S.; Choi, H. J.; Han, G. D.; Maspero, A.; Palmisano, G.; Masciocchi, N. and Long, J. R. *Chem. Sci.*, **2011**, *2*, 1311- 1319; b) Quartapelle Procopio, E.; Rojas, S.; Padial, N. M.; Galli, S.; Masciocchi, N.; Linares, F.; Miguel, D.; Oltra, J. E.; Navarro, J. A. R. and Barea, E. *Chem. Commun.*, **2011**, *47*, 11751- 11753; c) Colombo, V.; Montoro, C.; Maspero, A.; Palmisano, G.; Masciocchi, N.; Galli, S.; Barea, E. and Navarro, J. A. R. *J. Am. Chem. Soc.*, **2012**, *134*, 12830-12843; d) Tabacaru, A.; Galli, S.; Pettinari, C.; Masciocchi, N.; McDonald, T. M. and Long, J. R. *CrystEngComm*, **2015**, *17*, 4992-5001.

[9] a) Zagorodniy, K.; Seifert, G. and Hermann, H. *Appl. Phys. Lett.*, **2010**, *97*, 251905; b) Allendorf, M. D.; Schwartzberg, A.; Stavila, V. and Talin, A. A. *J. Chem. Soc.*, **2010**, *17*, 11372-11388; c) Usman, M.; Lee, C.-H.; Hung, D.-S.; Lee, S.-F.; Wang, C.-C.; Luo, T.-T.; Zhao, L.; Wu, M.-K. and Lu, K.-L. *J. Mater. Chem. C*, **2014**, *2*, 3762-3768; d) Warmbier, R.; Quandt, A. and Seifert, G. *J. Phys. Chem. C*, **2014**, *118*, 11799-11805; e) Yu, S.-S.; Yuan, G.-J. and Duan, H-.B. *RSC Adv.*, **2015**, *5*, 45213; f) Guo, H.; Wang, M.; Liu, J.; Zhu, S. and Liu, C. *Microporous and Mesoporous Mat.*, **2016**, *221*, 40-47.

[10] Dincă, M.; Yu, A. F. and Long, J. R. *J. Am. Chem. Soc.*, **2006**, *128*, 8904-8913.

[11] Maspero, A.; Galli, S.; Colombo, V.; Peli, G.; Masciocchi, N.; Stagni, S.; Barea, E.; Navarro, J. A. R. *Inorg. Chim. Acta*, **2009**, *362*, 4340–4346.

[12] Stern, N. *Stern Review on the Economics of Climate Change*, Cambridge University Press, Cambridge, **2006**.

[13] Metz, B.; Davidson. O.; de Coninck, H.; Loos, M.; Meyer, L.; *Intergovernmental Panel on Climate Change. Special Report on Carbon Dioxide Capture and Storage*, Cambridge University Press, Cambridge, **2005**.

[14] *Electric Power Research Institute, Program on Technology Innovation: Post-combustion CO_2 Capture Technology Development*, Electric Power Research Institute, Palo Alto, **2008**.

[15] D'Alessandro, D. M.; Smit, B. and Long, J. R. *Angew. Chem. Int. Ed.*, **2010**, *49*, 6058–6082

[16] Abu-Khader, M. M. *Energy Sources Part A*, **2006**, 28, 1261.

[17] a) Smiglak, M.; Metlen, A. and Rogers, R. D. *Acc. Chem. Res.*, **2007**, *40*,1182; b) Radosz, M.; Hu, X.; Krutkramelis, K. and Shen, Y. *Ind. Eng. Chem. Res.*, **2008**, *47*, 3783.

[18] a) Yong, Z.; Mata, V. and Rodrigues, A. E. *Sep. Purif. Technol.* **2002**, *26*, 195; b) Aaron, D. and Tsouris, C. *Sep. Sci. Technol.* **2005**, *40*, 321; c) Harlick, P. J. E. and Sayari, A. *Ind. Eng. Chem. Res.* **2006**, *45*, 3248; d) Figueroa, J. D.; Fout, T.; Plasynski, S.; McIlvried, H. and Srivastava, R. D. *Int. J. Greenhouse Gas Control*, **2008**, *2*, 9; S; e) Radosz, M.; Hu, X.; Krutkramelis, K. and Shen, Y. *Ind. Eng. Chem. Res.* **2008**, *47*, 3783; f) Lee, K. B.; Beaver, M. G.; Caram, H. S. and Sircar, S. *Ind. Eng. Chem. Res.* **2008**, *47*, 8048; g) Choi, S.; Drese, J. H. and Jones, C. W. *ChemSusChem* **2009**, *2*, 796.

[19] a) Hiyoshi, N.; Yogo, D. K. and Yashima, T. *Chem. Lett.* **2004**, *33*, 510; b) Harlick, P. J. E. and Sayari, A. *Ind. Eng. Chem. Res.* **2006**, *45*, 3248; c) Hicks, J. C.; Drese, J. H.; Fauth, D. J.; Gray, M. L.; Qi, G. and Jones, C. W. *J. Am. Chem. Soc.* **2008**, *130*, 2902.; d) Lee, S.; Filburn, T. P.; Gray, M.; Park, J.-W. and Song, H.-J. *Ind. Eng. Chem. Res.* **2008**, *47*, 7419.

[20] Pachfule, P.; Chen, Y.; Jiang, J. and Banerjee, R., *Chem. Eur. J.*, **2012**, 18, 688–694.
[21] Wang, H.-H.; Guo, T.-T., Xie, D.; Bai, Z.-Q.; Hou, L. and Wang, Y.-Y. *Eur. J. Inorg. Chem.*, **2015**, 5773–5780.
[22] Galli, S.; Maspero, A.; Giacobbe, C.; Palmisano, G.; Nardo, L.; Comotti, A.; Bassanetti, I.; Sozzani, P. and Masciocchi, N. *J. Mater. Chem. A*, **2014**, *2*, 12208-12221.
[23] Xue, M.; Liu, Y.; Schaffino, R. M.; Xiang, S.; Zhao, Zhu, X. G.-S.; Qui, S.-L. and Chen, B. *Inorg. Chem.*, **2009**, *48*, 4649.
[24] Miller, S. R.; Wright, P. A.; Devic, T.; Serre, C.; Ferey, G.; Llewellyn, P. L.; Denoyel, R.; Gaberova, L. and Filinchuk, Y.; *Langmuir*, **2009**, *25*, 3618.
[25] a) Ma, B.-Q.; Mulfort, K. L. and Hupp, J. T. *Inorg. Chem.*, **2005**, *44*, 4912; b) Mulfort, K. L. and Hupp, J. T. *J. Am. Chem. Soc.*, **2007**, *129*, 9604; c) Bae, Y. S.; Mulfort, K. L.; Frost, H.; Ryan, P.; Punnathanam, S.; Broadbelt, L. J., Hupp, J. T. and Snurr, R. Q. *Langmuir*, **2008**, *24*,8592.
[26] a) Wang, Q. M.; Shen, D.; Bülow, M.; Lau, M. L.; Deng, S.; Fitch, F. R.; Lemcoff, N. O. and Semanscin, J. *Microporous Mesoporous Mater.*, **2002**, *55*, 217; b) Millward, A. R. and Yaghi, O. M. *J. Am. Chem. Soc.*, **2005**, *127*, 17998; c) Chowdhury, P.; Bikkina, C.; Meister, D.; Dreisbach, F. and Gumma, S. *Microporous Mesoporous Mater.*, **2009**, *117*, 406; d) Liang, Z.; Marshall, M. and Chaffee, A. L. *Energy Fuels*, **2009**, *23*,2785.
[27] Llewellyn, P. L.; Bourrelly, S.; Serre, C.; Vimont, A.; Daturi, M.; Hamon, L.; Weireld, G.; Chang, J.-S.; Hong, D.-Y.; Hwang, Y. K.; Jhung, S. H. and Ferey, G. *Langmuir*, **2008**, *24*, 7245.
[28] Miller, S. R.; Pearce, G. M.; Wright, P. A.; Bonino, F.; Chavan, S.; Bordiga, S.; Margiolaki, I.; Guillou, N.; Ferey, G.; Bourrelly, S. and Llewellyn, P. L. *J. Am. Chem., Soc.*, **2008**, *130*, 15967.
[29] a) Caskey, S. R.; Wong-Foy, A. G. and Matzger, A. *J. Am. Chem. Soc.*, **2008**, *130*, 10870; b) Dietzel, P. D. C.; Besikiotis, V. and Blom, R. *J. Mater. Chem.*, **2009**, *19*, 7362; c) Britt, D.; Furukawa, H.; Wang, B.; Glover, T. G. and Yaghi, O. M. *Proc. Natl. Acad. Sci. USA*, **2009**, *106*, 20637.
[30] Chen, B.; Ma, S.; Hurtado, E. J.; Lobkovsky, E. B. and Zhou, H.-C. *Inorg. Chem.*, **2007**, *46*, 8490.
[31] Cheon, Y. E. and Suh, M. P. *Chem. Eur. J.*, **2008**, *14*, 3961.
[32] Cheon, Y. E.; Park, J. and Suh, M. P. *Chem. Commun.*, **2009**, 5436.
[33] Bourrelly, S.; Llewellyn, P. L.; Serre, C.; Millange, F.; Loiseau, L. and Férey, G. *J. Am. Chem. Soc.*, **2005**, *127*, 13519.
[34] Galli, S.; Masciocchi, N.; Tagliabue, G.; Sironi, A.; Navarro, J. A. R.; Salas, J. M.; Mendez-Linan, L.; Domingo, M.; Perez, M. and Barea, E. *Chem. Eur. J.*, **2008**, *14*, 9890.
[35] a) Choi, H.-S. and Suh, M. P. *Angew. Chem.*, **2009**, *121*, 6997; b) Choi, H.-S. and Suh, M. P. *Angew. Chem. Int. Ed.*, **2009**, *48*, 6865.
[36] Bae, Y.-S.; Farha, O. K.; Hupp, J. T. and Snurr, R. Q. *J. Mater. Chem.*, **2009**, *19*, 2131.
[37] Neofotistou, E.; Malliakas, C. D. and Trikalitis, P. N. *Chem. Eur. J.*, **2009**, *15*, 4523.
[38] a) Comotti, A.; Bracco, S.; Sozzani, P.; Horike, S.; Matsuda, R.; Chen, J.; Takata, M.; Kubota, Y. and Kitagawa, S. *J. Am. Chem. Soc.*, **2008**, *130*, 13664; b) Couck, S.; Denayer, J. F. M.; Baron, G. V.; Remy, T.; Gascon, J. and Kapteijn, F. *J. Am. Chem. Soc.*, **2009**, *131*, 6326.
[39] Keith, D. W.; Minh, H.-D.; and Stolaroff, J. K. *Clim. Change*, **2006**, *74*, 17.
[40] Cheary, R. W. and Coelho, A. J. *J. Appl*. Cryst., **1992**, *25*, 109-121.
[41] http://imagej.nih.gov/ij/
[42] Joule, J. A. and Mills, K *Heterocyclic Chemistry* Fifth Ed., John Wiley & Sons, Ltd. **2010**.
[43] a) Vermoortele, F.; Bueken, B.; Le Bars, G.; Van de Voorde, B.; Vandichel, M.; Houthoofd, K.; Vimont, A.; Daturi, M.; Waroquier, M.; Van Speybroeck, V.; Kirschhock, C. and De Vos, D. E. *J. Am. Chem. Soc.*, **2013**, *135*, 11465-11468; b) Wu, H.; Chua, Y. S.; Krungleviciute, V.; Tyagi, M.; Chen, P.; Yildirim, T. and Zhou, W. *J. Am. Chem. Soc.*, **2013**, *135*, 10525-10532; c) Shearer, G. C.; Chavan, S. M.; Ethiraj, J.; Vitillo, J. G.; Svelle, S.; Olsbye, U.; Lamberti, C.; Bordiga, S. and Lillerud, K. P. *Chem. Mater.*, **2014**, *26*, 4068-4071; d) Øien, S.; Wragg, D.; Reinsch, H.; Svelle, S.; Bordiga, S.; Lamberti, C. and Lillerud, K. P. *Cryst. Growth Des.*, **2014**, *14*, 5370-5372.
[44] Tao, Y.; Kanoh, H.; Abrams, L. and Kaneko, K. *Chem. Rev.*, **2006**, *106*, 896.
[45] Kitaura, R.; Matsuda, R., Kubota, Y.; Kitagawa, S.; Takata, M.; Kobayashi, T. C. and Suzuki, M *J. Phys. Chem. B*, **2005**, *109*, 23378.
[46] Li, D. and Kaneko, K. *J. Phys. Chem. B*, **2000**, *104*, 8940.
[47] a)Choi, S. B.; Furukawa, H.; Nam, H. J.; Jung, D. Y.; Jhon, Y. H.; Walton, A.; Book, D.; O'Keeffe, M.; Yaghi, O. M. and Kim, J. *Angew. Chem. Int. Ed.*, **2012**, *51*, 8791; b) Yang, S.; Lin, X.; Lewis, W.; Suyetin, M.; Bichoutskaia, E.; Parker, J. E.; Tang, C. C.; Allan, D. R.; Rizkallah, P. J. ; Hubberstey, P.; Champness, N. R.; Thomas, K. M.; Blake, A. J. and Schroder, M. *Nat. Mater.*, **2012**, *11*, 710; c) Bloch, W. M.; Babarao, R.; Hill, M. R.; Doonan C. J. and Sumby, C. J. *J. Am. Chem. Soc.*, **2013**, *135*, 10441; d) Chen, Q.; Chang, Z.; Song, W.-C.; Song, H.; Song, H.-B.; Hu,

T.-L. and Bu, X.-H. *Angew. Chem., Int. Ed.*, **2013**, *52*, 11550; e) Aggarwal, H.; Bhatt, P. M.; Bezuidenhout, C. X. and Barbour, L. J. *J. Am. Chem. Soc.*, **2014**, *136*, 3776; f) Zhou, D.-D.; Liu, Z.-J.; He, C.-T.; Liao, P.-Q.; Zhou, H.-L.; Zhong, Z.-S.; Lin, R.-B.; Zhang, W.-X; Zhang, J.-P. and Chen, X.-M. *Chem. Commun.,* **2015**, *51*, 12665-12668.

Chapter 5
Metal-organic framework as molecular rotors

5.1 Introduction

The term “molecular rotor” is commonly used to describe particular molecules constructed of two parts that can freely rotate relatively to each other around the same axis[1]. The whole molecule can be divided into three parts: the stator, the rotator and the axle. The stator is commonly viewed as the part with the highest moment of inertia, while the rotator is the part with the smallest one: consequently, as their name already suggests, the stator is the stationary part of the molecular rotor, while the rotator is the mobile part. This distinction is ambiguous because, in the absence of a rigid macroscopic framework, both the rotator and the stator turn around a common axis. Only if the stationary part is fixed on or within a massive object, the definition is completely unambiguous. The last component of the molecular rotor is the axle of rotation about which the rotator turns.

The scientific interest on molecular rotors has arisen from the observation of natural systems. The natural compound typically employed to describe a molecular rotor is the enzyme ATP synthase[2] (**Figure 5.1**). This enzyme is responsible for the production of adenosine triphosphate (ATP), the “molecular unit of currency” of intracellular energy transfer. Its mode of operation is based on the rotation of the *γ, ε* and *c* subunits relatively to the rest of the enzyme. The aim of the research on molecular rotors is to exploit this working principle to build artificial molecular machines able to perform various tasks. At the present time, the artificial molecular rotors are way simpler than ATP synthase.

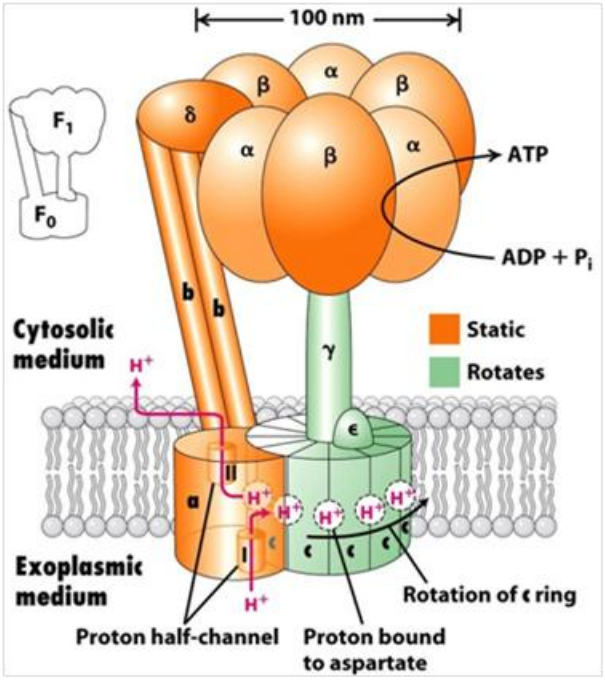

Figure 5.1: Schematic structure of the enzyme ATP synthase[3].

By now, the systems most extensively studied as molecular rotors are built up with an aromatic core, which acts as the rotator, connected with two bulky groups, which act as the stators. This molecular structure provides enough free space for the unhindered rotation of the rotator. As a general rule, bigger stators allow higher rotational frequencies[4] (**Figure 5.2**). In order to obtain higher rotational frequencies, triple C-C bonds can be fruitfully added between the rotator and the stator to fabricated a longer axle. Triple C-C bonds are suitable for this role because it has been demonstrated[5] that the rotation around an alkyne group is almost barrier-less; thus, they can greatly enhance the rotational frequencies.

Derivatives of the compounds shown in **Figure 5.2**, containing a substituent group on the aromatic core, such as a fluorine atom or a $–NH_2$ group, have also been reported[6]. The presence of a substituent on the rotator induces an asymmetry in the electronic density distribution of the ring, generating an electric dipole moment the movement of which can be influenced by external electric fields. Moreover, the dielectric properties of the material depend upon the orientation of the dipoles. Unfortunately, each rotator is completely isolated from the environment by the bulky

stators. This drawback prevents the free access to the rotators from the outside, which limits the applicability of molecular rotors in functional materials.

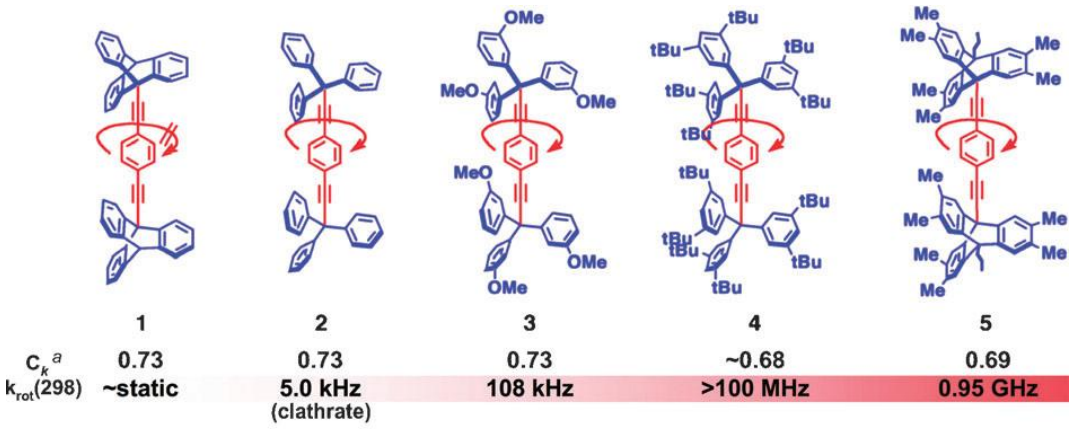

Figure 5.2: Typical molecular structure of single-molecule rotors and their rotational frequencies[7].

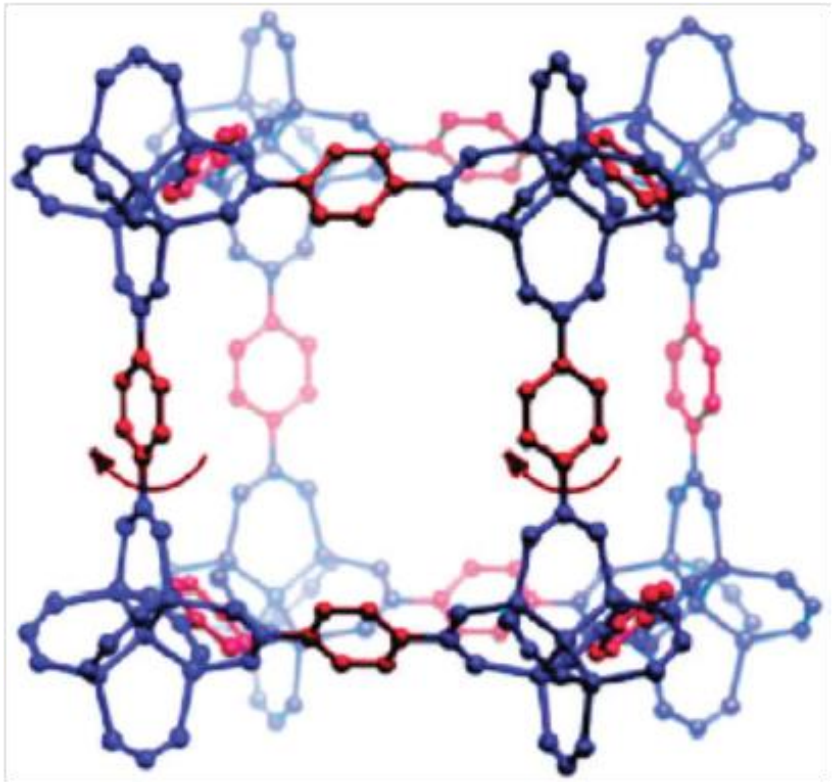

Figure 5.3: Portion of the crystal structure of MOF-5 visualized as an ordered array of rotors.

More recently, the idea of integrating molecular rotors in organic linkers for the synthesis of MOFs has emerged: due to the high porosity typical of MOFs, the rotators possess enough space to rotate; moreover, the intrinsic rigidity of the structure of the MOF act as an ideal stator for a collection of rotators. In order to demonstrate the possibility of building molecular rotors in MOF materials, the dynamics of the ligands in MOF-5[8] (**Figure 5.3**) was studied *via* variable temperature solid state NMR experiments[9]. Due to the structural features of MOF-5, the rotator possesses enough free space to rotate without steric hindrance. Since the rotational barrier can be viewed as a measure of the facility of rotation, the activation barrier for the rotation of the aromatic core in MOF-5 is much higher than that found for molecular systems like those shown in **Figure 5.2**, due to the lack of triple C-C bonds between the stator and the rotator. As a consequence, rotation of the aromatic core in MOF-5 can happen only at high temperature[9]. A similar result[10] has been found for MIL-47(V)[11] and MIL-53(Cr)[12].

Fast rotation of molecular rotors in porous systems has been reported for Periodic Mesoporous Organosilicates (PMOs)[13], Porous Aromatic Frameworks (PAFs)[14] and Porous Molecular Crystals (PMCs)[15]. Very recently a novel PMO containing ultra-fast dipolar molecular rotors has been reported[13c]. The reported materials represent interesting examples of functional porous materials containing molecular rotors. However, very few MOFs containing molecular rotors have been reported up to now in the literature and even fewer containing dipolar rotors. To the best of our knowledge, MOFs containing molecular rotors the dynamics of which can compete with those of molecular systems, PMOs or PAFs, do not exist. As will be illustrated in the following, the new MOFs studied during this Thesis work show an ultra-fast rotational dynamics of the aromatic core (molecular rotors) and fluorinated aromatic core (dipolar rotors) in MOFs.

5.2 Experimental Details

5.2.1 Synthesis of α-[Zn(BPEB-*d4*)]

H_2BPEB-*d4* (0.050 g, 0.19 mmol) was added to a 10-mL microwave vessel containing Py (5 mL). The mixture was stirred until complete dissolution of the ligand: an orange solution was obtained. Then, $Zn(ClO_4)_2 \cdot 6H_2O$ (0.067 g, 0.18 mmol) was added in a single portion. Finally, TEA (0.3 mL) was added dropwise; the upper part of the solution became transparent and a yellow precipitate was formed as soon as TEA entered the solution. The mixture was irradiated (300 W) till the temperature reached 100 °C and kept in this condition for 35 min. Then the reaction vessel was cooled down to 50 °C and the mixture was filtered to recover a yellow solid which was washed with Py (2 mL) and MeOH (10 mL). Then, the product was dried *in vacuo* at 130 °C overnight affording the title compound as an orange solid. (0.050 g, 80%). IR (ATR, cm^{-1}): 2217 (m), 1560 (m), 1433 (s), 1382 (s), 1338 (m), 1233 (m), 1161 (w), 1057 (vs), 1011 (s), 855 (s), 738 (m), 723 (s), 637 (vs). Elem. Anal. Calc. for $C_{16}H_4D_4N_4Zn$ (FW = 325.67 g/mol): C, 59.01%, H, 3.71%, N, 17.20%; found C, 58.45%, H, 3.23%, N, 17.56%.

5.2.2 Synthesis of α-[Zn(BPEBF)]

H_2BPEBF (0.050 g, 0.19 mmol) was added to a Schlenk flask containing benzonitrile (5 mL). The reaction mixture was heated up to 100 °C yielding a turbid orange suspension. Then $Zn(NO_3)_2 \cdot 6H_2O$ (0.053 g, 0.18 mmol) was added in a single portion, followed by DBU (0.10 mL); a precipitate was immediately formed. The mixture was heated up to 150 °C and stirred for 4 h. The mixture was slowly cooled down to RT. Then, the pale yellow solid was recovered by filtration and transferred to a small round bottomed flask. MeOH (5 mL) was added and the resulting slurry was stirred for 1 h. The slurry was filtered and dried at 150 °C *in vacuo* for 4 h affording the title compound as a pale yellow solid. (0.047 g, 73%). IR (ATR, cm^{-1}): 2227 (m), 1615 (w), 1543 (m), 1488 (s), 1416 (m), 1384 (m), 1359 (s), 1266 (w), 1237 (w), 1219 (w), 1111 (m), 1063 (s), 1015 (s), 944 (w), 855 (s), 847 (s), 823 (m), 785 (w), 746 (s), 636 (vs). Elem. Anal. Calc for $C_{16}H_7FN_4Zn$ (FW = 339.64 g/mol): C, 56.58%; H, 2.08%; N, 16.50%; found: C, 56.08%, H, 1.89%, N, 16.88%.

5.2.3 Sinthesis of [Ni(BPEBF)]

H_2BPEBF (0.070 g, 0.25 mmol) was added to a 10-mL microwave vessel containing Py (4 mL). The reaction mixture was stirred until complete dissolution of the ligand: a yellow solution was obtained. $Ni(ClO_4)_2 \cdot 6H_2O$ (0.088 g, 0.24 mmol) was added in a single portion. Then, TEA (1 mL) was added dropwise; the upper part of the solution became transparent and an orange precipitate was formed as soon as TEA entered the solution. The mixture was irradiated (300 W) till the temperature reached 100 °C and kept under these conditions for 25 min. Then the reaction vessel was cooled down to 50 °C and the reaction mixture was filtered to recover an orange solid which was washed with Py (2 mL) and MeOH (10 mL). Then, the product was dried *in vacuo* at 100 °C overnight affording the title compound as an orange solid. (0.061 g, 74%). IR (ATR, cm^{-1}): 2208 (s), 1613 (m), 1538 (m), 1484 (s), 1414 (m), 1360 (m), 1269 (w), 1229 (w), 1164 (w), 1106 (w), 1054 (w), 1012 (m), 944 (w), 844 (s), 822 (s), 789 (w), 745 (m), 675 (m), 639 (vs). Elem. Anal. Calc for $C_{16}H_7FN_4Ni$ (FW = 333.69 g/mol): C, 57.32%; H, 2.68%; N, 16.72%; found: C, 57.68%, H, 3.03%, N, 15.42%.

5.2.4 Powder X-ray diffraction structural analysis

Polycrystalline samples of **α-[Zn(BPEB-*d4*)]**, **α-[Zn(BPEBF)]**, and **[Ni(BPEBF)]** were ground in an agate mortar. Then, they were deposited in the hollow of a silicon zero-background plate. After fast preliminary acquisitions in the 2θ range 3-35° for qualitative analysis, diffraction data for structure refinements were collected overnight, at room temperature, in the 2θ range 3-105°, with steps of 0.02°, on a Bruker AXS D8 Advance diffractometer. Tentative unit cell parameters and space groups were adopted based on the isostructurality between **α-[Zn(BPEB-*d4*)]**, **α-[Zn(BPEBF)]** and **α-[Zn(BPEB)]**, **[Ni(BPEBF)]** and **[Ni(BPEB)]** as suggested by a visual comparison of their PXRD patterns. The independent portion of the **$BPEBF^{2-}$** and **BPEB-*d4*$^{2-}$** ligands was described through a rigid, idealized model. [To describe the ligand, the z-matrix formalism was used, imposing idealized bond distances (Å) and angles (°) as follows: C-N, N-N of the penta-atomic ring, 1.36; C-C of the hexa-atomic ring, 1.39; C-F, 1.31; C-D, 0.95; exocyclic C-C, refined in the range 1.45-1.50; penta-atomic

ring internal bond angles, 108; penta-atomic ring external bond angles, 126; hexa-atomic ring bond angles, 120°]. The position of the metal ions and the centre of mass of the ligand were adopted starting from the available structural information for **α-[Zn(BPEB)]**, and **[Ni(BPEB)]**. The structure refinements were carried out by the Rietveld method. In all of the cases, the peak shapes were described with the fundamental parameters approach[16]. The background was modelled by a polynomial function. A refinable, isotropic thermal parameter (B_m) was assigned to the metal atoms; lighter atoms were given an isotropic thermal parameter 2.0 $Å^2$ higher.

5.2.5 Variable-Temperature Powder X-ray Diffraction

Variable-temperature powder X-ray diffraction (VT-PXRD) experiments were performed on as-synthesized **α-[Zn(BPEB-*d4*)]**, **α-[Zn(BPEBF)]**, and **[Ni(BPEBF)]**. As a first experiment, 30-mg samples of the three compounds were ground in an agate mortar and deposited in the hollow of an aluminium sample holder. By means of a custom-made sample heater (Officina Elettrotecnica di Tenno, Ponte Arche, Italy), mounted on a Bruker AXS D8 Advance diffractometer, the samples were heated in air from 30 °C up to decomposition, with steps of 20 °C; a PXRD pattern was acquired at each step, covering a sensible low-to-medium-angle 2θ range. Treating the data acquired before loss of crystallinity by means of a Le Bail parametric refinement enable us to disclose the behaviour of the unit cell parameters as a function of the temperature. Note: when comparing the results of STA and VT-PXRD, the reader must be aware that the thermocouple of the VT-PXRD set-up is not in direct contact with the sample, this determining a slight difference in the temperature at which the same event is detected by the two techniques. The temperatures deriving from STA have to be considered more reliable.

5.3 Results and discussion

5.3.1 Synthesis of fluorinated and deuterated MOFs

As already reported by our group, **[Zn(BPEB)]**[17] can be obtained in two different phases, labelled **α-[Zn(BPEB)]** and **β-[Zn(BPEB)]**, possessing the same formula unit and the same unit cell metrics, but different relative intensities of the low-angle PXRD peaks, indicating a different structure (see **Figure 5.4**). This happens also for the compounds **[Zn(BPEBF)]** and **[Zn(BPEB-*d4*)]**, affording the expected four compounds **α-[Zn(BPEBF)]**, **β-[Zn(BPEBF)]**, **α-[Zn(BPEB-*d4*)]**, and **β-[Zn(BPEB-*d4*)]**, which are isostructural to **α-[Zn(BPEB)]** and **β-[Zn(BPEB)]**. We focused the attention on the synthesis of **α-[Zn(BPEB-*d4*)]** and **α-[Zn(BPEBF)]**, because the crystal structure of the β-phase has not been solved yet, while the structure of the α-phase is known[17].

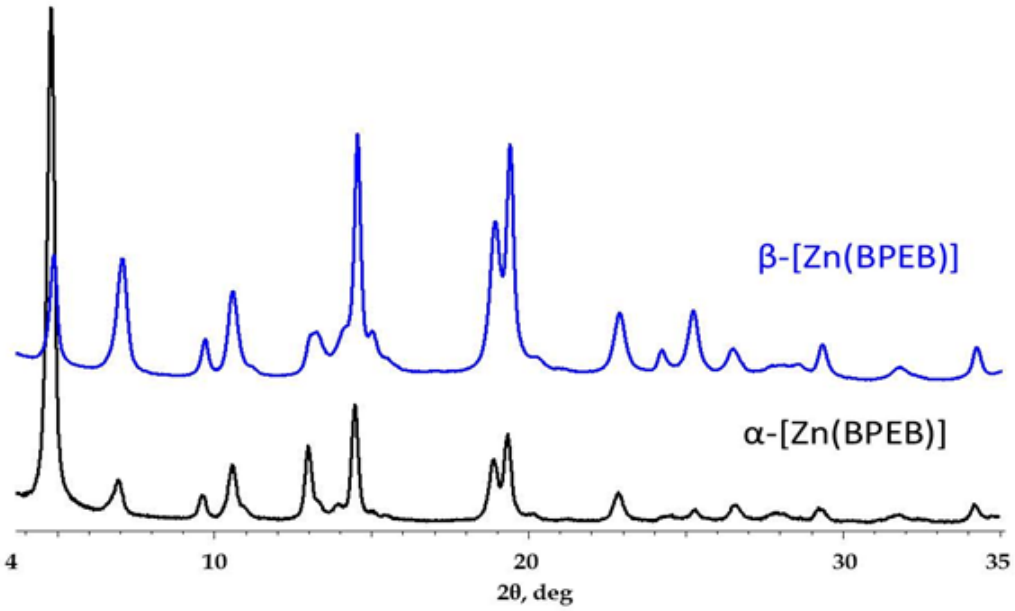

Figure 5.4: Comparison of the PXRD patterns of **α-[Zn(BPEB)]** and **β-[Zn(BPEB)]**.

In order to reach our aim, we tried different reaction conditions, modifying the solvent, the metal salt, the base and the reaction methodology achieving the better synthetic pathways, to the α-phase. Interestingly, for the synthesis of the two Zn(II) derivatives, two different synthetic pathways have been used. **α-[Zn(BPEB-*d4*)]** is prepared in Py at 100 °C using $Zn(ClO_4)_2 \cdot 6H_2O$ as source of Zn(II) ions under microwave irradiation for 35 min. The presence of a small amount of TEA is important to

deprotonate the organic linker, promoting the coordination to the Zn(II) ions. Conversely to **α-[Zn(BPEB-*d4*)]**, **α-[Zn(BPEBF)]** is synthesized following a conventional path, heating at 100 °C and using benzonitrile as solvent and $Zn(NO_3)_2 \cdot 6H_2O$ as source of Zn(II) ions. Also the base used is different: in this case DBU. For the sake of completeness, also the synthesis of the parent compound **α-[Zn(BPEB)]** is different[17]. This occurrence demonstrates how difficult is to predict the synthetic pathway for the synthesis of MOFs. **[Ni(BPEBF)]**, isostructural to **[Ni(BPEB)]**[17], was isolated by reacting $Ni(ClO_4) \cdot 6H_2O$ with **H_2BPEBF** in the presence of a base under microwave irradiation. Also in this case, the synthetic pathway followed is different for the two compounds.

5.3.2 Powder X-ray diffraction structural analysis

α-[Zn(BPEB-*d4*)] and **α-[Zn(BPEBF)]** crystallize in the orthorhombic space group *Cccm*. The asymmetric unit is constituted by one Zn(II) ion and one linker, both in special positions. Each metal centre is coordinated by four nitrogen atoms of four ligands and possesses a distorted tetrahedral stereochemistry (**Figure 5.5**). As expected, the linkers adopt the *exo*-tetradentate coordination mode: the nitrogen atoms of the same pyrazolato moiety bridge nearby metal ions building up 1-D chains of collinear metal centres running along the crystallographic axis *c*. Adjacent chains are connected by the spacers in such a way as to generate two mutually interpenetrated 3-D networks, reciprocally displaced along the crystallographic axis *b*. The interpenetration gave birth to two different type of channels, see **Figure 5.5**.

[Ni(BPEBF)] crystallizes in the orthorhombic space group *Imma*. The asymmetric unit is constituted by one Ni(II) ion and one linker, both in special positions. Each metal centre is coordinated in square-planar stereochemistry by four nitrogen atoms of four $BPEBF^{2-}$ moieties, overall adopting the *exo*-tetradentate coordination mode. Parallel 1-D chains of metal ions can be envisaged (**Figure 5.6**). Along the [0,1,1] direction, each chain is linked to four nearby chains by the spacers, with the consequent formation of a 3-D network possessing large rhombic channels running along the crystallographic axis *a*.

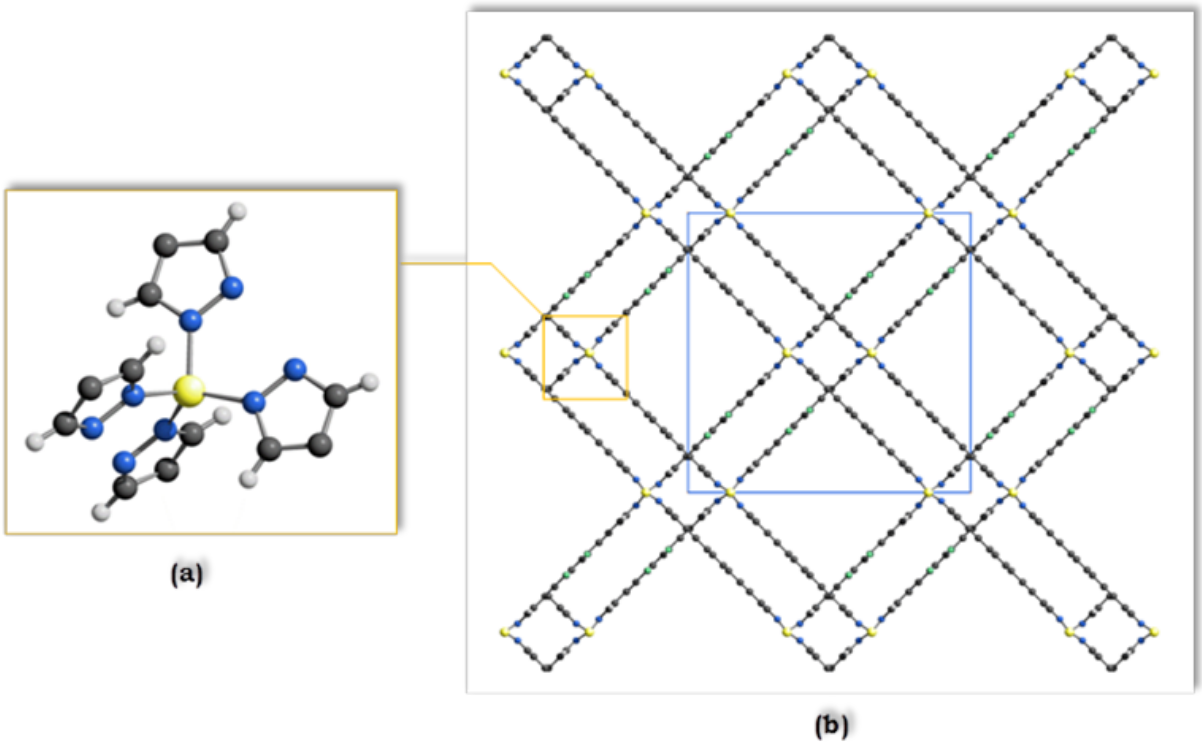

Figure 5.5: Schematic representation of the crystal structure of **[Zn(BPEDF)]**: (a) the tetrahedral coordination of the metal centre; (b) the crystal packing viewed along the crystallographic axis *c* (horizontal axis *a*; vertical axis *b*). The two different types of channels can be clearly distinguished. Carbon, grey; hydrogen, light grey; fluorine, green; nitrogen, blue; zinc, yellow. At the drawing level, **[Zn(BPED-*d4*)]** cannot be distinguished.

5.3.3 Thermal behaviour

As shown by STA and VT-PXRD, **α-[Zn(BPEBF)]** is stable, both under nitrogen and in air, up to 400 °C, temperature at which the decomposition starts. A parametric Le Bail treatment of the VT-PXRD data of **α-[Zn(BPEBF)]** acquired in the range 30-350 °C highlights an overall decrease of the unit cell volume of -1.0%, reasonably due to the loss of the solvent (**Figure 5.7a**).

As unveiled by STA and VT-PXRD, **α-[Zn(BPEB-*d4*)]** is stable, both under nitrogen and in air, up to 400 °C, temperature at which the decomposition starts. A parametric Le Bail treatment of the VT-PXRD data of **α-[Zn(BPEB-*d4*)]** acquired in the range 30-330 °C highlights an overall decrease of the unit cell volume of -1.8% due to solvent loss (**Figure 5.7b**).

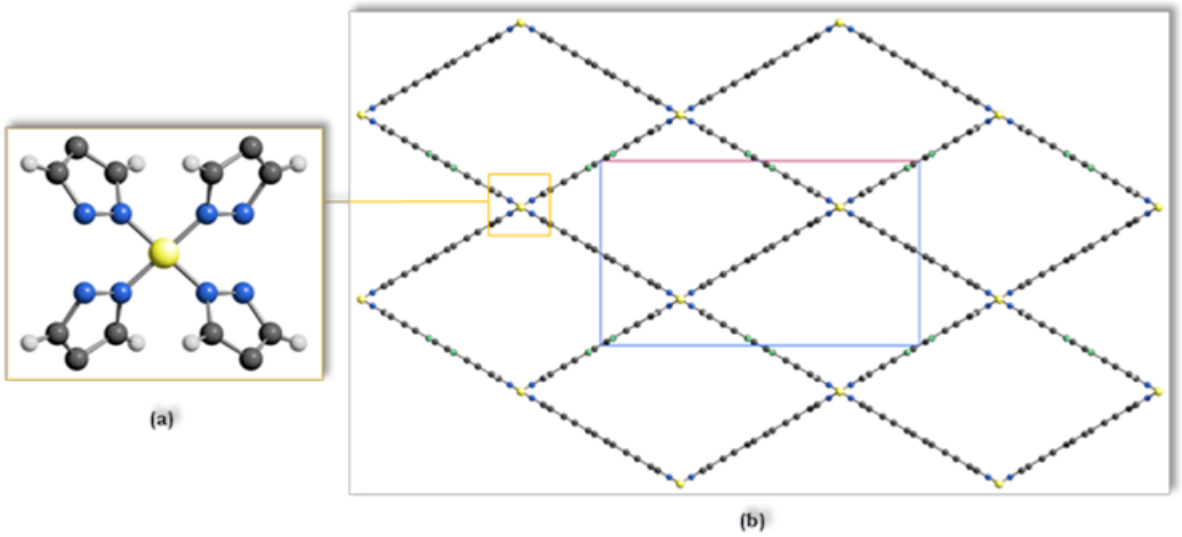

Figure 5.6: Schematic representation of the crystal structure of **[Ni(BPEBF)]**: (a) the square planar coordination sphere of the metal center; (b) the crystal packing, visualized along the crystallographic axis a (horizontal axis *b*; vertical axis *c*). The 1-D rhombic channels can be clearly seen running along *a*. Carbon, grey; hydrogen, light grey; fluorine, green; nickel, yellow; nitrogen, blue.

[Ni(BPEBF)] is stable, both under nitrogen and in air, up to 430 °C, temperature at which the decomposition is complete. The VT-PXRD experiment also highlights that, even if the structure does not collapse or decompose until 430 °C, a progressive loss of crystallinity starts already at 250 °C (**Figure 5.8**).

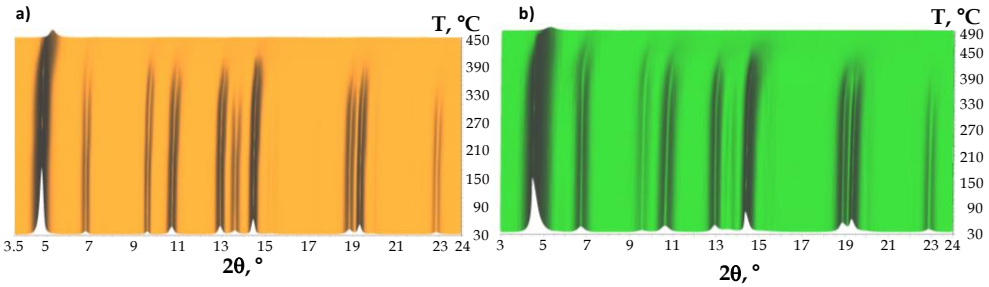

Figure 5.7: VT-PXRD data for a) **α-[Zn(BPEBF)]** and b) **α-[Zn(BPEB-*d4*)]**.

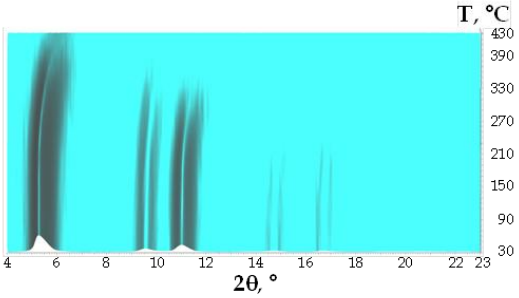

Figure 5.8: VT-PXRD data for **[Ni(BPEBF)].**

5.3.4 Solid State NMR spectroscopy

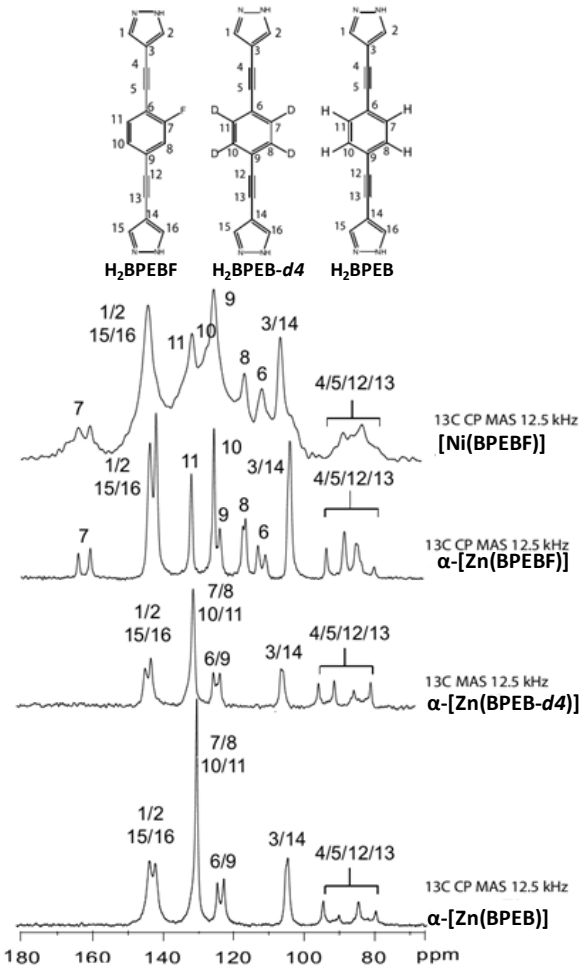

Figure 5.9: ^{13}C solid state MAS NMR spectra of MOFs **[Ni(BPEBF)]**, **α-[Zn(BPEBF)]**, **α-[Zn(BPEB-*d4*)]** and **α-[ZnBPEB]** collected at room temperature.

Solid state NMR analyses have been performed on **α-[Zn(BPEBF)]**, **[Ni(BPEBF)]** and **α-[Zn(BPEB-*d4*)]**. The results are listed in **Table 5.1** and the comparison between the main signals is shown in **Figure 5.9**, where, for the sake of completeness, the spectrum of **α-[Zn(BPEB)]** is also reported. The ^{13}C-NMR signals observed for the MOFs were assigned by comparing them with those of the free ligand in solution (**Table 5.1**). As shown in **Figure 5.9**, the ^{13}C-NMR spectra of **α-[Zn(BPEBF)]** and **α-[Zn(BPEB-*d4*)]** are more clear and resolved than that of **[Ni(BPEBF)]**. This different behaviour is probably due to the different degree of crystallinity of the compounds; indeed, solid state NMR analyses confirm the results obtained with PXRD analyses: the degree of crystallinity of **[Ni(BPEBF)]** is way lower than that of **α-[Zn(BPEBF)]** and **α-[Zn(BPEB-*d4*)]**. Despite the different degree of crystallinity, the ^{13}C-NMR spectra of **α-[Zn(BPEBF)]** and **[Ni(BPEBF)]** show the main features of the organic linker H_2BPEBF. The ^{13}C-NMR spectrum of **α-[Zn(BPEBF)]** shows four signals between 80 and 93 ppm associated to four chemically different alkyne carbons (C4, C5, C12, C13 – see Figure 5.9 and Table 5.1 for the labelling adopted throughout this Section); a single signal is observed at 104 ppm that can be assigned to carbons C3 and C14 of the pyrazole rings. The signals for C6 (111 ppm) and C8 (116 ppm) are doublets, due to the $^2J_{C\text{-}F}$ coupling. The signals at 124, 125 and 132 ppm can be attributed to C9, C10 and C11, respectively. Worthy of note, the carbon atoms belonging to the aromatic core (C6, C7, C8,

C9, C10, and C11) give six different signals because they are chemically non equivalent. At 104 ppm two signals are detected which can be assigned to the couples C1/C2 and C15/C16, which are the CH groups of the pyrazole ring. C7 gives a wide doublet, due to a strong $^{1}J_{C\text{-}F}$ coupling, as it is directly bonded to the fluorine atom. Interestingly, in the solution ^{13}C-NMR spectrum of the ligand, the $^{4}J_{C\text{-}F}$ of C10 is detected, while the $^{3}J_{C\text{-}F}$ coupling of C11 is not. Normally, the reverse situation is expected, because ^{3}J coupling is usually larger than ^{4}J coupling. However, this particular behaviour has been already observed for substituted fluoro-benzene[18].

Oddly, the ^{13}C CP MAS NMR spectrum of **α-[Zn(BPEB-*d4*)]** shows four signals between 79 and 94 ppm assigned to the alkyne carbons. According to the molecular structure of **H_2BPEB-*d4***, only two signals are expected from these atoms: one for the couple C5/C12 and one for the couple C4/C13. This occurrence is explained by analyzing the crystal structure of MOF **α-[Zn(BPEB-*d4*)]**: its asymmetric unit contains four different alkyne carbons, due to interpenetration. Thus, the alkyne carbons give four different signals because they are geometrically non-equivalent. At 104 ppm a signal is observed which can be attributed to carbons C3 and C14, while the two signals at 122 and 129 ppm are assigned to C6 and C9, respectively. Similarly as before, the non-equivalence of these two carbon atoms, due to the interpenetration of the crystal structure, generates two signals instead of one. The intense singlet at 129 ppm can be assigned to carbons C7, C8, C10 and C11. In this case, the non equivalence of the carbon atoms should generate two different peaks; the presence of only one singlet could be explained by assuming the existence of a fast, dynamic mechanism that mediates the two expected signals, demonstrating the fast rotation of the aromatic core. Finally, two peaks at 141 and 143 ppm can be assigned to the couples C1/C2 and C15/C16.

An ^{2}H-NMR spectrum has been collected at room temperature in order to evaluate the mobility of the aromatic core in **α-[Zn(BPEB-*d4*)]** (**Figure 5.10**). The spectrum shows two main peaks at 138 and -138 kHz, typical of a *p*-phenylene system with a very fast rotation.

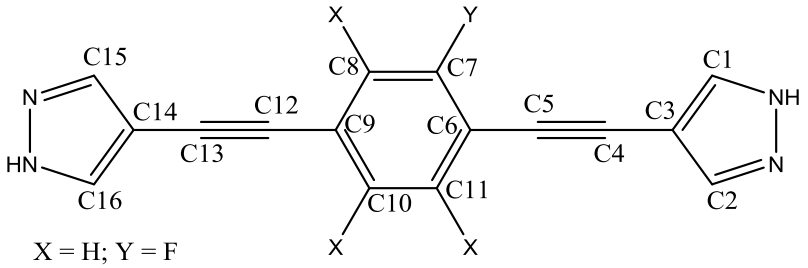

Compound (Type of NMR analysis)					
	H_2BPEBF (solution)	**α-[Zn(BPEBF)]** (solid state)	**[Ni(BPEBF)]** (solid state)	**H_2BPEB-*d4*** (solution)	**α-[Zn(BPEB-*d4*)]** (solid state)
C1	137.2	143.8	144.0	132.1	143.4
C2	137.2	143.8	144.0	132.1	143.4
C3	100.9	104.0	106.4	101.3	104.2
C4	85.6	85.3	83.2	84.5	84.1
C5	89.4	93.7	88.6	89.6	89.9
C6	124.9 $^2J_{C-F}$ = 10	111.0	111.7 $^2J_{C-F}$ = 156	122.8	122.2
C7	160.4 $^1J_{C-F}$ = 248	160.8 $^1J_{C-F}$ = 255	160.5; $^1J_{C-F}$ = 247	131.5 $^1J_{C-D}$ = 23	129.9
C8	118.1 $^2J_{C-F}$ = 22	116.7	116.6 $^2J_{C-F}$ = 53	131.2 $^1J_{C-D}$ = 23	129.9
C9	111.6 $^2J_{C-F}$ = 16	124.0	125.4	131.2 $^1J_{C-D}$ = 23	129.9
C10	127.9 $^4J_{C-F}$ = 3	125.6	127.6	131.2 $^1J_{C-D}$ = 23	129.9
C11	133.7	132.0	131.5	122.8	122.2
C12	89.4	88.6	86.2	89.4	94.1
C13	83.0	80.1	79.0	84.5	79.3
C14	100.9	104.0	106.4	101.3	104.2
C15	137.2	142.1	144.0	132.1	141.8
C16	137.2	142.1	144.0	132.1	141.8

Table 5.1. ^{13}C NMR chemical shifts (ppm) and coupling constants, J (Hz).

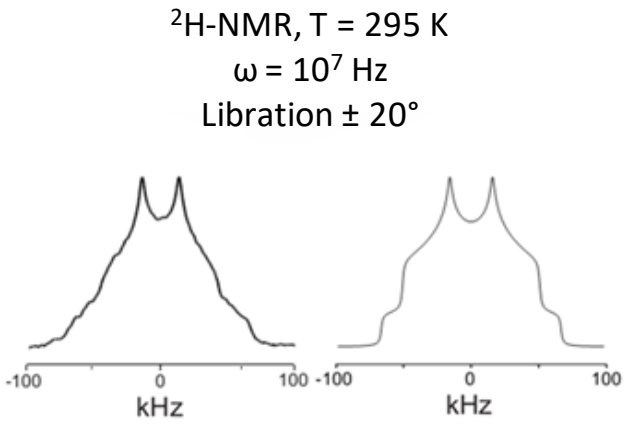

Figure 5.10: Solid state ^{2}H-NMR of **α-[Zn(BPEB-*d4*)]**. Left: the observed signals, collected at room temperature. Right: the simulated spectrum.

The comparison between the experimental signals and those calculated by assuming a 180° flip of the aromatic core and a libration with respect to the equilibrium position of 20° of amplitude highlights a rotational frequency of 10^7 Hz. This result demonstrate the high mobility of the aromatic core in **α-[Zn(BPEB-*d4*)]** already at room temperature. This is a remarkable result because such high mobility of the rotors has never been achieved before in MOFs based on *N*-ligands.

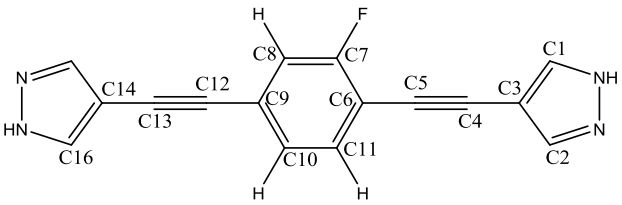

	Chemical shift (ppm)	T1 relaxation times (s)
C1	143.8	17.6
C2	143.8	17.6
C3	104.0	10.3
C4	85.7	15.1
C5	93.7	13.6
C6	111.0	5.5
C7	160.8	4.7
C8	116.7	3.4
C9	124.0	10.7
C10	125.6	3.2
C11	132.0	3.1
C12	88.6	19.2
C13	80.1	
C14	104.0	10.3
C15	142.1	8.8
C16	142.1	8.8

Table 5.2: ^{13}C SS-NMR chemical shifts and T_1 relaxation times for **α-[Zn(BPEBF)]**.

To evaluate the mobility of dipole-containing rotors, the dynamics of the fluoro-substituted aromatic core units of **α-[Zn(BPEBF)]** were explored. In particular, T_1 relaxation times of ^{13}C in **α-[Zn(BPEBF)]** were considered (**Table 5.2**). The short relaxation times, about 3 s, of C7, C8, C10 and C11 confirm that the dipolar rotors in **α-[Zn(BPEBF)]** are very mobile even at room temperature.

A number of applications, based on switchable dielectric, refractive, and optoelectronic properties[1,19], can be developed exploiting this rotational properties. However, in order to achieve these aims, robust materials containing ordered fast-rotating dipoles must be constructed. So far, as discussed in **Section 5.1**, the only example of dipolar rotors in porous materials has been achieved with fluoro-mesoporous organosilicas. Herein, we have presented the first dipolar rotor in robust MOFs. This aim was achieved by a judicious design of an appropriate building block bearing two ethynyl groups, which reduce the rotational barrier of the aromatic core, namely the rotator, and by the high stability of the pyrazolate-based MOFs.

5.3.5 Specific surface area and pore size distribution

The specific surface area of MOFs **[Ni(BPEBF)]**, **α-[Zn(BPEBF)]** and **α-[Zn(BPEB-*d4*)]** are shown in **Table 5.3**. For the sake of completeness, the specific surface area of **[Ni(BPEB)]** and **α-[Zn(BPEB)]** are reported too.

	[Ni(BPEB)]	**[Ni(BPEBF)]**	**α-[Zn(BPEB)]**	**α-[Zn(BPEBF)]**	**α-[Zn(BPEB-*d4*)]**
S_{BET} ($m^2\ g^{-1}$)	1900	949	985	847	1162
$S_{Langmuir}$ ($m^2\ g^{-1}$)	2378	1039	1224	950	1310

Table 5.3: Specific surface area values obtained from N_2 adsorption isotherms collected at 77 K.

The small difference in the values of specific surface area for **α-[Zn(BPEB)]** and **α-[Zn(BPEB-*d4*)]**, calculated with the BET model, indicates that the substitution of hydrogen atoms with deuterium atoms does not affect porosity. The small difference can be ascribed to the different degree of crystallinity, as already discussed in **Chapter 4**. The relatively lower specific surface area found for **α-[Zn(BPEBF)]** cannot be attributed only to a smaller degree of crystallinity of the material, but, principally, to the substitution of one hydrogen atom with one fluorine atom. The latter possesses a larger van der Waals radium: 1.47 Å for fluorine vs. 1.20 Å for hydrogen.

The specific surface area of **[Ni(BPEBF)]** is considerably lower than that of **[Ni(BPEB)]**. In this case, the steric effect of the fluorine atom, alone, cannot explain this huge variation. The difference could be ascribed to the very low degree of crystallinity of **[Ni(BPEBF)]**.

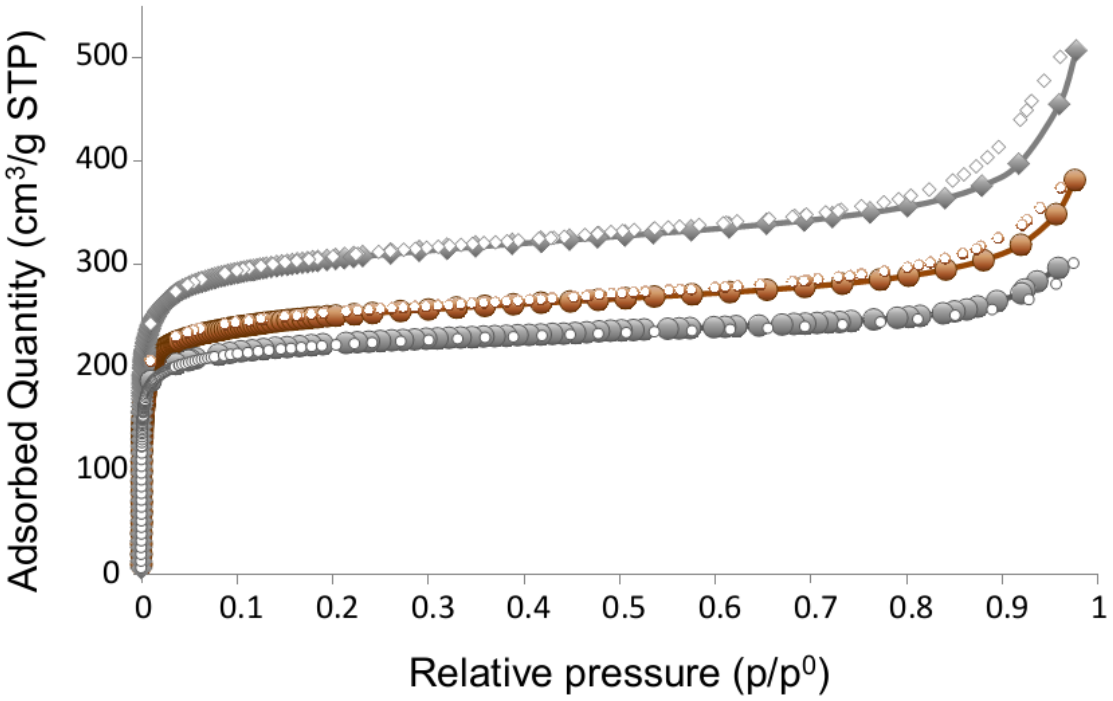

Figure 5.11: N_2 adsorption isotherms at 77 K for **α-[Zn(BPEB-*d4*)]** (grey diamonds), **[Ni(BPEB)]** (brown circles), and **α-[Zn(BPEBF)]** (grey circles). Desorption curves are depicted with hollow symbols.

The pore size distribution for the considered MOFs were calculated using the Tarazona method from the N_2 adsorption isotherms collected at 77 K. The results are shown in **Figure 5.12**.

As expected from the crystal structure, the pore distribution for the three MOFs have its maximum in the micropore region (2-20 Å). In particular, the pore distribution for **α-[Zn(BPEBF)]** and **α-[Zn(BPEB-*d4*)]** (**Figure 5.12a**) is very similar, thus confirming the small modification in pore dimension induced by the introduction of one fluorine atom or four deuterium atoms on the aromatic core.

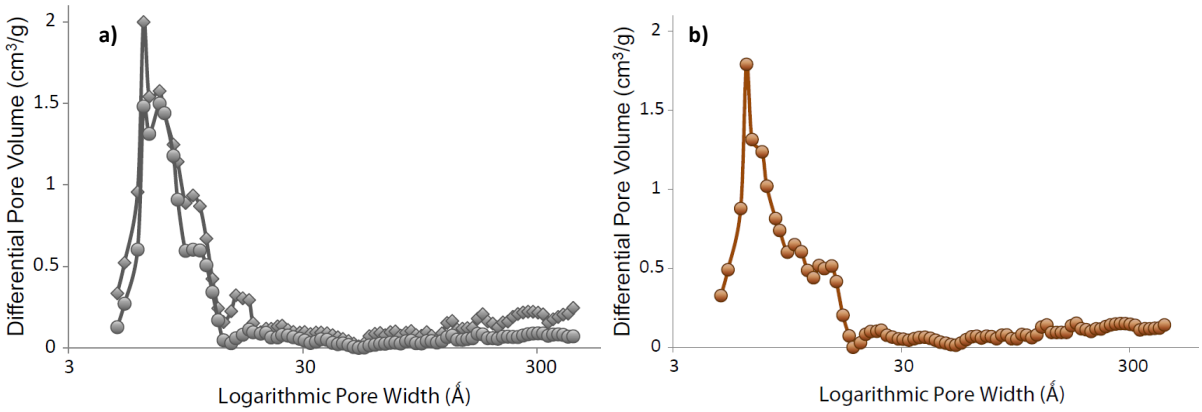

Figure 5.12: Pore size distribution plotted as the differential pore volume in logarithmic scale versus the pore width for compounds **α-[Zn(BPEBF)]** (grey circles), **α-[Zn(BPEB-*d4*)]** (grey diamonds) and **[Ni(BPEBF)]** (brown circles).

A maximum is observed at 8 Å, in agreement with the pore size of the larger channels for the Zn(II) derivatives, while the smallest ones cannot be probed by N_2 adsorption because the van der Waals radius of the N_2 molecule is bigger than the width of the channels, 3.1 Å vs. 2.1 Å. Thus, the N_2 molecule is too large to explore both types of channels of the Zn(II)-based MOFs.

In the case of **[Ni(BPEBF)]**, (**Figure 5.12b**), a maximum is observed at 6.5 Å, in agreement with the structural data obtained by PXRD.

The total pore volume for MOFs **[Ni(BPEBF)]**, **α-[Zn(BPEBF)]** and **α-[Zn(BPEB-*d4*)]** is shown in **Table 5.4**. For the sake of completeness, the values for **[Ni(BPEB)]** and **α-[Zn(BPEB)]** are reported as well.

The total pore volume found for **[Ni(BPEBF)]** is considerably lower than that of **[Ni(BPEB)]** (See **Table 5.4**). This occurrence is in agreement with the lower specific surface area found for **[Ni(BPEB)]**. Furthermore, the pore volume found for the Zn(II)-derivatives reflects the specific surface area values.

	[Ni(BPEB)]	**[Ni(BPEBF)]**	**α-[Zn(BPEB)]**	**α-[Zn(BPEBF)]**	**α-[Zn(BPEB-*d4*)]**
Total pore volumes (cm^3/g)	1.05	0.58	0.60	0.46	0.75

Table 5.4: Total pore volume of Ni(II)- and Zn(II)-based MOFs derived from N_2 adsorption isotherms collected at 77 K and calculated considering a cylindrical pore model and the Tarazona method.

5.4 Conclusions

The specific surface areas of MOFs **Zn(BPEBF)] [Zn(BPEB-*d4*)]**, and **[Ni(BPEBF)]** have been measured through N_2 adsorption at 77 K. In the case of **[Zn(BPEBF)]** and **[Zn(BPEB-*d4*)]** they show values comparable to that of **[Zn(BPEB)]**, confirming that the substitution of one hydrogen atom with one fluorine atom and four hydrogen atoms with four deuterium atoms on the aromatic core does not modify the steric properties of the MOFs towards gas adsorption. On the other hand, the specific surface area for **[Ni(BPEBF)]** is significantly lower than that for **[Ni(BPEB)]**. This behavior could be due to the low degree of crystallinity of **[Ni(BPEBF)]**.

The dynamics of the aromatic core in **[Zn(BPEB-*d4*)]** has been studied by ^{2}H-NMR line shape analysis. The core undergoes fast rotation around the 1,4-axis of the ligand, with frequency around 10^{7} Hz even at room temperature. A 180° flip mechanism is superimposed onto a libration of 20° around the equilibrium position. The fast mobility of the aromatic core of **[Zn(BPEBF)]** has been demonstrated by ^{13}C T_1 relaxation times measurement. Worthy of note, such a high mobility has never been reported before in MOF systems.

References and Notes

[1] Kottas, G. S.; Clarke, l. I.; Horinek, D. and Michl, J. *Chem. Rev.*, **2005,** *105*, 1281-1376.

[2] Boyer, P. D. *Annu. Rev. Biochem.*, **1997**, *66*, 717-749.

[3] Lodish, H.; Berk, A.; Kaiser, C. A.; Krieger, M.; Scott, M. P.; Bretscher, A.; Ploegh, H. and Matsudaira, P. Molecular cell biology, W. H. Freeman and Company, New York, **2007**, ISBN-13: 978-0-716-77601-7.

[4] Godinez, C. E.; Zepeda, G.; Mortko, C. J.; Dang, H and Garcia-Garibay, M. A. *J. Org. Chem.*, **2004**, *69*, 1652-1662.

[5] a) Saebo, S.; Almolof, J.; Boggs J. E. and Stark, J. G. *Theochem*, **1989**, *200*, 361; b) Sipachev, V. A.; Khaikin, L. S.; Grikina, O. E.; Nikitin, V. S. and Traettberg, M. *J. Mol. Struct*., **2000**, *523*, 1.

[6] Dominguez, Z.; Khuong, T.-A. V.; Dang, H.; Sanrame, C. N.; Nunez, J. E. and Garcia-Garibay, M. A. *J. Am. Chem. Soc.*, **2003**, *125*, 8827-8837.

[7] Vogelsberg, C. S. and Garcia-Garibay, M. A. *Chem. Soc. Rev.*, **2012**, *41*, 1892–1910.

[8] a) Li, H.; Eddaoudi, M.; O'Keeffe, M. and Yaghi, O. M. *Nature*, **1999**, *402*, 276-279; b) Kaye, S. S.; Dailly, A.; Yaghi, O. M. and Long, J. R. *J. Am. Chem. Soc.* **2007**, *129*, 14176-14177.

[9] Gould, S. L. ; Tranchemontagne D. ; Yaghi, O. M. and Garcia-Garibay, M. A., *J. Am. Chem Soc.*, **2008**, 130, 11, 3246.

[10] Kolokolov, D. I.; Jobic, H.; Stepanov, A. G.; Guillerm, V.; Devic, T.; Serre, C. and Férey, G. *Angew. Chem. Int. Ed.*, **2010**, *49*, 4791-4794.

[11] a) Barthelet, K.; Marrot, J.; Riou, D. and Férey, G. *Angew. Chem.*, **2002**, *114*, 291; b) Barthelet, K.; Marrot, J.; Riou, D and Férey, G. *Angew. Chem. Int. Ed.*, **2002**, *41*, 281.

[12] (a) Barthelet, K.; Riou, D. and Férey, G. *Chem. Commun.* **2002**, 1492. (b) Serre, C.; Millange, F.; Surblé, S. and Férey, G. *Angew. Chem. Int. Ed.* **2004**, *43*, 6285. (c) Volkringer, C. and Loiseau, T. *Mater. Res. Bull.* **2006**, *41*, 948. (d) Serre, C.; Millange, F.; Thouvenot, C.; Nogues, M.; Marsolier, G.; Louer, D. and Férey, G. *J. Am. Chem. Soc.* **2002**, *124*, 13519. (e) Millange, F.; Guillou, N.; Walton, R. I.; Greneche, J.-M.; Margiolaki, I. and Férey, G. *Chem. Commun.* **2008**, 4732. (f) Millange, F.; Serre, C. and Férey, G. *Chem. Commun.* **2002**, 822.

[13] a) Comotti A.; Bracco S.; Valsesia, P.; Beretta M. and Sozzani, P. *Angew. Chem. Int. Ed.,* **2010**, 49, 10, 1760-1764; b) Vogelsberg, C. S.; Bracco, S.; Beretta, M.; Comotti, A.; Sozzani, P. and Garcia-Garibay M. A., *Phys. Chem. B*, **2012**, *116*, 1623; c) Bracco, S.; Beretta, M.; Cattaneo, A.; Comotti, A.; Falqui, A.; Zhao, K.; Rogers, C. and Sozzani, P. *Angew. Chem. Int. Ed.,* **2015**, *54*.

[14] Comotti, A.; Bracco, S.; Ben, T.; Qiu, S. and Sozzani, P. *Angew. Chem. Int. Ed.,* **2014**, *53*, 1043-1047.

[15] Comotti, A.; Bracco, S.; Yamamoto, A.; Beretta, M.; Hirukawa, T.; Tohnai, N.; Miyata, M. and Sozzani, P. *J. Am. Chem. Soc.*, **2014**, *136*, 618-621

[16] Cheary, R. W. and Coelho, A. J. *J. Appl*. Cryst., **1992**, *25*, 109-121.

[17] Galli, S.; Maspero, A.; Giacobbe, C.; Palmisano, G.; Nardo, L.; Comotti, A.; Bassanetti, I.; Sozzani, P and Masciocchi, N *J. Mater. Chem. A*, **2014**, *2*, 12208-12221.

[18] Rae, I. D. ; Weigold, J. A. ; de Kowaleski, D. G. ; Biekofsky, R. R. and Contreras, R. H. *Magn. Reson. Chem.,* **1996**, *34*, 181-184.

[19] a) Tabe, Y.; Yokoyama, H. *Nat. Mater.*, **2004**, *2*, 806; b) Horinek, D.; Michl, J. *Proc. Natl. Acad. Sci. U.S.A.*, **2005**, *102*, 14175; c) Michl, J. and Sykes, E. C. H. *ACS Nano*, **2009**, *3*, 1042; d) Vogelsberg, C. S. and Garcia-Garibay, M. A. *Chem. Soc. Rev.*, **2012**, *41*, 1892; e) Rodriguez-Velamazan, J. A.; Gonzalez, M. A.; Real, J. A.; Castro, M.; Munoz, M. C.; Gaspar, A. B.; Ohtani, R.; Ohba, M.; Yoneda, K.; Hijikata, Y.; Yanai, N.; Mizuno, M.; Ando, H. and Kitagawa, S. *J. Am. Chem. Soc.*, **2012**, *134*, 5083.

Chapter 6
Adsorbent–adsorbate interactions in the oxidation of HMF catalyzed by Ni-based MOFs: a DRIFT and FT-IR insight

6.1 Introduction

In the past years, MOFs have emerged as successful heterogeneous catalysts for industrial applications[1], replacing traditional all-inorganic porous catalysts such as zeolites. The success of MOFs can be ascribed to the possibility of tuning the functional properties upon modulating the nature of the organic linker and inorganic node. Indeed, MOFs couple the organization of the active catalytic centres, typical of zeolites, with the modulation of the steric and electronic properties of the ligand, affording the best catalytic system for the desired reaction.

The oxidation of hydroxymethylfurfural (HMF) is a key reaction that leads to a number of highly valuable chemicals such as 2,5-diformylfuran (DFF), 5-hydroxymethylfuran-2-carboxylic acid (HMFCA), 5-formyl-2-carboxylic acid (FFCA), and 2,5-furandicarboxylic acid (FDCA)[2] (**Scheme 6.1**), which are key intermediates for various industrial applications. For example, DFF is a precursor in the synthesis of furanic polymers[3], pharmaceuticals, and antifungal agents[4], as well as renewable furan-urea resins[5]. By now, different approaches have been adopted to obtain DFF: *i)* one-pot syntheses directly from fructose, using both homogeneous and heterogeneous catalysts[6] and *ii)* selective oxidation of HMF to DFF, testing a range of oxidizing agents and solvents[2].

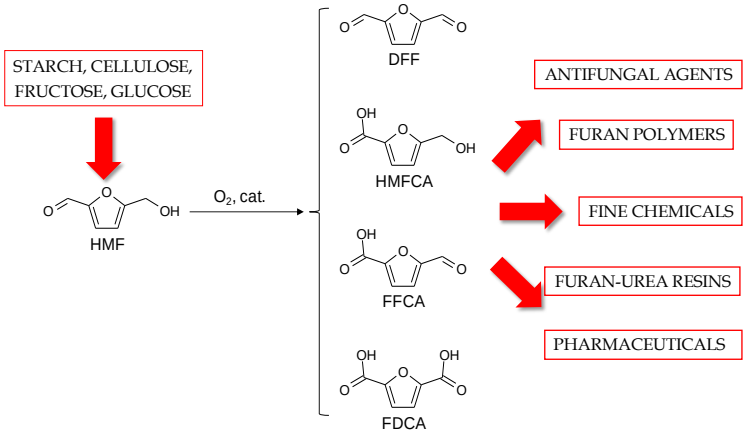

Scheme 6.1: Typical products of HMF catalytic oxydation.

In this context, MOFs were successfully used as scaffold to encapsulate large Bröensted acidic catalysts, for example phosphotungstic acid, $H_3PW_{12}O_{40}$, encapsulated into MIL-101(Cr) $[Cr_3(O)X(BDC)_3(H_2O)_2]$ (H_2BDC = benzene-1,4-dicarboxylic acid, X = OH or F[7]), to be employed in oxidation reactions to prepare HMF from fructose or glucose. In addition, MOFs (*e.g.* MIL-45(Fe,Co) ($K[M_3(BTC)_3]\cdot 5H_2O$, M = Fe and Co), have been used as sacrificial templates to produce the catalyst for the oxidation of HMF to DFF[8]. Nonetheless, to the best of our knowledge, no reports have appeared on the catalytic activity of MOFs for the oxidation of HMF to DFF.

In order to better understand the behaviour of MOFs as catalysts, it is important to rationalize the reaction mechanism, to promote the engineering and synthesis of new, optimized species to be employed as catalysts. Together with the mechanism, it is important to identify the active sites of the catalyst. In this context, DRIFT and FT-IR spectroscopy are a powerful tool, successfully applied in the recent past also in the case of MOFs[9].

As a case of study, the three known Ni-based MOFs, **[Ni(BDP)]**[10], **[Ni(BPEB)]**[11], and **$[Ni_3(BTP)_2]\cdot 3DMF\cdot 5CH_3OH\cdot 17H_2O$** (**$[Ni_3(BTP)_2]\cdot S]$**)[12], [**$H_2BDP$** = 1,4-bis(1*H*-pyrazolyl)benzene; **H_2BPEB** = 1,4-bis-(1*H*-pyrazolylethynyl)benzene; **H_3BTP** = 1,3,5-tris(1*H*-pyrazolyl)benzene, **Figure 6.1**] were tested in the selective oxidation of HMF to DFF. Despite the different structural motifs, the common feature of the three MOFs is the presence of square-planar NiN_4 nodes, potentially accessible when the MOF is thermally activated. As a matter of fact, metal open sites may be involved in adsorbent–adsorbate interactions beneficial for gas adsorption or separation[13] and catalysis[1d,14].

In the following, we report the study of the catalytic performances of the three Ni-based MOFs in the base-free selective oxidation of HMF to DFF by means of DRIFT and FT-IR spectroscopy, with a specific focus on the adsorbent–adsorbate interactions.

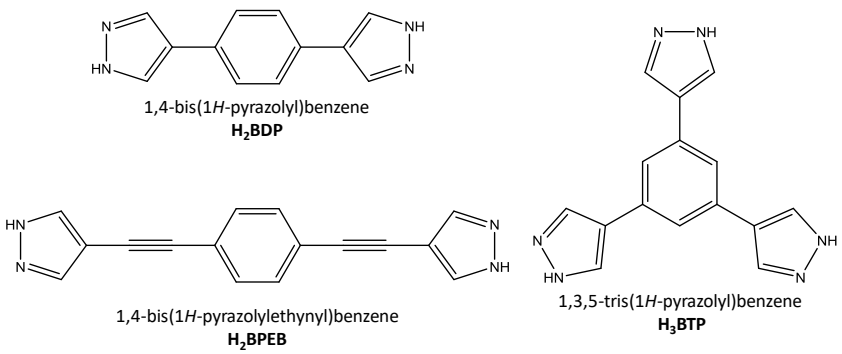

Figure 6.1: Molecular structure of the three poly(pyrazolyl)-based ligands used in this study.

6.2 Experimental Details

The purity of all the batches of MOFs isolated for the present work was assessed by combining elemental analysis, IR spectroscopy, and PXRD.

6.2.1 Synthesis of 1,4-bis(1*H*-pyrazolyl)benzene (H_2BDP)

H_2BDP was prepared following the previously reported synthetic path[15].

IR (KBr, cm^{-1}) 3144 (br), 1583 (w), 1527 (w), 1263 (w), 1236 (w), 1159 (s), 1037 (w), 965 (w), 951 (s), 866 (s), 824 (s), 719 (w), 657 (w), 627 (w). ^{1}H NMR (DMSO-*d6*) (δ, ppm) 7.58 (s, 2H), 8.05 (s, 2H), 12.5 (br s, 1H). ^{13}C NMR (DMSO-*d6*) (δ, ppm) 121.9 (C), 126.3 (HC–Ph), 131.3 (C), 137.0 (HC–pz).

Elem Anal. Calcd for $C_{12}H_{10}N_4$ (FW = 210.2 g/mol) C, 68.56; H, 4.79; N, 26.65%. Found: C, 67.98; H, 4.83; N, 26.26%.

6.2.2 Synthesis of 1,4-bis(1*H*-pyrazolylethynyl)benzene (**H_2BPEB**)

H_2BPEB was synthesized adopting the synthetic route optimized in the recent past[11].

IR(nujol, cm^{-1}) 3169 (br), 2221 (m), 1141 (s), 1101 (w), 1050 (vs), 1037 (vs), 1002 (vs), 992 (vs), 950 (s), 941 (s), 845 (w), 868 (s), 861 (s), 834 (vs), 798 (br), 654 (vs), 620 (vs). ^{1}H NMR (DMSO-*d6*) (δ, ppm) 13.3 (br s, 1H), 8.14 (s, 1H), 7.74 (s, 1H), 7.47 (s, 2H). ^{13}C NMR (DMSO-*d6*) (δ, ppm) 133.2 (CH),

131.6 (CH), 123.0 (C), 101.3 (C), 89.7 (C), 84.5 (C). Elem. Anal. Calcd for $C_{16}H_{10}N_4$ (FW = 258.3 g/mol) C, 74.40; H, 3.91; N, 21.69%. Found: C, 74.08; H, 3.21; N, 21.32%.

6.2.3 Synthesis of 1,3,5-tris(1*H*-pyrazolyl)benzene (H_3BTP)

H_3BTP was isolated through the published procedure[12].

IR (neat, cm^{-1}) 3164 (br), 2941 (br), 1605 (vs), 1371 (w), 1348 (w), 1232 (w), 1158 (s), 1044 (s), 994 (vs), 947 (s), 847 (s), 792 (s), 747 (vs), 690 (w), 656 (s), 619 (vs). ^{1}H NMR (DMSO-*d6*) (δ, ppm) 7.68 (s, 1H), 8.26 (br s, 2H), 12.94 (br s, 1H). Elem. Anal. Calcd for $C_{15}H_{12}N_6$ (FW = 276.3 g/mol) C, 65.21; H, 4.37; N, 30.42%. Found: C, 64.55; H, 4.50; N, 29.97%.

6.2.4 Synthesis of [Ni(BDP)]

[Ni(BDP)] was isolated according to the synthetic procedure recently reported in the literature[10].

Before carrying out the catalytic tests, the as-synthesized batches were thermally activated by heating them for 18 h at 150 °C and 10^{-6} bar.

IR (nujol, cm^{-1}) 1581 (s), 1270 (w), 1178 (w), 1144 (m), 1060 (s), 957 (m), 817 (vs), 723 (w). Elem. Anal. Calcd for $C_{12}H_8NiN_4$ (FW = 266.7 g/mol) C, 54.00; H, 3.02; N, 20.99%. Found: C, 53.70; H, 3.58; N, 20.87%.

6.2.4 Synthesis of [Ni(BPEB)]

[Ni(BPEB)] was isolated according to the synthetic path recently reported in the literature[11].

Before carrying out the catalytic tests and spectroscopic measurements, the as-synthesized samples were thermally activated by heating them for 18 h at 150 °C and 10^{-6} bar.

IR (nujol, cm^{-1}) 2203 (w), 1228 (w), 1164 (w), 1055 (w), 1015 (w), 1007 (w), 840 (w), 769 (w), 719 (w), 638 (w). Elem. Anal. Calcd for $C_{16}H_8NiN_4$ (FW = 315.0 g/mol) C, 60.96; H, 2.54; N, 17.78%. Found: C, 60.48; H, 2.87; N, 17.07%.

6.2.5 Synthesis of $[Ni_3(BTP)_2]\cdot 3DMF\cdot 5CH_3OH\cdot 17H_2O$.

$[Ni_3(BTP)_2]\cdot 3DMF\cdot 5CH_3OH\cdot 17H_2O$ was isolated according to the synthetic path recently reported in the literature[12].

IR (neat, cm^{-1}) 3370 (br), 1655 (s), 1609 (vs), 1557 (w), 1406 (w), 1385 (w), 1361 (w), 1329 (w), 1257 (s), 1196 (w), 1135 (w), 1078 (vs), 1015 (s), 854 (w), 761 (vs), 685 (w), 640 (s), 461 (w). Elem. Anal. Calcd for $C_{44}H_{93}Ni_3N_{15}O_{25}$ (FW = 1408.4 g/mol) C, 37.52; H, 6.66; N, 14.92%. Found: C, 37.66; H, 5.95; N, 14.35%.

To obtain the desolvated form for the catalytic tests and spectroscopic measurements, the as-synthesized samples were thermally activated by heating them for 18 h at 150 °C and 10^{-6} bar.

6.2.6 Synthesis of $[Cu_3(BTP)_2]\cdot 8CH_3OH\cdot 10H_2O$

$[Cu_3(BTP)_2]\cdot 8CH_3OH\cdot 10H_2O$ was isolated according to the synthetic path recently reported in the literature[12].

IR (neat, cm^{-1}) 3370 (br), 1608 (vs), 1557 (w), 1426 (w), 1385 (w), 1354 (w), 1322 (w), 1243 (w), 1180 (w), 1126 (s), 1061 (vs), 1012 (vs), 946 (w), 832 (s), 758 (vs), 681 (w), 637 (w), 460 (w). Elem. Anal. Calcd for $C_{38}H_{70}Cu_3N_{12}O_{18}$ (FW = 1173.70 g/mol) C, 38.89; H, 6.01; N, 14.32%. Found: C, 38.56; H, 5.63; N, 14.66%.

To obtain the desolvated form for the catalytic tests, the as-synthesized batches were thermally activated by heating them for 18 h at 150 °C and 10^{-6} bar.

6.2.7 Catalytic tests

HMF, DFF, sodium hydroxide, and benzyl alcohol were used in the catalytic tests. The oxidation reaction was performed using a Parr Instruments autoclave reactor of 100 mL capacity equipped with a mechanical stirrer (0−600 rpm) and an apparatus to measure temperature and pressure. A solution of HMF (0.205 g, 1.8 mmol) in water (25 mL) was charged in the reactor. Then, the appropriate amount of catalyst (0.180 g, corresponding to 0.7, 0.6, and 0.7 mmol of Ni in **[Ni(BDP)]**,

[Ni(BPEB)], and **[Ni_3(BTP)$_2$]**, respectively) was added. The autoclave was purged 3 times with O_2 (5 bar), then pressurized at 30 bar. The temperature was increased up to 120 °C, and the reaction mixture was stirred at *ca.* 400 rpm for 24 h. Once the reaction was finished, the autoclave was cooled down to room temperature, and the suspension was filtered. CH_3CN (25 mL) was added to the reaction mixture before filtration to increase the solubility of DFF (DFF is slightly soluble in water). The recovered catalyst was washed with CH_3CN in order to remove the product that could have remained absorbed onto it. The obtained solution was analyzed with an Agilent Infinity 1260 liquid chromatograph equipped with a 4.6 × 50 mm C18 Poreshell 120 column, using 40 vol % CH_3CN and 60 vol % water as mobile phase. The compounds were identified by calibration using commercial samples as references. The oxidation of benzyl alcohol was carried out in a high pressure stainless-steel autoclave of 50 mL capacity. Benzyl alcohol (0.512 g, 47.0 mmol) and **[Ni_3(BTP)$_2$]** (0.069 g, 0.049 mmol) were charged in the autoclave. The latter was purged 3 times with O_2 (5 bar), then pressurized at 30 bar. The temperature was increased up to 120 °C, and the reaction mixture was stirred at *ca.* 400 rpm for 1 or 18 h. The analysis of the obtained products was performed as already described for the oxidation of HMF.

6.2.8 In situ DRIFT spectroscopy

As a general procedure, in order to remove all the adsorbed molecules, a sample of MOF was loaded and pretreated at 150 °C under a flow of He (10 mL/min) for 45 min and then cooled down to 85 °C. The background was measured and, immediately after, a pulse of ethanol (1 µL) was introduced. To follow the adsorption process, IR spectra were acquired at 0.5 min time intervals. Afterward, the carrier gas was let flowing until weakly adsorbed ethanol was evacuated. The IR spectrum acquired after reaching this condition was used to compare the behaviour of the catalysts.

6.2.9 FT-IR monitoring of adsorption of a probe molecule in vacuum

Catalyst samples were pressed into self-supported wafers and activated *in situ* in the IR cell for 30 min at the maximum temperature of 150 °C and under vacuum (≤ 10^{-6} mbar). Then, at room temperature, the activated samples were put into contact with an increasing amount of benzyl alcohol. Finally, desorption spectra were recorded at increasing temperatures, from room temperature up to 150 °C.

6.2.10 PXRD monitoring of ethanol-impregnated MOFs

Samples of the MOFs (0.020 g) were ground in an agate mortar. Then, they were deposited in the hollow of a silicon zero-background plate. Preliminary acquisitions were carried out in the 2θ range 3-35° with a step of 0.02° and a time per step of 0.5 s. Then ethanol was added dropwise with the incipient wet impregnation technique. The sample was then laid down again on the sample-holder. PXRD patterns were acquired, using the same conditions as above, at different time intervals. Le Bail refinements were carried out on the acquired data with the software TOPAS-R[16].

6.3 Results and discussion

6.3.1 Overview on the structure of the catalysts

In order to better understand the catalytic properties of the MOFs, a quick overview of their crystal structures at room temperature and upon raising the temperature is presented.

[Ni(BPEB)][11] and **[Ni(BDP)]**[10] are isostructural. Both MOFs show a 3-D porous network with PtS topology (**Figure 6.2**). The network features 1-D rhombic channels 5.4×6.8 and 7.0×11.3 $Å^2$ wide, in **[Ni(BDP)]** and **[Ni(BPEB)]**, respectively, affording an empty volume amounting to 57 and 70%. Furthermore, they are stable in air up to 460 and 422 °C, respectively. VT-PXRD analyses evidenced a limited breathing[17] and a maximum variation of the unit cell volume of 1.0 % (in the temperature range 30−410 °C) and −0.8% (in the temperature range 30−290 °C), in **[Ni(BDP)]** and **[Ni(BPEB)]**,

respectively, before decomposition. **[Ni(BPEB)]** showed a Langmuir specific surface area of 2378 m^2/g at 1 bar, while **[Ni(BDP)]** showed a Langmuir specific surface area of 1600 m^2/g at 1 bar.

{[$Ni_3(BTP)_2$]·S}[12] and **{[$Cu_3(BTP)_2$]·S}**[12] possess a 3-D (4,6)-connected network with sodalite (**sod**) topology (**Figure 6.3**), in which the nodes are formed by square piramidal NiN_4O moieties. 1-D cylindrical channels 10.3×10.3 $Å^2$ wide run along all the three crystallographic axes; small octahedral cavities (1.9×1.9 $Å^2$) are present around the 1-D channels. VT-PXRD analyses showed absence of breathing: indeed the framework is rigid with a shrinkage of the unit cell volume, in the case of the Ni(II) derivative, of only 0.5% (in the temperature range 30−410 °C), probably due to the loss of solvent. After removal of the solvent, **[$Ni_3(BTP)_2$]** turns out to be porous, possessing a Langmuir specific surface area of 1900 m^2/g at 1 bar.

6.3.2 Catalytic tests

NaOH is thought to be essential for the selective oxidation of HMF to DFF when metal catalysts are used[18]. Accordingly, preliminary tests with **[$Ni_3(BTP)_2$]** as catalyst were performed using different amounts of NaOH in water. Oddly, the presence of NaOH degradates the catalyst (PXRD evidences) in the essayed experimental conditions (see **Table 6.1**, entries 1-3). In order to avoid the degradation of the catalysts, base-free reaction conditions were used: worthy of note, the absence of NaOH is considered as an added value[19] in the continuous search for environment-friendly catalytic systems. Consequently, the other parameters and reactants, namely temperature, oxygen pressure and reaction time, were increased in order to compensate the absence of the base. In order to demonstrate the catalytic activity of our MOFs, $Ni(NO_3)_2·6H_2O$ was used as source of nickel (**Table 6.1**, entry 4), and a blank test was performed in the absence of any catalyst (**Table 6.1**, entry 5). As expected, the latter test did not show any conversion, while the former one showed complete conversion of HMF into organics containing chromophores, as evidenced by UV−Vis spectroscopy, but no conversion towards the desired product, namely DFF, nor other typical oxidation products of HMF was observed.

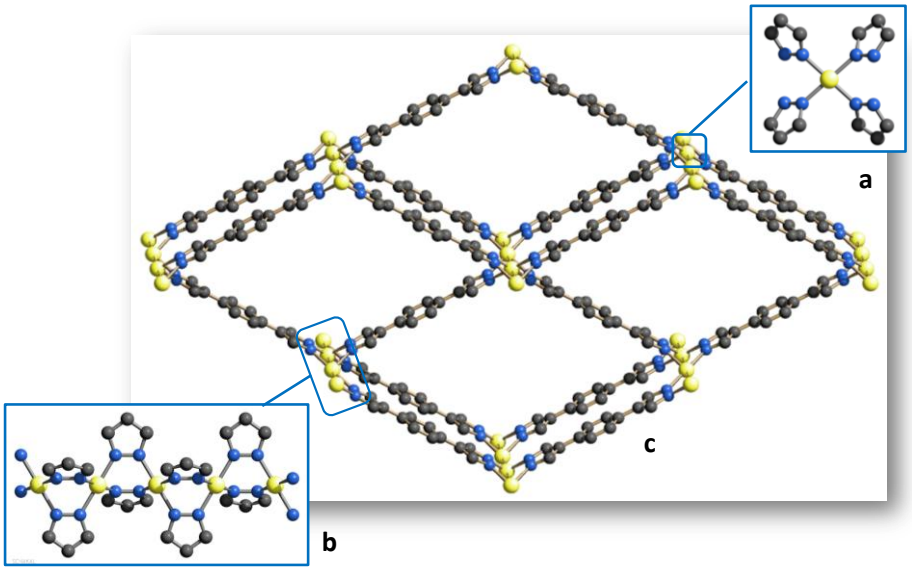

Figure 6.2: Representation of the crystal structure of **[Ni(BDP)]**: a) the NiN_4 node; b) portion of the 1-D chain of collinear metal ions; c) portion of the crystal packing viewed, in perspective, along the [100] direction; the 1-D rhombic channels can be appreciated. Carbon, grey; nickel, yellow; nitrogen, blue. The hydrogen atoms and the solvent molecules have been omitted for clarity.

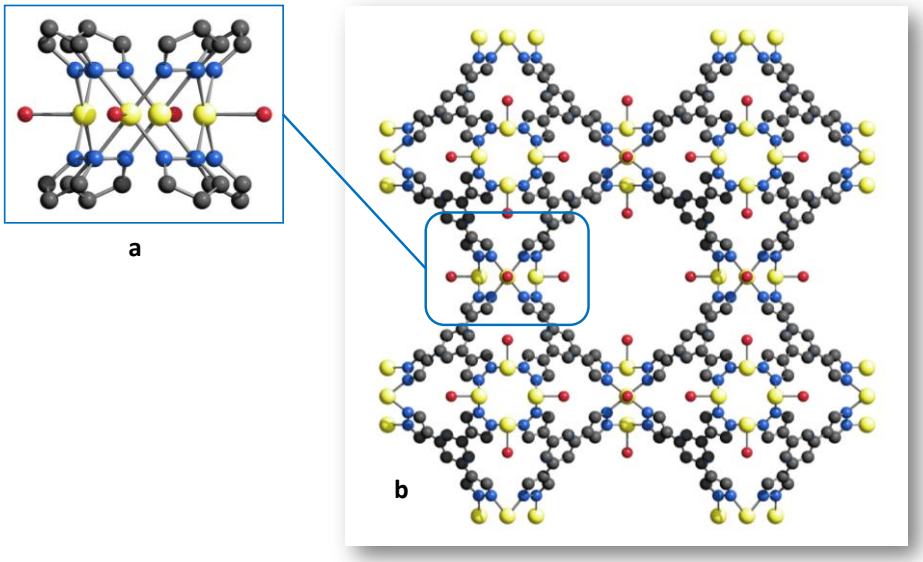

Figure 6.3: Representation of the crystal structure of **$[Ni_3(BTP)_2]\cdot S$**: a) the $Ni_4N_{16}O_4$ node; b) portion of the crystal packing viewed along the [100] direction; both the octahedral cavities and one of the 1-D channels can be appreciated. Carbon, grey; nickel, yellow; nitrogen, blue; oxygen, red. The hydrogen atoms and the solvent molecules have been omitted for clarity, except the oxygen atom of the solvent molecule bound to the metal center.

By comparing the activity of **[Ni(BDP)]**, **[Ni(BPEB)]**, **[$Ni_3(BTP)_2$]** and **[$Cu_3(BTP)_2$]**, different activities were noticed. As shown in **Table 6.2**, **[$Ni_3(BTP)_2$]** is the most active catalyst, yielding 3% of DFF in 8 h and up to 27% of DFF in 24 h, with a selectivity towards DFF close to 100% without the presence of any undesired products. More important, the catalyst is recovered intact (PXRD evidences). To prove the activity and the selectivity of **[$Ni_3(BTP)_2$]**, we also used **[$Ni_3(BTP)_2$]·S]**, the non evacuated MOF, as catalyst. Obviously, the conversion resulted to be lower, but the selectivity remained very high, **Table 6.2**, entry 3. This occurrence demonstrates that the unsaturated coordination site plays a key-role in the development of the catalytic reaction; indeed, the saturation decreases the reaction yields. **[Ni(BPEB)]** showed a very high selectivity, see **Table 6.2**, close to 100%, but after 24 h of reaction it yielded only 3% of DFF. Moreover, after the catalytic cycle, the catalyst had partially lost crystallinity (PXRD evidences).

entry	catalyst	T (°C)	P_{O2} (bar)	T (h)	NaOH (eq)	HMF conv (%)	DFF yield (%)
1	**[$Ni_3(BTP)_2$]**	100	10	4	4	HMF degradation	0
2	**[$Ni_3(BTP)_2$]**	100	10	4	2	HMF degradation	0
3	**[$Ni_3(BTP)_2$]**	100	10	4	1	HMF degradation	0
4	[$Ni(NO_3)_2·6H_2O$]	120	30	24	0	100	0
5	none	120	30	24	0	0	0

Table 6.1: Results of the preliminary catalytic tests carried out with **[$Ni_3(BTP)_2$]** and with an inorganic source of nickel ([$Ni(NO_3)_2·6H_2O$]) as catalyst, as well as of the blank test in the absence of any catalyst.

One possible explanation of this difference of activity between **[$Ni_3(BTP)_2$]** and **[Ni(BPEB)]**, assuming that the ambient conditions structural features are strictly maintained, is the different accessibility of the unsaturated metal sites in the two frameworks. Anyway, due to the known flexibility of MOFs sharing the same topology of **[Ni(BPEB)]** in response to external stimuli[20], the existence of a closed-pore form under the essayed experimental conditions cannot be excluded. Lastly, the catalytic activity could be strongly influenced by the degree of crystallinity of the two materials: the lower the

degree of crystallinity, the shorter the coherence domains in which the catalytically active centers are periodically and homogeneously distributed (as a matter of fact the average crystal size for **[$Ni_3(BTP)_2$]** and **[Ni(BPEB)]** is 100 and 20 nm, respectively). Finally, **[Ni(BDP)]** is inactive, as it undergoes degradation to a low-crystallinity phase in the reaction conditions (PXRD evidences), probably inhibiting the catalytic activity of the MOF.

In order to demonstrate the importance of nickel as active catalyst, **[$Cu_3(BTP)_2$]**, isostructural to **[$Ni_3(BTP)_2$]**, was also tested. **[$Cu_3(BTP)_2$]** catalyzed the formation of DFF with a lower yield and selectivity (**Table 6.2**, entry 6) than **[$Ni_3(BTP)_2$]**. This test confirmed the importance of the presence of nickel active sites for the selective oxidation of HMF to DFF using MOF catalysts.

entry	catalysts	HMF conv. (%)	DFF yield (%)	DFF sel. (%)
1	**[$Ni_3(BTP)_2$]**[a]	3	3	>99
2	**[$Ni_3(BTP)_2$]**[b]	27	27	>99
3	**[$Ni_3(BTP)_2$]·S**[b]	11	11	>99
4	**[Ni(BPEB)]**[b]	3	3	>99
5	**[Ni(BDP)]**[b]	0	0	0
6	**[$Cu_3(BTP)_2$]**[b]	38	11	29

a) Reaction conditions: 120 °C, 30 bar O_2, 8 h, water as solvent.
b) Reaction conditions: 120 °C, 30 bar O_2, 24 h, water as solvent.

Table 6.2: Results of the catalytic tests carried out with the three Ni-based MOFs and with the copper homologue of **[$Ni_3(BTP)_2$].**

To futher prove the catalytic activity of **[$Ni_3(BTP)_2$]** in oxidation reactions, the model reaction of benzyl alcohol oxidation to benzaldehyde was performed affording 7 and 13% yields after 1 and 18 h of reaction.

6.3.3 *In situ* DRIFT spectroscopy

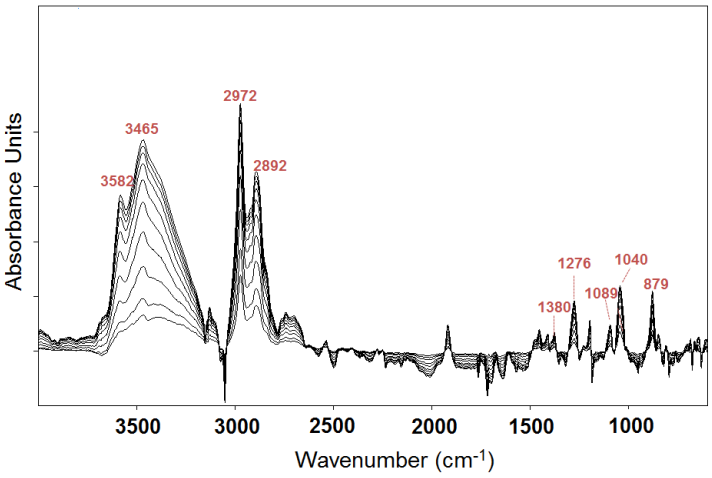

Figure 6.4: Evolution of the DRIFT spectra acquired at 85 °C on the clean surface of **[Ni_3(BTP)$_2$]** during ethanol adsorption.

In order to evaluate the different adsorbent–adsorbate interactions in **[Ni_3(BTP)$_2$]** and **[Ni(BPEB)]** to explain their different catalytic activity, we performed *in situ* DRIFT experiments, using ethanol as probe molecule. The spectra acquired at 85 °C during ethanol adsorption on the clean surface of thermally activated **[Ni_3(BTP)$_2$]** are shown in **Figure 6.4**: the most relevant bands detected during the experiment, together with their assignment, are listed in **Table 6.3**. As easily appreciable from the obtained data, three events take place during adsorption: *i*) new hydrogen bond interactions are detected by the growth of the bands centered at 3582 and 3465 cm^{-1}, demonstrating the insurgence of an interaction of the probe molecule with the MOF. In addition, the dissociation of ethanol to ethoxylate is suggested by the insurgence and growth of bands in the 1090–1040 cm^{-1} region, which can be confidently ascribed[21] to the C–O and C–C stretching of ethoxylate. Last but not least, and definitely more interesting is the insurgence and growth of a new band peaked at 879 cm^{-1}, which can be interpreted as the Ni–O(H) stretching[21], revealing that the probe molecule directly interacts with the metal centers through it oxygen atom.

vibrational frequency (cm^{-1})	vibrational mode	assignation
3582	*v* OH	free OH (NH)
3465	*v* OH	H-bonded ethanol
2972	$\nu_{(as)}$ CH_3	ethoxylate
2892	$\nu_{(s)}$ CH_3	ethanol/ethoxylate
1379	δ CH_3	ethanol
1275	δ OH	ethanol
1094	$\nu_{(as)}$ CO/ $\nu_{(as)}$ CC	ethoxylate
1043	$\nu_{(s)}$ CO	ethoxylate
879	δ Ni-OH	ethanol/ethoxylate-Ni

Table 6.3: assignment of the IR bands observed during adsorption of ethanol at 85 °C on the clean surface of thermally activated **[Ni_3(BTP)$_2$]**.

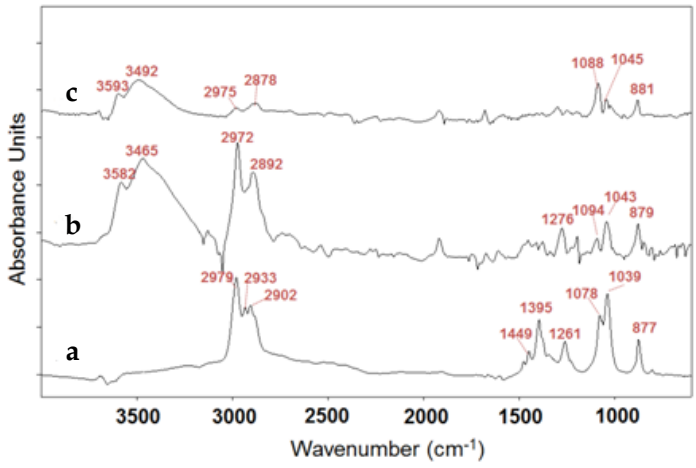

Figure 6.5: DRIFT spectra acquired at 85 °C, after ethanol pulse and successive flushing, on the clean surface of **a**) $NiCl_2$; **b**) **[Ni_3(BTP)$_2$]** and **c**) **[Ni(BPEB)]**.

Experimental observations and already reported theoretical calculations[22] could explain the insurgence of Ni–O(H) interactions between **[Ni_3(BTP)$_2$]** and the Lewis basic probe. The insurgence of Ni(II)-probe interaction were not observed by Shearer and coworkers when probing **[Ni_3(BTP)$_2$]** with the weak Lewis base CO, by means of FT-IR spectroscopy. The absence of a positive electrostatic potential on the Ni_4 nodes when Ni(II) is in low-spin state (typical for Ni(II) in square planar coordination), could be the reason why no interactions were observed. A positive region could be conversely calculated under the assumption that the metal centers were in high-spin state. If a switch from low-spin to high-spin state is at work when the Ni–O bond is formed, then more basic probes such as ethanol/ethoxylate[23] might establish Ni(II)-probe interactions energetic enough to overcome the 75 kJ[22] necessary to a mol of Ni(II) ions to undergo the switch, in spite of the higher kinetic diameter of ethanol versus CO (4.5 vs 3.3 Å, respectively). Also in the case of **[Ni(BPEB)]**, the bands peaked at 1088 and 1045 cm^{-1} (**Figure 6.5a**) indicate partial dissociation of the alcohol, but the intensity of the bands associated to the formation of hydrogen bond interactions, centered at 3593 and 3492 cm^{-1}, and the band associated to the formation of Ni-O(H) interactions, are less pronounced than in the previous case, suggesting less pronounced interactions between the adsorbent and the adsorbate.

Given the fact that **[Ni(BPEB)]** and **[Ni(BDP)]** are isostructural and their metal centers possess very similar stereochemistry and second shell environment, experimental observations and already reported theoretical calculations[24] already performed for **[Ni(BDP)]** could explain the insurgence Ni–O(H) interactions between **[Ni(BPEB)]** and the Lewis basic probe. The presence of a positive electrostatic potential around the low-spin state metal centers (the negative cavities near the Ni(II)

ions are partially shielded by the ligands) is addressed by Albanese and colleagues[24] to explain the lack of insurgence of metal-probe interactions between **[Ni(BDP)]** and the apolar probe H_2 or the weak Lewis acid CO_2. In spite of the positive electrostatic potential around the metal centers, even the weak base CO underwent only physisorption; the amount of energy (65 kJ per mol of Ni(II) ions) required to switch from low-spin to high-spin state could be the reason of this occurrence. On the basis of this assumption, if a switch from low-spin to high-spin state is at work when the Ni–O bond is formed, then stronger bases such as ethanol or ethoxylate might establish Ni(II)–probe interactions energetic enough to promote the switch.

To further confirm the insurgence of Ni(II)–ethanol interactions on **[$Ni_3(BTP)_2$]** and **[Ni(BPEB)]**, the same experiment was performed over $NiCl_2$. As expected, FT-IR monitoring of the adsorption on $NiCl_2$ (**Figure 6.5c**) revealed the insurgence and progressive growth of a band centered at 877 cm^{-1}. The different accessibility of the metal centre of the two MOFs is confirmed by the higher difficulty faced by ethanol to be adsorbed on **[Ni(BPEB)]** rather than on **[$Ni_3(BTP)_2$]**. This occurrence was already suggested by the crystallographic features: as a matter of fact, despite both MOFs possess a square planar coordination sphere, in **[Ni(BPEB)]** the free coordination site is obstructed by the two nearest metal ions along the 1-D chain (**Figure 6.6**), while, in desolvatated **[$Ni_3(BTP)_2$]**, the free coordination site shows a higher accessibility (**Figure 6.6**).

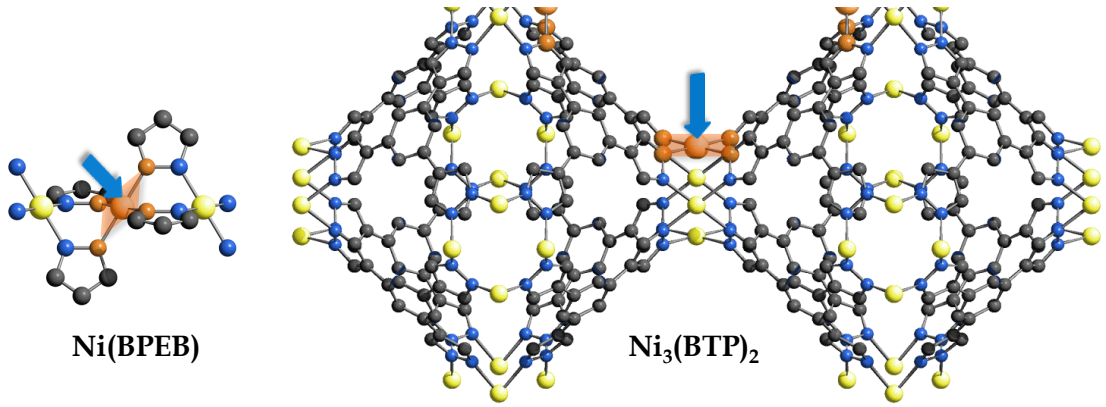

Figure 6.6: Portion of the crystal structure of **[Ni(BPEB)]** and **[$Ni_3(BTP)_2$]**, showing the different accessibility of the square planar Ni(II) sites in the two cases, as indicated by the green arrows.

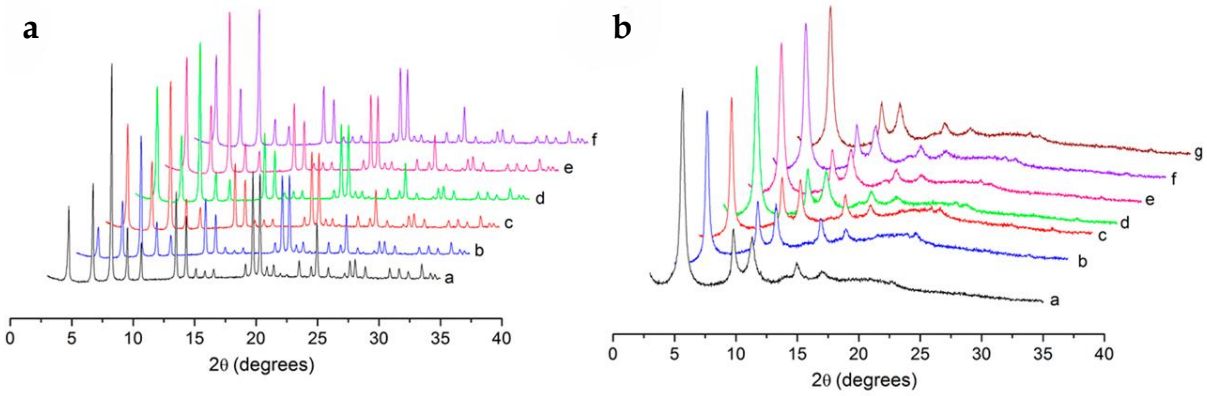

Figure 6.7: PXRD monitoring of **a**) **$[Ni_3(BTP)_2]$** and **b**) **[Ni(BPEB)]** after impregnation with ethanol. In both **a** and **b**: trace a, before impregnation; trace b, after impregnation and drying; trace c, after 30 min from drying; trace d, after 2 h from drying; trace e, after 4 h from drying; trace f, after 24 h from drying; trace g, after 36 h from drying.

As further experiment to understand this aspect, PXRD monitoring was performed on thermally activated **[Ni(BPEB)]** and **$[Ni_3(BTP)_2]$** impregnated with ethanol. During the adsorption of ethanol on **$[Ni_3(BTP)_2]$**, as suggested by the variation of the relative intensity of the low-angle peaks, the probe enters the pores, even if the unit cell volume is almost unaffected (shrinking by only −0.1%) (**Figure 6.7a**), while a breathing effect is observed for **[Ni(BPEB)]**: impregnation causes an initial increment of the unit cell volume (**Figure 6.7b**), namely 2.1% after 2 h, followed by shrinkage (by −2.8% after 6 h), as highlighted by Le Bail refinements.

For the sake of completeness, FT-IR monitoring of ethanol adsorption was performed under the same experimental conditions also on **$[Ni_3(BTP)_2]$·S**: as expected, the behaviour of the solvatated form is the same of **$[Ni_3(BTP)_2]$**, namely, insurgence of hydrogen bond interactions, partial deprotonation of the probe, and formation of Ni–O(H) bonds. Notably, the band ascribed to the presence of Ni-O(H) bonds is more intense for the activated adsorbent, while the bands ascribable to the ethoxylate are more intense for the non

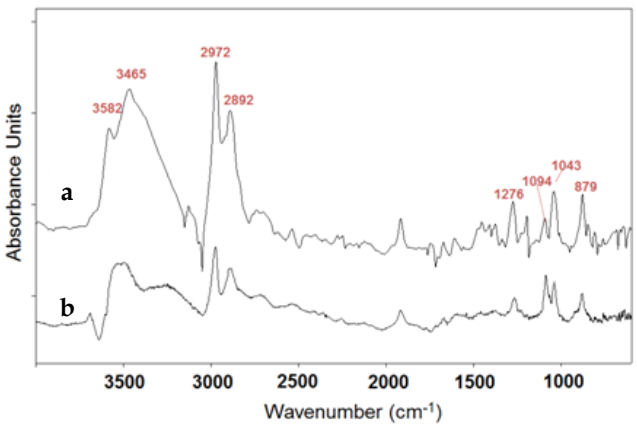

Figure 6.8: DRIFT spectra acquired at 85 °C, after ethanol pulse and successive flushing, on the clean surface of **a**) activated and **b**) non-activated **$[Ni_3(BTP)_2]$**.

activated one: this occurrence confirms the importance of the open coordination site in the catalytic activity of the MOF, demonstrating the reason why **$[Ni_3(BTP)_2]\cdot S$** is less active than the evacuated counterpart.

6.3.4 FT-IR monitoring of adsorption of benzyl alcohol in vacuum

To confirm the investigation reported above, further FT-IR experiments were performed under vacuum in the presence of a probe molecule. HMF was initially chosen as probe molecule but, due to its high boiling point (114-116 °C at 1 mbar), the planned experiment was unfeasible. Benzyl alcohol was chosen as substitute of HMF because of its lower boiling point, 205 °C at 1 bar; notably, it is the organic molecule best resembling HMF because it owns both the aromaticity and the O-H functionality. In order to evacuate all the water molecules eventually adsorbed from air, both MOFs samples were thermally activated, heating them up to 150 °C *in vacuo* for 30 minutes. FT-IR spectra were collected during the thermal activation: while for **[Ni(BPEB)]** no significant modifications are observed, for **$[Ni_3(BTP)_2]$** some changes in the FT-IR spectra are spotted (**Figure 6.9**).

The disappearance of the bands in the range 3700–3200 cm^{-1} confirms the loss of water molecules (**Figure 6.9a**). Consequently, the bands ascribable to the aromatic C-H stretching in the range 3160-3050 cm^{-1} become more clearly visible. Further modifications can be noticed in the range 1800–450 cm^{-1} (**Figure 6.9b**) and 1050–750 cm^{-1}. In the former range, the temperature increase brings about a sharpening and an ipsochromic shift (to 1675 cm^{-1}) of the broad peak initially centered at 1668 cm^{-1},

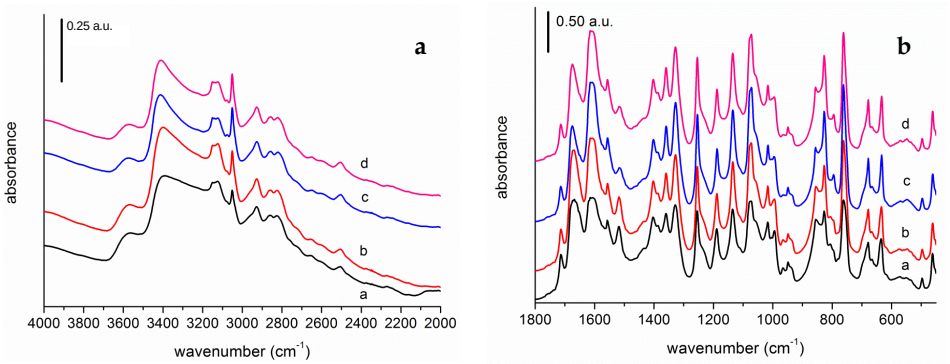

Figure 6.9: FT-IR spectra acquired during thermal activation of **$[Ni_3(BTP)_2]$**: **a**) the 4000-2000 cm^{-1} range; **b**)the 1800-450 cm^{-1} range. Black line, RT; red line, 100 °C; blue line, 150 °c; fuchsia line, RT post treatment

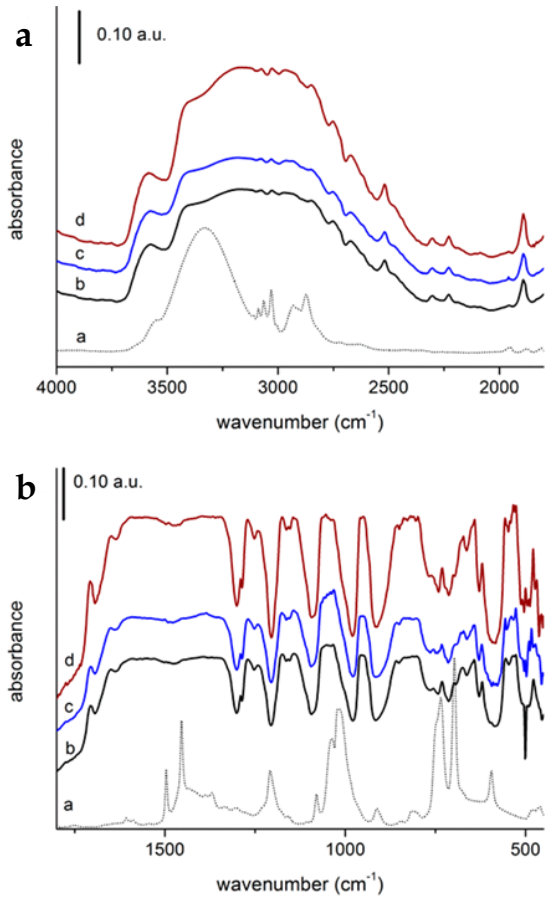

Figure 6.10: FT-IR spectra acquired during adsoption and desoption of benzyl alcohol on **[Ni(BPEB)]**: **a**) 4000−1850 cm^{-1} range; **b**) 1850−450 cm^{-1} range. In both **a** and **b**, spectrum a, pure benzyl alcohol; spectrum b, thermally activated **[Ni(BPEB)]**; spectrum c, benzyl alcohol adsorption; spectrum d, benzyl alcohol desorption at ambient temperature.

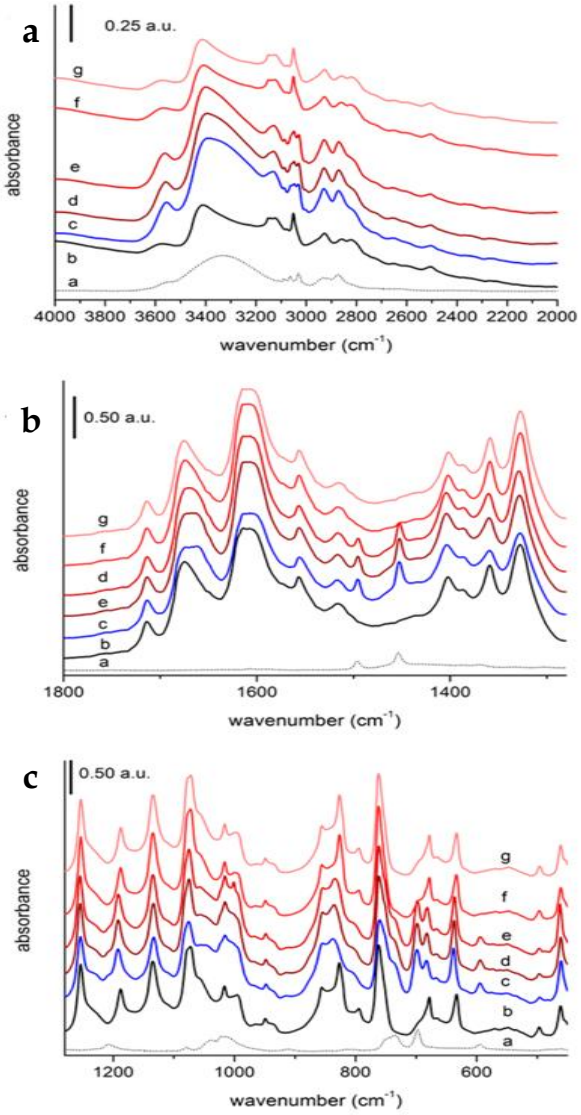

Figure 6.11: FT-IR spectra acquired during the adsoption and desorption of benzyl alcohol on **$[Ni_3(BTP)_2]$**: (**a**) 4000−2000 cm^{-1} range; (**b**) 1800−1250 cm^{-1} range; (**c**) 1250−450 cm^{-1} range. In **a** − **c** : spectrum a, pure benzyl alcohol; spectrum b, thermally activated **$[Ni_3(BTP)_2]$**; spectrum c, benzyl alcohol adsorption; spectra d−g, benzyl alcohol desorption at ambient temperature and 50, 100, and 150 °C, respectively.

while in the latter region (**Figure 6.9b**) the bands peaked at 995, 967, 806, and 781 cm^{-1} undergo a severe intensity drop or even a complete disappearance.

The adsorption and the desorption of benzyl alcohol was carried out on both catalysts *in vacuo*. Adsorption was performed at room temperature, while desorption was performed by increasing the temperature up to 150 °C. The spectra are shown in **Figure 6.10** for **[Ni(BPEB)]** and **Figure 6.11** for **$[Ni_3(BTP)_2]$**. To facilitate the comparison, the spectra of benzyl alcohol and of thermally activated

MOFs are reported as references. As easily gathered from the spectra, no adsorption of benzyl alcohol was observed when **[Ni(BPEB)]** was tested (**Figure 6.10**). The low activity of **[Ni(BPEB)]** towards HMF is then upheld also by this experiment. The bigger kinetic diameter of benzyl alcohol, 6-7 Å, with respect to that of ethanol, 5.5 Å, may explain the different interactions with **[Ni(BPEB)]**. Conversely, as shown in **Figure 6.11**, during the adsorption of benzyl alcohol on **[$Ni_3(BTP)_2$]** the insurgence of bands ascribed to the probe molecule is observed. To facilitate the interpretation, in **Table 6.4** the main IR bands are listed for pure, thermally activated **[$Ni_3(BTP)_2$]**, pure benzyl alcohol, and **[$Ni_3(BTP)_2$]** after adsorption, together with their assignments[22,25]. The comparison between the IR spectra (**Figure 6.11**) emphasizes four main fenomena: *i)* the insurgence of the new bands (bold values in **Table 6.4**) attributable to the vibrational frequencies of benzyl alcohol. These bands undergo only modest shifts, symptom that the alcohol is barely perturbated by the interaction with **[$Ni_3(BTP)_2$]**; *ii)* the intensity of the bands of the catalyst undergo significant modification during the adsorption of benzyl alcohol, and are restored during desorption already at 100 °C, demonstrating the insurgence of reversible adsorbate-adsorbent interactions; in particular, the bands peaked at 496 and 462 cm^{-1}, relative to the Ni–N symmetric stretching and to N-Ni-N bending in plane, respectively, undergo a reversible increase of the intensity. The perturbation of the coordination sphere of Ni(II) is suggested by this occurrence, which supports the formation of interactions between the probe molecule and the metal ion. Finally, after the desorption process, the original coordination sphere of the metal centres is restored; *iii)* the bands corresponding to the N–C–H bending out of phase in plane, peaked at 1188 cm^{-1}, and the bands corresponding to the aromatic C–C–C bending out of phase out of plane and the inter-ring C–C–C bending, peaked at 679 and 633 cm^{-1}, undergo a significant shift towards higher values, symptom that also the aromatic core of the ligand is perturbed by the interaction with the probe molecule; *iv)* new bands not ascribable to either the pure catalyst or benzyl alcohol appear in the spectrum, namely at 3550 cm^{-1}, 3128 cm^{-1} and 838 cm^{-1}. The first band can be assigned to a free O-H stretching, the second one can be reasonably assigned to an N-H stretching vibrational mode and the latter one can be related to the

formation of an Ni-O-R bond due to the interaction of the metal site with the oxygen atom of the probe molecule. This interpretation is in agreement with the DRIFT experiments performed with ethanol as probe molecule on **[$Ni_3(BTP)_2$]**. We suggest that benzyl alcohol deprotonates, with the consequently formation of an N-H interaction, while bonding to the metal site, as shown in **Figure 6.12**, as purported by the simultaneous insurgence of the new bands peaked at 3128 and 838 cm^{-1} and the modification of the band peaked at 496 cm^{-1}. Moreover, all the interactions developed between **[$Ni_3(BTP)_2$]** and the probe molecule are fully reversible and weak, as confirmed by the low desorption temperature, 150 °C, which lead to the complete restoration of the original spectrum (**Figure 6.11**).

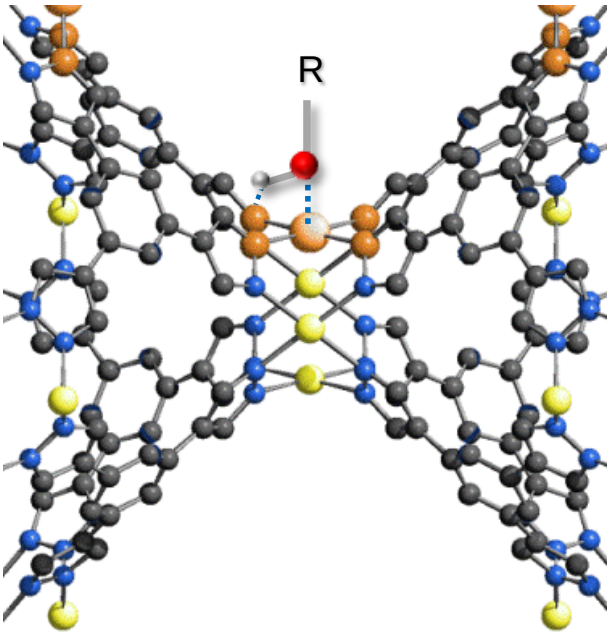

Figure 6.12: Schematic representation of the interaction between the **[$Ni_3(BTP)_2$]** adsorbent and a molecule of adsorbate, as suggested by IR spectroscopy, in term of insurgence of the Ni-O(H) and N-H(O) interactions. Carbon, gray; nitrogen, blue; nichel, yellow; oxygen, red; hydrogen, light grey, except for the highlighted coordination site: nickel and nitrogen, orange.

	Vibrational frequency (cm^{-1})		
		$[Ni_3(BTP)_2]$	
vibrational mode[a]	benzyl alcohol	after activation	after adsorption
v O-H		3572	
v O-H free		3550	3550
v intermolecular hydrogen bonded O-H	3332 (br)	3412 (br)	3396 (br)
v N-H			3128
v aromatic C-H		3152	3152
v aromatic C-H	3088	3121	**3087**
v aromatic C-H	3065	3077	**3062**
v aromatic C-H		3052	3052
v aromatic C-H	3031	3052	**3047**
v methylene C-H	2933	2927	2929
v methylene C-H	2874	2859	**2871**
v inter-ring C-C		1556	1556
v aromatic C=C overlapped with *δ*s CH_2 at *ca.* 1471 cm^{-1}	1496		**1496**
v aromatic C=C overlapped with δs CH_2	1454		**1453**
v sym C-C + *v* asym C-N		1359	1360
v sym C-N		1328	1328
v N-N stretching + *δ* ip C-H		1255	1254
δ O-H possibly augmented by *δ* ip C-H	1209		**1208**
δ op N-C-H		1188	1192
δ ip phenylic H-C-C		1135	1134
δ ip N-C-H bending ip		1074	1075
v C-O	1020		1016
δ ip pyrazolic C-H + *δ* op phenylic		855	856
v Ni-O			838
δ op phenylic C-C-C		762	761
δ op aromatic C-H	736		735
δ aromatic C=C	698		**699**
δ op phenylic C-C-C		679	683
δ inter-ring C-C-C		633	638
v asym Ni-N		496	496
δ ip N-Ni-N		462	461

[a]op = out of phase; ip = in phase

Table 6.4: Assignment of the main FT-IR bands observed for pure benzyl alcohol, thermally activated **$[Ni_3(BTP)_2]$**, and **$[Ni_3(BTP)_2]$** during adsorption of the alcohol in vacuum.

6.4 Conclusions

With these results we have demonstrated that the accessibility of the metal centres plays a key role when MOFs are used as catalysts. More important, we have proved that, in base-free conditions, the active catalytic sites are not only those on the surface of the catalyst, but also those decorating the pore walls. Furthermore, the crystal structure of the MOFs strongly influences the accessibility of the open coordination sites, as highlighted by the different activity of **[Ni(BPEB)]** and **[Ni_3(BTP)$_2$]**. Finally, as a proof of the activity of the metal centres decorating the pore walls we have shown that the activity strongly decreases when the pores are filled with solvent.

Last but not least, we have also proved that the presence of Ni(II) ions is crucial for the catalytic activity in the oxidation reaction studied.

References and Notes

[1] a) Corma, A.; Garcia, H. and Llabres i Xamena, F. X. *Chem. Rev.*, **2010**, *110*, 4606−4655; b) Yoon, M.; Srirambalaji, R. and Kim, K. *Chem. Rev.*, **2012**, *112*, 1196−1231; c) Liu, J.; Chen, L.; Cui, H.; Zhang, L.; Zhang, J. and Su, C.-Y. *Chem. Soc. Rev.*, **2014**, *43*, 6011-6061; d) Chughtai, A. H.; Ahmad, N.; Younus, H. A.; Laypkov, A. and Verpoort, F. *Chem. Soc. Rev.*, **2015**, *44*, 6804−6849.

[2] a) Rose, M.; Hausoul, P. J. C. and Palkovits, R. In Producing fuels and fine chemicals from biomass using nanomaterials; Luque, R., Balu, A. M., Eds.; CRC Press: Boca Raton, FL, **2014**; Chapter 8; b) Alam, M. I. and Saha, B. In Sustainable catalytic processes; Saha, B.; Fan, M., Wang, J., Eds.; Elsevier: Amsterdam, The Netherlands, **2015**; Chapter 4.

[3] Gandini, A. and Belgacem, N. M. *Polym. Int.*, **1998**, *47*, 267−276.

[4] a) del Poeta, M.; Schell, W. A.; Dykstra, C. C.; Jones, S.; Tidwell, R.R.; Czarny, A.; Bajic, M.; Kumar, A.; Boykin, D. and Perfect, J. R. *Antimicrob. Agents Chemother.*, **1988**, *42*, 2495−2499; b) Hopkins, K. T.; Wilson, W. D.; Bender, B. C.; McCurdy, D. R.; Hall, J. E.; Tidwell, R. R.; Kumar, A.; Bajic, M. and Boykin, D. W. *J. Med. Chem.*, **1998**, *41*, 3872−3878.

[5] Amarasekara, A. S.; Green, D. and Williams, L. D. *Eur. Polym. J.*, **2009**, *45*, 595−598.

[6] a) Takagaki, A.; Takahashi, M.; Nishimura, S. and Ebitani, K. *ACS Catal.*, **2011**, *1*, 1562−1565; b) Halliday, G. A.; Young, R. J., Jr. and Grushin, V. V. *Org. Lett.*, **2003**, *5*, 2003−2005; c) Carlini, C.; Patrono, P.; Galletti, A. M. R.; Sbrana, G. and Zima, V. *Appl. Catal. A*, **2005**, *289*, 197−204.

[7] Zhang, Y.; Degirmenci, V.; Li, C. and Hensen, E. J. M. *ChemSusChem*, **2011**, *4*, 59−64.

[8] Fang, R.; Luque, R. and Li, Y. *Green Chem.*, **2016**, *18*, 3152−3157.

[9] a) Gascon, J.; Aktay, U.; Hernandez-Alonso, M. D.; van Klink, G.P. M. and Kapteijn, F. *J. Catal.*, **2009**, *261*, 75−87; b) Chizallet, C.; Lazare, S.; Bazer-Bachi, D.; Bonnier, F.; Lecocq, V.; Soyer, E.; Quoineaud, A.-A. and Bats, N. *J. Am. Chem. Soc.*, **2010**, *132*, 12365−12377; c) Vermoortele, F.; Ameloot, R.; Vimont, A.; Serre, C. and De Vos, D. *Chem. Commun.*, **2011**, *47*, 1521−1523; d) Wang, R.; Liu, X.; Qi, D.; Xu, Y.; Zhang, L.; Liu, X.; Jiang, J.; Dai, F.; Xiao, X. and Sun, D. *Inorg. Chem.*, **2015**, *54*, 10587−10592.

[10] Galli, S.; Masciocchi, N.; Colombo, V.; Maspero, A.; Palmisano, G.; Lòpez-Garzòn, F. J.; Domingo-García, M.; Fernàndez-Morales, I.; Barea, E. and Navarro, J. A. R. *Chem. Mater.*, **2010**, *22*, 1664−1672.

[11] Galli, S.; Maspero, A.; Giacobbe, C.; Palmisano, G.; Nardo, L.; Comotti, A.; Bassanetti, I.; Sozzani, P.; Masciocchi, N. *J. Mater. Chem. A*, **2014**, *2*, 12208−12221.

[12] Colombo, V.; Galli, S.; Choi, H. J.; Han, G. D.; Maspero, A.; Palmisano, G.; Masciocchi, N. and Long, J. R. *Chem. Sci.*, **2011**, *2*, 1311−1319.

[13] a) Dinca, M. and Long, J. R. *Angew. Chem., Int. Ed.*, **2008**, *47*, 6766−6679; b) Dietzel, P. D. C.; Besikiotis, V.and Blom, R. *J. Mater. Chem.*, **2009**, *19*, 7362−7370; c)Bentley, J.; Foo, G. S.; Rungta, M.; Sangar, N.; Sievers, C.; Sholl, D. S. and Nair, S. *Ind. Eng. Chem. Res.*, **2016**, *55*, 5043−5053.

[14] Liu, J.; Chen, L.; Cui, H.; Zhang, J.; Zhang, L. and Su, C.-J. *Chem. Soc. Rev.*, **2014**, *43*, 6011−6061.

[15] Maspero, A.; Galli, S.; Masciocchi, N. and Palmisano, G. *Chem. Lett.*, **2008**, *37*, 956−957.

[16] TOPAS, version 3.0: Bruker AXS: Karlsruhe, Germany, 2005

[17] a) Schneemann, A.; Bon, V.; Schwedler, I.; Senkovska, I.; Kaskel, S. and Fischer, R. A. *Chem. Soc. Rev.*, **2014**, *43*, 6062−6096; b) Ferey, G. and Serre, C. *Chem. Soc. Rev.*, **2009**, *38*, 1380−1399.

[18] a) Davis, S. E.; Zope, B. N. and Davis, R. J. *Green Chem.*, **2012**, *14*, 143−147; b) Pasini, T.; Piccinini, M.; Blosi, M.; Bonelli, R.; Albonetti, S.; Dimitratos, N.; Lopez-Sanchez, J. A.; Sankar, M.; He, Q.; Kiely, C. J.; Hutchings, G. J. and Cavani, F. *Green Chem.*, **2011**, *13*, 2091−2099.

[19] Wan, X.; Zhou, C.; Chen, J.; Deng, W.; Zhang, Q.; Yang, Y. and Wang, Y. *ACS Catal.*, **2014**, *4*, 2175−2185.

[20] a) Schneemann, A.; Bon, V.; Schwedler, I.; Senkovska, I.; Kaskel, S. and Fischer, R. A. *Chem. Soc. Rev.*, **2014**, *43*, 6062−6096; b) Ferey, G. and Serre, C. *Chem. Soc. Rev.*, **2009**, *38*, 1380−1399.

[21] Nakamoto, K. Infrared and Raman Spectra of Inorganic and Coordination Compounds, 3rd ed.; Wiley-Interscience Publication, John Wiley & Sons: New York, **1978**.

[22] Shearer, G. C.; Colombo, V.; Chavan, S.; Albanese, E.; Civalleri, B.; Maspero, A. and Bordiga, S. *Dalton Trans.*, **2013**, *42*, 6450−6458.

[23] The gas-phase proton affinity of ethanol is 788 kJ/mol, in comparison with the value of 596 kJ/mol for CO. Lias, S. G.; Liebman, J. F. and Levin, R. D. *J. Phys. Chem. Ref. Data*, **1984**, *13*, 695−808.

[24] Albanese, E.; Civalleri, B.; Ferrabone, M.; Bonino, F.; Galli, S.; Maspero, A. and Pettinari, C. *J. Mater. Chem.*, **2012**, *22*, 22592−22602.

[25] Silverstein, R. M.; Webster, F. X. and Kiemle, D. J. Spectrometric Identification of Organic Compounds; John Whiley & Sons: New York, **2005**.

Chapter 7
Conclusions

The scientific activity of the Ph. D candidate has been mainly dedicated to three research lines:

I) Synthesis of fluorinated and perfluorinated bis(tetrazole)- and bis(pyrazole)-based ligands, and one triazole spacer, to fabricate and characterize Zn(II)-, Ni(II)-, Cu(II)- and Ag(I)-containing Metal-Organic Frameworks (MOFs) or Coordination Polymers (CPs) to be used as low dielectric constant (low-κ) materials. The porous derivatives were tested also for gas adsorption applications.

II) Synthesis as well as functional characterization of new MOFs to be used as molecular rotors.

III) Study of the performances, as heterogeneous catalysts in the oxidation of alcohols, of three known (pyrazolato)-based MOF possessing exposed metal sites.

I) In the field of low-κ materials, starting from the already known CP **[Ag_2(BTB)]** and MOFs **[Cu(BTB)]**, (**H_2BTB** = 1,4-bis(tetrazolyl)benzene), **[Ni(BPEB)]** and **[Zn(BPEB)]** (**H_2BPEB** = 1,4-bis(1*H*-pyrazolylethynyl)-benzene), we synthesized the fluorinated counterparts, **[Ag_2(FBTB)]** (**FN-PCP-1**), **[Cu(FBTB)]** (**FMOF-3**), (**H_2FBTB** = 1,4-bis(tetrazolyl)-tetrafluorobenzene), **[Ni(BPEBF_4)]** and **[Zn(BPEBF_4)]**, (**H_2BPEBF_4** = 1,4-bis(1*H*-pyrazolylethynyl)-tetrafluorobenzene) possessing the same structural motif of their non fluorinated counterparts. All of these materials were fully characterized by Infrared Spectroscopy (IR), Elemental Analysis (EA), Powder X-Ray Diffraction (PXRD) and Variable-Temperature Powder X-Ray Diffraction (VT-PXRD).

The stability of **FN-PCP-1** and **FMOF-3** was tested under water vapours and in liquid water; their contact angles were estimated; their dielectric properties were investigated not only at ambient conditions, but

also under water vapours; N_2 adsorption isotherms were acquired at 77 K. While powdered samples of **FN-PCP-1** are stable under water vapours for at least 48 days and suspended in water for 3 days, **FMOF-3** samples do not survive to either environment. The experimental contact angle of the silver derivative follows the expected trend: it shows a higher contact angle than the non-fluorinated counterpart, 75° vs. 55°, even if it cannot be classified as superhydrophobic. Due to some experimental difficulties, the contact angle for the Cu derivatives could not be measured. Remarkably, pressed pellets of both materials possess κ values lower than 2.6 at room temperature and 2 MHz.

N_2 adsorption at 77 K confirmed the lack of porosity of **FN-PCP-1**, as highlighted by its crystal structure. Amazingly enough, even if not unique for a material showing permanent porosity, when thermally activated, **FMOF-3** is not pervious to N_2 at 77 K. Moreover, when recovered from 77 K, the sample is light violet, this colour lasting few seconds, then turning to the original (cyan) one. This cyan sample is a monoclinic polymorph of the original orthorhombic phase, which is restored in a few days. This intriguing behaviour prompted us to further test low temperature structural features and adsorption performances of **FMOF-3**: these studies are in progress.

Thanks to the ongoing collaboration with Professor Mohammad Omary, at the University of North Texas (UNT), where I have been spent 15 months, the well know compound **FMOF-1** ($\{Ag_2[Ag_4\text{-}Tz_6]\}_n$; Tz: 3,5-bis(trifluoromethyl)-1,2,4-triazolate), the first fluorous MOF ever appeared in the literature, could be fruitfully tested as low-κ material together with **FN-PCP-1** and **FMOF-3**. To complement the studies already performed on **FMOF-1**, we analyzed its thermal stability in air, *via* VT-PXRD experiments, and its dielectric properties. Interestingly, while **FN-PCP-1** and **FMOF-3** preserve their crystal structure when pressed into pellets, **FMOF-1** undergoes progressive amorphization. Due to this inconvenience, the measurements on **FMOF-1** were carried out on a partially amorphous material, affording excellent values lower than 2.2.

As anticipated above, the adsorption behaviour of **FMOF-3** was further investigated: at 298 K, the material adsorbs both CO_2 and CH_4 with different affinity. Interestingly, in none of the two cases saturation is reached. Hence, high pressure measurements (up to 50 bar) have been carried out to complete the

landscape. Finally, to shed light upon the structural changes possibly experienced by **FMOF-3** at 77 K, *ad hoc* neutron diffraction experiments were carried out at the Oak Ridge National Laboratory, by varying temperature, gas probe (CX_4, X_2, X = H, D) and pressure. Presently, we are working on the obtained data.

Adsorption measurements were performed also on **[Ni(BPEBF$_4$)]** and **[Zn(BPEBF$_4$)]** and the results were compared to those obtained on their non-fluorinated counterparts. Interestingly, even if the fluorinated MOFs show a lower specific surface area than the non-fluorinated ones and a lower degree of crystallinity, their uptake of CO_2, at 195 K expressed as cm^3/mol, is perfectly comparable (for the Ni(II) derivative) or even higher (for the Zn(II) derivative when $p/p^0 > 0.2$).

Finally, a new perfluorinated tetrazole ligand was designed and prepared: 1-(1*H*-tetrazolyl)-perfluorobenzene was synthesized and fully characterized. Its Ag(I) and Zn(II) derivatives were subsequently prepared. The Py solvate of the Ag(I) derivative and the ZN(II) derivative were characterized by single crystal X-ray diffraction. Stability tests and dielectric measurements are in progress on this two derivatives.

II) In the field of molecular rotors, despite some synthetic difficulties due to the high fluorination of the precursors, three new pyrazolyl-containing derivatives were isolated and characterized, namely, 1,4-bis(1*H*-pyrazolylethynyl)-2-fluorobenzene (**H$_2$BPEBF**), 1,4-bis(1*H*-pyrazolylethynyl)-2,3-difluorobenzene (**H$_2$BPEBF$_2$**) and [$^2H_4$]-1,4-bis(1*H*-pyrazolylethynyl)benzene (**H$_2$BPEB-*d4***). Zn(II) and Ni(II) derivatives of **H$_2$BPEBF** and the Zn(II) derivative of **H$_2$BPEB-*d4*** were synthesized; their crystal structure and thermal behaviour were characterized by PXRD and Simultaneous Thermal Analyses. Solid-state NMR studies were performed to test them as potential molecular rotors, while gas adsorption experiments were carried out to study their textual properties. These experiments were carried out in the laboratories of Prof. Piero Sozzani and Prof. Angiolina Comotti at Università degli Studi di Milano Bicocca. Further analyses are ongoing for the already characterized MOFs and synthetic attempt to construct MOFs with **H$_2$BPEBF$_2$** as spacer are in progress.

III) The already known porous MOF **[Ni$_3$(BTP)$_2$]** (**H$_3$BTP** = 1,3,5-tris(1*H*-pyrazolyl)benzene) exhibits an expanded sodalite-like (hence porous) framework with exposed metal sites, and possesses remarkable

thermal and chemical robustness, being stable in air up to 430 °C, and in boiling aqueous solutions of pH 2 to 14 for at least two weeks. Together with **[Ni(BDP)]**, (**H_2BDP** = 1,4-bis(1*H*-pyrazolyl)benzene) and **[Ni(BPEB)]**, we tested it as catalyst. As a case of study, thanks to the expertise of Dr. Carlo Lucarelli, we explored the role of the exposed metal sites when **[Ni_3(BTP)$_2$]**, **[Ni(BDP)]** and **[Ni(BPEB)]** are adopted as heterogeneous catalysts in the oxidation reaction of 5-(hydroxymethyl)furfural (HMF) to obtain 2,5-diformylfuran (DFF), employing standard reaction conditions *yet* in the absence of NaOH. **[Ni_3(BTP)$_2$]** resulted to be the best catalyst because it is able to promote the oxidation toward DFF, the typical result being the complete oxidation toward the carboxylic acid. Notably, the yield after 24 hours, 30%, and the selectivity close to 100% in DFF, is a remarkable result. The formation of the aldehyde was observed also when another probe molecule (benzyl alcohol) was adopted as initial substrate, this suggesting that **[Ni_3(BTP)$_2$]** might catalyze the formation of the aldehyde from a number of alcohols. *In situ* DRIFT and FT-IR monitoring of adsorption of benzyl alcohol in vacuum on **[Ni_3(BTP)$_2$]** demonstrated the existence of preferential interactions between the metal centers and the probe. To prove the importance of having nickel-based active sites, **[Cu_3(BTP)$_2$]**, isostructural to **[Ni_3(BTP)$_2$]**, was also tested. **[Cu_3(BTP)$_2$]** catalyzed the formation of DFF but with lower yield and selectivity than **[Ni_3(BTP)$_2$]**, and with the concomitant formation of still uncharacterized byproducts, confirming that nickel is fundamental for the selective oxidation of HMF using MOF catalysts.

Materials and methods

Unless otherwise stated, all the solvents and reagents were obtained from commercial suppliers and used without further purification. 4-iodo-(1-ethoxyethyl)-pyrazole[1], 1,3,5-tris(1*H*-pyrazol-4-yl)benzene **(H_3BTP)**[2], **Ni_3(BTP)$_2$·3DMF·5CH_3OH·17H_2O**[2], **Ni_3(BTP)$_2$·3CH_3OH·10H_2O**[2], **Cu_3(BTP)$_2$·8CH_3OH·10H_2O**[2], **Cu_3(BTP)$_2$·6H_2O[2],** 1,4-bis(1*H*-tetrazol-5-yl)benzene (**H_2BTB**) [3], **[Cu(BTB)]**,[4] [**Ag_2(BTB)]**,[5] ammonium 3,5-bis(trifluoromethyl)-1,2,4-triazolate (**NH_4Tz**),[6]and **{Ag_2[Ag_4-Tz_6]}$_n$ (FMOF-1)**,[7] were prepared according to previously reported procedures. 1,4-bis(ethynyl)-fluorobenzene[8], 1,4-diiodo-tetrafluorobenzene[9] and 1,4-bis(ethynyl)-tetrafluorobenzene[8,9] were prepared by adaptation of the literature methods. IR spectra were acquired, either in nujol mull or in attenuated total reflectance (ATR) on a diamond, by means of a Nicolet iS10 instrument with a resolution of 1 cm^{-1} in the region 4000-500 cm^{-1}; in the following, band maximum positions are reported in cm^{-1}, while band shapes and intensities are denoted as: s = sharp, br = broad, vs = very strong, s = strong, m = medium, w = weak and vw = very weak. DRIFT experiments were acquired in situ with a Bruker Vertex 70 instrument equipped with a Pike DiffusIR cell attachment. The spectra were recorded using an MCT detector after 128 scans and with a 4 cm^{-1} resolution in the region 4000−450 cm^{-1}. Under vacuum FT-IR spectra were recorded using a PerkinElmer Spectrum One spectrometer after 36 scans with a resolution of 4 cm^{-1} in the region 4000−450 cm^{-1}. ^{1}H spectra were recorded at 400 MHz, ^{19}F spectra were recorded at 376 MHz and ^{13}C(APT) NMR spectra were recorded at 100 MHz on a Bruker Avance 400 spectrometer. ^{1}H, ^{19}F and ^{13}C NMR data are reported as follows: chemical shifts (in ppm, and referenced to internal TMS for ^{1}H and ^{13}C and TFA for ^{19}F), integration, multiplicity (s = singlet, d = doublet, dd = doublet of doublets, dt = doublet of triplet, t = triplet, q = quartet, m = multiplet), and coupling constants ^{n}J (in Hz). Solid-state ^{2}H-NMR spectroscopy experiments were performed on a Bruker 300 Avance spectrometer at 46.07 MHz under a static magnetic field of 7.04 T, using a Bruker 5 mm wide-line probe. Fully relaxed spectra (15 s recycle delay) were acquired with the quadrupolar spin−echo pulse sequence, $(\pi/2)x-t_1-(\pi/2)y-t_2$, with a $\pi/2$ pulse of 2.1 μs and a pulse spacing of $t_1 = t_2 = 30$ μs. The stability and

accuracy of the temperature controller (Bruker B-VT2000) were approximately 1 K. Theoretical simulation of ^{2}H-NMR spectra for a two-site 180° jump model was performed by the program Express 1.0, with a quadrupolar coupling constant of 180 kHz and an asymmetry parameter of $\eta = 0.02$. Nitrogen adsorption−desorption isotherms were measured at 77 K using a Micromeritics ASAP 2020 analyzer. The samples were degassed overnight at 120 °C under vacuum. Specific surface area was calculated using the Brunauer, Emmet, and Teller (BET[10]) model and the Langmuir model. The pore-size distributions were evaluated following non-local density functional theory (NLDFT) analysis for cylindrical pores and the Tarazona method[11]. Thermogravimetric analyses (TGA) and differential scanning calorimetry (DSC) were performed simultaneously with a Netzsch STA 409 instrument under a N_2 flow, in the temperature range 30-900 °C, with a ramp of 5 °C min^{-1}. Elemental analyses were obtained with a Perkin Elmer CHN Analyzer 2400 Series II. Drying *in vacuo* was performed at 10^{-6} mBar (0.6 Pa) Powder X-ray diffraction patterns for preliminary characterization of the isolated batches were recorded on a Bruker AXS D8 Advance diffractometer equipped with Ni-filtered Cu-Kα radiation (λ = 1.5418 Å), a Lynxeye linear position-sensitive detector, and the following optics: primary beam Soller slits (2.3°), fixed divergence slit (0.5°), receiving slit (8 mm). The generator was set at 40 kV and 40 mA.

The dimensions of the channels were estimated, by adopting ordered structural models, as the distance between hydrogen atoms pointing inward the channels and belonging to opposite walls, taking into account the van deer Waals radius of hydrogen. The empty volume was estimated with the software PLATON on the ambient temperature crystal structure, disregarding the presence of solvent molecules. Spek, A. L. PLATON, an integrated tool for the analysis of the results of a single crystal structure determination[12].

References and Notes

[1] Lin, Q.; Meloni, D.; Pan, Y.; Xia, R.; Rodgers, J.; Shepard, S.; Li, M.; Galya, L.; Metcalf, B.; Yue, T.-N.; Liu, P. and Zhou, J. *Org. Lett.*, **2009**, *11*, 1999–2002.

[2] Colombo, V.; Galli, S.; Choi, H. J.; Han, G. D.; Maspero, A.; Palmisano, G. and Masciocchi, N.; Long, J. R. *Chem. Sci.,* **2011**, *2*, 1311–1319.

[3] Demko Z. P. and Sharpless K. B. *J. Org. Chem.*, **2001**, *66*, 7945-7950.

[4] Dincă, M.; Yu, A. F. and Long, J. R. *J. Am. Chem. Soc.,* **2006**, *128*, 8904-8913.

[5] Maspero, A.; Galli, S.; Colombo, V.; Peli, G.; Masciocchi, N.; Stagni, S.; Barea, E. and Navarro, J. A. R. *Inorg. Chim. Acta*, **2009**, *362*, 4340–4346.

[6] Abdul-Ghani, M. M. and Tipping, A. E. *J. Fluorine Chem.* **1995**, *72*, 95-106.

[7] Yang, C.; Wang, X. and Omary, M. A. *J. Am. Chem. Soc.*, **2007**, *129*, 15454-15455.

[8] a) Khan, S. M.; Al-Mandhary, M. R. A.; Al-Suti, M. K.; Corcoran, T. C.; Al-Mahrooqi, Y.; Attfield, J. P.; Feeder, N.; David, W. I. F.; Shankland, K.; Friend, R. H.; Köhler, A.; Marseglia, E. A.; Tedesco, E.; Tang, C. C.; Raithby, P. R.; Collings, J. C.; Roscoe, K. P.; Batsanov, A. S.; Stimsong, L. M. and Marde, T. B. *New J. Chem.*, **2003**, *27*, 140-149; b) Huynh, T. H. V.; Mantel, M. L. H.; Mikkelsen, K.; Lindhardt, A. T.; Nielsen, N. C.; Otzen, D. and Skrydstrup, T. *Org. Lett.*, **2009**, *11*,999–1002.

[9] Neenan, T. X. and Whitesides, G. M. *J. Org. Chem.*, **1988**, *53*, 2489-2496.

[10] Brunauer, S.; Emmett, P. H. and Teller, E. *J. Am. Chem. Soc.*, **1938**, *60*, 309.

[11] Tarazona, P. *Phys. Rev. A*, **1985**, *31*, 2672.

[12] *Acta Crystallogr., Sect. A*, **1990**, *46*, C34; abstract no. MS-02.01.05.

List of publications

"Synthesis, Structural Features and Luminescence Properties of a 1-D Poly(azolato)-based Coordination Polymer" Valentina Colombo, Angelo Maspero, Luca Nardo, Alessia Aprea, Fátima Linares, **Alessandro Cimino**, Simona Galli, *Polyhedron*, 92, (2015), 130–136. doi:10.1016/j.poly.2015.03.021

"Adsorbent-adsorbate Interactions in the Oxidation of HMF Catalyzed by Ni-based MOFs: a DRIFT and FT-IR Insight" Carlo Lucarelli,Simona Galli, Angelo Maspero, **Alessandro Cimino**, Claudia Bandinelli, Alice Lolli, Juliana Velasquez Ochoa, Angelo Vaccari, Fabrizio Cavani, Stefania Albonetti *J. Phys. Chem. C* published on line. doi: 10.1021/acs.jpcc.6b05428

"Fluorescence studies on 2-(het)arylperimidine derivatives" Arianna Maria Giani, Marco Lamperti, Angelo Maspero, **Alessandro Cimino**, Roberto Negri, Giovanni Battista Giovenzana, Giovanni Palmisano, Luca Nardo, *J. Lumin.*, Manuscript accepted; DOI: 10.1016/j.jlumin.2016.07.033.

Aknowledgements

I would like to thank all the people who worked and helped me to reach the results exposed in this Thesis work and contributed directly or indirectly to my growth as a person and as a chemist.

I would like to thanks Prof. Giovanni Palmisano and Prof. Stefano Tollari for the helpful support and all the synthetic advices.

I would like to thank also Prof. Mohammad A. Omary for the support given on the work about the dielectric materials and gas adsorption analyses for poly(tetrazolate) derivatives.

I want to acknowledge all the people at Università degli Studi di Milano, Bicocca: Prof. Piero Sozzani and Prof. Angiolina Comotti's research group, in particular Dr. Silvia Bracco, for the support they have provided for the work on molecular rotors, for the sold state NMR analyses and gas adsorption analyses for poly(pyrazolate) derivatives.

I would like to express my very special thanks to Dr. Carlo Lucarelli and all the people at Università di Bologna for the catalytic studies on MOFs.